

NORTHWESTERN UNIVERSITY

Contributions to modern quantification of seismic sources

A DISSERTATION

SUBMITTED TO THE GRADUATE SCHOOL
IN PARTIAL FULFILLMENT OF THE REQUIREMENTS

for the degree

DOCTOR OF PHILOSOPHY

Field of Earth and Planetary Sciences

By

Nooshin Saloor

EVANSTON, ILLINOIS

June 2020

ABSTRACT

This dissertation addresses problems in the source properties of major earthquakes. It is composed of four largely independent studies.

In chapter 2, we explore the possible theoretical origin of the distance-depth correction $q(\Delta, h)$ introduced 75 years ago by B. Gutenberg for the computation of the body wave magnitude m_b , and still in use today. We synthesize a large dataset of seismograms using a modern model of P -wave velocity and attenuation, and process them through the exact algorithm mandated under present-day seismological practice, to build our own version, q_{SO} , of the correction, and compare it to the original ones, q_{45} and q_{56} , proposed by B. Gutenberg and C.F. Richter. While we can reproduce some of the large scale variations in their corrections, the origin of the small-scale details which they built into them remains mysterious. We discuss a number of possible sources of bias in the datasets used at the time, and suggest the need for a complete revision of existing m_b catalogs.

In chapter 3, we study the spectral amplitudes of the first two Earth radial modes excited by the Sea of Okhotsk earthquake of 24 May 2013, the largest deep event ever recorded, in the search for an isotropic component to its source. In contrast to the case of the 1994 Bolivian earthquake, we detect an implosive component equivalent to 3% of the deviatoric moment, but 14% of the lone component exciting

the Earth's radial modes. An implosive component to the source is expected in the model of transformational faulting in which deep earthquake rupture nucleates and grows upon transformation of metastable olivine to ringwoodite in the cold subducting slab. This interpretation is supported by quantitative estimates (0.9-4m) of the thickness of the transformed shear zone, which scale favorably, relative to earthquake fault length, with the upper end of the range of laboratory results reported for ices, germanates and silicates.

In chapter 4, we extend to distances beyond 80° the computation of the energy-to-moment slowness parameter Θ , by defining a regional empirical correction based on recordings at distant stations for events otherwise routinely studied. In turn, this procedure allows the study of earthquakes in a similar source-station geometry, but for which the only available data are located beyond the original distance threshold, notably in the case of historical earthquakes predating the development of dense networks of short-period seismometers. This methodology is applied to the twin 1947 earthquakes off the Hikurangi coast of New Zealand for which we confirm slowness parameters characteristic of tsunami earthquakes. In addition, we identify as such the large aftershock of 21 July 1934 in the Santa Cruz Islands, which took place in the immediate vicinity of the more recent 2013 shock, which also qualifies as a tsunami earthquake. In that subduction zone, the systematic compilation of Θ for both recent and pre-digital events shows a diversity in slowness correlating with local tectonic regimes controlled by the subduction of fossil structures.

In chapter 5, we extend the slowness parameter originally introduced by Newman and Okal (1998) to intermediate and deep earthquakes. We define four depth bins featuring slightly different algorithms for the computation of Θ . We apply this methodology to a global dataset of 598 intermediate and deep earthquakes and find a slight increase with depth in average values of Θ which however all have intersecting one- σ bands narrower than their counterpart for a reference dataset of 146 shallow earthquakes. Similarly, we find no correlation between values of Θ and focal geometry.

Acknowledgments

Getting to this stage of my life would not have been possible without the support and guidance that I received from many people.

First, I would like to thank my PhD supervisor Emile Okal for all his support and encouragement during my PhD and even before I started at Northwestern. He was the one who sparked my interest in seismology by letting me audit his plate tectonics class and trusting me to work on projects with him at the same time. I truly believe that I could not have reached this stage without receiving all his helps.

I would like to express my gratitude to my dissertation committee members, Donna Jurdy, Seth Stein and Craig Bina for their support and invaluable advice. I will always be thankful for all I learned from them as I was very fortunate to have them as my committee members and having attended their classes in the past.

I specially thank Trish Beddows and Ed Mallon for their hospitality during the first days when I came to the US. I stopped for help by Trish's office many times and she was always there for me. I also like to thank Suzan van der Lee for her encouraging words. I am thankful to Steve Jacobsen for mentoring me in my second candidacy project.

Margo Okal has my gratitude for being kind to me in the harsh moments during the past six years. I am incredibly fortunate to know someone like her in my life. I should also thank Sarah Simpson for being such a fantastic landlady.

I am also pleased to say thank you to all the folks in the Earth and Planetary Sciences department office who sometimes went out of their ways to help during the last couple of years. They are all awesome!

I am also thankful to Robert Herrmann for sharing his Computer Programs in Seismology and coaching me in making synthetic seismograms. I thank Dmitry Storchak and Domenico di Giacomo for detailed insight on the operational procedures at ISC. I thank Hiroo Kanamori who provided copies of ancient calibration ledgers of the Caltech seismometers, and also Bernard Dost, Reinoud Sleeman, James Dewey and Harley Benz for access to the seismological archives at De Bilt and Golden. I am grateful to George Choy for sharing his unpublished dataset of energy values. Meredith Nettles has my gratitude for trying various frequency ranges in calculation of alternative Sea of Okhotsk CMT solutions. Stephen Kirby was a great help in understanding tectonic roots of our results in the Sea of Okhotsk project. Miaki Ishii also provided us with a catalog of splitting parameters for higher overtones for which we are grateful. Some figures in this thesis were created using Generic Mapping Tools (Wessel & Smith, 1991).

To my friends Eddie Brooks, Josh Townsend, Fei Wang, Mike Witek and Emily Wolin and many more who helped me in my research at Northwestern, I express my gratitude. I am grateful for all their help as I learned a lot from them all.

Wonderful friends motivated me to work better through fantastic chats (both scientific and casual). For this reason, I thank Grace Andrews, Matt Jones, Stella Kim, Everett Lasher, Jamie McFarlin, Jamie Neely, Leah Salditch, Niloo Sarvian, Vivian Tang and Jiuyuan Wang.

I want to thank all my Iranian friends either here in the US or in Iran. I have been lucky to have such good company (too many to list here but you know who you are!). In this context I should thank Dr. Nabi-Bidhendi for all his help and support.

In the end, it is very important to me to thank to my family as the most valuable thing in my life. I want to thank my Dad whom I miss a lot, for all his support in my life, especially for all those times he was there for me when I felt disappointed. Definitely special thanks are due to my Mom for all the sacrifices she has made for me over the years. She is one of the most extraordinary people whom I have known in my life and I am the luckiest to have her beside me as an inspiration. I truly believe if it were not for my parents, I would not be where I am today. I owe them both a great deal and hope I will be able to make them proud. I deeply thank my very very kind brother Sepehr who has always supported me in my life. Again, I am lucky to have him. I would also like to thank my kind in-laws for their support even though from far away. I am very grateful to have them all. I also thank for heart-warming kindness from Baran and Radman.

Last but not least, I want to thank someone who made my life better by joining me. I cannot say how much I am happy to have you in my life as my friend, my

advisor's senior student, and more importantly: the other half of me. Thanks Amir for being there for me always and as a source of support and encouragement during the challenges of graduate school and life! I could not have made it this far if you were not standing by my side.

*To **Mahsa**, I wish she was still with us.*

Table of Contents

ABSTRACT	2
Acknowledgments	5
List of Tables	14
List of Figures	16
Chapter 1. Introduction	19
Chapter 2. The body-wave magnitude m_b : An attempt to rationalize the distance-depth correction $q(\Delta, h)$	23
2.1. Introduction and Background	23
2.2. The derivation of (2.1)	28
2.2.1. Shallow sources (Gutenberg, 1945a)	30
2.2.2. Deep sources (Gutenberg, 1945b)	34
2.2.3. Later investigations	35
2.2.4. Shortcomings of the Prague $q(\Delta, h)$	39
2.3. Computational approach	40
2.3.1. Model and parameters	40
2.3.2. The instrument	41

	11
2.3.3. The sources	42
2.3.4. The magnitude measurement	43
2.4. Results	45
2.4.1. General trends	45
2.4.2. Comparison metrics	50
2.4.3. Possible sources of additional bias	63
2.5. Conclusion and Perspective: A preliminary test of q_{SO} vs. q_{JD}	73
Chapter 3. An implosive component to the source of the deep Sea of Okhotsk earthquake of 24 May 2013: Evidence from radial modes and CMT inversion	77
3.1. Introduction and historical perspective	77
3.2. Methodology	83
3.3. Results: Evidence for an implosive component	84
3.3.1. Preliminary investigation: the spheroidal modes	84
3.3.2. The radial modes	86
3.3.3. The case of the 2015 Bonin earthquake	91
3.3.4. The Case of the 2018 Fiji events	94
3.4. Verifying the robustness of M_I	95
3.4.1. Possible artifacts for radial mode measurements	95
3.4.2. Unconstrained CMT inversions: an independent approach	99
3.5. A possible interpretation	106

	13
5.2.3. Selection of $\langle (F^{gP})^2 \rangle$	182
5.3. Data Selection	183
5.4. Results and Discussion	185
5.4.1. General Results	185
5.4.2. Possible influence of focal mechanism	196
5.4.3. Regional trends, outliers and special groups	204
5.5. Conclusion	213
References	214
Appendix A. Determination of 1947 short-period instrument magnification at Tucson (TUC)	244
Appendix B. Tables	247

List of Tables

2.1 Statistical comparison of the various corrections $q(\Delta, h)$	52
2.2 Parameters of smoothing filters used on Fig. 2.11	61
2.3 Influence of instrumentation on m_b measurements	67
2.4 Magnitudes computed in preliminary experiment	74
3.1 Results of Moment Tensor Inversion Experiments: 2013 Sea of Okhotsk	100
3.2 Results of Moment Tensor Inversion Experiments: 2015 Bonin Islands event	102
3.3 Results of Moment Tensor Inversion Experiments: 19 August 2018 Fiji event	103
3.4 Results of Moment Tensor Inversion Experiments: 1994 Bolivian event	103
3.5 Deep earthquakes with the ten largest known moments (Fig. 3.1)	115
4.1 Relocation of the 1934 Santa Cruz sequence.	138
4.2 Parameters Θ computed in this study: Hikurangi Trench	154
4.3 Parameters Θ computed in this study: Santa Cruz and Vanuatu.	163
5.1 Summary of results	187
5.2 Influence of focal mechanism on populations of Θ	200

	15
5.3 Values of Θ for specific events or subsets.	205
B.1 Full dataset used in Chapter 5	247
B.2 Reference dataset of 146 shallow earthquakes used in Chapter 5	265

List of Figures

2.1 “Revised” correction $q_{56}(\Delta, h)$ mandated	25
2.2 Same as Fig. 2.1 for the original correction	27
2.3 Correction q_{VC} , proposed by	38
2.4 Sketch of the measurement of	45
2.5 Contoured plot of the correction	46
2.6 Sketch outlining critical features of $q_{SO}(\Delta, h)$	47
2.7 Contoured plot of the residual	51
2.8 Plot of individual values of	54
2.9 Residuals for other combinations of corrections	56
2.10 Spectral amplitudes of corrections $q(\Delta, h)$	58
2.11 Smoothed versions $q_{SO}^{(n)}(\Delta, h)$	60
2.12 Comparison metrics M (2.15) for	63
2.13 (a) Distribution of recent seismicity	65
2.14 Distribution of GlobalCMT sources	69
2.15 Dominant period T (averaged over all focal geometries)	71
2.16 Exploratory experiment comparing magnitudes	76

	17
3.1 Sketch of the only ten	81
3.2 The Sea of Okhotsk deep	82
3.3 Seismic moment of the 2013 Sea of Okhotsk	86
3.4 Best fits to the stacked spectra of	89
3.5 Isotropic and deviatoric components of t	90
3.6 The Bonin	93
3.7 Same as Fig. 3.3 for the 1994	104
3.8 Comparison of proposed transformational	108
4.1 Short-period P	123
4.2 Relocations of the 1947 Hikurangi	126
4.3 Representative examples of	129
4.4 Mantle magnitudes	131
4.5 Same as the top frame of	132
4.6 Epicenters of the 1934	136
4.7 Relocation of the 1934	137
4.8 Same as Fig. 4.4 for the	141
4.9 Extension of the Θ algorithm	147
4.10 Residuals r_i plotted as a	148
4.11 Same as Figure 9 for the Santa Cruz	149
4.12 Same as Figure 10 for the	151

	18
4.13 Plot of energy E^E versus M_0	157
4.14 Distribution of parameters	162
4.15 (a): Cross-section of the seismicity of	166
5.1 Plot of the estimated energy, E^E vs. seismic moment M_0	172
5.2 Travel-time delays of reflected pP (solid) and sP	178
5.3 Plot of estimated energy E^E vs. seismic moment M_0	188
5.4 Same as Fig 5.3 for t	189
5.5 Same as Fig. 5.3 for the D-1 dataset (300 to 450 km)	190
5.6 Same as Fig. 5.3 for	191
5.7 Cumulative plot of Θ for all depths categories	192
5.8 Whole dataset of 598 intermediate and deep earthquakes	195
5.9 Ternary diagrams for the four depth bins.	199
5.10 Same as Fig. 5.9 for the Tonga-Kermadec subset	203
5.11 Maps of the dataset of 598 intermediate and deep	206
5.12 Close-up of the results in the Vanuatu-Santa Cruz region	209
5.13 <i>Top</i> : Map of our results for the Hindu Kush cluster using th	212
A1 Excerpt from the entry for station	246

CHAPTER 1

Introduction

This dissertation regroups a number of studies of earthquake sources in the framework of modern seismological theory.

- (1) Towards the end of the 19th century, modern seismology was born as a special branch of the physical sciences. This was primarily the result of earlier progress in the theory of elasticity and of the development of adequate instrumentation, with classic contributions by such forefathers as Milne (1886) and Wiechert (1903). As such, those early studies concentrated almost exclusively on the propagation of seismic waves, in the absence of an adequate physical model of their source.

A few decades later, the first quantification of earthquake sources was proposed by Richter (1935) through his landmark introduction of a magnitude scale for California earthquakes, but its basis remained empirical, as recognized by the author himself who stated (Richter,1935 p.7).

“This definition is in part arbitrary; an absolute scale, in which the numbers referred directly to shock energy or intensity measured in physical units, would be preferable. At present the data for correlating the arbitrary scale

with an absolute scale are so inadequate that it appears better to preserve the arbitrary scale for its practical convenience”.

Richter’s (1935) magnitude concept was later adapted into various scales for use in global seismology, in particular as the body-wave magnitude m_b measured on short-period P waves (Gutenberg, 1945a,b). In this framework, and even though m_b is still in use to this day (Anonymous, 2013), it relies on an empirical contour plot (Gutenberg, 1945b) which has never been theoretically justified.

Chapter 2 provides the first such attempt, which uses a large number (~ 40 million) of synthetic seismograms computed through modern algorithms to generate a theoretically-justified alternative to Gutenberg’s (1945b) empirical contours. This work is under review as Saloor and Okal at *Geophysical Journal International*.

- (2) In this general context, the search for an appropriate physical model of an earthquake source can be traced back to Nakano (1923), who first proposed its representation by a so-called “double-couple” combination of forces, an idea finally brought to fruition more than 30 years later by Vvedenskaya (1956) with additional contributions by Steketee (1958), Chinnery (1960) and Knopoff & Gilbert (1959).

In the following years and in the framework of the then-developing theory of plate tectonics, that model proved immensely successful for the overwhelming majority of seismic sources (e.g. Isacks et al., 1968; Isacks & Molnar, 1971), even though the existence of deep earthquakes (Wadati, 1927) raised the question of seismogenesis in a medium expected to preclude brittle rupture under extreme pressure and temperature conditions.

In this context, a long-standing controversy has existed for the past 45 years regarding the possible existence of isotropic (implosive) components, attributable to phase transitions (e.g., Gilbert & Dziewonski 1975; Okal & Geller 1979).

Chapter 3 provides definitive evidence of such a component following the largest deep earthquake ever recorded, the 2013 Sea of Okhotsk event ($M_0 = 3.95 \times 10^{28}$ dyn*cm). We use radial free oscillations of the Earth (e.g., Gilbert, 1971), to demonstrate a significant implosive component (3–8%) in the moment tensor of the source. This result is generally supportive of transformational faulting as a mechanism of deep seismogenesis, as proposed e.g. by Kirby et al. (1996). This chapter was published as Okal et al. 2018 in *physics of the earth and planetary*.

- (3) A remarkable aspect of modern earthquake source theory is the success of scaling laws expressing the similarity of seismic sources over as much as 17 orders of magnitude in seismic moment (Ide & Beroza, 2001). However some diversity has been documented for shallow earthquakes, related to

variations in the static and dynamic environments of their sources. Such variations arise from kinematic properties of the seismic sources, such as their velocity of rupture, and are expressed across the broad spectrum of seismic waves. They have been quantified e.g. through the slowness parameter Θ introduced by Newman & Okal (1998), which has been used to characterize in real-time anomalously slow earthquakes with enhanced tsunami potential (Weinstein & Okal, 2005).

Because the computation of Θ involves the processing of high-frequency waveforms, its extension to analog data presents significant challenges, for example in the case of many historical events whose detailed characteristics remain unknown. Chapter 4 describes a methodology for this purpose in the case of these historical tsunami earthquakes in the Southwest Pacific.

- (4) Along similar lines, the question of the source diversity of non-shallow earthquakes, in particular regarding energy-to-moment ratios related to apparent stress, remains controversial. Chapter 5 presents an extension to intermediate and deep earthquakes of the concept of the parameter Θ .

CHAPTER 2

**The body-wave magnitude m_b : An attempt to rationalize
the distance-depth correction $q(\Delta, h)$** **2.1. Introduction and Background**

Ever since Vvedenskaya (1956) and later Knopoff & Gilbert (1959) introduced the double-couple as a physical representation of a seismic source, its moment M_0 has been used as the preferred quantitative measure of earthquake sources, notably through algorithms of centroid moment tensor inversion (Dziewonski et al., 1981). Yet, the body-wave magnitude m_b , initially introduced by Gutenberg (1945a,b), remains to this day a valuable quantifier of the high-frequency characteristics of a seismic source. Its algorithm was formalized as one of the “Prague formulæ” by a committee of Russian and Czech scientists following recommendations formulated at the 1960 Helsinki meeting of the International Union of Geodesy and Geophysics (Kárník et al., 1962) and has remained unchanged under the recommendations of successive working groups of the International Association of Seismology and Physics of the Earth Interior [IASPEI], most recently in their 2013 Report (Anonymous, 2013).

Specifically, we recall that the computation of m_b proceeds as follows:

- (i) a time window following the P -wave first arrival is isolated from a short-period seismogram, containing the generalized P wave (including surface reflections pP and sP);
- (ii) the maximum amplitude of ground motion in that window (A , in μm) is retained;
- (iii) the dominant period T of the wavetrain at the time of that maximum amplitude is measured (in seconds); it is recommended that this period be close to 1 s, but in no case should it exceed 3 s;
- (iv) the magnitude m_b is then obtained as

$$m_b = \log_{10} \frac{A}{T} + q(\Delta, h) \quad (2.1)$$

where $q(\Delta, h)$ is an empirical correction depending on distance Δ and focal depth h , proposed by Gutenberg & Richter (1956, Fig. 5) and later reproduced by Richter (1958, Fig. VIII-6, p. 688). It is shown here on Fig. 2.1.

The use of the ratio $\frac{A}{T}$ in (2.1) expresses the goal, by the founding fathers of magnitude scales, B. Gutenberg and C.F. Richter, to associate magnitude with energy, the latter taken in its kinetic form as proportional to the square of ground velocity, hence the use of the ratio of amplitude to period. However, and as discussed

in detail by Okal (2019), this relationship exists only in the case of a harmonic oscillator, whereas any seismic source generally features a broad spectrum.

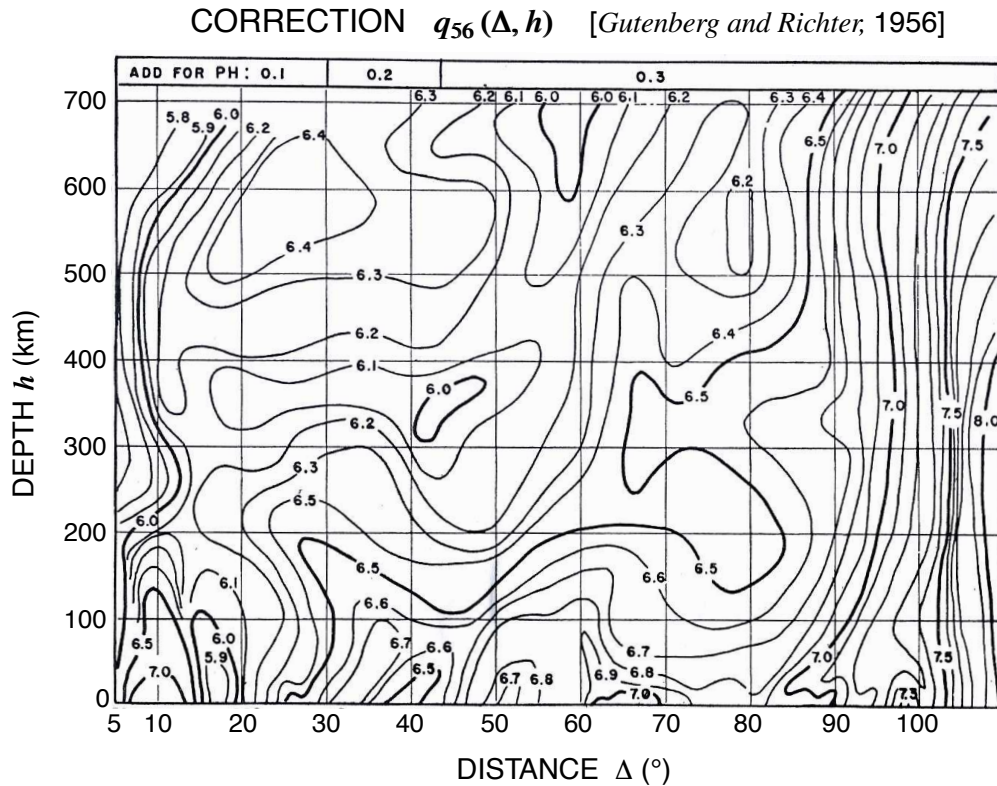


Figure 2.1. “Revised” correction $q_{56}(\Delta, h)$ mandated by the Prague Commission (Kárník et al., 1962), and still in use today (Anonymous, 2013). Adapted from Gutenberg & Richter (1956).

The situation is made intriguing by the fact that the correction $q(\Delta, h)$ on Fig. 2.1 differs significantly from its original version introduced by Gutenberg (1945b; Figure 2) and reproduced here on Fig. 2.2. As explained by Veith & Clawson (1972), it appears that this revision was effected to smooth excessive scatter among magnitude residuals by introducing station corrections reaching ± 0.3 units of magnitude (Gutenberg & Richter, 1956), which we would interpret in modern terms as

reflecting lateral heterogeneity in receiver crustal structure; however, we will show in Section 2.4 that such corrections may be biased by other factors.

Note further that C.F. Richter uses the notation $A(\Delta, h)$ and Gutenberg (1945b) $Q(\Delta, h)$; however, throughout this study, we shall keep the notation $q(\Delta, h)$ to avoid confusion with ground displacement (A in most of B. Gutenberg and C.F. Richter's relevant papers), and with the anelastic attenuation coefficient, nowadays universally referred to as Q^{-1} . To ease the language, we will refer to Gutenberg's (1945b) correction factor (Fig. 2.2) as $q_{45}(\Delta, h)$, and to Gutenberg & Richter's (1956) more definitive version, shown on Fig. 2.1, as $q_{56}(\Delta, h)$.

To our knowledge, the shapes of the contours in Fig. 2.1 have never been explained, and it is the purpose of the present chapter to explore their possible justification in the framework of modern theoretical seismology.

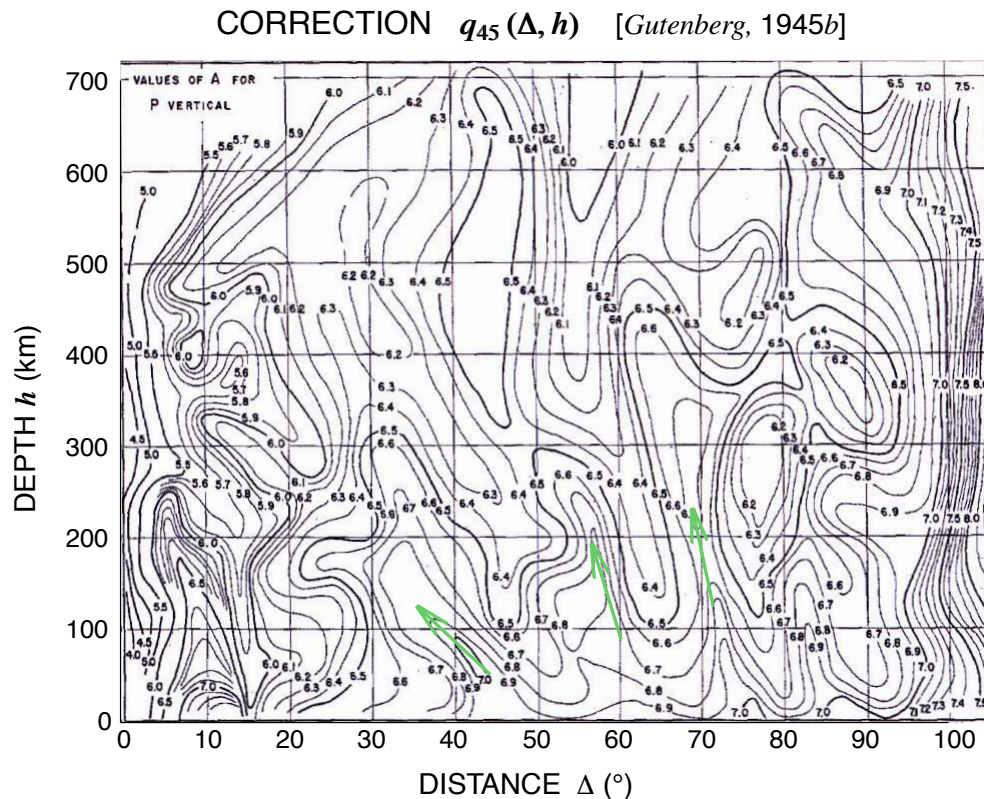


Figure 2.2. Same as Fig. 2.1 for the original correction $q_{45}(\Delta, h)$, adapted from Gutenberg (1945b). As discussed in the text, the green arrows indicate domains where a strong gradient of q cuts obliquely across the diagram.

In this context, we start with a detailed review of the origin of (2.1), and of the probable method by which the various versions of the function q were obtained. Unfortunately, in addition to B. Gutenberg (1889-1960) and C.F. Richter (1900-1985), all the Prague committee members whose insight might have been invaluable in this context, since they probably examined the question in great detail, have now passed away, the last one being Dr. Jiří Vaněk who died in 2018 at age 90. Thus, the only materials helping shed light on this problem are the original contributions by B. Gutenberg and C.F. Richter.

We then use a large set of modern synthetic seismograms computed for various source depths and receiver distances, but for the same seismic moment, to generate our own version of the correction, $q_{SO}(\Delta, h)$ and compare it to q_{45} and q_{56} (Gutenberg, 1945b; Gutenberg & Richter, 1956). We conclude that we can reproduce some large scale features of the original q functions, but cannot explain the nature or origin of the more detailed variations introduced on a small scale in those functions by the founding fathers.

2.2. The derivation of (2.1)

In this section, we examine and paraphrase the fundamental contributions by Gutenberg & Richter (1942) and Gutenberg (1945a,b), in order to reconstruct as best as possible the steps they took to obtain (2.1). The occasionally excruciating detail in the following paragraphs is motivated by the need to keep track of the limitations underlying many assumptions openly or tacitly made by the authors, following the approach in Okal's (2019) recent investigation of the various relations they proposed over the years between energy and magnitude.

As stated by Gutenberg (1945a), the obvious motivation behind the development of (2.1) was to extend the concept of magnitude to earthquakes of all depths. We recall that magnitudes were originally defined by Richter (1935) for Southern California earthquakes, all of them shallow and recorded locally on strong-motion torsion instruments (an algorithm which would correspond to a present-day local

magnitude M_L). The concept was soon extended to teleseismic distances by Gutenberg & Richter (1936), using the dominant phases on global records, i.e., surface waves with periods around 20 s.

In principle, the generation of a distance correction in any magnitude scale is relatively straightforward since a common earthquake, which should have a single magnitude, can be recorded over a large interval of distances. The concept of a distance correction was already present in Richter's (1935) original algorithm.

The situation is of course different for a depth correction, since from an observational standpoint, there should be no obvious reason why a shallow earthquake and a deep one should have the same magnitude. In this context, Gutenberg & Richter (1942) and later Gutenberg (1945a,b) relied on a theoretical approach to estimate the seismic motion at the Earth's surface from a buried source of a given "size", which Gutenberg (1945b) clearly related to radiated energy, stating:

"...it seems best by far to define the magnitude in such a way that two earthquakes of the same magnitude have the same energy, regardless of depth."

The problem is that, at such an early stage in the development of theoretical seismology, and despite valiant efforts in this respect, B. Gutenberg only had what must be regarded today as a rudimentary command of the energy radiated by a seismic source (Okal, 2019).

2.2.1. Shallow sources (Gutenberg, 1945a)

In preparation for the extension of magnitudes to deep earthquakes, which do not generate significant surface waves, Gutenberg (1945a) first investigated the possibility of measuring magnitudes of shallow earthquakes on shorter-period body waves, including the phases P , PP and S . In the present work, we consider only P , since short-period magnitudes are no longer measured from PP or S phases, which suffer considerable anelastic attenuation. We note, however, that a detailed reading of Gutenberg (1945a) fails to state precisely the period (or more probably the range of periods) used by the author: a mention is made on p. 60 of “waves having a period of a very few seconds”, and specifically of a period of 0.5 s on p. 62, albeit in the context of local shocks. From his statement on p. 58 regarding the Benioff short-period seismometer (Benioff, 1932), and based on our experience with such records, it can be assumed that at least a subset of Gutenberg’s (1945a) measurements were performed around $T = 1$ s.

The approach taken by Gutenberg (1945a,b) for the calculation of body-wave magnitudes uses the theoretical model of a point source buried at a depth h , and geometrical optics, to estimate the seismic energy flux at a distance Δ which can be teleseismic or regional. In the first paper, Gutenberg (1945a, Table 4) derives distance corrections for body-wave magnitudes of shallow earthquakes, based on the now classical expression of geometrical spreading (which he had helped formulate as L. Geiger’s co-author of Zöppritz et al. (1912), written up following Karl Zöppritz’ untimely death in 1908). The author first relates epicentral ground displacement

to the energy E_1 in a “single body wave”, meaning a single oscillation of period T . Proceeding to simply add the energies of such oscillations, B. Gutenberg then makes the assumption that the “duration” of the wavetrain at the epicenter, t_0 , grows with magnitude like the dominant period T_0 at the epicenter, in other words that the number of oscillations in the P wave at the epicenter is independent of magnitude, which in turn means that the total energy E radiated at the source should be proportional to E_1 , or to the quantity $(A/T)^2$ measured on a single oscillation.

Gutenberg (1945a) then combines this result with the empirical formula between energy and magnitude proposed by Gutenberg & Richter (1942, Eq. 35).

$$\log_{10} E = 11.3 + 1.8M \quad (2.2)$$

(E in ergs) to suggest that the quantity

$$0.9M - \log_{10} \frac{A}{T} + \log_{10} W \quad (2.3)$$

where W is the geometrical spreading factor, should have a “nearly constant value for all [...] P waves” (note that Gutenberg uses the notation w for the vertical ground displacement A). He then replaces the factor 0.9 with the rounded value 1, yielding

$$m_b = \log_{10} \frac{A}{T} + q(\Delta) + 0.1(M - 7) \quad (2.4)$$

where the distance correction $q(\Delta)$ is just $(\log_{10} W)$ plus the constant 0.7. Noting further that

“As most shocks [studied] at distant stations have magnitudes between 6 and 8, the absolute value of 0.1 (M - 7) rarely exceeds 0.1”,

Gutenberg (1945a) simply discards the correction in the last term of (2.4), which then takes the form (2.1) with fixed h , where the function $q(\Delta)$ can be computed theoretically.

We note here that the “geometrical spreading” function used by Gutenberg (1945a) contains an “absorption factor” that we would relate in modern terms to anelastic attenuation, and which he represents in the form of an the energy decay

$$a = \exp(-kD) \tag{2.5}$$

where D is the “whole path” of the waves, and the constant k is taken as $1.2 \times 10^{-4} \text{ km}^{-1}$.

Before proceeding to the case of deep sources, it is worth examining critically some of the assumptions underlying the above algorithm. Okal (2019) has pointed out that the slope 1.8 in (2.2), a crucial element of the above derivation, was obtained empirically by the authors from the variations with magnitude of epicentral ground acceleration and signal duration, both of which are unsustained by modern seismological theory. Note also that the value 1.8 in (2.2) was replaced with 1.6 in Gutenberg & Richter (1954) and later 1.5 in Gutenberg & Richter (1956). Such

lower values would tend to increase the correction term to the right of (2.4), and make it less justifiable to simply discard it to obtain (2.1).

In addition, the proposed linear growth between source duration t_0 and dominant period T_0 is questionable. As discussed by Okal (2019), modern theory could indeed suggest that both would grow like $M_0^{1/3}$ since the former would be controlled by the duration of rupture, and hence fault length, while the latter could be related to rise time, through the inverse of a source corner frequency. However, this simple argument will break down for a very large earthquake, especially since the waves actually recorded on a seismogram have been filtered by anelastic attenuation and instrument response.

Finally, the handling of anelastic attenuation in the form of (2.5) is highly questionable, since modern studies describe its effect on energy through a factor

$$a' = \exp(-\omega t/Q) \tag{2.6}$$

where Q is quality factor of the wave (unrelated to the correction q in 2.1). In particular, for the energy of P waves generated by shallow shocks, a first-order approximation to the effect of attenuation is often taken as $\exp(-\omega t^*)$ with $t^* = 1$ s (Carpenter, 1965), which can be explained by the concentration of anelastic attenuation during the wave's transits through the asthenosphere, largely independent of distance Δ . The expressions a and a' could be reconciled, e.g., for a "whole path" D on the order of the Earth's radius, typical of a teleseismic layout, only by assuming

a period $T = 2\pi t^*/kD = 8$ s, much longer than the realm of short-period body waves, mandated to remain under 3 s under modern practice (Anonymous, 2013). Note finally that Gutenberg (1945a) proposes to apply (2.5) to both P and S waves with the same value of k , and ends his paper with the conclusions that absorption is similar in the mantle and the core, and that radiated energy is partitioned equally at the source between P and S waves, all statements irrevocably negated under modern seismological theory.

2.2.2. Deep sources (Gutenberg, 1945b)

Turning now to the case of deeper sources, Gutenberg (1945b) provides only scant information on the procedures he used to achieve the degree of complexity of Fig. 2.2. The author assumed that the same relationship (2.2) applies between energy and magnitude regardless of depth, and that ground displacement could be similarly related to radiated energy through geometrical spreading. No mention is made of the handling of “absorption” (anelastic attenuation), but it can be assumed from the universal character which Gutenberg (1945a) gives (2.5) that it was also used, with the same value of k , for deep sources.

Gutenberg (1945b, p. 118, 4th paragraph) then computed theoretically the resulting values of $q(\Delta, h)$ (that he calls A) at 200, 400, and 600 km, and interpolated the results at other depths. Note at this stage that there is no way to obtain the level of complexity of $q_{45}(h)$ (at fixed Δ) evidenced on Fig. 2.2, e.g., at $\Delta=25^\circ$,

65° or 85°, from an interpolation between just four values of depth (including the shallow one from Gutenberg (1945a)).

In the same paragraph, B. Gutenberg states that additional corrections were made by considering, for shallow sources and as a function of distance Δ , individual residuals observed between actual measurements and theoretical ones predicted from geometrical spreading. Such “shallow” corrections were then included in the final $q_{45}(\Delta, h)$ for deeper sources, under the assumption that they could be equally applied, as long as the ray parameter (p in modern theory) remained constant, which he mentioned, implied only a slight reduction in distance with increasing source depth. This remark could conceivably explain the bending of some of the resulting contours (see green arrows on Fig. 2.2); however the slopes of this bending (about -16° over 200 km around $\Delta = 40^\circ$, -8° over 200 km at 60° , and -10° over 400 km at 70°) would lead to take-off angles at the source of 83° , 76° and 68° , respectively, which are unrealistic at those distances. This leaves the origin of the complex contours on Fig. 2.2 unexplained.

2.2.3. Later investigations

In the late 1960s, and following investigations of the anelastic attenuation inside the Earth (e.g., Anderson et al. 1965), the inadequacy of modeling absorption through (2.5) had become evident, as well as the presence of lateral heterogeneity in attenuation at short distances and for shallow sources, notably in the recordings of underground explosions (Evernden, 1967).

Veith & Clawson (1972) later used records from large explosions (both conventional and nuclear and located both underground and in the oceanic column), as well as from a number of well-located earthquakes, all at distances ranging from 0° to 100° , to separate true geometrical spreading from the effect of anelastic attenuation, modeled using the more realistic form (2.6). They then inverted their observations into a model (which they call \hat{Q}) of the intrinsic quality factor Q_α of P waves as a function of depth in the mantle, following a technique of incremental depth penetration reminiscent of the classical Herglotz-Wiechert inversion. Combining it with a model of geometrical spreading derived from a profile of P -wave velocities in the mantle, they obtained a new distance-depth correction for body-wave magnitudes (which they call a “ P ” factor), shown in Fig. 2.3, which is clearly much smoother than either Gutenberg’s (1945b) q_{45} or Gutenberg & Richter’s (1956) q_{56} . Note that Veith & Clawson (1972) use measurements of peak-to-peak amplitudes, whereas B. Gutenberg and C.F. Richter’s are made in the lineage of Richter’s (1953) zero-to-peak measurements; furthermore, Veith & Clawson (1972) express their amplitude-to-period ratios in nanometers per second. Thus, in order to compare them to q_{45} or q_{56} , a constant of 3.3 must be added to their P factors. We will refer to the resulting values as corrections $q_{VC}(\Delta, h)$.

Veith & Clawson’s (1972) \hat{Q} model (shown on their Figure 4) features prominent attenuation in the asthenosphere, between depths of 80 and 300 km, and is more in line with our present understanding of the Earth’s structure (Romanowicz & Mitchell, 2007) than predecessors such as Anderson et al.’s (1965) MM8 model,

which generally features too little attenuation by today's standards, or Teng's (1968) Model G, which has too much. However, \hat{Q} obviously trades off with details of the velocity structure used, and in this respect, it is unfortunate that it was built using Herrin's (1968) velocity profile, which features neither a prominent low-velocity zone in the asthenosphere, nor the mantle discontinuities delimiting the transition zone, around 410 and 660 km (Johnson, 1967; Julian & Anderson, 1968). The latter induce classical triplications leading to caustics and strong variations in amplitude at distances less than 30° (Johnson, 1967; Burdick & Helmberger, 1978; Ebeling & Okal, 2012).

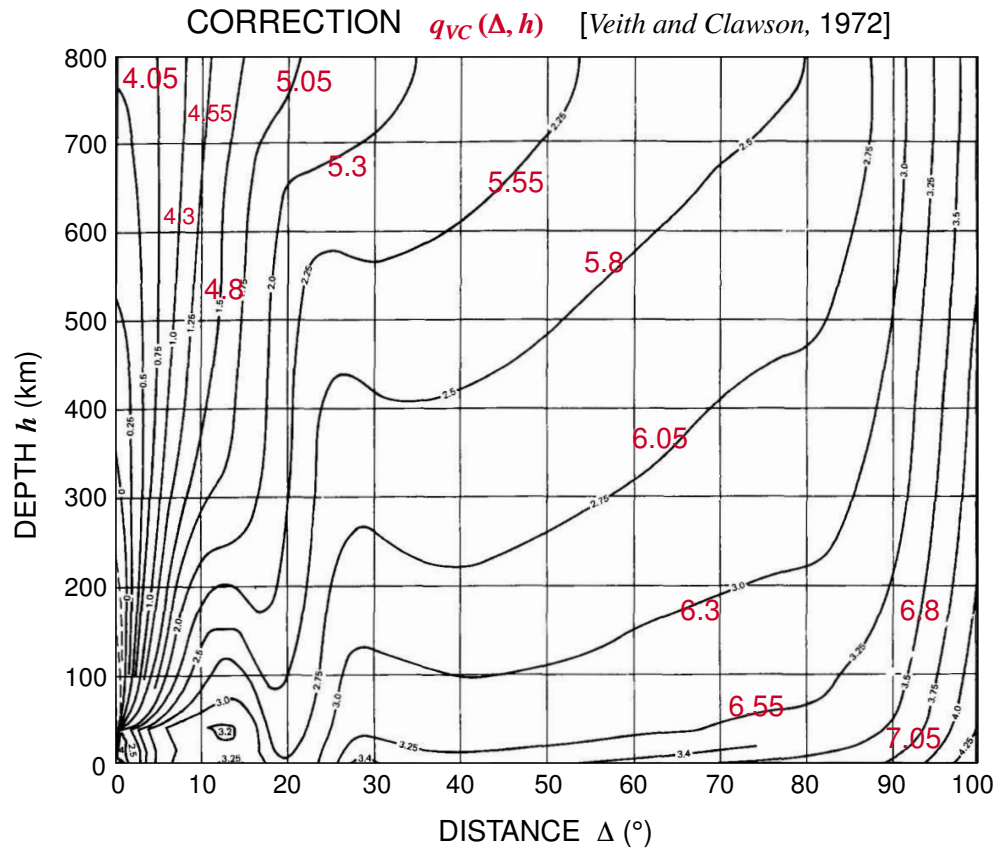


Figure 2.3. Correction q_{VC} , proposed by Veith & Clawson (1972) (adapted from their Figure 9). The small numbers relate to their parameter P (amplitude measured peak-to-peak in nm). The superimposed red numbers, obtained by adding a constant of 3.3, relate to the correction q_{VC} .

Finally, we note that the data file annexed to Anonymous (2013) as a digitized version of $q_{56}(\Delta, h)$ and used under operational procedures at agencies such the United States Geological Survey's National Earthquake Information Center (NEIC) and the International Seismological Center (ISC) [J. Dewey and D. di Giacomo, pers. comm., 2019], is significantly smoothed with respect to the original published by Gutenberg & Richter (1956), as a result of both a coarse sampling in depth, and

of rounding values to 1/10 of a logarithmic unit. We will refer to the digital version of that correction as $q_{JD}(\Delta, h)$.

2.2.4. Shortcomings of the Prague $q(\Delta, h)$

In summary, the function $q_{56}(\Delta, h)$ proposed by Gutenberg & Richter (1956) and enshrined by the Prague committee (Kárník et al., 1962) suffers from the following shortcomings (as well as its predecessor q_{45} (Gutenberg, 1945b)):

- it features too much complexity to be realistically derived from our present knowledge of the Earth’s interior;
- it is based on a direct relationship between $(A/T)^2$ and energy, which holds only for monochromatic wavetrains;
- it uses (2.2), itself based, at least tacitly, on perceived scaling laws which are not upheld by present-day observations (Okal 2019, e.g., p. 3842);
- it uses an unrealistic formulation of anelastic attenuation;
- it was derived before the existence of structure in the Earth’s mantle was documented (transition zone discontinuities) or confirmed (low-velocity zone).

In the next section, we compute a large number of synthetic seismograms, using a common seismic moment which should eventually lead to a single magnitude, process them through the Prague-mandated algorithm for m_b , and build our own version of the correction, $q_{SO}(\Delta, h)$.

2.3. Computational approach

2.3.1. Model and parameters

Our synthetic seismograms are built using Herrmann’s (2013) Computer Programs in Seismology, which use a layer matrix method (Carpenter, 1965; Hudson, 1969), itself based on Haskell propagators (Haskell, 1962). The seismic moment is fixed at $M_0 = 10^{25}$ dyn*cm. The Earth model used here is ak135 (Kennett et al., 1995), which includes the mantle discontinuities at 410 and 660 km, with an attenuation model (Montagner & Kennett, 1996) featuring a low $Q_\alpha \approx 120$ in the asthenosphere. Note that this model, which features a maximum value of Q around 700 km, followed by a decrease in the lowermost mantle, differs substantially from Veith & Clawson’s (1972) \hat{Q} . This decrease of Q_α in the deep mantle, already proposed by Okal & Jo (1990), will have significant implications for the correction $q_{SO}(\Delta, h)$.

Our procedure forces a constant relationship, independent of depth, between magnitude and moment M_0 . This could be a departure from Gutenberg’s (1945b) approach, in which he was seeking to impose a constant one between magnitude and energy E , at the time the only quantity considered as a possible physical quantifier of seismic sources. The ratio E/M_0 of the two quantities, directly related to strain release, is expected to vary with depth, although recent studies have suggested that this influence is relatively contained, to about 0.4 logarithmic units (Chapter 5), or perhaps even untraceable (Vallée, 2013; Poli & Prieto, 2016). In this context, it

seems preferable to associate a constant magnitude to a constant seismic moment, since the latter has become the universal measure of seismic sources. Note in particular that even though the subscript w in M_w was introduced by Kanamori (1977) through a reference to energy, that scale constitutes a moment magnitude, not an energy one, as clearly evidenced by the numerous studies of variations in E/M_0 (e.g., Choy & Boatwright 1995; Newman & Okal 1998; Choy et al. 2006).

2.3.2. The instrument

In order to reproduce the observational conditions under which magnitudes are measured, we include in our synthetics an instrumental response. This can be a delicate issue, since different instruments were used over the years, from torsion systems (Richter, 1935) to broadband seismometers, now the standard equipment at modern seismological stations. As our goal here is to explore the origin of B. Gutenberg’s functions q_{45} and q_{56} , we elect to use the Pasadena Benioff short-period instrument (Benioff, 1932) on which most of his personal readings were probably made, as suggested in Gutenberg (1945a, p.58). The Benioff short-period seismometer is a classical electromagnetic system, featuring a pendulum period $T_p = 1$ s, a galvanometer period $T_g = 0.23$ s, weak coupling ($\mu^2 = 0.05$), and critical damping. It was to become the prototype of the short-period instrument later used in the WWSSN, albeit with a longer $T_g = 0.8$ s (Peterson & Hutt, 2014). Of course, Gutenberg (1945a,b) also relied on readings mailed to him from other observatories, since not all combinations of distance and depth were observable at Pasadena, and

those records were taken on other instruments, for which the maximum amplitude could have been obtained at a different period; this point will be examined more in detail in Section 2.4.3.

2.3.3. The sources

In order to minimize saturation effects due to source finiteness, we use a point source and a moment-rate function in the form of a parabola with a width of only 0.2 s (Herrmann, 2013). Our synthetics are thus built in conditions where the magnitude m_b should be directly proportional to $\log_{10} M_0$ (Geller, 1976). We refer to Okal (2019 Eq. (20a)) for an updated version of that relationship, under which the common seismic moment used in our synthetics, $M_0 = 10^{25}$ dyn*cm, should correspond to $m_b = 6.82$.

For a given combination of source depth h and receiver distance Δ , our approach consists of generating synthetics for a large number of focal geometries and station azimuths, and then averaging the resulting logarithmic measurements. Specifically, we loop over 10 values of the dip angle δ from 45° to 90° , 18 values of the slip angle λ from 0° to 170° , and 36 values, from 0° to 350° , of $\phi = \phi_f - \phi_s$, defined as the difference between the azimuths of the fault strike and of the great circle from source to receiver (in practice, we vary the fault strike, and fix the station azimuth, $\phi_s = 0^\circ$). This amounts to a total of 6480 source-receiver geometries, which should remove the influence of focal geometry on the recorded amplitude of the generalized P wave.

Note that we do not need to consider events with a normal faulting component ($-180^\circ \leq \lambda < 0^\circ$), since they correspond to the exact opposite slip of thrust events, and their records can be obtained by simply flipping the sign of the synthetics. Nor do we need to consider dip angles less than 45° , since a double-couple always has at least one fault plane dipping 45° or more.

We then loop over source depth in 10-km increments from $h = 10$ km to 690 km, and over receiver distance Δ in 1° increments from 10° to 95° , for a grand total of 38,452,320 synthetic seismograms.

2.3.4. The magnitude measurement

Once the synthetics are created, the algorithm for the measurement of m_b follows the practice mandated by the Prague formula and the recent IASPEI working group (Anonymous, 2013). An example of the computation of amplitude A and period T is detailed on Fig. 2.4. First, the amplitude of the recorded seismogram, S_{max} , is simply obtained as the maximum absolute value of the trace of the seismogram in the time window considered. The period T (in s) is obtained by doubling the interval separating the first zero-crossings of the time series on either side of that maximum. The ground motion A is then computed by dividing S_{max} by the gain G of the instrument at the period T , and the result expressed in microns (μm). The logarithm

$$L = \log_{10} \left[\frac{A}{T} \right] \quad (2.7)$$

is then computed, and its average taken over all source-receiver geometries, at constant distance and depth:

$$\langle L \rangle (\Delta, h) = \frac{\sum_{i=1}^{180} w_i \sum_{j=1}^{36} \log_{10} \left[\frac{A}{T} \right]_{i,j}}{36 \sum_{i=1}^{180} w_i} \quad (2.8)$$

In (2.8), j is the index varying the fault strike ϕ_f (in increments of 10° and for $\phi_s = 0^\circ$), and i a double index combining dip and slip angles. We recall that, in order to minimize the number of synthetics computed, we consider only dips $\delta \geq 45^\circ$. Of the resulting 180 different focal mechanisms, 108 (trending towards a strike-slip geometry) feature an auxiliary plane dipping more than 45° , and thus are sampled twice by our algorithm (once per fault plane), while the remaining 72 (approaching a thrust mechanism) are sampled only once. For that reason, we introduce in (2.8) a weighting factor, $w_i = 0.5$ for the former type and $w_i = 1$ for the latter. The two groups are easily separated by considering the discriminant

$$\tan^2 \lambda + \frac{1}{\cos(2\delta)} \quad (\delta > 45^\circ) \quad (2.9)$$

which is negative in the former case, positive in the latter. The denominator in (2.8) is then $36 \times 126 = 4536$, which is the number of independent combinations of focal mechanism and fault strike. Since all synthetics were computed for a moment $M_0 = 10^{25}$ dyn*cm, which should correspond to a magnitude $m_b = 6.82$ (Okal, 2019), the correction $q_{SO}(\Delta, h)$ is then simply

$$q_{SO}(\Delta, h) = 6.82 - \langle L \rangle (\Delta, h) \quad (2.10)$$

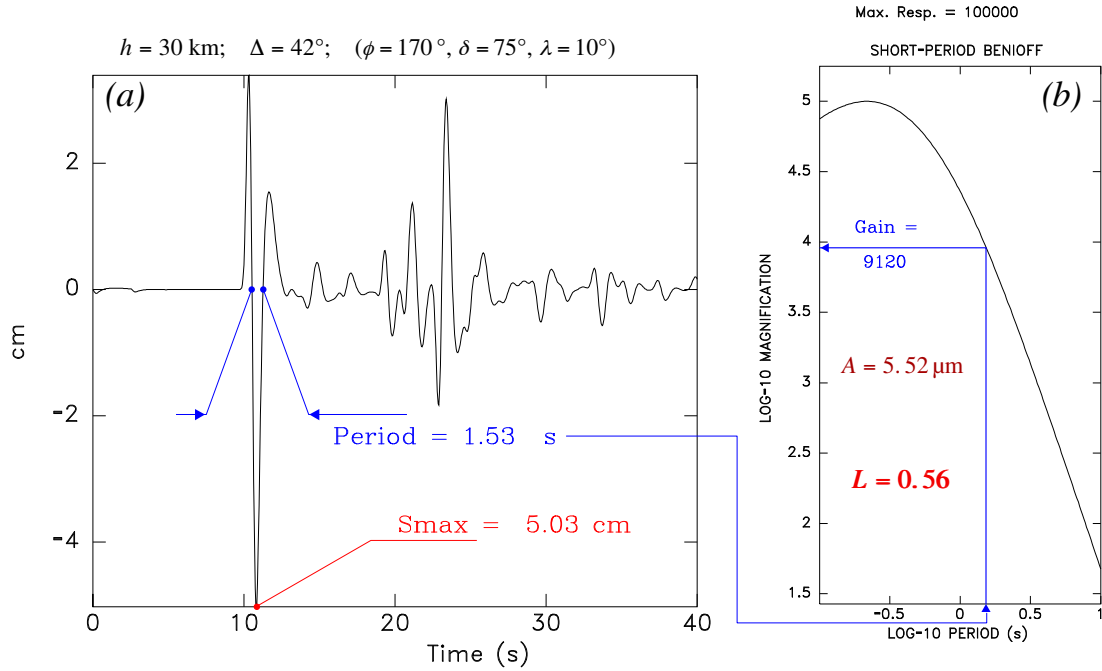


Figure 2.4. Sketch of the measurement of $L = \log_{10} \left[\frac{A}{T} \right]$ on a synthetic seismogram. The maximum absolute amplitude S_{max} (in this case 5.03 cm) is measured on the synthetic time series (a), and the period $T = 1.53$ s of that oscillation retained and transferred to the response curve of the instrument (b), from which the gain $G = 9120$ is computed. The ratio $A = S_{max}/G$ amounts to $5.52 \mu\text{m}$ from which $L = 0.56$ is inferred.

2.4. Results

2.4.1. General trends

The function q_{SO} is shown on Fig. 2.5. A number of trends, schematized on 2.6, are immediately evident in its distribution in the (Δ, h) plane.

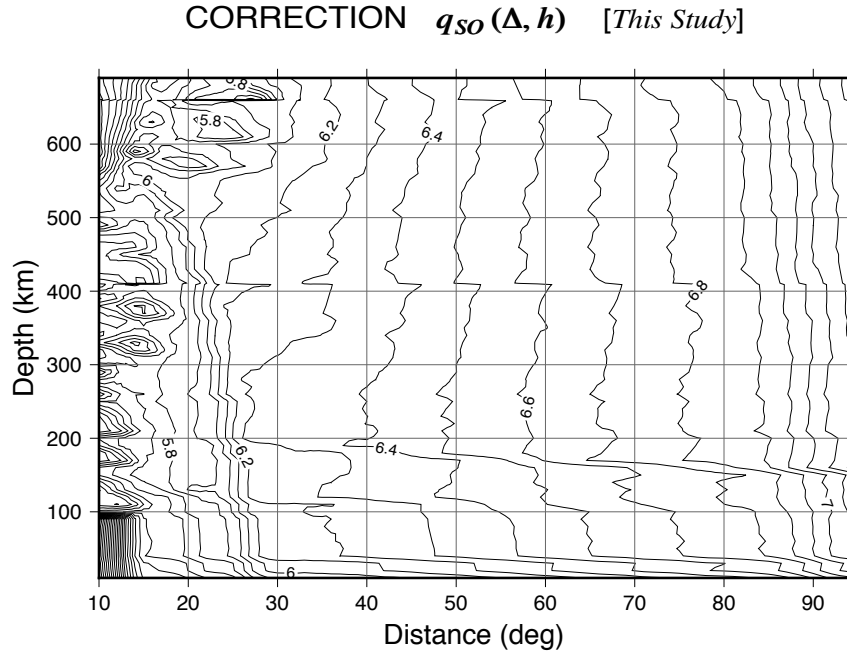


Figure 2.5. Contoured plot of the correction $q_{SO}(\Delta, h)$ obtained in the present study.

- A.** A broad arc featuring strong gradients of q_{SO} is identified at distances shorter than 30° . It illustrates the triplications characteristic of waves bottoming at the mantle discontinuities located at 410 and 660 km. As expected, the relevant distances decrease with increasing h , and the arc fades and eventually disappears at the short distances reached by a ray taking off horizontally at each mantle discontinuity. This feature is obviously absent from Models q_{45} , q_{56} and q_{VC} that do not include the mantle discontinuities.
- B.** At shorter distances and shallow depth, the bottom left corner of Fig. 2.5 features an extremely rapid variation of q_{SO} . Similar, but not immediately comparable, trends are found in q_{VC} , q_{45} , and to a lesser extent q_{56} .

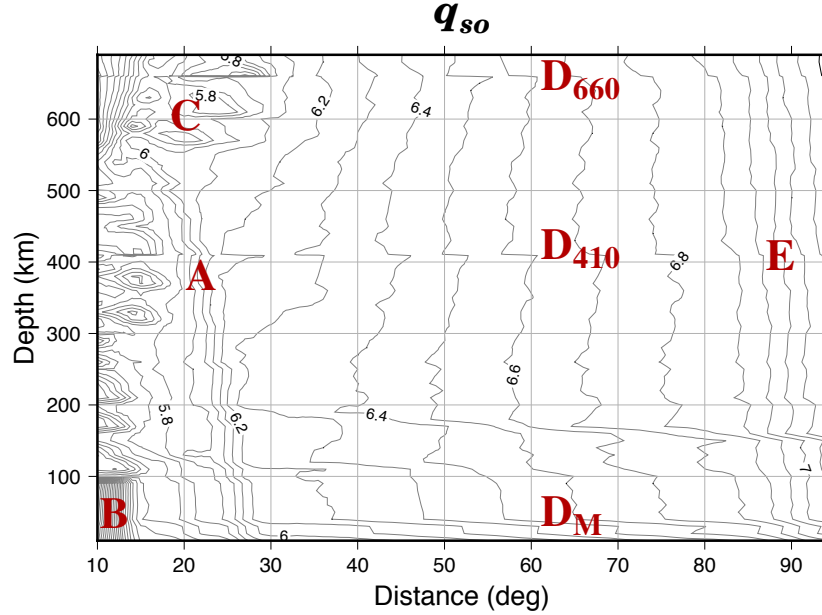


Figure 2.6. Sketch outlining critical features of $q_{SO}(\Delta, h)$. See text for details.

C. At much greater depths ($h > 550$ km), and in the distance range $15^\circ - 30^\circ$, we observe a zone of systematically low values of q_{SO} , which illustrate high amplitudes for rays not penetrating the deep mantle, and thus bottoming in the mantle layers featuring the highest Q_a values. This interpretation is verified by the fact that this zone is largely absent from Veith & Clawson's (1972) q_{VC} , which has a homogeneous (and high) \hat{Q} in all of the lower mantle, below 800 km.

In consideration of the above trends (**A**, **B**, **C**), we will restrict our further comparison of the various corrections q to distances $\Delta > 20^\circ$. Indeed, we

note that this limitation corresponds *de facto* to that of the rounded table of q_{JD} corrections proposed by the IASPEI working group (Anonymous, 2013).

- D.** At larger distances, the downwards transition of the source across the mantle discontinuities is marked by an increase in q_{SO} on the order of 0.05 logarithmic unit. As discussed e.g., by Okal (1992), the amplitude of a teleseismic P wave is controlled, irrespective of its radiation pattern R^P and of anelastic attenuation, by the product of the Somigliana moment tensor excitation and the geometrical spreading factor:

$$\frac{M_0}{4\pi\rho_h\alpha_h^3} \left[\frac{\rho_h\alpha_h}{\rho_0\alpha_0} \frac{\sin i_h}{\sin \Delta} \frac{1}{\cos i_0} \left| \frac{di_h}{d\Delta} \right| \right]^{1/2} \quad (2.11)$$

where subscripts h and 0 refer to source depth and Earth surface, respectively. Given $\sin i_h = \frac{\alpha_h}{r_h} \frac{dT}{d\Delta}$, one derives

$$\sin i_h \frac{di_h}{d\Delta} = \frac{\alpha_h}{r_h} \frac{\sin i_h}{\cos i_h} \frac{d^2T}{d\Delta^2} = \frac{\alpha_h^2}{r_h^2} \frac{1}{\cos i_h} \frac{dT}{d\Delta} \frac{d^2T}{d\Delta^2} \quad (2.12)$$

Assuming that the distance derivatives $\frac{dT}{d\Delta}$ and $\frac{d^2T}{d\Delta^2}$ vary only slightly across the mantle discontinuities, together with $\cos i_h$ which at large distances is always close to 1, one predicts a ratio of amplitudes at constant distance Δ for a source crossing a discontinuity from top to bottom

$$R = \frac{A^{bottom}}{A^{top}} \approx \left[\frac{\rho_h^{top}}{\rho_h^{bottom}} \right]^{1/2} \left[\frac{\alpha_h^{top}}{\alpha_h^{bottom}} \right]^2 \quad (2.13)$$

equal to 0.86 and 0.88, for the 410 and 660 km discontinuities, respectively, in the ak135 model. In turn, this predicts an increase in q_{SO} of 0.066 and 0.056 logarithmic units respectively, in general agreement with our results (Fig. 2.5).

Similarly, at the Mohorovičić discontinuity ($h = 35$ km in ak135; D_M on Fig. 2.6), R is expected to fall to ~ 0.61 , and the jump in q_{SO} to reach 0.2 logarithmic units, again in good agreement with our results.

- E.** At the greatest distances ($\Delta > 85^\circ$) and for all depths, q_{SO} features a regular and strong increase with Δ , on the order of 0.04 logarithmic unit per degree, which compensates for the decrease of the geometrical spreading factor $g(\Delta)$ expressing the divergence of seismic rays bottoming in the deepest layers of the mantle. This feature, which corresponds to a loss of curvature in the travel-time $T(\Delta)$, was recognized even in early travel-time tables, and is therefore also present in q_{56} , albeit with a greater amplitude of ~ 0.055 unit/degree, and in q_{VC} (at 0.065 unit/degree). Note that this gradient with distance becomes even larger in q_{56} beyond 102° , where however geometrical optics no longer applies to the phase P_{diff} , and which at any rate lies beyond our domain of study.

We similarly examine briefly the trends in the other corrections. At intermediate depths ($200 < h < 600$ km), $q_{56}(\Delta, h)$ remains relatively constant between $\Delta = 20^\circ$ and 60° , and then grows systematically with increasing distance. In addition, we note a general decrease of q_{56} with increasing depth; in particular, the shallow values

($h < 100$ km) are generally large, in contrast to the case of q_{SO} . Fluctuations about these general trends are erratic, and their origin remains mysterious.

In the case of $q_{45}(\Delta, h)$, similar general trends may be present, but they are superimposed by large local fluctuations, which tend to make them less perceptible.

Finally, and expectedly, $q_{VC}(\Delta, h)$ is a much smoother function, which shares the general trends of q_{56} , but with significantly more pronounced variations.

2.4.2. Comparison metrics

**Simple statistics*

In Table 2.1, we examine statistics for comparison of the various corrections $q(\Delta, h)$. For each pair of models q_A and q_B , we define a residual

$$r_{A,B}(\Delta, h) = q_A(\Delta, h) - q_B(\Delta, h) \quad (2.14)$$

and list its minimum and maximum values, average $\langle r \rangle$ and standard deviation σ over the distance-depth domain, the average of its absolute value, $\langle |r| \rangle$, and the slope and zero-offset of the best-fitting regression ($q_A = a q_B + b$), as well as its relevant correlation coefficient.

We first focus on the comparison between the corrections q_{SO} , developed from our synthetics, and q_{56} mandated by the Prague formula (Kárník et al., 1962) and the more recent IASPEI working group (Anonymous, 2013). The relevant residual $r_{SO,56}(\Delta, h)$ is contoured on Fig. 2.7. While the residuals

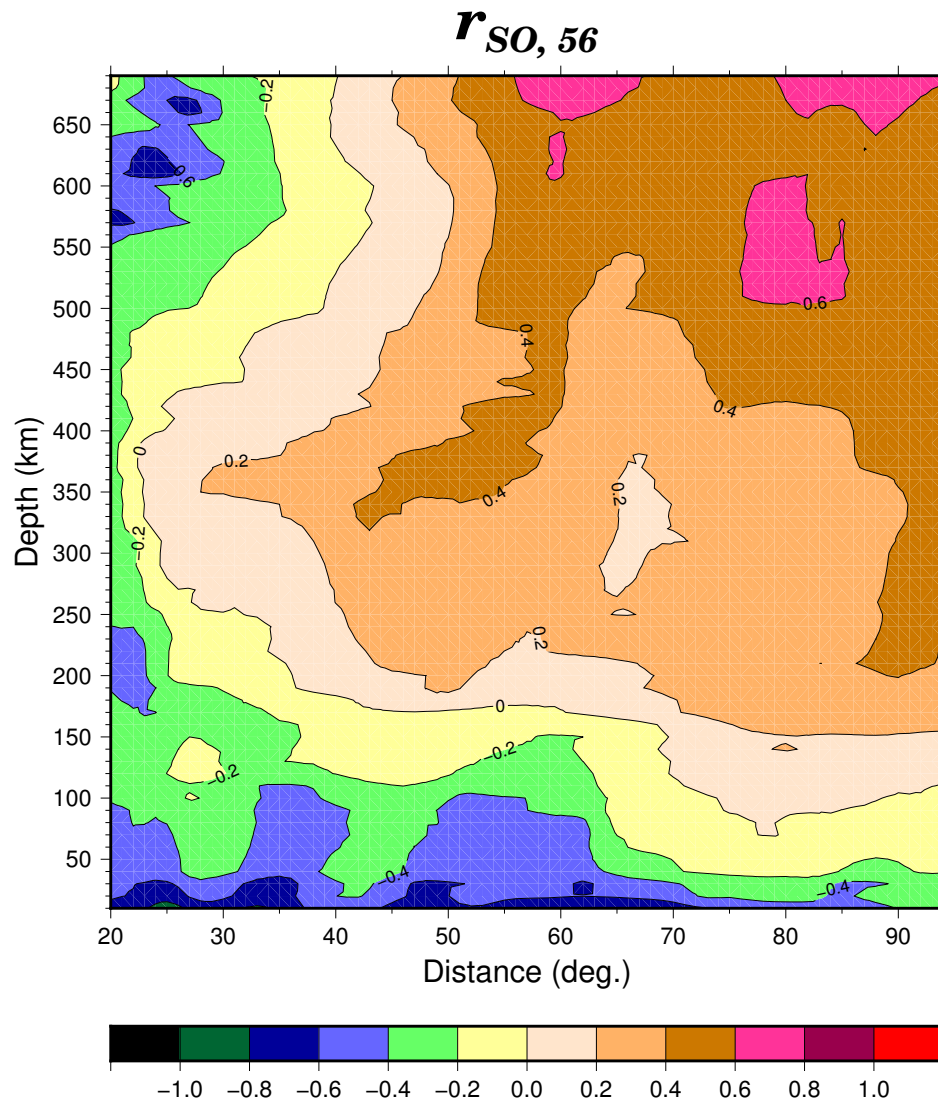


Figure 2.7. Contoured plot of the residual $r_{SO,56}$. Note the general increase with distance and depth.

do range from -0.89 to 0.74 units, these extreme values are concentrated at the corners of the (Δ, h) domain; otherwise, the only regions with large, negative r are domain **B**, described above, and generally most distances at shallow depths, especially short ones for which paths are concentrated in

the crust, where the model used in our study features the lowest anelastic attenuation (Montagner & Kennett, 1996). In the rest of the (Δ, h) plane, the residuals are much smaller, leading to an overall average value of $\langle r_{SO,56} \rangle = 0.12$ units, with a standard deviation $\sigma = 0.34$. These values are shown as the red line and shaded band respectively, on Fig. 2.8 which gives a point by point comparison of q_{SO} and q_{56} . The figure also reflects more of a good average fit between the two corrections than a similarity in pattern, since the correlation coefficient between q_{SO} and q_{56} is mediocre (0.37), suggesting that local fluctuations in the empirical q_{56} are not reflected in the more theoretical q_{SO} .

Table 2.1. Statistical comparison of the various corrections $q(\Delta, h)$

	r_{min}, r_{max}	Average $\langle r \rangle \pm \sigma$	Average $\langle r \rangle$	Regression a,b	Correlation Coefficient
$r_{SO,56}$	-0.89, 0.74	0.12 ± 0.34	0.32	0.53, 3.12	0.37
$r_{SO,JD}$	-0.89, 0.76	0.12 ± 0.34	0.31	0.55, 3.01	0.38
$r_{SO,45}$	-1.01, 0.94	0.08 ± 0.36	0.36	0.43, 3.75	0.30
$r_{SO,VC}$	-0.86, 1.11	0.47 ± 0.36	0.53	0.47, 3.71	0.46
$r_{VC,56}$	-1.04, 0.11	-0.35 ± 0.21	0.35	1.12, -1.09	0.79
$r_{VC,JD}$	-1.04, 0.14	-0.35 ± 0.20	0.35	1.13, -1.21	0.80
$r_{VC,45}$	-1.00, -0.27	-0.39 ± 0.23	0.40	1.01, -0.48	0.72
$r_{56,45}$	-0.54, 0.54	-0.04 ± 0.19	0.15	0.70, 1.87	0.70
$r_{JD,45}$	-0.52, 0.53	-0.04 ± 0.19	0.15	0.71, 1.86	0.71
$r_{JD,56}$	-0.14, 0.13	0.00 ± 0.03	0.03	1.00, 0.03	0.99

$r_{A,B}$ is defined as $(q_A - q_B)$

In addition, we separate on Fig. 2.8 shallow sources ($h < 100$ km), plotted in green and the deepest ones ($h \geq 500$ km) plotted in blue. With the exception of a string of deep negative residuals belonging to domain **C** of Fig. 2.6, the results confirm a possible systematic bias between magnitudes

computed using $q_{56}(\Delta, h)$ for deep and shallow events. This question will be address more in detail in section 2.5.

Remarkably, these conclusions are essentially unchanged when comparing q_{SO} with the original correction q_{45} . Expectedly, since the latter is less smooth than q_{56} , the extreme values of $r_{SO,45}$ (-1.01 and 0.94) are somewhat larger, but the average properties ($\langle r_{SO,45} \rangle = 0.08$ and $\sigma = 0.36$) are comparable to the previous case with, however, an even smaller correlation coefficient (0.30).

The poorest fit is obtained when comparing q_{SO} with Veith & Clawson's (1972) q_{VC} , the residuals being systematically positive ($\langle r_{SO,VC} \rangle = 0.47$ or a factor of nearly 3 on ground motion amplitude). However, because q_{VC} is a smoother function than q_{56} , its correlation coefficient with q_{SO} is slightly higher (0.46). On the opposite, q_{VC} has a significantly better coefficient correlation with q_{56} (0.79), despite its systematic negative bias.

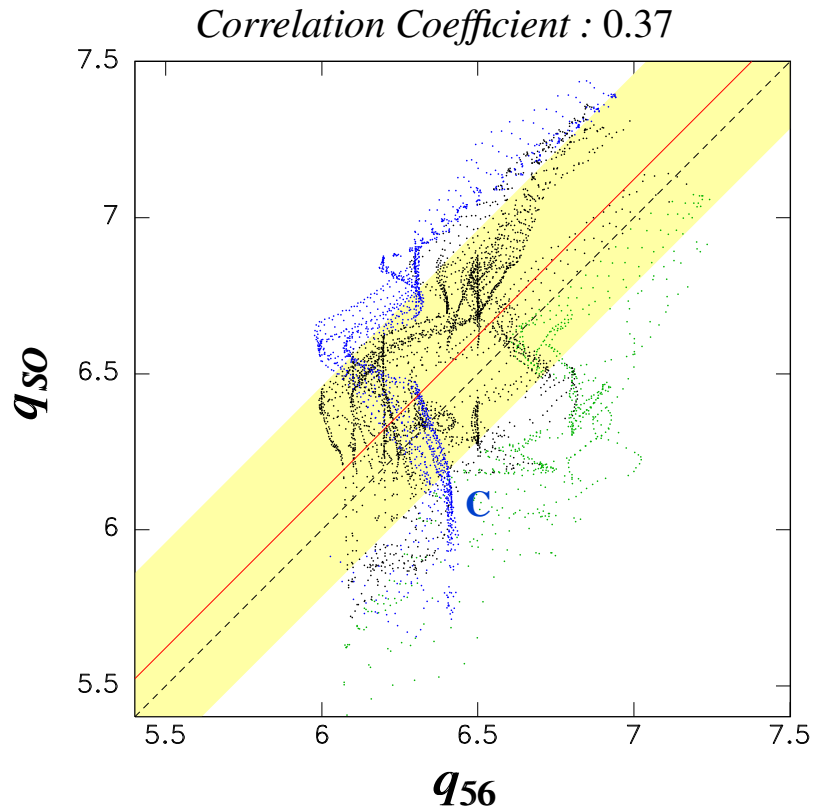


Figure 2.8. Plot of individual values of q_{SO} vs. q_{56} . The dashed line is the bisector of the plane, the solid red line represents the average residual $\langle r_{SO,56} \rangle$ and the shaded area a bandwidth of $\pm 1\sigma$ centered on the average. Data points for $h < 100$ km and $h \geq 500$ km are shown in green and blue, respectively.

In addition, an interesting comparison is that between the two versions of the founding fathers' correction, Gutenberg's (1945b) original q_{45} and Gutenberg & Richter's (1956) more definitive q_{56} (Fig. 2.9). The minimum value of the residual $r_{56,45}$ (-0.54 at $\Delta = 45^\circ$; $h = 350$ km) reflects a nearly universal local maximum in q_{45} at that distance and for all depths, as

opposed to a more local low in q_{56} , which drops below 6.0 in that region, both of which remain unexplained.

The maximum value $r_{max} = 0.54$ relates to a pronounced low in q_{45} which drops below 6.2 at ($\Delta = 90^\circ; h = 350$ km) in the midst of the regular increase of q with Δ observed in all models at those large distances. Again, the origin of this feature is unexplained. Otherwise, the correlation between the two models is good (0.70), and the average residual and standard deviation are minimal (0.04 ± 0.19 logarithmic units), confirming the “consanguinity” of the models, q_{56} having been, unavoidably if mysteriously, derived from q_{45} . Finally, and expectedly, replacing q_{56} with its smoothed version q_{JD} leaves all statistics practically unchanged.

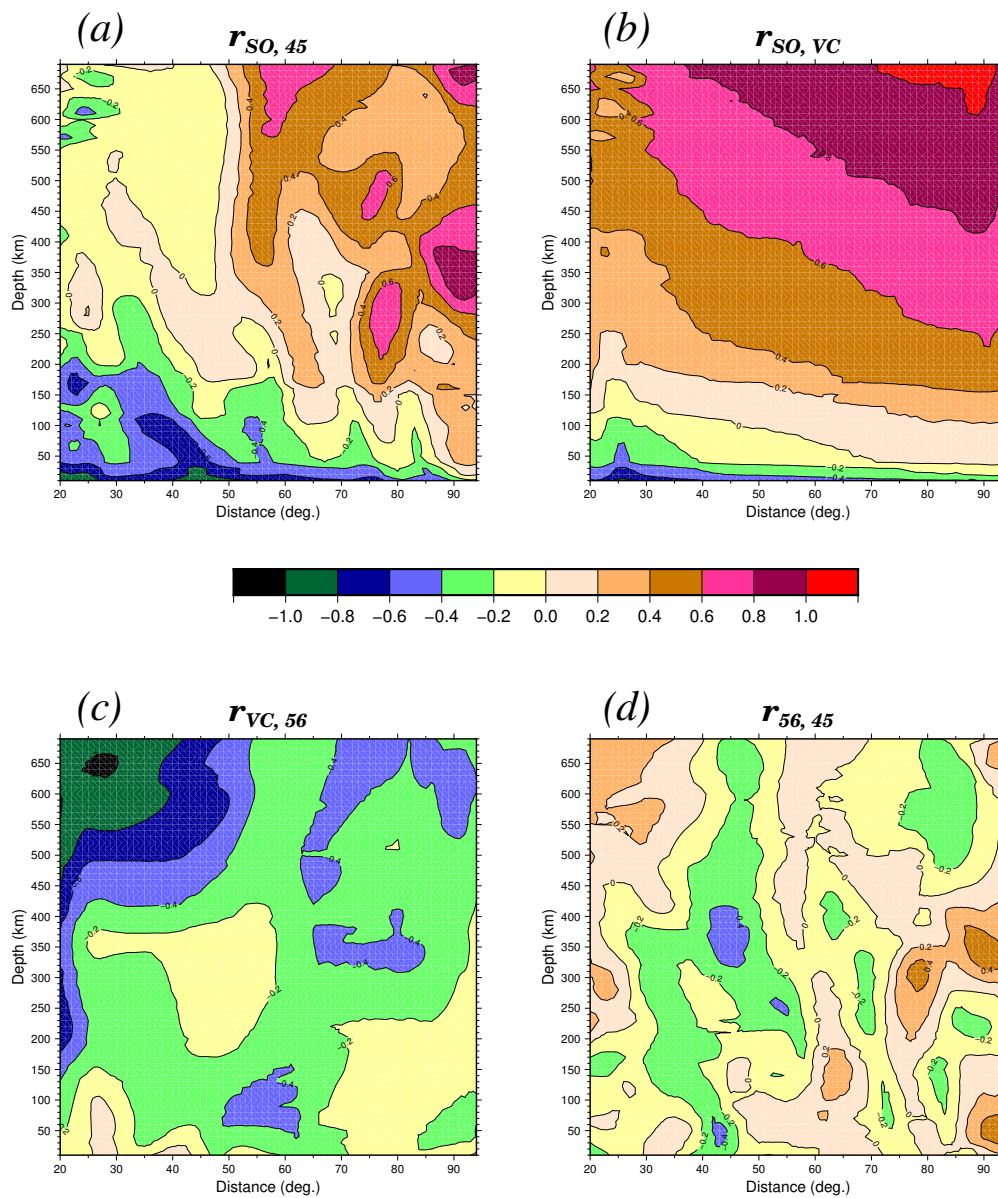


Figure 2.9. Residuals for other combinations of corrections $q(\Delta, h)$. The same palette is used for all plots in Fig. 2.7 and Fig. 2.9.

* Spectra

Fig. 2.10a is a contour plot of the spectral amplitude of the correction q_{SO} , obtained by taking its double Fourier transform into the spatial frequency plane $(k_{\Delta}; k_h)$. The amplitude is concentrated mainly for a combination of $k_{\Delta} = 0.05$ rad/deg and $k_h = 0.005$ rad/km (albeit with a few side lobes), which would correspond to spatial "wavelengths" of 125° and 1250 km, respectively. Both express the systematic increase of q_{SO} with Δ (at most depths) and with h (at most distances), over ranges comparable to half those wavelengths. The spectrum is richer in distance than in depth wavenumbers.

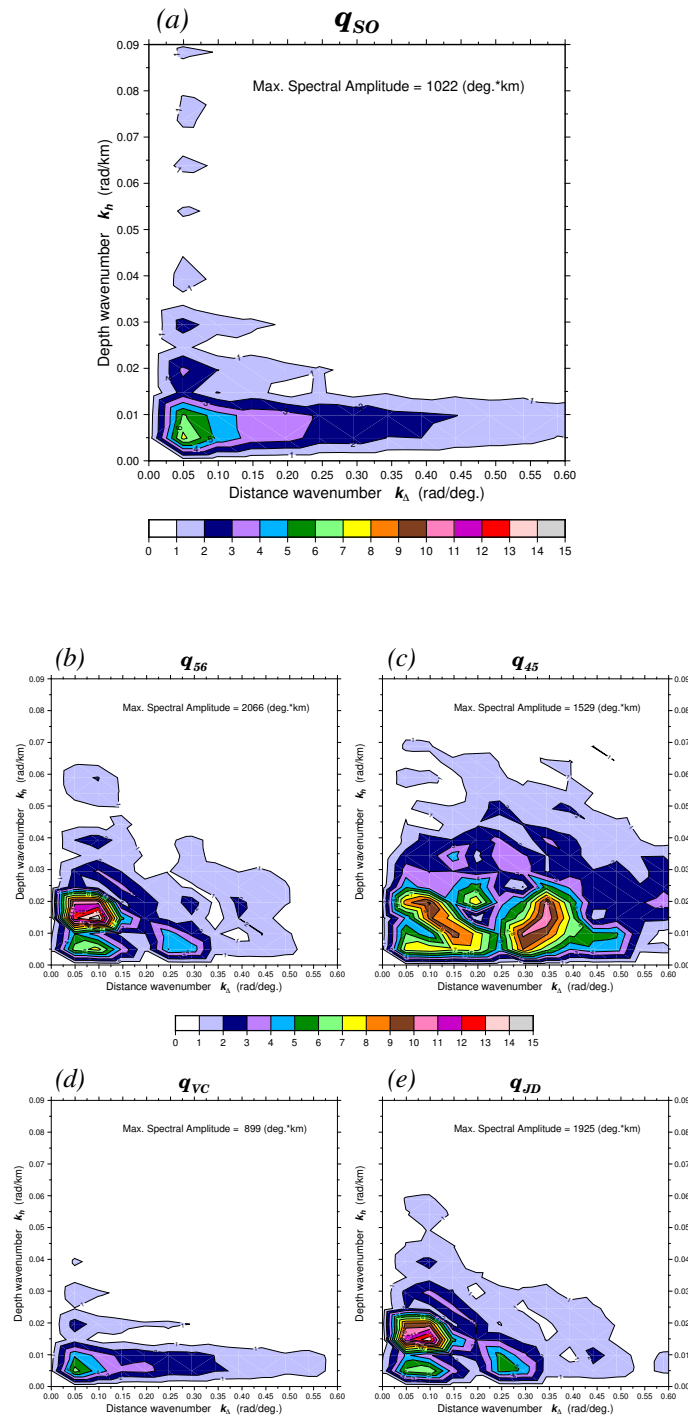


Figure 2.10. Spectral amplitudes of corrections $q(\Delta, h)$ contoured and color-coded in the (k_Δ, k_h) wavenumber plane. The palette is common for all frames, using a linear scale extending from 0 to 15, the latter corresponding to 2100 $\text{deg} \cdot \text{km}$. Except in the case of q_{45} (Frame c), note the preponderance of low frequency spectral components, and the generally richer spectrum along the k_Δ direction.

Figs. 2.10b-e similarly examine the spectra of other corrections q . While a low-frequency character is preserved in all cases, q_{56} shows a shift of the maximum spectral components to shorter distance wavelengths ($k_{\Delta} = 0.1$ rad/deg), which expresses the different pattern in q_{56} for $\Delta < 55^{\circ}$ (little variation with distance) and $\Delta > 55^{\circ}$ (more systematic increase with Δ). As expected, the interpolated “Working Group” correction q_{JD} has a spectrum sharing these properties. By contrast, the spectrum of the much more complex $q_{45}(\Delta, h)$ is clearly blue-shifted to higher spatial frequencies, especially along the distance wavenumber, with a maximum around $k_{\Delta} = 0.35$ rad/deg, corresponding to a wavelength of 18° . Finally, Veith & Clawson’s (1972) correction q_{VC} is red-shifted with respect to q_{56} , and its spectrum is reminiscent of that of q_{SO} .

** Advanced metrics using spatial filtering*

In this section, we characterize quantitatively the correlation between the various corrections $q(\Delta, h)$ by considering increasingly smoothed variations of these functions. Specifically, each frame n of Fig. 2.11 shows the correction $q_{SO}^{(n)}$ resulting from applying a low-pass two-dimensional filter with cut-off values $k_{\Delta}^{(n)}$ and $k_h^{(n)}$ listed in Table 2.2, selected to correspond to filtering wavelengths $\Lambda^{(n)}$ equivalent to n sampling points in distance and depth, respectively.

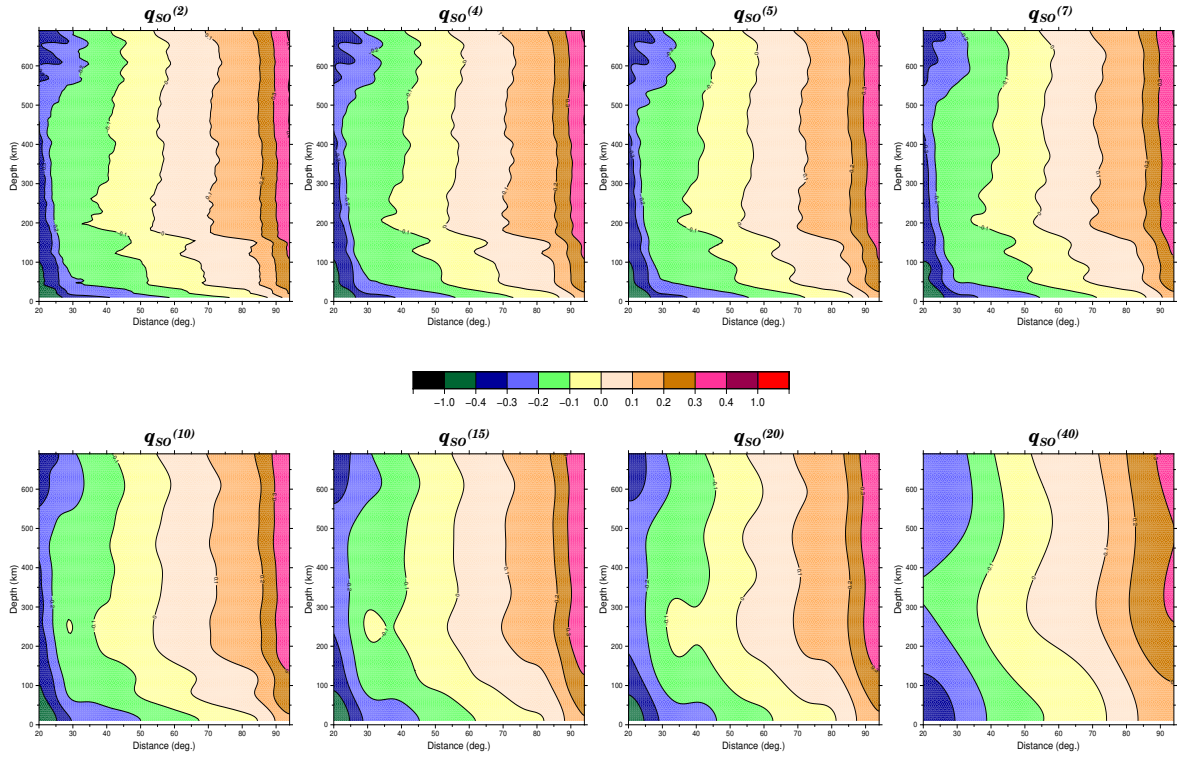


Figure 2.11. Smoothed versions $q_{SO}^{(n)}(\Delta, h)$ obtained by low-pass filtering the correction q_{SO} at increasingly low maximum wavenumbers, listed in Table 2.2.

At each step of smoothing, indexed n , we define a metric characterizing the fit between the filtered versions of two corrections

$$M_{A,B}^{(n)} = \frac{\sum_{i,j} \left(q_A^{(n)}(\Delta_i, h_j) - q_B^{(n)}(\Delta_i, h_j) \right)^2}{\left[\sum_{i,j} \left(q_A^{(n)}(\Delta_i, h_j) \right)^2 \cdot \sum_{i,j} \left(q_B^{(n)}(\Delta_i, h_j) \right)^2 \right]^{1/2}} \quad (2.15)$$

This formula is adapted from Stein et al. (2015) and Salaree (2019), who applied this concept to other two-dimensional problems in geophysics. A good fit between the compared datasets is expressed by a low value of the metric M .

Table 2.2. Parameters of smoothing filters used on Fig. 2.11

Index	$k_{\Delta}^{(n)}$	$k_h^{(n)}$	Λ_{Δ}	Λ_h
n	(rad/deg.)	(rad/km)	(deg.)	(km)
2	3.14	0.314	2	20
4	1.57	0.157	4	40
5	1.26	0.126	5	50
7	0.90	0.009	7	70
10	0.628	0.0628	10	100
15	0.419	0.0419	15	150
20	0.314	0.0314	20	200
40	0.157	0.0157	40	400
50	0.126	0.0126	50	500

We examine here the variation with n of metrics computed between our corrections q_{SO} on the one hand, and the corrections q_{56} , q_{45} or q_{VC} on the other, with $n = 0$ corresponding to the raw unfiltered datasets. In all cases, the average values $\langle q \rangle$ have been removed before computing the metrics M through (2.15).

Fig. 2.12 shows that the metrics generally decrease with increasing n , and that their values stabilize for $n \geq 4$ and are then comparable for all three couples of corrections considered. The asymptotic value for large n , $M_{SO,56} \approx 0.12$, expresses the systematic linear trend (with Δ and h) controlling q_{SO} , but less prominent, and shifted to slightly higher values of k in the empirical q_{56} (see the spectra on Figs. 2.10a and 2.10b). As n is reduced, the irregular components in q_{56} become more important and

dominate its pattern at the lowest values $n = 0$ and $n = 2$, leading to enhanced values of M . The situation is essentially unchanged in the case of $M_{SO,45}$, and interestingly of $M_{SO,VC}$, although the low- n values are more contained for the latter, because of the generally smoother nature of q_{VC} . Finally, Fig. 2.12 also compares the two original versions, q_{45} and q_{56} ; while their profile is similar, the metrics $M_{56,45}$ are significantly reduced, their asymptotic values (≈ 0.015) by as much as one order of magnitude. This expresses the fact that the difference between those two models is mostly contained in their high-frequency spectrum, with their low frequency components being comparable.

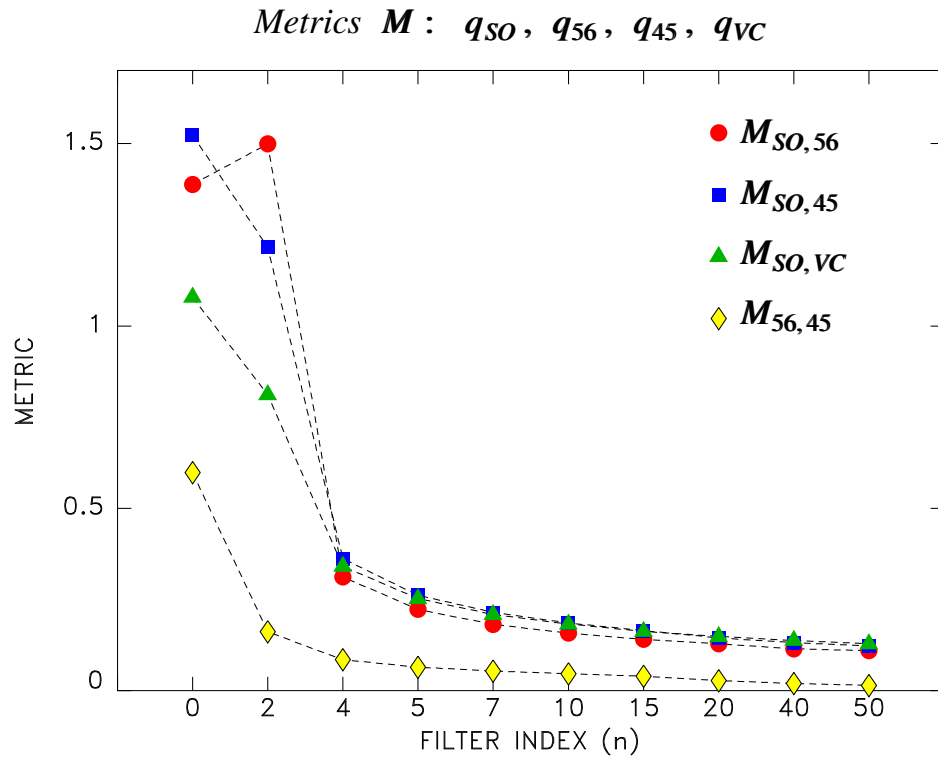


Figure 2.12. Comparison metrics M (2.15) for relevant couples of corrections, as a function of the smoothing index n . Note the rapid convergence for $n \geq 4$.

2.4.3. Possible sources of additional bias

A number of issues transcending the primary effects of geometrical spreading and attenuation are expected to significantly affect, and possibly bias, any function

* *The distribution of stations across the (Δ, h) plane*
 $q(\Delta, h)$ obtained empirically, such as q_{56} or q_{45} . Among them, we identify

To explore this question, we extracted from the NEIC catalog all 76,067 earthquakes featuring at least one magnitude $M \geq 5$ for the years 1970-2015, for which source characteristics can be assumed to be accurate by modern standards; the hypocentral distribution of such a dataset is expected to be reasonably comparable to those which went into the preparation of the corrections q_{45} and q_{56} . We then plot these individual events on Fig. 2.13a as a function of depth and distance to Pasadena. As expected, large sections of the (Δ, h) plane are not covered, which simply expresses the irregular geographical distribution of subduction zones, but also means that B. Gutenberg had to rely exclusively on mailed-in reports for those combinations of Δ and h . We further the experiment in Fig. 2.13b, by including distances, color-coded by stations, to Jena, La Paz, Kobe, and Adelaide, which, according to Gutenberg (1945b), contributed, after Pasadena, the largest number of measurements of deep shocks into the q_{45} database.

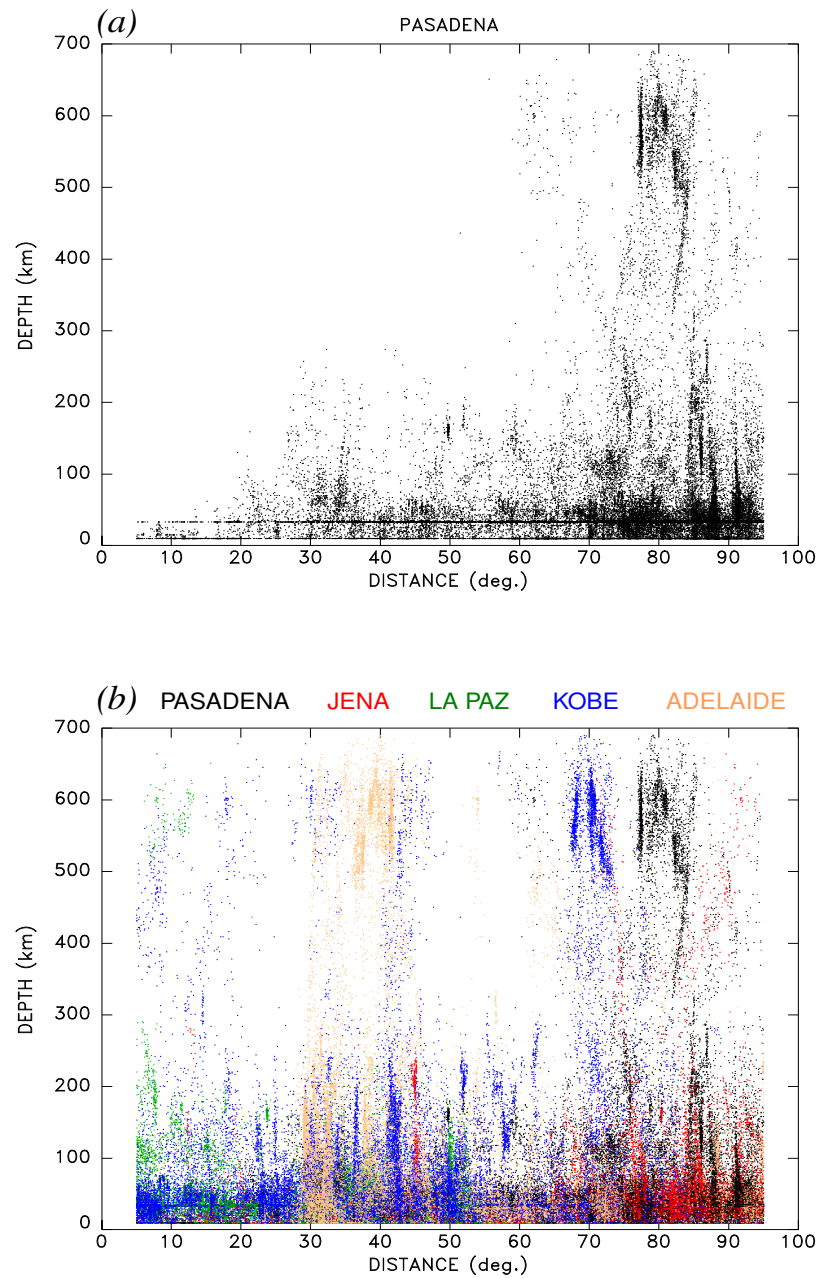


Figure 2.13. (a) Distribution of recent seismicity (1970-2015; $M \geq 5$) as a function of source depth and distance to Pasadena. Note that large sections of the (Δ, h) lack coverage. (b) Same as (a) but including distances to four other stations contributing the bulk of Gutenberg's (1945b) dataset for deep earthquakes, color-coded according to stations. Note that several regions of the (Δ, h) plane are covered principally or exclusively by one of the five stations.

Notwithstanding the (presumably fewer) contributions of all other stations, Fig. 2.13b suggests that certain domains of the (Δ, h) plane are sampled primarily by a single, or a single group of stations, e.g., Pasadena (and other Southern California stations) would control the combination $(\Delta \approx 80^\circ, h = 500 - 650 \text{ km})$, Kobe, and possibly Japanese stations nearby, $(\Delta \approx 70^\circ, h = 500 - 650 \text{ km})$, and Adelaide, and possibly other Australian stations such as Riverview, $(\Delta \approx 40^\circ, h = 500 - 650 \text{ km})$.

This could bias the computation of $q(\Delta, h)$ in two ways. First, the instruments in use at these stations could be drastically different from that at Pasadena, which means that the dominant period recorded in the P wave, and hence the windows sampled in the frequency domain, could have been different. For example, Adelaide operated a single North-South Milne-Shaw instrument with a period of 12 s, while Jena and Kobe operated Wiechert instruments with periods of 8 and 4 s, respectively. La Paz used a bi-filar system with a period of 2.4 s (McComb et al., 1931; Parham et al., 1988). In order to illustrate this issue, we built seismograms in the same geometry as on Fig. 2.4, but using the responses of these various instruments; we also included the case of a modern digital broadband system. The resulting logarithmic values L , listed on Table 2.3, emphasize that using a different instrument could significantly affect the computed magnitudes, by as much as ~ 0.3 logarithmic units. Note in particular that even common types of instruments, such as Wiechert mechanical seismometers, could feature

widely differing constants (period and damping parameters), displacing the dominant period beyond the presently mandated upper bound of 3 s. In this respect, it is highly probable that a large number of measurements used by B. Gutenberg in the building of q_{45} and q_{56} would now be in violation of the modern algorithm (Anonymous, 2013). Not surprisingly, the use of a modern broadband instrument, or of a mechanical system operating far below its pendulum period (e.g., Adelaide) minimizes this potential bias.

Table 2.3. Influence of instrumentation on m_b measurements

System simulated					S_{max}	T	G	A	L
Instrument	Station	T_p	V	ϵ	(cm^\dagger)	(S)		(μm)	
<i>Historical Instruments</i>									
Benioff SP (Fig. 2.4)	Pasadena	Electromagnetic			5.03	1.53	9120	5.52	0.56
Wiechert	Jena	8	210	3.5	0.38	3.91	509	7.45	0.28
Bi-filar	La Paz	2.4	700	2	0.96	2.52	1506	6.37	0.40
Wiechert	Kobe	3.1	61	4.6	0.64	3.20	67	9.64	0.48
Milne-Shaw	Adelaide	12	150	20	0.24	3.97	150	16.07	0.61
<i>Modern Digital Instrument</i>									
STS-2	GSN	Broadband Digital			1.02×10^8	2.80	8.20×10^{10}	12.39	0.6

† Units are digital counts in the case of broad-band instrument

As a second source of bias, the combination of Δ and h controlled by a single station often (but not always) corresponds to a particular geographic epicentral area. For example, deep earthquakes at a distance of $\sim 80^\circ$ from Pasadena can sample Fiji, South America and the Sea of Japan, and those 40° from Adelaide, Fiji and Java, but deep events 70° from Kobe are exclusively from Fiji. Since plate

dynamics predict that earthquakes at the bottom of subduction zones should have a preferential down-dip compressional mechanism (Isacks & Molnar, 1971), events from a single region (e.g., Fiji) will have a consistent radiation pattern coefficient for P waves, R^P , to a given station (e.g., Kobe). That could introduce a bias when a single epicenter-station combination controls a domain of distances and depths (in that case, 70° and 500-650 km) in the $q(\Delta, h)$ diagram. We explore this possibility by examining P -wave radiation patterns to the five stations Pasadena, Jena, La Paz, Kobe and Adelaide from all available GlobalCMT solutions (Dziewonski et al., 1981; Ekström et al., 2012) with $M_0 > 10^{24}$ dyn*cm for the years 1977-2018 (a total of 26571 events). Results are shown on Fig. 2.14 color-coded according to the value of $|R^P|$. We recall that its average value over the focal sphere is $2/\sqrt{15} \approx 1/2$. Note that for very shallow sources ($h < 50$ km), radiation patterns trend systematically from lower values at shorter distances, largely controlled by Kobe and La Paz, in a geometry where rays emerge close to the low-angle plane characteristic of nearby subduction events, to large $|R^P|$ beyond 70° where the continental stations Pasadena and Jena come into play. Deficient amplitudes may have induced the founding fathers to artificially increase q_{56} at shorter distances; this effect could account for a bias of ~ 0.12 logarithmic units out of the 0.35 observed for $r_{SO,56}$ across the full distance range (Fig. 2.7).

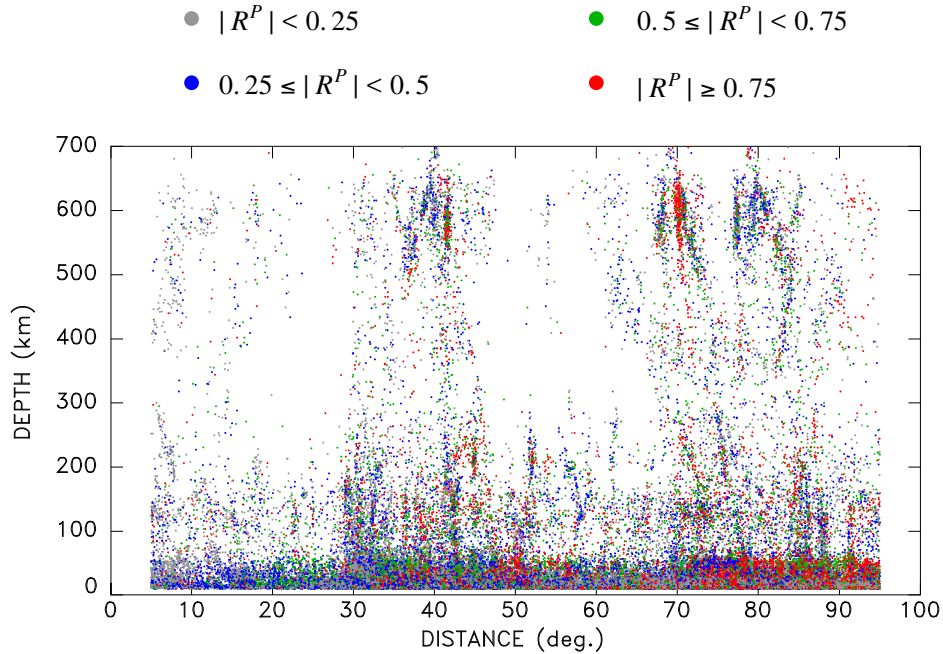


Figure 2.14. Distribution of GlobalCMT sources ($M_0 \geq 10^{24}$ dyn*cm) color-coded according to absolute radiation patterns $|R^P|$ at the five stations in Fig. 2.13, as a function of station distance and source depth. A prominent color in a subsection of the diagram could indicate a systematic bias during an empirical determination of q .

Rapid variations as a function of distance are also observed at great depths ($h > 500$ km), e.g., in the interval $67^\circ \leq \Delta \leq 75^\circ$, including many large values greater than 0.75 (shown as red dots), as opposed to generally lower values in the 75° - 85° window. However, a direct correlation with the corrections q_{56} or q_{45} is not present. Without precise information on the events which formed the datasets used in the preparation of those corrections, we can only speculate as to the possibility of any bias introduced by systematic focal geometries in deep portions of the (Δ, h) plane.

* *The systematic variation of period T across the (Δ, h) plane*

Another source of possible bias stems from the systematic variation of the dominant period T across the (Δ, h) plane. Fig. 2.15 contours the period T resulting from the processing of our synthetics, averaged over all focal geometries, as a function of those parameters. In simple terms, we find that it increases from ~ 0.9 s at short distances and for deep events to ~ 1.8 s at the largest distances and for shallow sources. This is easily explained as a result of the preferential anelastic attenuation of high frequencies, which is more efficient over those paths which are long and/or intensely sample the asthenosphere.

In principle, in order to recover a true ground motion A , the algorithm described on Fig. 2.4 requires the use of the exact gain G at the relevant period T (Anonymous, 2013); in the case of the Benioff short-period instrument used in our synthetics, the difference in gain between 0.9 and 1.8 s is a factor of 4.5 (or 0.65 logarithmic units). If, for a number of reasons, one used a constant gain, the instrument response would be underestimated for short distances (and/or deep sources) relative to longer paths (and/or shallow sources), and in turn the ground motions would be overestimated at short distances and underestimated for long paths. When attempting to match measurements made for the same earthquake at various distances, one would then force an artificial, additional increase in $q(\Delta)$ (at fixed h) from short to long distances. For example, in the case of shallow sources and as previously noted, $r_{SO,56}$ increases by about 0.35 unit from -0.7 to

-0.35 between 20° and 90° (Fig. 2.7) , while the dominant period T increases from 1.4 to 1.8 s (Fig. 2.15).

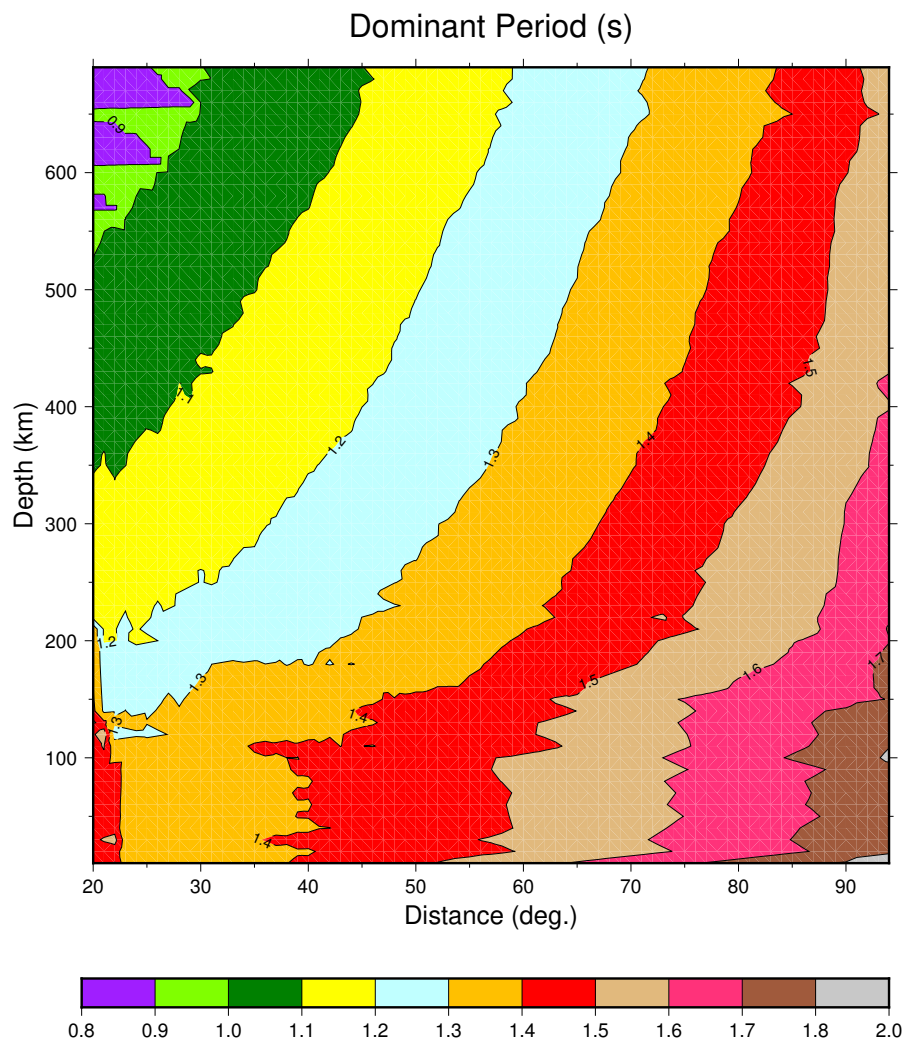


Figure 2.15. Dominant period T (averaged over all focal geometries) extracted from our synthetic seismograms by the algorithm of Fig. 2.4, contoured as a function of distance and depth. Note systematic increase with Δ , and decrease with h .

Clearly, it would have been extremely challenging (if not straight impossible) to manually detect such a difference in T , which would amount to 0.2 mm for half-period oscillations on the paper records read by B. Gutenberg, with a typical time scale of 6 cm/mn. Yet, the difference in gain at such periods represents a factor of 1.8 (or 0.26 logarithmic units), which when combined with the probable radiation pattern bias of 0.12 units mentioned above, could explain the full increase of ~ 0.35 units in $r_{SO,56}$. We stress that this interpretation is based of the assumption that B. Gutenberg was using the short-period Benioff instrument, which is supported by a detailed reading of Gutenberg (1945b), even though that use was most probably not exclusive. On the other hand, the variation in dominant period is negligible when using mechanical instruments such as the Wiechert or Milne-Shaw seismometers, since they have an essentially flat response at periods much shorter than that of their pendulum.

This situation could then create a bias between stations operating mechanical vs. electromagnetic instruments, that the founding fathers could have sought to compensate with station corrections when such records involved similar distances. However, this effect may have been incorporated directly into q for those combinations of (Δ, h) controlled by single stations operating different instruments or perhaps simply using different operational procedures, i.e., adjusting or not the gain to the precise period retained at maximum amplitude.

2.5. Conclusion and Perspective: A preliminary test of q_{SO} vs. q_{JD}

We have explored the origin of the correction $q(\Delta, h)$ used for the computation of the body-wave magnitude m_b (2.1), defined on a largely empirical basis by Gutenberg (1945b) as q_{45} , revised as q_{56} by Gutenberg & Richter (1956), and later enshrined into operational practice (Kárník et al., 1962; Anonymous, 2013). Using a large number of synthetic seismograms computed for a full range of source depths and station distances, but at constant seismic moment, we obtain our own correction $q_{SO}(\Delta, h)$. While it retains some commonality with the original versions of q , especially at low distance and depth wavenumbers, we could not find any explanation for the small-scale variations over the (Δ, h) plane of q_{56} , and especially q_{45} . Seventy-five years after the original papers were published, their origin thus remains a mystery. However, we identify some possible sources of systematic bias which may have played a role in the inclusion of fine structure in the corrections q_{45} and q_{56} .

Having derived a new correction $q_{SO}(\Delta, h)$ more solidly rooted in modern theory than its empirical predecessor q_{56} (and its operational version q_{JD}), the question arises naturally of the effect that its use may have on the routine computation and cataloguing of m_b .

For this purpose, we ran an exploratory test based on a small dataset of 17 large earthquakes, listed in Table 2.4 in order of increasing depth, from 14 to 687 km. For each of them, we extracted from the ISC Bulletin reported values of amplitude A and period T , and recomputed values of m_b through (2.1), using both the correction q_{JD} standardized by the Working Group (Anonymous, 2013) and our newly derived

Table 2.4. Magnitudes computed in preliminary experiment

Date D M (J) Y	Region	Latitude (°N)	Longitude (°E)	Depth (km)	m_b		
					From q_{JD}	From q_{SO}	Residual
28 OCT (302) 2012	Haida Gwaii	52.79	-132.10	14	6.44	5.82	-0.62
03 MAY (123) 2006	Tonga	-20.19	-174.12	55	7.04	6.85	-0.19
04 OCT (277) 1994	Kuril Islands	43.60	147.63	68	7.23	7.03	-0.20
23 JUN (174) 2014	Aleutian Is.	52.00	178.43	104	6.59	6.51	-0.08
22 JAN (022) 2017	Solomon Is.	-6.03	154.94	150	6.89	6.85	-0.04
29 JUL (211) 2016	Mariana Is.	18.50	145.70	209	6.63	6.82	0.19
08 AUG (220) 2007	Java	-6.03	107.58	305	6.10	76.35	0.25
27 JAN (027) 2006	Banda Sea	-5.61	128.20	397	6.91	7.20	0.29
21 JUL (202) 1994	Primorye	42.34	132.87	460	6.41	6.79	0.38
24 NOV (329) 2008	Sea of Okhotsk	54.20	154.32	492	6.49	76.91	0.42
05 FEB (036) 2005	Mindanao	5.29	123.34	540	6.34	6.62	0.28
19 AUG (231) 2018	South of Fiji	-17.86	-177.85	555	6.92	7.09	0.17
17 JUN (169) 1996	Flores Is.	-7.38	123.02	584	6.39	6.61	0.22
24 MAY (144) 2013	Sea of Okhotsk	54.61	153.77	611	7.34	7.68	0.34
09 JUN (160) 1994	Bolivia	-13.82	-67.25	647	7.04	7.56	0.52
30 MAY (150) 2015	Bonin Islands	27.94	140.56	681	7.04	7.47	0.43
06 SEP (249) 2018	South of Fiji	-18.24	179.86	687	6.50	6.80	0.30

q_{SO} . We list in the last column of Table 2.4 and plot on Fig. 2.16 the residual $(m_b)_{SO} - (m_b)_{JD}$, which is simply $r_{SO,JD}$ (2.14), for the appropriate source depth and averaged over the reporting stations. A clear trend is present, which regresses with a slope of ~ 0.1 logarithmic unit per 100 km (red line on Fig. 2.16). At shorter distances, our dataset clearly follows the green curve, which plots, as a function of h , the theoretical average of $r_{SO,JD}$ between $\Delta_{min} = 20^\circ$ and $\Delta_{max} = 94^\circ$:

$$\overline{r_{SO,JD}}(h) = \frac{1}{\Delta_{max} - \Delta_{min}} \int_{\Delta_{min}}^{\Delta_{max}} r_{SO,JD}(\Delta, h) \cdot d\Delta \quad (2.16)$$

The agreement simply expresses that the average residual taken over the reporting stations is comparable to the residual averaged mathematically over all distances, or in other words that the distribution of stations over distance is appropriately

regular. This interpretation is upheld by noting that the fit between our dataset and the predicted residual (green curve on Fig. 2.16) deteriorates for $h > 400$ km.

Indeed, the blue dashed line is a plot of average residuals (2.16) computed for $\Delta_{min} = 50^\circ$, which is in better agreement with outliers in our dataset. The difference between the green and blue curves reflect the fact that $r_{SO,56}$ has a weak distance gradient for shallow sources, but a much stronger one at greater depths (Fig. 2.7). We have verified that outlying events such as the 2008 Sea of Okhotsk and 1994 Bolivia and Primorye earthquakes have a distribution of amplitude reporting stations strongly biased towards greater distances, with e.g., the Bolivian earthquake having none below 55° (for unclear reasons). This remark emphasizes the possibility of further and subtle biases in the computation of m_b . It is clear that this limited experiment may not be statistically significant, on account on the meager size of the processed dataset. However, it would suggest that a systematic bias exists when comparing catalogued m_b values for shallow and deep earthquakes, which may be close to a full logarithmic unit; we recall that such comparisons were the driving force behind the extension of magnitude scales to deep sources by Gutenberg (1945b). The inescapable conclusion would then be the need to revise the entire existing catalog of published values of m_b . This truly Herculean project obviously falls beyond the scope of the present study.

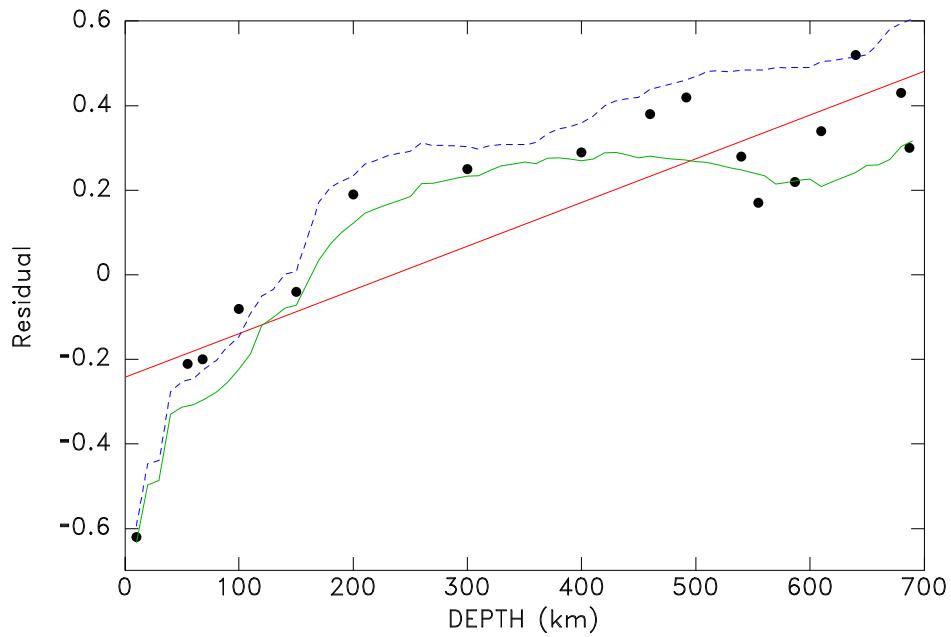


Figure 2.16. Exploratory experiment comparing magnitudes computed using q_{JD} and q_{SO} from amplitude and period data actually reported to the ISC for 17 large earthquakes. The individual dots are the differences in magnitudes listed in the last column of Table 2.4. The red line is their linear regression as a function of depth. Also shown are the predicted average residuals from 2.16 for $\Delta_{min} = 20^\circ$ (solid green curve) and $\Delta_{min} = 50^\circ$ (dashed blue curve).

CHAPTER 3

An implosive component to the source of the deep**Sea of Okhotsk earthquake of 24 May 2013:****Evidence from radial modes and CMT inversion****3.1. Introduction and historical perspective**

The existence of deep earthquakes was definitely proven by Wadati (1927, 1928, 1929) who noticed that for such events, it was impossible to reach their focus at distance zero, using observables at the surface of the Earth, such as $S - P$ travel times or the increase of felt intensities in the epicentral area. This remarkable observation reopened the question of the origin of seismogenesis at great depths, where high temperatures and pressures would *a priori* exclude the possibility of brittle rupture, an argument forcibly used by Jeffreys (1924) to counter earlier and less robust suggestions of deep seismicity (Pilgrim, 1913; Mainka, 1915; Turner, 1922). In this context, Bridgman (1945) first proposed that phase transitions could play a role in the mechanism of deep earthquakes, even though studies such as Stechschulte's (1932) or Leith & Sharpe's (1936) had argued for a largely common mechanism of rupture (a "consanguinity" in the latter's terms) between deep and shallow earthquakes. Indeed, a most remarkable result of modern seismology has

been that focal mechanisms of deep earthquakes could be modeled, at least to an excellent approximation, by double couples, *i.e.*, by the same representation as their shallow counterparts (*e.g.*, Isacks & Molnar, 1971). In this framework, the role of a phase transition might be only that of a component to the focal mechanism, possibly a small one (Vaišnys & Pilbeam, 1976), meaning that it might be detected only during very large deep events, the latter being of course comparatively rare.

A phase transformation at the source should involve a change in volume, and hence an isotropic component to its moment tensor. Using a systematic inversion of hand-digitized analog seismograms from the 1963 Peru-Bolivia and 1970 Colombia deep shocks, Gilbert & Dziewonski (1975) first proposed that they did indeed feature an implosive component (as large as 40% of the deviatoric one), but Okal & Geller (1979) later suggested, and Russakoff et al. (1997) proved, that their result was an artifact of various simplifications in both the Earth model used and the inversion algorithm. With the advent of digital data, it became possible to explore the source of smaller events, and a review of 19 deep shocks by Kawakatsu (1991a) failed to identify any isotropic component to their moment, with a threshold of detection of 10% of the full moment. The occurrence of the 1994 Bolivian deep earthquake whose moment, 2.7×10^{28} dyn*cm, was twice that of the 1970 Colombian shock, motivated a number of systematic searches for an isotropic component to the moment tensor, which however, returned either no such evidence (Hara et al., 1995; Okal, 1996), or a suggestion marred by systematic trade-offs (Kikuchi & Kanamori, 1994). The conclusion of these studies was that any isotropic component had to be

small enough to evade detection, and thus had to represent at most a nucleation of the principal element of stress release, the latter taking place through a process essentially equivalent to the source of shallow earthquakes, represented by a pure double-couple.

This concept is in general agreement with the model of “transformational faulting”, in which rupture nucleation and growth accompany the phase transformation of olivine that persists in a metastable state, due to unfavorable kinetics in the cold subducting slab (Kirby, 1987; Kirby et al., 1991, 1996). The emission of acoustic energy upon transformation of metastable materials has been observed in the laboratory on samples of ices (Kirby et al., 1996), germanates (Green & Burnley, 1989; Burnley et al., 1991) and forsterite (Green et al., 1990; Wang et al., 2017). More recently, Officer & Secco (2020) have observed transformational faulting in fayalite (Fe_2SiO_4) samples at high pressures and temperatures in the presence of deviatoric stress, further mimicking the conditions in subducting slabs.

The rupture nucleation process has been referred to as “anti-cracking” by Green & Burnley (1989) and Green et al. (1990). The olivine wedge inside the subducted Western Pacific slab has recently been imaged in the Southwest Japan and Mariana slabs using receiver function techniques (Kaneshima et al., 2007; Kawakatsu & Yoshioka, 2011), and below the Sea of Japan and Northeastern China using seismic tomography (Jiang et al., 2015).

In this context, the occurrence of the Sea of Okhotsk deep earthquake of 24 May 2013 provides a new opportunity to conduct an in-depth search for an isotropic component to its moment tensor. At $M_0 = 3.95 \times 10^{28}$ dyn*cm, this event is the largest deep earthquake ever recorded (its moment being 1.4 times that of the 1994 Bolivian earthquake (Fig. 3.1 and 3.2)), and incidentally, the eighth-largest regardless of depth in the GlobalCMT catalog. In the present study, we apply the analysis of Okal (1996) to the 2013 event and, this time, document a resolvable implosive component M_I amounting to 3% of the deviatoric moment.

We confirm this result, albeit with a larger value for M_I , through unconstrained moment tensor inversions using a variation of the Global CMT algorithm.

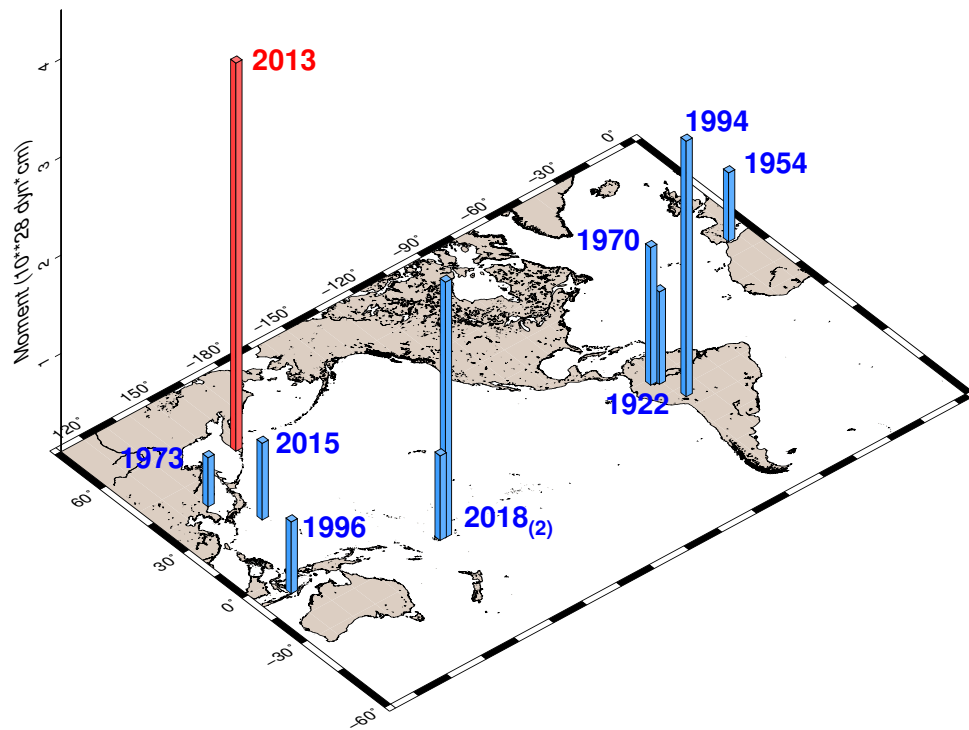


Figure 3.1. Sketch of the only ten deep events ($h > 300$ km) known since 1900 with measured moments $M_0 \geq 5 \times 10^{27}$ dyn*cm. The bars are scaled to moment.

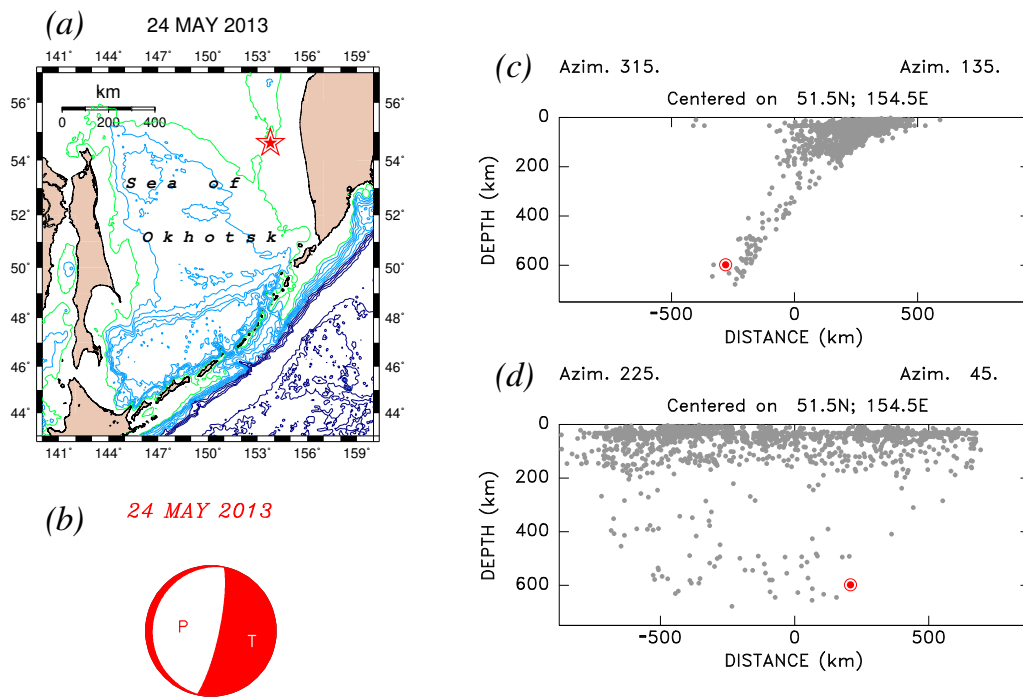


Figure 3.2. The Sea of Okhotsk deep earthquake of 24 May 2013. (a): Situation map showing the epicenter (red star). (b) Focal mechanism determined by standard GlobalCMT Inversion (Table 3.1, Solution 1c). (c): Background seismicity (gray dots) plotted in cross-section along a 135° azimuth; (d): Same as (c) along a 45° azimuth; note that the 2013 hypocenter (bull's eye symbol) is located at the edge of the Wadati-Benioff Zone.

3.2. Methodology

A significant problem in the detection of an isotropic component M_I to the moment tensor \mathbf{M} is that it can trade off with other, deviatoric, ones during the inversion of observable seismic waveforms. While Kawakatsu (1996) showed that M_I can in principle be resolved from the spectra of classical spheroidal modes at frequencies less than 2 mHz, Okal (1996) elected to focus on the spectral amplitudes of the two radial modes ${}_0S_0$ and ${}_1S_0$. The advantage of this approach stems from the fact that in radial modes the non-diagonal elements of the eigenstrain are identically zero, and additionally $\varepsilon_{\theta\theta} = \varepsilon_{\phi\phi} = \frac{u_r}{r}$, leaving only two independent non-zero components of the strain tensor. Since the excitation of any mode by a moment tensor \mathbf{M} is proportional to its scalar product with the eigenstrain at the source (Gilbert, 1971), it follows that radial modes are excited by only two independent components of a general 6-dimensional symmetric moment tensor, which can be taken as $M_I = \frac{1}{3} M_{ii}$, and $[M_{rr} - (M_{\theta\theta} + M_{\phi\phi})/2]$, in principle resolvable from the inversion of just two radial mode amplitudes.

The combination $[M_{rr} - (M_{\theta\theta} + M_{\phi\phi})/2]$ is equivalent to $-3/2$ times the vertical CLVD component of Kawakatsu's (1996) decomposition of the most general moment tensor \mathbf{M} . If we then assume the deviatoric part of the source to be a pure double-couple, this combination takes the form $M_D \cdot s_R$, where M_D is the moment of the double-couple, and $s_R = \sin \lambda \sin \delta \cos \delta$ in the notation of Kanamori and Cipar (1974), is a trigonometric coefficient expressing the component of thrusting ($s_R > 0$)

or normal faulting ($s_R < 0$) in the deviatoric source. The excitation of the radial mode is then proportional to $[N_0 \cdot M_I + K_0 \cdot M_D s_R]$, where N_0 and K_0 are two excitation coefficients depending only on source depth. As discussed by Okal (1996), and for the deepest earthquake sources, the modes ${}_0S_0$ and ${}_1S_0$ are particularly suited to this inversion, since the two excitation coefficients are comparable for ${}_1S_0$ (${}_1K_0 = -0.094$; ${}_1N_0 = -0.115$) and of comparable amplitude but opposite signs for ${}_0S_0$ (${}_0K_0 = 0.280$; ${}_0N_0 = -0.313$; all values in units of $10^{-31} \text{ dyn}^{-1}$, using the PREM model (Dziewonski & Anderson, 1981) and the 2013 GlobalCMT centroid depth of 611 km). This makes the inversion matrix very well-behaved, with complex conjugate eigenvalues and hence a condition number of 1. This property (which was essentially unchanged at the 1994 Bolivian shock's depth of 640 km) allowed Okal (1996) to solve for M_I independently of the deviatoric component $M_D \cdot s_R$, and to conclude that no resolvable M_I could be identified in the source of the 1994 Bolivian earthquake.

3.3. Results: Evidence for an implosive component

3.3.1. Preliminary investigation: the spheroidal modes

Following earlier investigations of the 2004 Sumatra, 2005 Nias, 2010 Maule and 2011 Tohoku events (Okal & Stein, 2009; Okal et al., 2012; Okal, 2013), we first conducted a systematic study of the excitation of spheroidal modes by the 2013 deep Sea of Okhotsk earthquake, in the range 0.63 – 2.70 mHz, with the aim

of documenting any possible source slowness. The great depth of the 2013 event allows the systematic use of many spheroidal overtones.

We recall that, given a focal mechanism geometry, this procedure consists, at each station, of computing the excitation of each split singlet ${}_nS_l^m$ within a multiplet ${}_nS_l$ (Stein & Geller, 1977), producing a synthetic record and scaling its spectrum to the observed one to derive a value of the seismic moment at the relevant frequency; all details can be found in Okal et al. (2012). Fig. 3.3 shows that no trend is present in the spectrum of the 2013 Sea of Okhotsk earthquake, with the gravest mode resolvable, ${}_0S_4$ ($T = 1565$ s), yielding a moment not significantly different from that of the GlobalCMT solution obtained at 200 s. This result, in contrast to the case of the 2004 Sumatra earthquake (Stein & Okal, 2005; Okal & Stein, 2009), means that in the range of frequencies considered, the stress release can be regarded as a step function in time. Its importance is that it precludes interpreting any anomalous spectral amplitudes of the radial modes ${}_0S_0$ and ${}_1S_0$ as simply due to source slowness, and any such behavior must then be explained by an ancillary component to the moment tensor.

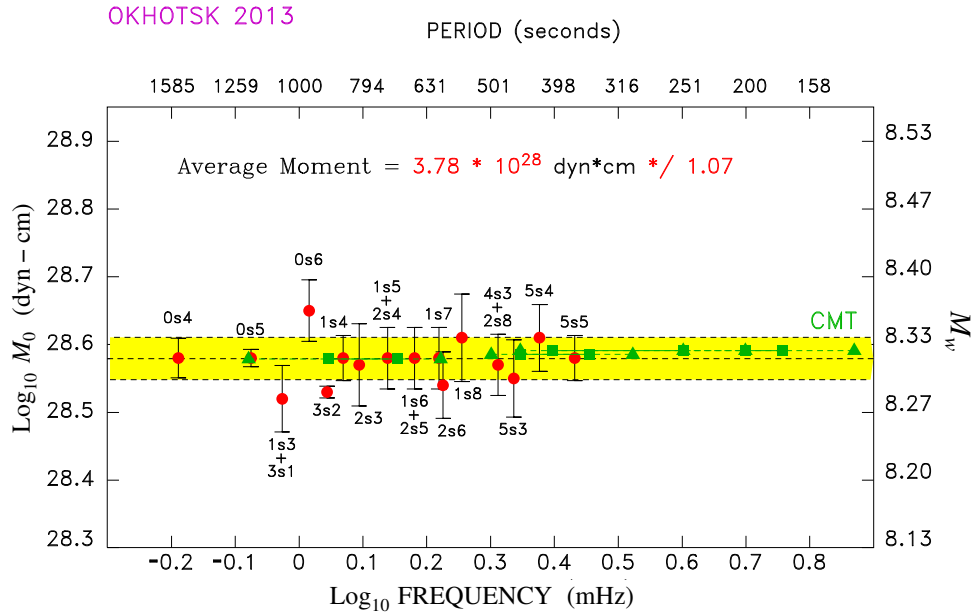


Figure 3.3. Seismic moment of the 2013 Sea of Okhotsk deep earthquake computed from the spectra of the Earth’s spheroidal modes. For each mode, the moment is obtained by fitting the observed spectrum of the multiplet to its theoretical shape in the geometry of the GlobalCMT solution. The geometrical average for all usable stations is shown as the red dot, with corresponding standard deviation. The dashed line (and colored band) represent the average value (and standard deviation) of these moments at the various frequencies. Note the absence of any trend with frequency, contrary to the case of the 2004 Sumatra earthquake (Okal & Stein, 2009; Figure 7). Shown in green are results of unconstrained CMT inversions in various frequency bands, as listed in Table 3.1 and discussed in Section 3.4; triangles and squares define the cut-off and taper limits, respectively, of the filters used for each band. Note full consistency of results.

3.3.2. The radial modes

For the present study, we recover the spectra of the radial modes ${}_0S_0$ and ${}_1S_0$ from time series of VHZ channels at stations of the GEOSCOPE and Global Seismological networks. As discussed by Dahlen (1982), the proper resolution of a spectral line of

period T and quality factor Q requires a time series lasting on the order of $(T \cdot Q/2)$, or 40 days for ${}_0S_0$ and 7 days for ${}_1S_0$, using $Q = 5579$ and 2017 , respectively (Okal & Stein, 2009). We note that a somewhat deep earthquake ($h = 386$ km) with a moment of 1.1×10^{27} dyn*cm occurred in the Solomon Islands on 07 July 2013, 44.5 days after the Okhotsk event, with a normal faulting mechanism favorable for the excitation of radial modes. For this reason, we use only 40-day time windows. We retain only records unperturbed by gaps or spikes in the relevant windows, leaving us with a dataset of seven stations: ADK, CAN, IVI, KMB, MAKZ, NNA, and PAYG.

Since the particle displacements of the radial modes are the same at all points on the surface of the Earth, it is possible to stack their complex spectra at the various stations to improve signal-to-noise ratios. Fig. 3.4 presents the final stacked spectra (using simple, unweighted stacking) for the fundamental mode ${}_0S_0$ and first overtone ${}_1S_0$. The moment values reported on the figures represent the best fits obtained under the assumption of a purely deviatoric source in the geometry of the GlobalCMT best double-couple ($\delta = 11^\circ$, $\lambda = -93^\circ$). It is immediately evident that, with respect to the GlobalCMT solution ($M_0 = 3.95 \times 10^{28}$ dyn*cm), the moment obtained for ${}_0S_0$ is significantly deficient (by 15% at only 3.42×10^{28} dyn*cm), while that for ${}_1S_0$ is similarly excessive (by 21% at 4.77×10^{28} dyn*cm). We will refer to these values of the moment as ${}_0m$ and ${}_1m$, respectively.

On the other hand, if we assume that the source is composed of a double-couple with the GlobalCMT geometry (and moment M_D), plus an isotropic component of

moment M_I , then M_I and M_D can be resolved from the system of equations

$$\begin{bmatrix} {}_0N_0 & {}_0K_0 \\ {}_1N_0 & {}_1K_0 \end{bmatrix} \begin{bmatrix} M_I \\ M_D s_R \end{bmatrix} = \begin{bmatrix} {}_0m \cdot {}_0K_0 s_R \\ {}_1m \cdot {}_1K_0 s_R \end{bmatrix} \quad (1)$$

whose solution is $M_I = -1.08 \times 10^{27}$ dyn*cm and $M_D = 4.06 \times 10^{28}$ dyn*cm. Thus, the excitation of the radial modes is explained by the superposition of a deviatoric moment essentially identical to the GlobalCMT solution, and a negative isotropic (*i.e., implosive*) component M_I amounting to 3% of the deviatoric one (but as much as 14% of the deviatoric component relevant to the excitation of normal modes, $M_D s_R = -7.60 \times 10^{27}$ dyn*cm).

Following Okal (1996), we estimate error bars on M_I and M_D through a jackknifing procedure consisting of running $N = 7$ inversions from stacks of $N - 1$ stations (eliminating one common station at a time), and fitting an ellipse to the resulting dataset in the $[M_I, M_D]$ space. Results are shown on Fig. 3.5, together with those for the 1994 Bolivian earthquake, replotted on a common scale from Figure 2 of Okal (1996). They suggest an uncertainty of 11% on M_I and 2% on M_D , which emphasizes the robust character of the isotropic component. By contrast, and as recalled on Fig. 3.5, in the case of the 1994 Bolivian earthquake, the isotropic component was not robust, with the ellipse intersecting the neutral line $M_I = 0$, meaning that the dataset was inconclusive as to even the sign of any putative isotropic component (implosion or explosion).

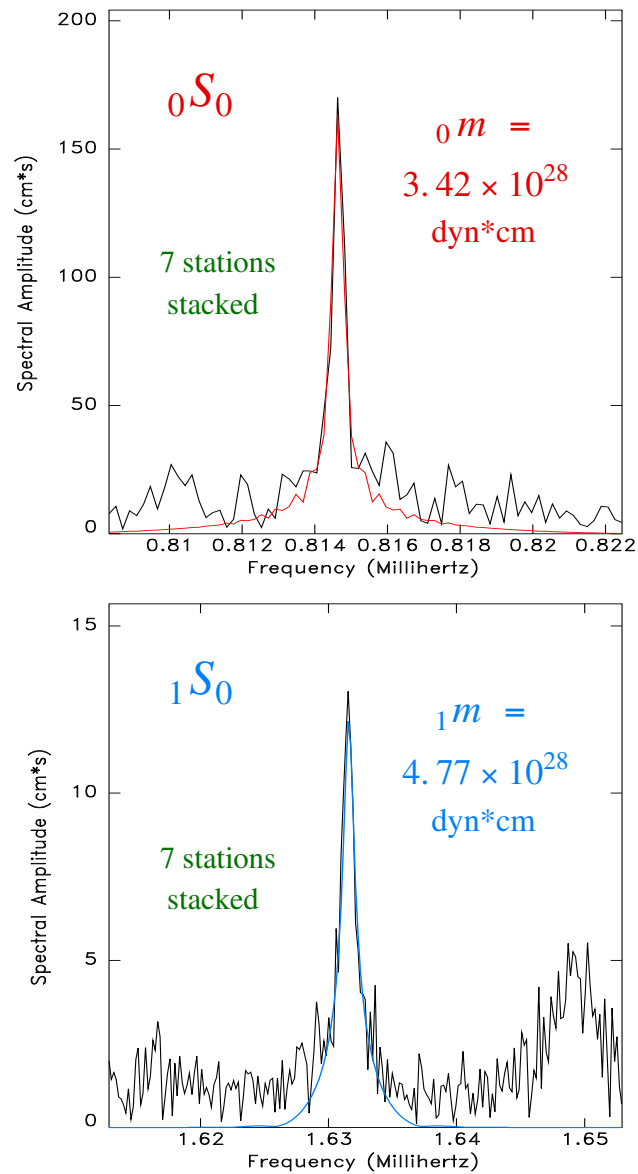


Figure 3.4. Best fits to the stacked spectra of ${}_0S_0$ (Top) and ${}_1S_0$ (Bottom), under the assumption of a purely deviatoric source in the geometry of the GlobalCMT solution. In both frames, the black trace is the observed stacked spectrum, and the colored one its theoretical fit for the computed moment.

We thus conclude that the 2013 Okhotsk Sea earthquake does possess an implosive isotropic component, on the order of 3% of the deviatoric moment M_D .

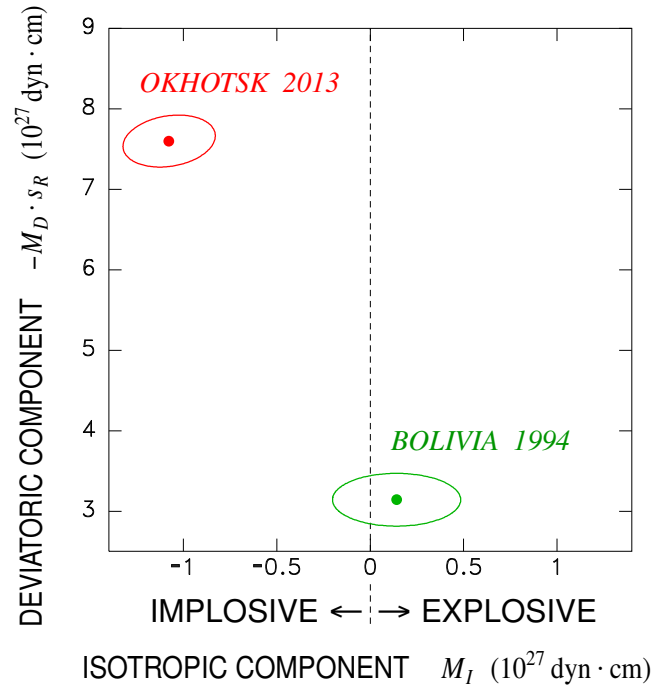


Figure 3.5. Isotropic and deviatoric components of the source of the 2013 Okhotsk (red) and 1994 Bolivia (green) events, inverted from the spectra of the radial modes ${}_0S_0$ and ${}_1S_0$. The error ellipses are obtained from the jackknifing procedure. The 1994 ellipse was simply replotted from Figure 2 of Okal (1996), using a common scale. Note the robust character of the 2013 solution, contrary to the 1994 case, where even the polarity of the isotropic component could not be asserted.

Finally, we note that the inclusion of a relatively small isotropic component to the moment tensor cannot affect significantly the inversion for the best-fitting double-couple, since the isotropic term excites only the $m = 0$ singlet of each mode. In the

particular geometry of the deep Sea of Okhotsk earthquake (a décollement on a plane dipping only 11°), the $m = 0$ singlet is only marginally excited by the deviatoric tensor, and thus the geometry and scalar moment of the best-fitting double-couple is essentially unaltered by the addition of M_I . In other words, the small isotropic component excites only marginally the main seismological observables (*i.e.*, the mantle Rayleigh waves or the non-radial modes) which are essentially unaffected by its presence, a result already described by Okal & Geller (1979).

3.3.3. The case of the 2015 Bonin earthquake

A surprising, large deep earthquake took place at the bottom of the Bonin Islands Wadati-Benioff Zone on 30 May 2015 (27.94°N ; 140.56°E ; Fig. 3.6). With a seismic moment of 7.7×10^{27} dyn*cm, this earthquake is the fifth largest deep event in the GlobalCMT catalog (after the 2013 Okhotsk, 1994 Bolivian, first 2018 Fiji, and 1970 Colombian shocks). As shown in Fig. 3.6 several properties make it particularly intriguing (Okal & Kirby, 2016; Ye et al., 2016). First, estimates of its source depth place it at 664 km (hypocentral, NEIC), 682 km (hypocentral, JMA), 667 km (hypocentral, Zhao et al. (2017)), and 681 km (centroid, GCMT), in rough numbers 100 km deeper than all seismicity previously known in that segment of the subduction system. Next, it did not take place in the linear prolongation of the seismic zone, but rather 200 km East of it, *i.e.*, oceanwards of the downgoing slab. Finally, its focal mechanism features tensional stress in the direction of sinking of the slab, rather than the usual down-dip compression characteristic of stress release

at the bottom of slabs (Isacks & Molnar, 1971). All these properties fuel speculation (Okal & Kirby, 2016) as to whether the event took place in a mechanically detached section of slab recumbent on the bottom of the transition zone (Okal & Kirby, 1998; Okal, 2001) or in a highly contorted one. Detailed tomography of the Bonin slab system by Zhao et al. (2017; Figs. 4 and 6) would suggest a tear in the slab around 29°N, with the Southern segment curling back oceanwards, perhaps in conjunction with the further Eastward regression of the subduction in the Marianas to the South, in the general geometry suggested by Čížková & Bina's (2015) geodynamic models. In Zhao et al.'s (2017) model, and at the latitude of the 2015 event, the slab squeezes through a narrow neck at the level of the 410-km discontinuity, followed by an effusive outpouring down to ~ 850 km, which would contain the 2015 hypocenter (their Fig. 4); the wide expansion of the slab below the 410-km neck, as opposed to its abutting against the 660-km discontinuity, may also help explain the unusual down-dip tensional mechanism. On the other hand, the isolated character of the 2015 earthquake would argue in favor of its occurrence in a mechanically detached portion of slab, recumbent on the 660-km discontinuity (Okal & Kirby, 2016), and where the orientation of stresses released seismically could be essentially random, as observed in the deep seismic cluster under the Fiji Basin (Okal & Kirby, 2016).

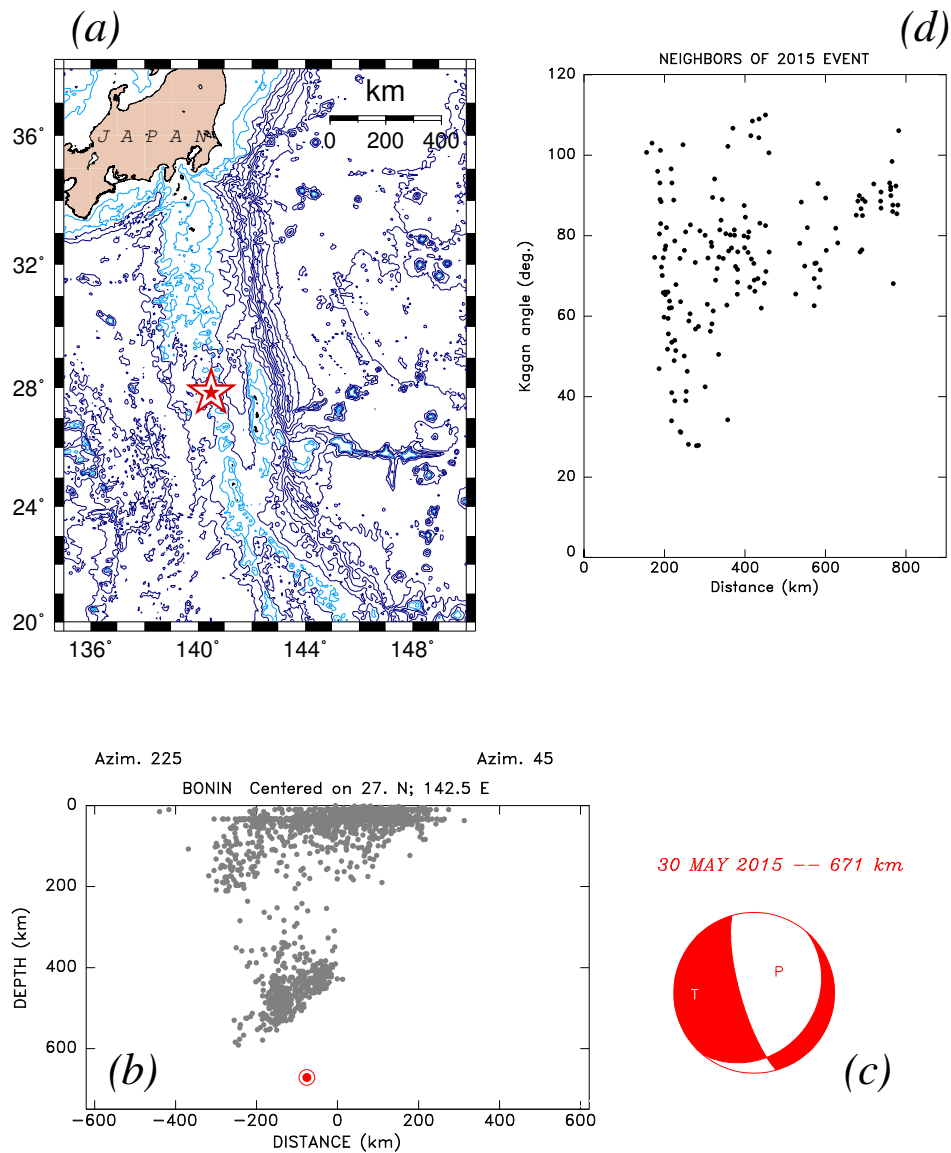


Figure 3.6. The Bonin Islands deep earthquake of 30 May 2015. (a): Situation map showing the epicenter (red star). (b): Background seismicity (gray dots) plotted in cross-section at a 45° azimuth; the 2015 source (bull's eye symbol) clearly appears much deeper than other events, and misaligned with the Wadati-Benioff zone. (c): Focal mechanism of the 2015 event, incompatible with the prevailing down-dip compressional geometry. (d): Closest neighbors of the 2015 event plotted as a function of their 3-d distance to its hypocenter (abscissa) and of the solid angle rotation angle between their mechanisms (Kagan, 1991).

Given its large moment, and regardless of the exact environment of the 2015 Bonin earthquake, it would then be natural to investigate its radial modes, to explore the possible presence of an isotropic component in its source. Unfortunately, the 2015 earthquake was just too small to sufficiently excite the radial modes, and we simply failed to extract either ${}_0S_0$ or ${}_1S_0$ above noise level.

3.3.4. The Case of the 2018 Fiji events

More recently, two large deep earthquakes took place near the bottom of the Fiji-Tonga subduction zone. The first event occurred at 00:19 on 19 August 2018 at 17.86°S, 177.85°W and 555 km depth, with a moment of 2.5×10^{28} dyn*cm, and the second one at 15:49 on 06 September 2018, at 18.24°S, 179.86°E and 687 km depth, with a moment of 9×10^{27} dyn*cm. Their moments make them the third and sixth largest deep events ever recorded, with the 19 August shock practically equal in size to the 1994 Bolivian earthquake.

This would make the first event a primary target for the investigation of its radial modes. Unfortunately, the second one acts to reset the modes, and in particular to pollute the spectrum of ${}_0S_0$: note that the 18.6 days interval between the two events is shorter than the minimum length of the window required to analyze its spectral amplitude, $(T \cdot Q/2) \approx 40$ days (Dahlen, 1982). By the time of the second event, the amplitude of the mode has decayed only by a factor of 2, but it has undergone more than 1300 periods. While it could be conceivable to subtract from the spectrum the contribution of the second event, a precision of even 45° (1/8 of a cycle) on the phase

of the oscillation at its origin time would require the knowledge of the period of ${}_0S_0$ with an accuracy of 0.1 s, which is probably illusory, thus making the interpretation of the amplitude of ${}_0S_0$ impossible.

3.4. Verifying the robustness of M_I

Given the historical controversy attached to the question of the isotropic component of deep earthquakes, it is important to examine the robustness of our results in view of some of the simplifying assumptions underlying our methodology, which for example ignores lateral heterogeneity in the Earth's structure.

3.4.1. Possible artifacts for radial mode measurements

We first address the robustness of our results by using a different laterally homogeneous Earth model, namely 1066A (Gilbert & Dziewonski, 1975). We find negligible changes in the result of the inversion (1) (less than 0.1% in M_D and 1.5% in M_I).

Next, we recall that Okal & Geller (1979) studied the effect of ignoring lateral heterogeneity in Earth structure on moment tensor inversion, showing that the introduction of a simple degree-two perturbation in the phase velocity of synthetic surface waves, followed by inversion using a laterally homogeneous model, was enough to add an artificial isotropic component to an otherwise deviatoric source. They suggested that the large isotropic component to the source of the 1970 Colombian event proposed by Gilbert & Dziewonski (1975) resulted from such an artifact. In simple

terms, by using a slightly inappropriate phase velocity, this effect amounts to introducing an improper time shift between the various records used in the inversion. In the present case, and since the radial modes involve no propagation (their “phase velocity” being infinite), this effect is not expected.

As discussed by Russakoff et al. (1997), a more complex situation may arise from mode-to-mode coupling, due to the combined effects of the Earth’s rotation, ellipticity and lateral heterogeneity. In particular, those authors showed that the former was most probably responsible for the isotropic component proposed by Gilbert & Dziewonski (1975) for the 1970 event, which disappeared below detection level once this “Coriolis coupling” effect was properly taken into account. Briefly stated, coupling can deform the eigenfunction of a mode (*e.g.*, a toroidal mode may acquire a small radial component to its displacement), which in turn affects its excitation coefficients by various moment tensor components, and hence perturbs the result of the inversion. As detailed theoretically by Woodhouse (1980), Coriolis and ellipticity coupling will be significant between (i) spheroidal modes of identical angular degree l ; and (ii) modes of different type (one spheroidal, one toroidal) whose degrees l differ by 1. In addition (iii), ellipticity may couple modes of the same kind (S or T) with degrees differing by 2. In all cases, efficient coupling between two modes requires that the difference in their unperturbed multiplet frequencies be comparable to the range of splitting induced by the perturbation; we stress that this identity of frequency between two modes required for efficient coupling must occur in the complex domain, *i.e.* taking into account the imaginary part of the

eigenfrequency due to anelastic attenuation. The exceptionally high values of Q for the radial modes (5579 and 2017 respectively for ${}_0S_0$ and ${}_1S_0$) further minimize the possibility of coupling to non-radial modes. Incidentally, type (i) coupling requires that two branches of physically different S modes cross each other (Okal, 1978).

Millot-Langet (2004) has introduced a Frobenius normalization of the coupling between two modes indexed k and k' through the quantifier

$$F_{kk'} = -\log_{10} \left| \frac{\langle \mathbf{v}_k | \delta \mathbf{H} | \mathbf{u}_{k'} \rangle}{\omega_k^2 - \omega_{k'}^2} \right| \quad (2)$$

where $\langle \mathbf{v}_k |$ and $|\mathbf{u}_{k'} \rangle$ are “bra” and “ket” descriptions of orthonormalized eigenfunctions for modes k and k' , and $\delta \mathbf{H}$ the perturbation induced by rotation and ellipticity on the Hamiltonian operator. In general, coupling with F values on the order of 2 or greater is deemed negligible.

Here, we consider the radial modes ${}_pS_0$ ($p = 0$ and 1), whose frequencies closely follow ${}_p\omega_0 = (p + 1) {}_0\omega_0$; they will clearly be immune to (i). Type (ii) coupling would require a toroidal mode ${}_nT_1$ with a period approaching either 1227 or 613 s, which we can exclude given the periods of ${}_0T_1$ (solid rotation, infinite period), ${}_1T_1$ (807 s) and ${}_2T_1$ (456 s); at any rate, a detailed examination of the structure of the coupling kernels (*e.g.*, Millot-Langet (2004)) shows that they vanish at first order for all coupling of the form ${}_pS_0 - {}_nT_1$. As for (iii), the closest candidate for coupling with ${}_1S_0$ would be ${}_4S_2$ ($T = 580$ s). Using the parameters listed by Dahlen & Sailor (1979) we find that the width of its split multiplet is 0.006 mHz, 15 times smaller

than its difference in frequency with ${}_1S_0$; the resulting coefficient $F_{{}_1S_0\ 4S_2}$ is 1.92. For ${}_0S_0$, the closest contenders would be ${}_1S_2$ ($T = 1470$ s) and ${}_2S_2$ ($T = 1057$ s). For the former, its split width is similarly 0.011 mHz, or 12 times smaller than its distance to ${}_0S_0$ in the frequency domain, and $F_{{}_0S_0\ 1S_2} = 2.14$. The latter is an inner core mode (${}_1K_2$ in Okal's (1978) classification), hardly excited by any earthquake at any depth, and whose singlets are mixed with those of ${}_3S_1$ and ${}_1S_3$; the Frobenius coefficient $F_{{}_0S_0\ 2S_2}$ is 3.22. We conclude that the effect of coupling induced by rotation and ellipticity on the first two radial modes is negligible.

Another possible effect leading to the observation of an artificial isotropic component could be structural anisotropy at the source, as discussed *e.g.*, by Kawasaki & Tanimoto (1981) and later Vavryčuk (2005). However, in an investigation of events at ridge-transform intersections showing significant minor double-couples, Kawakatsu (1991b) has shown that the latter could not be explained by structural anisotropy at the source, even though such environments are known to feature strong and coherent anisotropy. In addition, Vavryčuk (2004) has suggested that the level of anisotropy necessary to account for observed CLVD components at the bottom of the Tonga slab would translate into an artificial isotropic component of about 1%. We conclude that it is unlikely that our observation of an implosive component of 3% of M_D is an artifact of anisotropy.

3.4.2. Unconstrained CMT inversions: an independent approach

In an independent approach, we proceed to verify our detection of an implosive component to the 2013 Okhotsk earthquake through 6-dimensional centroid-moment tensor inversions unconstrained to a zero-trace condition. The procedure consists of running the inversion algorithm applied to the routine computation of GlobalCMT solutions (Dziewonski et al., 1981; Ekström et al., 2012), but after relaxing the zero-trace constraint imposed in its standard version. This yields a six-dimensional symmetric moment tensor \mathbf{M} , rather than a five-dimensional one.

Table 3.1 compares the results of both inversions. The first solution, 1c (for constrained), reproduces the entry of the 2013 Okhotsk event in the standard GlobalCMT catalog. The second solution, 2u (for unconstrained), features a trace $M_{rr} + M_{\theta\theta} + M_{\phi\phi} = -9.04 \times 10^{27}$ dyn*cm, corresponding to $M_I = -3.01 \times 10^{27}$ dyn*cm. The best double-couple is then computed in the standard way, after obtaining the new deviatoric five-dimensional tensor by subtracting from the six-dimensional \mathbf{M} the isotropic component $M_I \cdot \mathbf{I}$ where \mathbf{I} is the identity matrix. The last two columns of Table 3.1 express the so-called “Compensated Linear Vector Dipole” characterizing the relative importance of the moment tensor components remaining after subtraction of the best-fitting double-couple, through the parameter

$$\varepsilon = \frac{\lambda_{\text{int}}}{\max[\lambda_{\text{max}}, -\lambda_{\text{min}}]} \quad (3)$$

Table 3.1. Results of Moment Tensor Inversion Experiments: 2013 Sea of Okhotsk

No.	Centroid				Inverted Moment Tensor								Best Double-Couple				M_I	ϵ	ϵ_D
	Lat.	Lon.	Depth	Offset	M_{rr}	$M_{\theta\theta}$	$M_{\phi\phi}$	$M_{r\theta}$	$M_{r\phi}$	$M_{\theta\phi}$	Residual	M_D	ϕ	δ	λ	(%) [†]			
<i>2013 OKHOTSOK: Standard Inversion</i>																			
1c	54.61	153.77	611	19.35	-1.67	0.382	1.28	-0.784	-3.57	0.155	0.0891	3.94	188.6	11.1	-93.5	0		-0.087	
2u	54.61	153.82	607	19.34	-1.89	0.026	0.960	-0.783	-3.54	0.158	0.0888	3.90	188.2	10.8	-94.0	-0.301 (-7.7)	-0.0007	-0.075	
<i>Improved Station Dataset</i>																			
3c	54.61	153.79	611	19.38	-1.69	0.372	1.31	-0.789	-3.57	0.128	0.0971	3.96	186.2	11.3	-95.8	0		-0.087	
4u	54.61	153.84	606	19.37	-1.94	-0.0271	0.946	-0.787	-3.54	0.134	0.0967	3.91	185.8	11.0	-96.2	-0.340 (-8.7)	+0.087	-0.117	
<i>Remove Cross-Branch Stations</i>																			
5c	54.59	153.78	610	19.40	-1.69	0.415	1.27	-0.807	-3.57	0.206	0.0791	3.95	192.9	11.2	-89.9	0		-0.089	
6u	54.59	153.83	606	19.40	-1.94	0.0153	0.902	-0.806	-3.54	0.210	0.0782	3.90	192.6	10.9	-90.2	-0.341 (-8.7)	+0.007	-0.267	
<i>Short-Period Window 135-250 s</i>																			
7c	54.68	153.73	611	20.61	-1.47	0.334	1.14	-1.00	-3.54	0.142	0.1205	3.91	188.0	9.9	-97.3	0		-0.078	
8u	54.68	153.76	611	20.61	-1.74	0.0228	0.837	-1.00	-3.54	0.146	0.1200	3.90	187.9	9.8	-97.4	-0.293 (-7.5)	-0.001	-0.102	
<i>Long-Period Window 300-500 s</i>																			
9c	54.64	153.80	611	18.57	-1.76	0.352	1.40	-0.503	-3.51	0.147	0.0968	3.89	187.7	12.1	-90.4	0		-0.082	
10u	54.64	153.90	604	18.57	-1.92	0.106	1.20	-0.507	-3.48	0.149	0.0966	3.85	187.3	12.0	-90.9	-0.205 (-5.3)	-0.021	-0.073	
<i>Ultra-Long-Period Window 600-1200 s</i>																			
11c	54.44	152.63	597	19.75	-1.55	0.450	1.10	-0.811	-3.39	0.131	0.2580	3.74	190.8	10.5	-92.4	0		-0.108	
12u	54.39	153.00	576	19.60	-2.02	0.224	0.914	-0.826	-3.39	0.145	0.2573	3.79	191.3	11.5	-92.2	-0.294 (-7.6)	-0.045	-0.121	
<i>Ultra-Long-Period with Longer Records</i>																			
13c	54.40	152.23	602	22.10	-1.61	0.502	1.11	-0.850	-3.31	0.148	0.2677	3.68	192.9	11.0	-91.3	0		-0.120	
14u	54.34	152.57	580	21.90	-2.06	0.285	0.926	-0.862	-3.31	0.162	0.2670	3.74	193.4	11.9	-91.1	-0.283 (-7.6)	-0.058	-0.132	

[†] Value of M_I/M_D expressed in percent.

All moment values in units of 10^{28} dyn*cm.

which is the ratio of the intermediate eigenvalue of the moment tensor (zero for a pure double-couple) to the one of largest absolute value. In Table 3.1, ϵ refers to the full six-dimensional tensor and ϵ_D to its deviatoric part; they are obviously equal in the constrained inversion.

The most important result in Solution 2u is that $M_I = -0.30 \times 10^{28}$ dyn*cm, is *negative*, corresponding to an implosion and supporting our radial mode results. However, its amplitude is about 2.8 times larger. Other important results concern the robustness of the centroid location (which moves less than 5 km in 3 dimensions),

and of the centroid time offset (which changes by an insignificant 0.01 s, less than the time sampling of the data used, and hence than the precision of the algorithm); however, the quality of the solution improves only marginally, by less than 1%. The geometry of the best double-couple is changed less than 1° in all angles, and its moment is reduced by only 1%.

The robustness of the inversion results is further examined by altering details of either the dataset or the parameters of the algorithm. In Solutions 3c (constrained) and 4u (unconstrained), we exclude stations whose response characteristics may be questionable, but on the other hand include data from other networks, such as GEOSCOPE, MEDNET or GEOFON; in Solutions 5c and 6u, we exclude components involving cross-branch coupling visible in the time domain. In the next experiments, we alter the period band over which the inversion is carried (originally 200-400 s in Solutions 1-6). First, we reproduce the shorter-period band (135-250 s) used in the CMT algorithm prior to 2004 (Solutions 7c (constrained) and 8u (unconstrained)). On the opposite, we consider a long-period band (300-500 s; Solutions 9c and 10u), and even an ultra-long-period one (600-1200 s; Solutions 11c and 12u). Finally, for Solutions 13c and 14u, we consider the ultra-long-period band, but with extended time windows.

Table 3.1 lists all details of the various solutions. We note that, with the exception of the long-period experiment (300-500 s), all inverted moment components remain remarkably stable, featuring a standard deviation of less than 0.12×10^{28} dyn*cm. Consequently, the isotropic component also remains robust, at $(-0.308 \pm$

Table 3.2. Results of Moment Tensor Inversion Experiments: 2015 Bonin Islands event

No.	Centroid				Inverted Moment Tensor							Best Double-Couple				M_I	ϵ	ϵ_D
	Lat.	Lon.	Depth	Offset	M_{rr}	$M_{\theta\theta}$	$M_{\phi\phi}$	$M_{r\theta}$	$M_{r\phi}$	$M_{\theta\phi}$	Residual	M_D	ϕ	δ	λ	(%) [†]		
<i>2015 BONIN ISLANDS: Standard Inversion</i>																		
15c	27.94	140.56	681	8.94	-0.386	-0.0657	0.452	-0.287	0.561	0.110	0.1918	0.765	35.6	24.8	-38.8	0	-0.077	
16u	27.93	140.55	680	8.95	-0.414	-0.101	0.417	-0.287	0.558	0.109	0.1917	0.761	35.7	24.8	-38.5	-0.033 (-5.1)	-0.033 -0.075	
<i>Short-Period Window 135-250 s</i>																		
17c	27.90	140.56	679	9.21	-0.383	-0.0740	0.457	-0.260	0.541	0.102	0.1691	0.742	35.0	25.2	-40.4	0	-0.050	
18u	27.90	140.55	679	9.22	-0.424	-0.113	0.419	-0.260	0.540	0.101	0.1688	0.741	34.9	25.2	-40.5	-0.039 (-5.4)	+0.002 -0.050	

[†] value of M_I/M_D expressed in percent.
All moment values in units of 10^{28} dyn*cm.

$0.023) \times 10^{28}$ dyn*cm. The best-fitting double-couples are also rotated at most 3° from each other in the formalism of Kagan (1991). However, in the long-period experiment (Solution 10u), most components, and in particular $M_{\phi\phi}$ and $M_{r\theta}$, feature large deviations of up to 30%, that in turn impact the isotropic component, which falls by about one third, to -0.21×10^{28} dyn*cm, or only -5.3% of M_D ; the best fitting double-couple rotates by a Kagan angle of 7° . The deviatoric moment M_D also varies slightly (by about 2%), but, as shown on Fig. 3.3, remains within the standard deviation of the values inverted from ultra-long-period spheroidal modes (see 3.1. above).

We similarly examined the 2015 Bonin Islands event (Table 3.2) and the first 2018 Fiji earthquake (Table 3.3). In the former case, our results are comparable to those of the 2013 Okhotsk source: unconstrained inversions result in a small implosive component, amounting to $\sim 5\%$ of M_D (in absolute value); furthermore, the inversion results are robust, *i.e.*, they do not depend on the frequency window

Table 3.3. Results of Moment Tensor Inversion Experiments: 19 August 2018 Fiji event

Solution	Centroid				Inverted Moment Tensor							Best Double-Couple				M_I	ε	ε_D
	Lat.	Lon.	Depth	Offset	M_{rr}	$M_{\theta\theta}$	$M_{\phi\phi}$	$M_{r\theta}$	$M_{r\phi}$	$M_{\theta\phi}$	Residual	M_D	ϕ	δ	λ	(%) †		
<i>Standard GlobalCMT Inversion</i>																		
19c	-17.88	-177.83	552	20.62	-1.49	-0.085	1.58	-0.399	-1.84	0.726	0.0804	2.52	13.62	69.33	-96.00	0		-0.12
20u	-17.89	-177.81	550	20.62	-1.56	0.195	1.47	-0.396	-1.83	0.723	0.0803	2.50	13.53	69.44	-96.06	-0.095	(-3.8)	-0.17 -0.13

† value of M_I/M_D expressed in percent.
All moment values in units of 10^{28} dyn*cm.

Table 3.4. Results of Moment Tensor Inversion Experiments: 1994 Bolivian event

No.	Centroid				Inverted Moment Tensor							Best Double-Couple				M_I	ε	ε_D
	Lat.	Lon.	Depth	Offset	M_{rr}	$M_{\theta\theta}$	$M_{\phi\phi}$	$M_{r\theta}$	$M_{r\phi}$	$M_{\theta\phi}$	Residual	M_D	ϕ	δ	λ	(%) †		
<i>1994 BOLIVIA: Short-Period Window 135-250 s</i>																		
21c	-13.89	-67.32	650	30.57	-0.784	0.820	-0.0360	-2.50	0.0539	-0.363	0.1354	2.65	311.0	11.5	-51.7	0		+0.02
22u	-13.89	-67.32	650	30.57	-0.773	0.833	-0.0223	-2.50	0.0540	-0.362	0.1354	2.65	310.9	11.5	-51.8	+0.0125	(+0.5)	+0.02 -0.023
<i>Standard Inversion 200-400 s</i>																		
23c	-13.91	-67.00	654	27.99	-0.935	0.859	0.0756	-3.34	0.215	-0.0763	0.0679	3.46	276.9	7.5	-86.9	0		-0.02
24u	-13.94	-67.01	651	27.97	-1.17	0.595	-0.221	-3.31	0.21	-0.0833	0.0675	3.43	227.6	7.5	-86.2	-0.265	(-7.7)	+0.06 -0.011
<i>Ultra-Long-Period Window 600-1200 s</i>																		
25c	-13.98	-68.24	655	31.54	-0.671	0.738	-0.0671	-3.08	0.0636	-0.308	0.3269	3.18	310.2	8.3	-51.7	0		+0.02
26u	-14.00	-68.24	654	31.53	-0.700	0.729	-0.0796	-3.08	0.0636	-0.308	0.3269	3.18	309.8	8.4	-52.1	-0.0169	(-0.5)	+0.03 -0.025

† value of M_I/M_D expressed in percent.
All moment values in units of 10^{28} dyn*cm.

used in the inversion, and the value of M_D is unaffected by the nature of the inversion (constrained or unconstrained).

Similar results are also obtained from a preliminary investigation of the first 2018 Fiji event, for which an implosive $M_I \approx 4\%$ of M_D is obtained using the standard CMT algorithm unconstrained for zero trace (Table 3.3).

However, the situation is different in the case of the 1994 Bolivian event. As shown in Table 3.4, inversions performed at short periods (135-250 s; Solution 22u) yield a negligible isotropic component, but at longer periods (200-400 s; Solution

24u), an implosive $M_I = -0.265 \times 10^{28}$ dyn*cm is obtained, equivalent to -7.7% of M_D , a ratio similar to that obtained for Okhotsk; in addition, while the best-fitting double-couple rotates only by a Kagan angle of 7° , its scalar value M_D increases significantly (by about 30%). At much longer periods (Inversion 26u), the value of M_D decreases back towards its short-period value, and the isotropic component disappears. Constrained inversions (21c, 23c, 25c) feature the same behavior of M_D . These results are summarized on Fig. 3.7 which analyzes them in the context of a quantification of ultra-low-frequency spheroidal modes of the Bolivian earthquake.

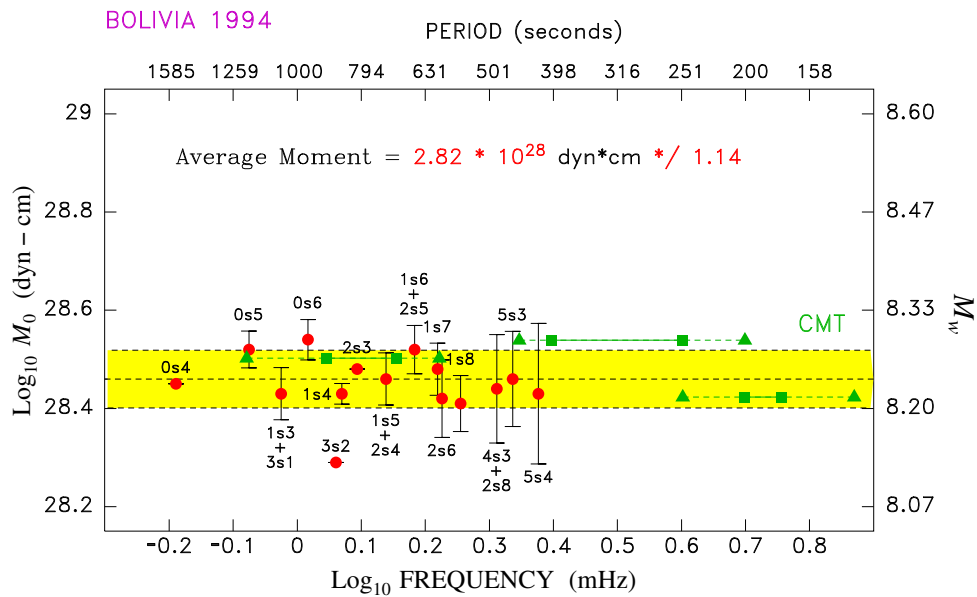


Figure 3.7. Same as Fig. 3.3 for the 1994 Bolivian earthquake. Note again the absence of any trend in the normal mode dataset, but this time the irregular behavior of M_D from unconstrained CMT inversions, depending on the frequency band used. See text for details.

Note that, as in the case of the Okhotsk event (Fig. 3.3), the mode results do not exhibit a trend with frequency suggestive of source slowness, and are compatible with the published CMT solution, which was obtained with a filter similar to the 135-250 s filter used here. However, the moment M_D for Solution 24u falls outside the standard deviation band, which does include the values obtained for Solutions 22u and 26u.

The inversion results for the Bolivian event are similar to those of Russakoff et al. (1997) for the 1970 Colombian deep shock: as shown *e.g.*, on their Figure 7, those authors were unable to document an isotropic component outside the 2.5-3.5 mHz range, where mode-to-mode coupling (under scenario (ii) above) does take place, but inversions ignoring that effect produced an artificial M_I . In this context, we elect to disregard from the present study all inversion results in the “Coriolis frequency band” and conclude that, as in the case of the 1970 Colombian earthquake, unconstrained CMT inversions of the 1994 Bolivian event do not yield a resolvable isotropic component, thereby confirming Okal’s (1996) results using radial modes. This is in contrast to the case of the 2013 Okhotsk earthquake, for which all results obtained outside the Coriolis frequency band show a robust implosive component.

We conclude that the unconstrained CMT inversions support the essential difference in the sources of the two events evidenced by our radial mode studies, namely the presence of an implosive component in Okhotsk, and its absence in Bolivia. However, we presently have no explanation for the different amplitudes of M_I from CMT inversions and radial modes, especially given the good agreement between the

corresponding values of M_D . Similarly, in the Coriolis frequency band, we lack a simple explanation for the relative weakness of the perturbations observed in the Okhotsk solution, as compared to the substantial ones for Bolivia.

Finally, we note that our results for the Okhotsk event are confirmed by recent work by Hara & Kawakatsu (2016), who detected an implosive component amounting to $\sim 3\%$ of the total moment tensor for the 2013 Sea of Okhotsk earthquake, but none above noise level for both the 1994 Bolivian and 2015 Bonin events. These authors, who used a CMT inversion technique, further documented the robustness of their results with respect to lateral heterogeneity in Earth structure.

3.5. A possible interpretation

In this section, we use the approach of Kirby et al. (1992) in an attempt to quantify the episode of phase transformation suggested by the implosive component of the deep 2013 Sea of Okhotsk earthquake, under the general concept of transformational faulting of metastable olivine. In this model, the phase transformation of metastable olivine is assumed to take place in the planar shear zone expressed by the deviatoric moment (Kirby, 1987). We use the simple model of a rectangular fault of length L and width W , the thickness of the zone undergoing the phase transformation being H (Fig. 3.8).

If we assume a relative volume change $\alpha = -7.3\%$ (Jeanloz & Thompson, 1983) during a complete phase transformation in the zone, the total volume change will

be $\delta V = \alpha (L \cdot W) \cdot H$, and the implosive moment release

$$M_I = K \cdot \delta V = K \cdot \alpha \cdot (L \cdot W) \cdot H \quad (4)$$

where K is the bulk modulus of the material, taken as 2.49×10^{12} dyn/cm² in the PREM model (Dziewonski et al., 1981). Given the deviatoric moment $M_D = \mu \cdot (L \cdot W) \cdot \Delta u$, where μ is the rigidity and Δu the seismic slip on the fault, we obtain two expressions for H :

$$H = \frac{1}{\alpha \cdot K} \cdot \frac{M_I}{L \cdot W} = \Delta u \cdot \frac{1}{\alpha} \cdot \frac{\mu}{K} \cdot \frac{M_I}{M_D} \quad (5)$$

The first expression allows a direct estimate of H from M_I and the dimensions of the fault zone. A number of source tomography studies of the Sea of Okhotsk event suggest average values $L = 135$ km; $W = 50$ km (Wei et al., 2013; Ye et al., 2013; Zhan et al., 2014). This yields $H \approx 90$ cm, using $M_I = -1.1 \times 10^{27}$ dyn*cm as inverted from the radial modes, but up to 4 m for the source obtained by CMT inversions; we can retain an order of magnitude of 2 m. The second expression allows the direct scaling of H to the slip on the fault Δu through the dimensionless quantities α , M_I/M_D , and $\frac{\mu}{K} = \frac{1}{(V_P/V_S)^2 - 4/3} = \frac{3}{2} \cdot \frac{1 - 2\nu}{1 + \nu}$, where ν is the material's Poisson ratio. Using the PREM value $\nu = 0.295$ (Dziewonski et al., 1981), we obtain $\mu/K = 0.475$, and a ratio $R_1 = H/\Delta u \approx 0.17$ from the radial

modes inversion, and 0.5 from the CMT solution. Note that R_1 does not depend on the exact values of L and W used to model the fault.

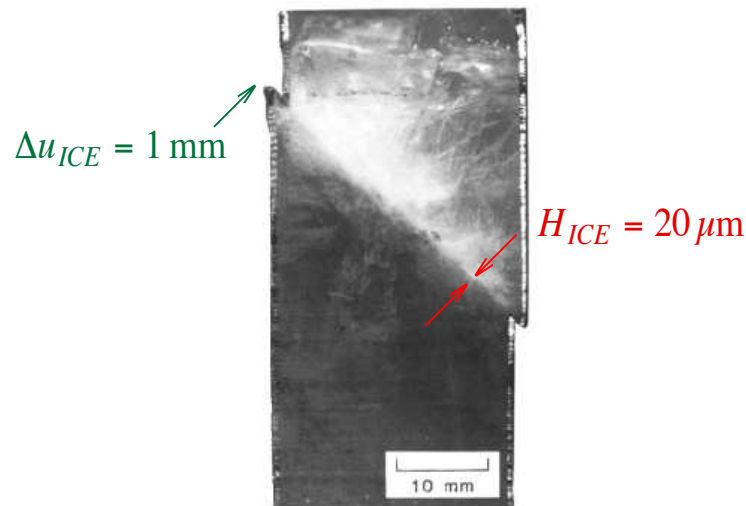
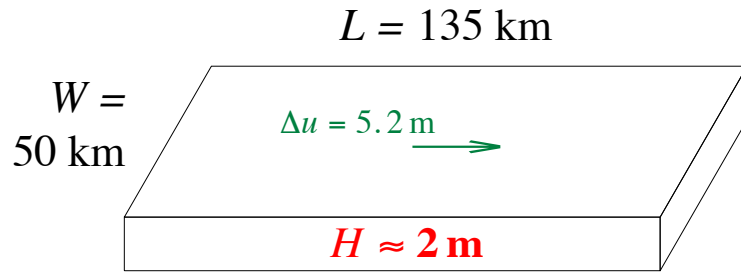


Figure 3.8. Comparison of proposed transformational faulting model for the source of the 2013 Okhotsk earthquake (top) with observed laboratory experiment (bottom), adapted from Kirby et al. (1992)

Shear zones of transformational faults produced experimentally in the laboratory offer some insights into their thicknesses in relation to their shear displacements and fault lengths, albeit with some caveats. They exhibit the metrics of such faults at the very beginning of transformational fault nucleation, and faults that offset sample boundaries may not feature metrics directly comparable to those that would have developed in source regions tens of kilometers in scale, and then sheared and run freely. Experimental results reported in the literature include Burnley et al.'s (1991), who observed faulting offsets of 15-120 μm upon transformation of 1- μm grains in Mg_2GeO_4 ($R_1 = 0.01$ to 0.07), Green et al.'s (1990) in natural silicate olivine (10-30 μm offsets for 1- μm grains; $R_1 = 0.03$ to 0.1), and Kirby et al.'s (1992) in ice ($H = 20 \mu\text{m}$; $\Delta u = 1 \text{ mm}$; $R_1 = 0.02$; Fig. 3.8).

In addition, a recent study of transformational faulting in Mg_2GeO_4 also showed micrographic evidence of submicron fault thickness (Wang et al., 2017). These authors employed an array of ultrasonic transducers to demonstrate that their shear zones radiate elastic waves and hence propagate dynamically. They provided estimates of fault thickness of $\sim 100 \text{ nm}$ for a slip of $\sim 1 \mu\text{m}$, suggesting $R_1 \approx 0.1$, a value comparable to other laboratory experiments at much larger scales, as described above. Furthermore, Wang et al. (2017) used the waveforms recorded from these transducers to invert for the moment tensor of individual transformational faulting events, down to typical values of $M_0 \approx 30 \text{ dyn}\cdot\text{cm}$ ($M_w \approx -9.8$). Although they publish histograms of the isotropic component of these moment tensors (with a

slight preponderance of positive, *i.e.*, explosive events), their transducers were uncalibrated and their solutions may be less reliable than for the largest, best-recorded events of their previous study (Schubnel et al., 2013), conducted on significantly larger samples, and for which little if any isotropic component was reported.

In summary, and in general terms, the values obtained in the present study, $R_1 = 0.17$ to 0.5 , are somewhat higher than the reported experimental values, with which however they share a comparable order of magnitude. In this context, we note that ductile shear zones in crustal rocks tend to show an increase in fault thickness with total cumulative fault displacement and therefore that shear-zone thickness increases with increasing total displacement. If transformational faults in cold subducting lithosphere show similar scaling, one could anticipate that reactivation of transformational faults in the mantle transition zone would widen with increasing cumulative shear displacement and produce larger R_1 values than those observed in the experimental studies cited above.

This lends considerable support to our interpretation of the implosive component of the moment tensor as expressing the nucleation of transformational faulting, even though the earthquake and the laboratory experiments took place on linear scales differing by 6 to 7 orders of magnitude, and in the case of ices, in materials of clearly different chemistry.

Another means of comparing our results from the 2013 Sea of Okhotsk earthquake to experimental ones would be to scale H to the fault length L , which amounts to defining the aspect ratio $R_2 = H/L$ of the zone undergoing the phase transition.

In this case, we find $R_2 \approx 1.5 \times 10^{-5}$, differing significantly from the laboratory experiments: Kirby et al. (1992) suggest $L = 2$ cm and hence $R_2 = 10^{-3}$, a figure also proposed by Wang et al. (2017); Green et al. (1990) suggest a failure extending over 3 mm, hence $R_2 = 3 \times 10^{-4}$; no information on length of faulting is available from Burnley et al. (1991). Note however that Wang et al. (2017) have observed that their fault thicknesses ($H \approx 100$ nm) may not scale directly with fault lengths L . This diversity in R_2 might express a variation in the strains released during transformational faulting, which are directly related to the ratios $\Delta u/L = R_2/R_1 \approx 10^{-4}$ in our case, but as much as 0.05 in Kirby et al.'s (1992) experiments on ices. Clearly, the latter figure would be excessive for an earthquake rupture: estimates of strain release during deep earthquakes, using energy-to-moment ratios have been found to be somewhat higher than for shallow sources, but only by less than one order of magnitude (Choy et al. 2006; Vallée 2013; and Chapter 5).

6. Discussion and Conclusion

We have established by two independent methods that the source of the deep Sea of Okhotsk earthquake of 24 May 2013 included an implosive component, with an amplitude of between 3 and 8% of the deviatoric moment of the earthquake. CMT inversion results tentatively suggest a similar component of 5% of M_D for the 2015 Bonin earthquake and 4% for the (first) 2018 Fiji event. These results

would be a natural consequence of transformational faulting as a mechanism of deep seismogenesis in the downgoing slab.

Ever since transformational faulting was suggested as a source of deep seismicity, its application to very large earthquakes, such as the 1994 Bolivian, and now the 2013 Okhotsk, events, has run into the argument that the inherently large size of their fault zones may not fit inside the relatively narrow domain of olivine metastability derived from thermal models (*e.g.*, Wiens et al., 1994; Silver et al., 1995; Myers et al., 1995; Tibi et al., 2003; Wei et al., 2013; Ye et al., 2013; Zhan et al., 2014; Zhang et al., 2016).

However, a number of observations can reconcile the spatial extent of large earthquakes with the general concept of deep seismicity nucleating from transformational faulting: First, Green et al. (1992) have documented an experimental case in which the resulting crack extended outside the particular crystal involved in the phase transformation, suggesting that not all the seismic fault zone has to be contained inside the metastable wedge; in this context, Meng et al.'s (2014) suggestion, for the 2013 Okhotsk earthquake, of a fault zone extending outside the olivine wedge would not necessarily preclude transformational faulting. In addition, Chen (1995) had proposed, for the deep Bolivian earthquake, a model of discontinuous, *en échelon*, rupture leading to a transverse dimension (30 km) for the fault significantly narrower than inferred from the distribution of its aftershocks. Finally, the structure of the slab in the vicinity of the 660-km discontinuity is expected to be strongly perturbed

from the simple thermal model used, *e.g.*, by Kirby et al. (1996), to advocate nucleation and growth by transformational faulting. In several subduction zones, the slab has been mapped, either by tomography or precise relocation of seismicity, to be horizontally deflected and thickened as it reaches the bottom of the transition zone, *e.g.*, in the Izu-Bonin system (Fukao et al., 1992) or in Tonga (Van der Hilst, 1995; Okal & Kirby, 1998). This thickening is due to down-dip compression of the slab as it encounters resistance to penetration caused by the strong viscosity contrast at the discontinuity and by the buoyancy cost of metastable olivine attempting to penetrate the lower mantle (Kirby et al., 1996; Bina, 1997; Okal & Kirby, 1998); it would argue for a larger metastable wedge of dimensions than in simplified models such as Kirby et al.'s (1996). More generally, slabs are complex, internally deformed regions, that can feature significant heterogeneity in their history, and hence in their mineralogical and thermal structures, a classical example being the plate age discontinuity “memorized” into the South American slab as a result of a reorganization of plate boundaries at around 82 Ma (Engebretson & Kirby, 1992; Kirby et al., 1995).

In the context of the 2013 Sea of Okhotsk earthquake, the geometry of the slab was poorly mapped prior to the event due to the scarcity of background seismicity, and in this respect the local details of the Slab1.0 model (Hayes et al., 2012), and hence the estimated location and size of the metastable wedge, may have some uncertainty, as suggested by the distribution of 2013 aftershocks (Zhan et al., 2014). Most source models (Tsuboi et al., 2013; Ye et al., 2013; Zhan et al., 2014) favor

rupture along a very shallow dipping fault plane ($\delta \sim 10^\circ$) which might be contained inside the olivine wedge if the slab is locally deflected to a sub-horizontal geometry (Wei et al., 2013). (Note however that some competing models would favor rupture along the sub-vertical fault plane, or stacking of *en échelon* horizontal rupture segments along a vertical extent reaching 40 km (Chen et al., 2014; Zhang et al., 2016).) One possible re-interpretation of these observations would be that the slab deviates from the Slab1.0 model by striking essentially North-South and being deflected sub-horizontally (Wei et al., 2013; Figs. 1A and 3a). This geometry would be consistent with the GlobalCMT focal mechanism ($\phi = 189^\circ$; $\delta = 11^\circ$; $\lambda = -93^\circ$). A rupture propagating from the hypocenter southwards, essentially parallel to the strike and across a sub-horizontal width of ~ 50 km may be contained inside the olivine wedge of a locally deflected slab, thus vitiating the argument against transformational faulting as a process nucleating large deep earthquakes and controlling their rupture.

It is also noteworthy that the 2013 deep Okhotsk earthquake took place at the Northeastern end of the Kuril-Kamchatka subduction system (Fig. 3.2). It thus follows the trend identified by Kirby et al. (1996) for the largest deep earthquakes to occur near the local spatial (including lateral) limits of Wadati-Benioff zones. These authors attributed this pattern to internal or “self” stresses generated, upon transformation, by the effects of heterogeneous volume changes and by significant gradients in the structural and elastic properties of the material composing the

slabs (Goto et al., 1987; Kirby et al., 1991); such gradients would be enhanced at the lateral limits of a seismogenic metastable wedge.

Table 3.5. Deep earthquakes with the ten largest known moments (Fig. 3.1)

Date	Region	Latitude (N°)	Longitude (E°)	Depth (km)	Moment (10^{28} dyn cm)	Implosive Component	Reference
24 MAY 2013	Sea of Okhotsk	54.61	153.77	611	3.95	YES	This study
09 Jun 1994	Bolivia	-13.82	-67.25	647	2.6	NO	This study; <i>Okal (1996)</i>
19 Aug 2018	Fiji	-17.86	-177.85	555	2.5	YES	This study
31 Jul 1970	Colombia	-1.86	-72.29	623	1.4	NO	<i>Russakoff et al. (1997)</i>
17 JAN 1922	Peru	-3.76	-71.89	635	0.94		<i>Okal & Bina (1994); Huang et al. (1998)</i>
06 SEP 2018	Fiji	-18.24	179.86	687	0.85		GlobalCMT
30 MAY 2015	Bonin Is.	27.94	140.56	681	0.77	YES	This study
17 JUN 1996	Flores Is.	-7.38	123.02	584	0.73		GlobalCMY
29 MAR 1954	Spain	36.98	-3.54	635	0.70		<i>Chung & Kanamori (1976)</i>
29 SEP 1973	Sea of JAPAN	42.16	131.12	593	0.50		<i>Huang et al. (1997)</i>

In addition, a number of thermal models have been proposed for the exothermic transformation of olivine into ringwoodite (e.g., Bina 1998; Kanamori et al. 1998; Bina et al. 2001; Schubnel et al. 2013) which suggest that runaway frictional heating may lead to local melting which could conceivably help the propagation of the rupture outside the metastable olivine domain where its nucleation took place (Green, 2007; Renshaw & Schulson, 2017), a mechanism apparently observed in situ on fayalite samples by (Officer & Secco, 2020).

In conclusion, our study opens a significant new chapter in the 45-year old controversy about the observation of implosive components in deep earthquakes. Table 3.5 summarizes our results in the context of the ten largest deep events for which

a modern estimate of seismic moment is available. We now have two independent proofs that the largest one, the 2013 Sea of Okhotsk earthquake, featured a detectable implosive component. Evidence from unconstrained CMT inversions supports a similar conclusion for the third (2018) and seventh (2015) largest events.

However, the second and fourth largest, the 1994 Bolivian and 1970 Colombian earthquakes, when subjected to modern, careful studies, failed to exhibit similar evidence (Hara et al., 1995; Okal, 1996; Russakoff et al., 1997), as did the many smaller shocks studied by Kawakatsu (1991a). This situation remains intriguing and deserves further discussion.

We note that under the model of transformational faulting, the phase transformation expressed as the implosive moment tensor component M_I serves as a nucleation and growth process for the faulting. Overwhelming evidence, going back to Isacks & Molnar (1971) and upheld by countless studies based on the more modern GlobalCMT solutions, indicates that such faulting releases slab stresses featuring spatial coherence and successfully interpreted in the framework of plate tectonics as down-dip compression resulting from the resistance to penetration of the deep mantle encountered by the slab as it approaches the 660-km discontinuity (with the exception of chunks of subducted material mechanically detached from their slab, and recumbent on the bottom of the transition zone, as evidenced by Okal & Kirby (1998) under the Fiji Basin).

In this framework, the phase transformation and the main episode of faulting draw their energies from different reservoirs, and there may not necessarily be a direct scaling between by their relative sizes, which would be expressed as an invariant ratio between M_I and M_D . This would be supported, *e.g.*, by the scatter in the ratio R_1 computed from Burnley et al.'s (1991) experiments.

Fig. 3.7 shows that the 1994 Bolivian event could not have included an implosive component of the same size, relative to $M_D \cdot s_R$, as for the 2013 Okhotsk earthquake, which would have amounted to $M_I = -3.0 \times 10^{26}$ dyn*cm if referred to our radial mode solution, and $M_I = -1.2 \times 10^{27}$ dyn*cm using the CMT one; such values would plot outside the relevant confidence ellipse. On the other hand, the Bolivian event could have included an isotropic component scaling on the lower end of the laboratory values, say $R_1 = 0.02$, since the corresponding value of M_I would have been only -8×10^{25} dyn*cm, which would fit inside the ellipse on Fig. 3.5, meaning that the data analyzed by Okal (1996) could not exclude it. Thus, the detection of an isotropic component in 2013 and its absence in 1994 could be a result of a scatter in values of R_1 , *i.e.*, in the ratio of the isotropic to deviatoric moments, which may itself express a difference in slab environment, perhaps traceable to plate kinematics, affecting the rupture process of large deep earthquakes, as suggested *e.g.*, by Wiens & McGuire (1995), Lundgren & Giardini (1995), and more recently Zhan et al. (2014).

In this general framework, the quantitative examination of the laboratory results, including those of Green et al. (1990) which come closest to reproducing the

conditions inside the slab (but for the absence of externally applied stresses), would suggest that the amplitude of the isotropic component could in most cases be so small relative to its deviatoric counterpart as to prevent its detection, including by methods such as the spectral ratio of radial modes used in the present study, which are supposed to optimize such detection. In the general context of Okal & Geller's (1979) conclusions, this would have made it impossible to detect any putative isotropic component to the source of the 1994 Bolivian earthquake, despite the advent of digital data allowing the resolution of radial mode spectra, a task clearly impossible using the analog data of the 1970s. It is probably along this framework that the apparently contradictory results on the 1970 Colombian, 1994 Bolivian and 2013 Sea of Okhotsk sources can be reconciled and the isotropic source controversy resolved.

CHAPTER 4

An extension to $\Delta > 80^\circ$ of the energy-to-moment parameter \ominus **4.1. Introduction**

This chapter, published as Okal & Saloor (2017), examines quantitatively three historical “tsunami earthquakes” in the Southwest Pacific. We recall that this class of events was defined by Kanamori (1972) as earthquakes whose tsunamis are significantly larger than expected from their seismic magnitudes, especially classical ones; charter examples included the famous 1896 Sanriku and 1946 Aleutian earthquakes. Such events obviously pose enormous challenges, since tsunami warning remains largely based on an assessment of the parent earthquake (Okal, 2008a).

While several models have been proposed to explain the occurrence of tsunami earthquakes in various environments (Fukao, 1979; Tanioka et al., 1997; Bilek & Lay, 2002), the systematics of their occurrence at any given subduction zone remain elusive. In this context, and because tsunami earthquakes are relatively rare, it is crucial to investigate as quantitatively as possible those events predating the development of digital networks. In the present study and for this purpose, we extend to distances $\Delta > 80^\circ$ the computation of the Energy-to-Moment parameter

Θ , introduced by Newman & Okal (1998) and used as a robust discriminant to characterize source slowness, notably during tsunami earthquakes.

Following the work of Boatwright & Choy (1986), Newman & Okal (1998) developed an estimate E^E of the seismic energy radiated by an earthquake into teleseismic body waves, not requiring the precise knowledge of focal mechanism and source depth (assuming the earthquake remains shallower than 80 km), and defined a slowness parameter:

$$\Theta = \log_{10} \frac{E^E}{M_0} \quad (4.1)$$

where M_0 is the seismic moment of the source. Under seismic scaling laws, Θ should remain constant, its theoretical value being -4.90, but earthquakes featuring an anomalous source spectrum can have excessive or deficient Θ values, by as much as 2 logarithmic units, the latter being the case of tsunami earthquakes. In their original study, Newman & Okal (1998) had shown that three tsunami earthquakes postdating Kanamori's (1972) study (Nicaragua, 1992; Java, 1994; and Chimbote, Peru, 1996) all featured deficient values of Θ , in the -5.8 to -6.3 range. The computation of Θ was later implemented as part of routine procedures at a number of tsunami warning centers (Weinstein & Okal, 2005).

In order to allow a proper, theoretically justifiable, implementation of a distance correction into the Θ algorithm, Newman & Okal (1998) originally restricted its use to the window $25^\circ < \Delta < 90^\circ$. Later studies (Okal & Newman, 2001; Weinstein &

Okal, 2005; Okal, 2013) used a narrower range of distances, $35^\circ < \Delta < 80^\circ$, made possible by the abundance of digital stations deployed in recent years. At shorter distances, this guards against the effects of the triplications resulting from mantle discontinuities, and at greater ones, against complexities due to reflections such as PcP , and more generally to the interaction of the generalized P wave with the D'' boundary layer, known to feature considerable lateral heterogeneity (e.g. Garnero & Helmberger 1996), even before the initiation of genuine diffraction by the core-mantle boundary around 102° . In a previous contribution, Ebeling & Okal (2012) used large digital datasets to define an empirical correction allowing the extension of Θ to distances as short as 5° ; in the context of tsunami warning in the regional field, these authors were motivated by the desire to obtain information on potential source slowness as soon as possible following the event, and hence from stations located as close as possible to the source.

Our motivation in the present chapter is different. A number of previous studies have shown that the Θ concept can be successfully applied to historical events, helping define or confirm the anomalous behavior of both slow tsunami earthquakes such as the Mexican aftershock of 22 June 1932 ($\Theta = -6.18$) and the Aleutian event of 01 April 1946 ($\Theta = -7.03$) (López & Okal 2006; Okal & Borrero 2011), and fast, “snappy” events, such as the Chillán shock of 25 January 1939 ($\Theta = -4.04$) and the great Showa Sanriku earthquake of 02 March 1933 ($\Theta = -4.24$) (Okal & Kirby, 2002; Okal et al., 2016). However, such investigations must rely on short-period records

of body-wave arrivals offering adequate and documented response in the relevant frequency range (typically 0.1 to 2 Hz). While torsion seismometers (Anderson & Wood, 1925) can occasionally provide adequate records for historical events, those instruments were typically low-gain, and were deployed only in a few active areas such as Southern California, restricting their use to relatively short distances (e.g., 19° at Pasadena, for the 1932 Mexican earthquakes (Okal & Borrero, 2011)). In the specific cases of the 1947 New Zealand and 1934 Santa Cruz earthquakes detailed below, it was not possible to find appropriate short-period records allowing quantification of body-wave energy at distances less than 80° , even though short-period instruments (Benioff, 1932) were by then deployed at greater distances, either as prototypes (1934; Pasadena), or in regular operation (1947; Pasadena, Tucson). The present study derives a methodology to quantify the information in those seismograms, reproduced on Fig. 4.1.

In addition, and as will be discussed in Section 4.4, the extension of the algorithm beyond 80° allows the occasional processing of large earthquakes from the era of the World-Wide Standardized Seismic Network (WWSSN), for which records at conventional distances may have gone off-scale.

4.2. The 1947 Hikurangi doublet

The Eastern coast of the North Island of New Zealand, fringed by the Hikurangi Trench, was the site of two exceptional earthquakes on 25 March and 17 May 1947 (hereafter Events I and II, respectively). Their local magnitudes did not exceed M_L

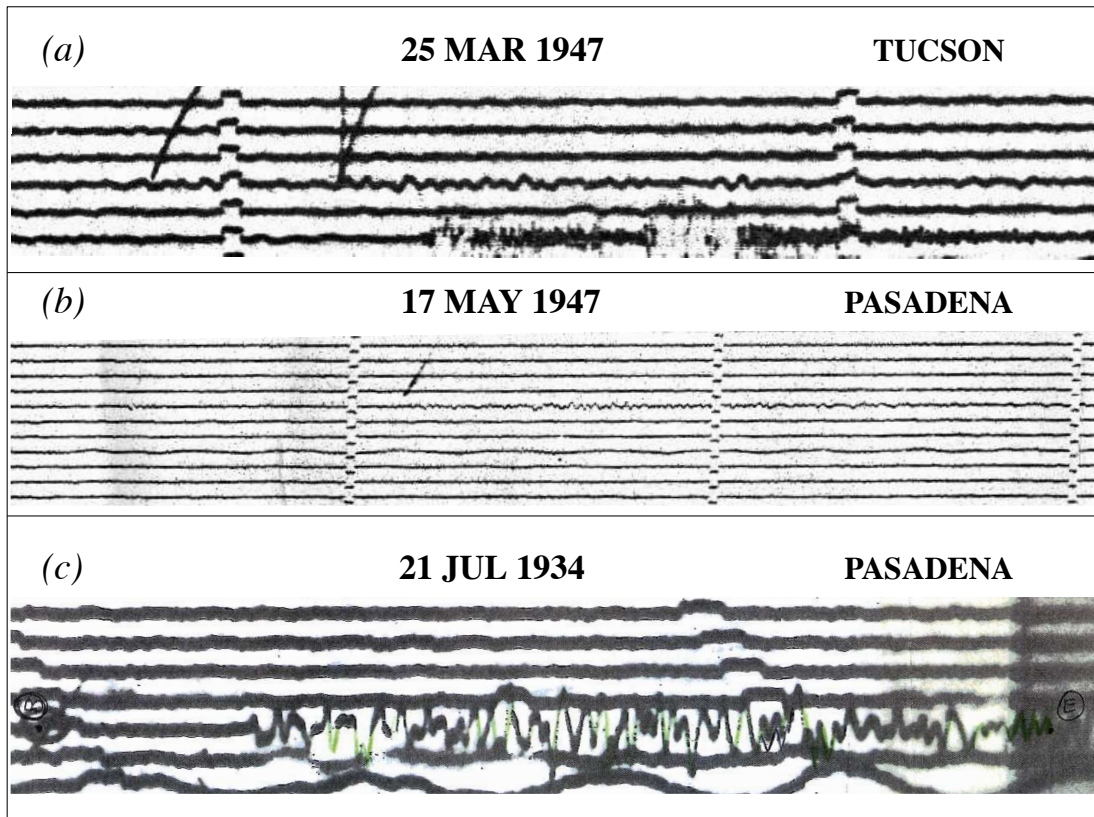


Figure 4.1. Short-period P -wave seismograms used in this study. Time marks are minutes, uncorrected for clock errors. The duration of the seismograms are 106 (a), 179 (b) and 90 (c) seconds. On (a), the high-frequency signal recorded half-an-hour later is a local shock, unrelated to the New Zealand earthquake.

= 5.9 and 5.6, respectively, while their conventional surface magnitudes were $M_s = 7.2$ for both events (Bell et al., 2014). They were followed by local tsunamis running up 10 m and 6 m, respectively (Engdahl & Villaseñor, 2002; Solov'ev & Go, 1984a). Eiby (1947) documented that Event I was hardly if at all felt (maximum MMI IV) in areas which were to be devastated 30 minutes later by the tsunami, while Event II was felt at a maximum MMI of V. These properties clearly classify the two 1947

events as tsunami earthquakes.

The 1947 Hikurangi earthquakes were particularly poorly located by global agencies, including during modern relocation efforts such as the Centennial and ISC-GEM projects (Storchak et al., 2013). As shown on Fig. 4.2, the original ISS source for Event I, as well as its two modern estimates, locate as much as 150 km inside the North Island, and were assigned clearly erroneous depths of about 160 km. The ISS location for Event II, originally on the outer rise oceanwards of the trench, was moved onland during the ISC-GEM relocation, this supposedly improved epicenter being incompatible with the primary source of a large tsunami. We were able to relocate Event I to 38.66°S , 178.59°E , from phase data listed in the ISS, but excluding times at the nearby station Tuai (TUA; see below), using Wysession et al.'s (1991) algorithm which includes a Monte Carlo estimate for confidence ellipses obtained by injecting into the dataset Gaussian noise (with a standard deviation $\sigma_G = 3$ s for events in the 1940s). A similar effort for Event II could not converge satisfactorily; that event is also absent from B. Gutenberg's personal notes (Goodstein et al., 1980) and from the Centennial catalog.

As detailed by Downes et al. (2001), this unparalleled scattering of relocations, and especially the failure of global modern techniques, reflect the emergent character of arrivals, poorly correlated between stations, itself due to the slowness of the earthquake source. However, careful relocations by these authors, including a reappraisal of arrival times on original seismograms at New Zealand stations, led

them to hypothesize that the closest station (TUA) may have recorded weak foreshocks; once the TUA times were removed, Downes et al. (2001) obtained solutions on the plate boundary in the immediate vicinity of the trench, at 38.85°S , 178.80°E for Event I, and 38.42°S , 178.87°E for Event II. These are shown as diamonds on Fig. 4.2, and will be used in this study. Note that our confidence ellipse for Event I grazes their solution; it is also remarkable that Gutenberg & Richter's (1954) epicenter, rounded to the nearest quarter-degree, fits inside our ellipse, a mere 28 km from Downes et al.'s (2000).

The mechanisms of the 1947 Hikurangi earthquakes were studied by Doser & Webb (2003) using Downes et al.'s (2000) relocations. They proposed moments of $(4\text{--}5.1) \times 10^{26}$ dyn cm for Event I and $(2.8\text{--}4.5) \times 10^{26}$ dyn cm for Event II, based on teleseismic body-wave inversions; they were however unable to fully constrain the focal mechanisms. Assuming a low-angle thrust fault at the interface between the Pacific and Australian plates [one of Doser & Webb's (2003) mechanisms], Bell et al. (2014) obtained a value of 4.7×10^{26} dyn cm for Event I from the modeling of regional and teleseismic body waves. Most significantly, their results require an exceptionally slow rupture velocity, on the order of 150–300 m/s, that is 10–20 times slower than standard rupture velocities and even 3–5 times slower than documented in recent tsunami earthquakes (e.g. Pelayo & Wiens 1992; Kikuchi & Kanamori

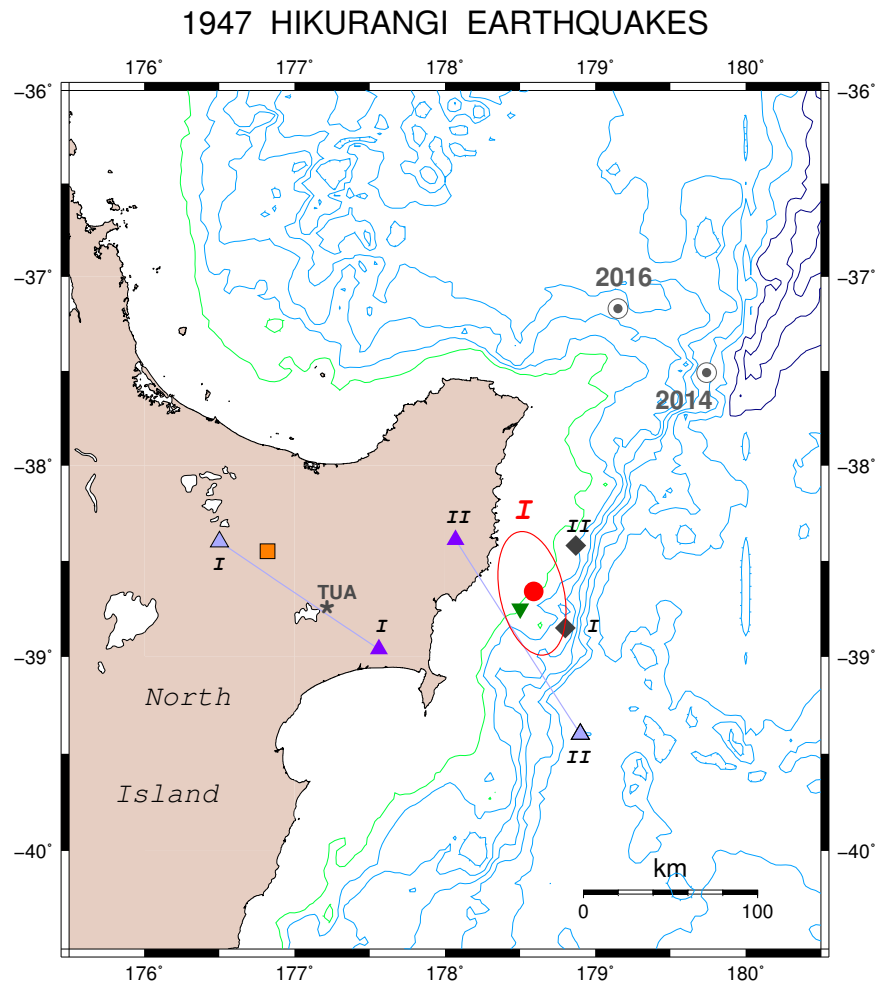


Figure 4.2. Relocations of the 1947 Hikurangi Events I and II. The red dot (with Monte Carlo ellipse) is our relocation of Event I (25 March), the green inverted triangle Gutenberg & Richter's (1954) epicenter, the light grey triangle the original ISS location linked to the purple triangle showing the ISC-GEM solution; the orange square is the Centennial location (Engdahl & Villaseñor, 2002), and the black diamond Downes et al.'s (2000). For Event II (17 May), the only locations available are the ISS (shaded triangle) and ISC-GEM (purple triangle), and Downes et al.'s (2000)(diamond). The asterisk shows the location of the incriminating station Tuai (TUA). The normal faulting validation events of 2014 and 2016 are shown as bull's eye symbols. Isobaths are at 500 m intervals (green at 500 m; dark blue at 4000 m and deeper).

1995; López & Okal 2006)¹; the corresponding source duration could be on the order of 300 s.

In this context, we computed the low-frequency source spectra of Events I and II from long-period surface waves. A number of previous studies have shown that it is possible to derive the seismic moment of comparably sized events (with moments between 10^{26} and 10^{28} dyn cm) from historical records written on instruments such as the long-period Golitsyn system or the broad-band Benioff 1–90 (e.g. Okal & Borrero 2011; Ebeling & Okal 2012; Okal 2012). In the present study, we obtained records of mantle waves from Events I and II at Pasadena, Tucson, De Bilt and San Juan, with representative examples of waveforms shown on Fig. 4.3 (the earthquakes were too small to be meaningfully recorded on Wiechert mechanical instruments). We processed them through the M_m algorithm (Okal & Talandier, 1989), with results shown on Fig. 4.4 in the form of the variation with frequency of the mantle magnitude corrected for focal mechanism and depth, related to seismic moment through:

$$M_c = \log_{10} M_0 - 20 \quad (4.2)$$

where M_0 is in dyn cm. We use dips of 8° for Event I, as suggested by Bell et al. (2014), and of 10° for Event II (Doser & Webb, 2003). In the frequency range 6–8

¹Incidentally, such extremely low rupture velocities would affect the directivity patterns of a far-field tsunami (Ben-Menahem & Rosenman, 1972), since they would become comparable to its phase velocity in deep water, and thus rotate the maximum lobe of radiation towards the azimuth of rupture; however, this remark becomes moot in the case of the 1947 earthquakes, which were not large enough to excite an appreciable far-field tsunami in the first place.

mHz, we obtain average values of ~ 2 and 1×10^{27} dyn cm, respectively for Events I and II, both significantly larger than previously proposed. We also note a significant trend of increase in M_0 with period, reaching values of 4 and 3×10^{27} dyn cm around 5 mHz, respectively for Events I and II. This trend is verified on Fig. 4.5, which uses a more traditional logarithmic scale for frequency (López & Okal, 2006); it suggests that any source corner frequency would have a very low value, on the order of 3 mHz, which could not be precisely quantified, as it lies beyond our domain of investigation.

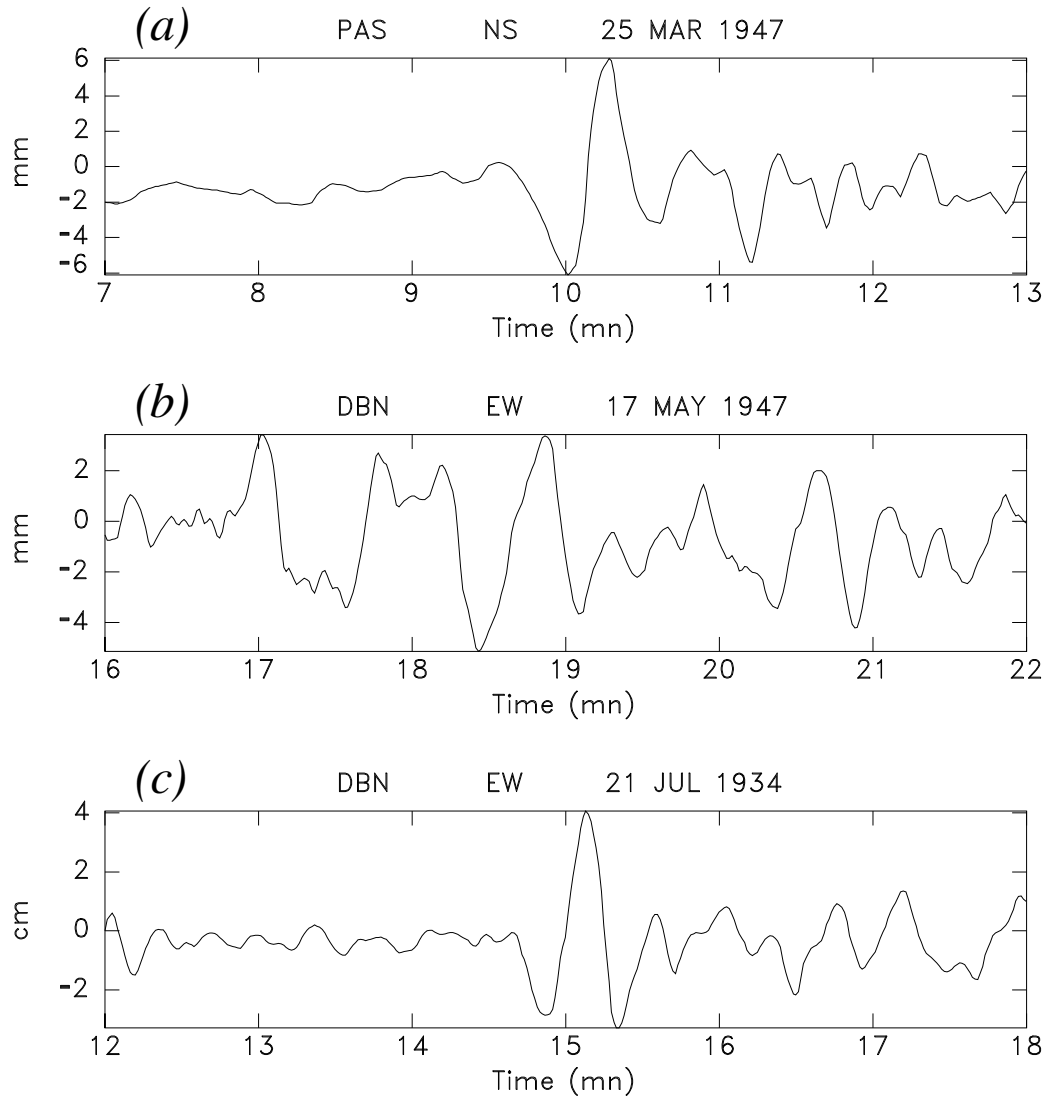


Figure 4.3. Representative examples of digitized mantle Love waves G_1 used for the evaluation of low-frequency moments: (a) Benioff 70-s strainmeter North-South record at Pasadena for Event I; (b) Golitsyn East-West record at De Bilt for Event II; (c) Golitsyn East-West record at De Bilt for the 1934 Santa Cruz tsunami earthquake.

These results support the conclusions of Bell et al. (2014) for Event I and their extension to Event II; we retain as low-frequency values $M_0 = 4$ and 3×10^{27} dyn cm, respectively for Events I and II, representative of our measurements around 5

mHz.

In this context, we use the slopes of M_c versus frequency f on Fig. 4.4. as empirical parameters characterizing the slowness of the sources; previous studies (Okal & Borrero, 2011; Okal, 2014) have documented that tsunami earthquakes generally feature slopes on the order of -0.07 logarithmic units per mHz or more (in absolute value) in the 5–12 mHz range (e.g., Java, 2006 (-0.11), and Mentawai, 2010 (-0.08)). By contrast, regular earthquakes feature slopes not exceeding -0.05 (e.g., Maule, 2010 (-0.05), Illapel, 2015 (-0.05), Kaikoura, 2016 (-0.03)), the contrast being particularly strong for the 1932 Manzanillo series with slopes of -0.05 (mainshock, 03 June), -0.01 (regular main aftershock, 18 June) and -0.14 (tsunami earthquake aftershock, 22 June) (Okal & Borrero, 2011). In the present case, we obtain values of -0.07 and -0.08 respectively for Events I and II, comparable to those obtained for several tsunami earthquakes.

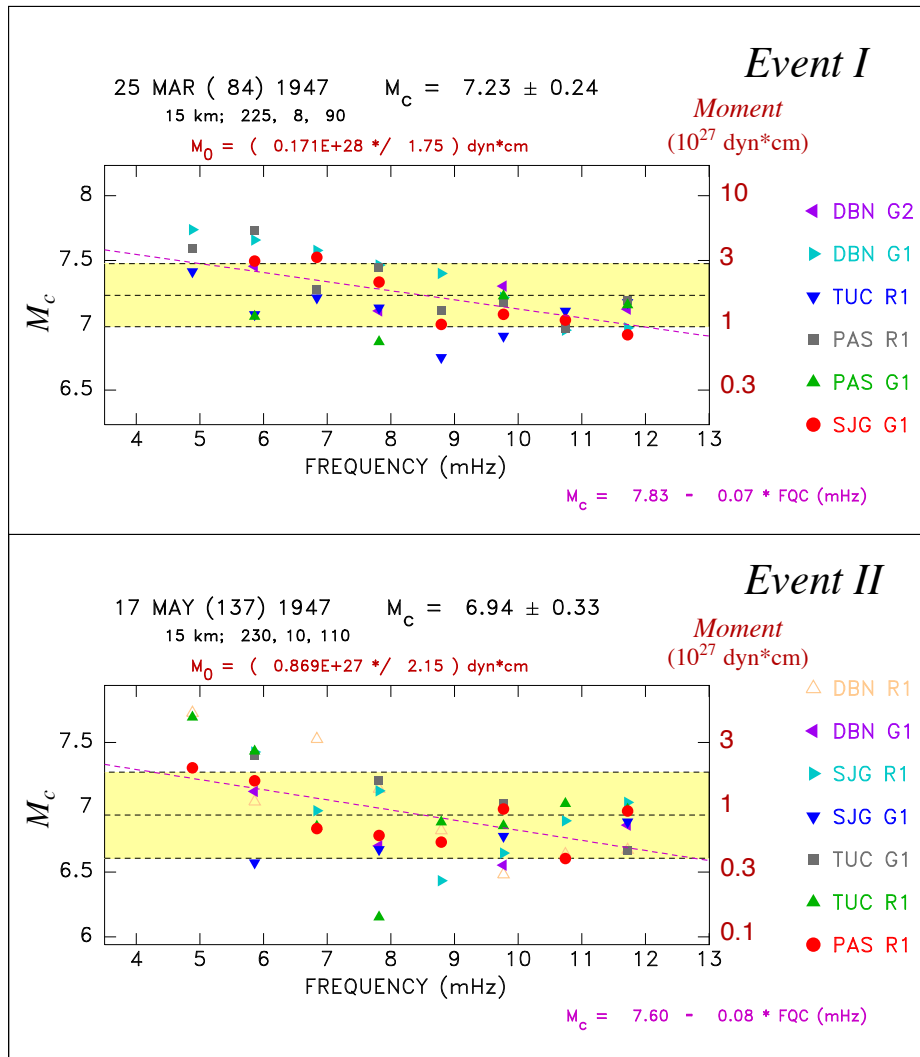


Figure 4.4. Mantle magnitudes M_c (Okal & Talandier, 1989) computed for 1947 Hikurangi Events I (Top) and II (Bottom). The average value and its 1- σ confidence interval are shown as the horizontal dashed lines and yellow bands. Note the slowness of the events, formalized as the magenta dashed lines which regress the datasets with frequency, the slopes (-0.07 and -0.08 logarithmic units per mHz) being characteristic of tsunami earthquakes.

We note that Doser & Webb (2003) obtained a vastly different mechanism (with a fault strike of 314° , essentially perpendicular to the local plate boundary) when inverting their body-wave dataset for Event I using the formalism of McCaffrey & Abers (1988). We have verified that the resulting solution is poorly matched by our mantle wave dataset, and thus select the mechanism expressing low-angle subduction, as also preferred by Bell et al. (2014).

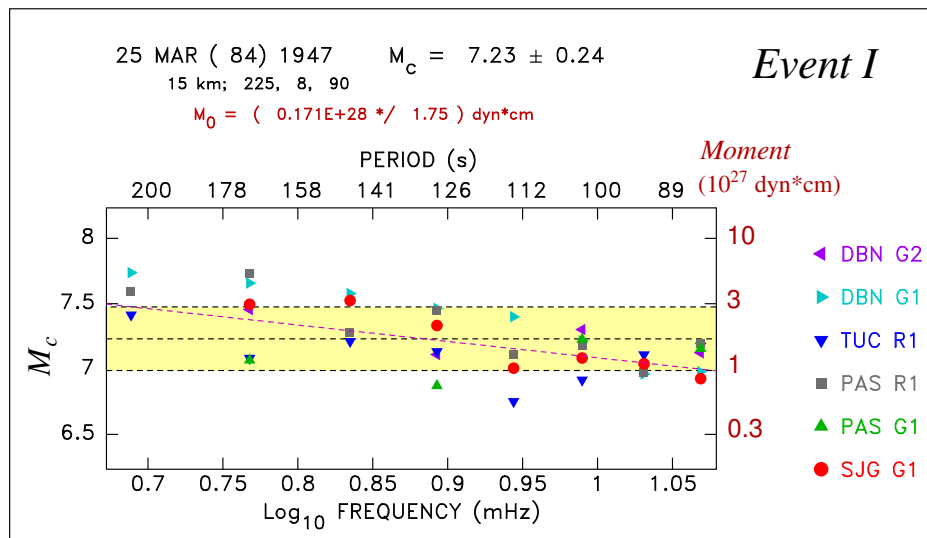


Figure 4.5. Same as the top frame of Fig. 4.4, but plotted using a logarithmic scale for frequencies. Note that any corner frequency must be lower than the spectral window used in our study.

In conclusion, our results confirm in the domain of mantle waves the slow nature of both 1947 sources, and their character as tsunami earthquakes, identified at

generally shorter periods by previous authors. They suggest the need for a more quantitative investigation using energy-to-moment ratios and the parameter Θ . Unfortunately, in 1947, there were no stations operating well calibrated short-period instruments in the distance range of Newman & Okal’s algorithm (35° to 80°). In addition, the regional records used by Bell et al. (2014) were written at distances shorter than allowed in Ebeling & Okal’s (2012) extension. By contrast, we were able to obtain records at Tucson (TUC; $\Delta = 96.2^\circ$) for Event I and Pasadena (PAS; $\Delta = 93.0^\circ$) for Event II, which are reproduced on Fig. 4.1. (a) and (b), motivating the development of an algorithm to extend the computation of E^E and hence Θ to distances beyond 80° .

4.3. The Santa Cruz aftershock of 21 July 1934 (06:18 GMT)

4.3.1. Evidence for a Tsunami Earthquake

This event occurred off Nendö (Santa Cruz) Island, as an aftershock of a major earthquake that took place three days earlier off Vanikolo (see Fig. 4.6). The aftershock on 21 July 1934 is clearly smaller than the mainshock on 18 July, with “Pasadena” magnitudes estimated by Gutenberg & Richter (1954) at $M_{PAS} = 7.3$ and 8.1 , respectively. Unfortunately, the only available reports regarding the tsunamis of 18 and 21 July are from the Northern coast of New Caledonia, 1000 km to the South. Anonymous (1935) describes the arrival of a tsunami in Hienghène and Touho (see Fig. 4.6) around 8 a.m. local time on the 19th, which fits the expected arrival time from the mainshock, assuming the present local time zone (GMT +11).

By contrast, arrivals in Poindimié in the [local] evening on the 19th are difficult to reconcile. The amplitude of the wave was interpreted by Solov'ev & Go (1984b) as a run-up of 0.6 m. Tsunami arrivals from the aftershock are reported at Touho and Thio in the evening of the 21st (they would be expected around 19:00 local time), and described as stronger (if shorter in duration) than for the mainshock. In addition, an intriguing harbor oscillation was reported on the 22nd (local time) in Nouméa on the Southern coast of New Caledonia, during an ebbing tide (but with no precise indication of time), while no such phenomenon was described following the mainshock. This report is difficult to interpret, since, in order to be observed presumably in daylight, it would require a propagation time of at least 13 hours for a distance (around New Caledonia) not exceeding 1500 km (see Fig. 4.6); it could involve harbor resonance at a frequency propagating outside the undispersed shallow-water approximation (Okal et al., 2006). Nevertheless, these observations generally uphold the character of a tsunami earthquake for the aftershock on 21 July 1934.

This pattern of a seismically smaller event generating a larger tsunami than the mainshock, constitutes one class of “tsunami earthquakes”, initially described by Fukao (1979) in the Kuril Islands, with other examples including the 1932 Manzanillo series (Okal & Borrero, 2011), and the 2010 Mentawai earthquake following the 2007 Bengkulu megathrust event (Borrero et al., 2009; Hill et al., 2012). They are often modeled as releasing stress transferred by the mainshock either onto the shallowest section of the interplate contact or onto splay faults in an accretionary wedge

featuring deficient mechanical properties, resulting in decreased rupture velocities and red-shifting of the source spectrum towards the lower frequencies responsible for tsunami genesis. Okal (1988) has verified that rupture in softer “sedimentary” material can amplify tsunami excitation relative to that of seismic waves. We will refer to such events as “aftershock tsunami earthquakes”, or ATEs, as opposed to “primary tsunami earthquakes” (PTEs) occurring as mainshocks (e.g., Aleutian, 1946; Nicaragua, 1992; Java, 1994 and 2006).²

In this general context, we conducted a systematic seismological reassessment of the 1934 mainshock-aftershock sequence.

4.3.2. Relocation of the 1934 Santa Cruz sequence

We relocated the mainshock and 16 aftershocks occurring over the next 20 days, using arrival times listed by the International Seismological Summary and the method of Wyss et al. (1991), with a larger Gaussian noise standard deviation, $\sigma_G = 5$ s, for an event in the 1930s. Results are listed in Table 4.1 and mapped on Fig. 4.7(a). As shown on Fig. 4.7(d), none of these relocations can resolve depth, but epicenters feature very little moveout when constrained depth varies between 10 and 150 km (small yellow circles on Fig. 4.7(b) and 4.7(d)), and

² Note that we use here the term “aftershock” in a broad sense, to describe generally smaller earthquakes following in the vicinity of a main event, without the restriction that they should take place on the same fault, a condition that “true” aftershocks should satisfy, for example if used in the quantification of a rupture area.

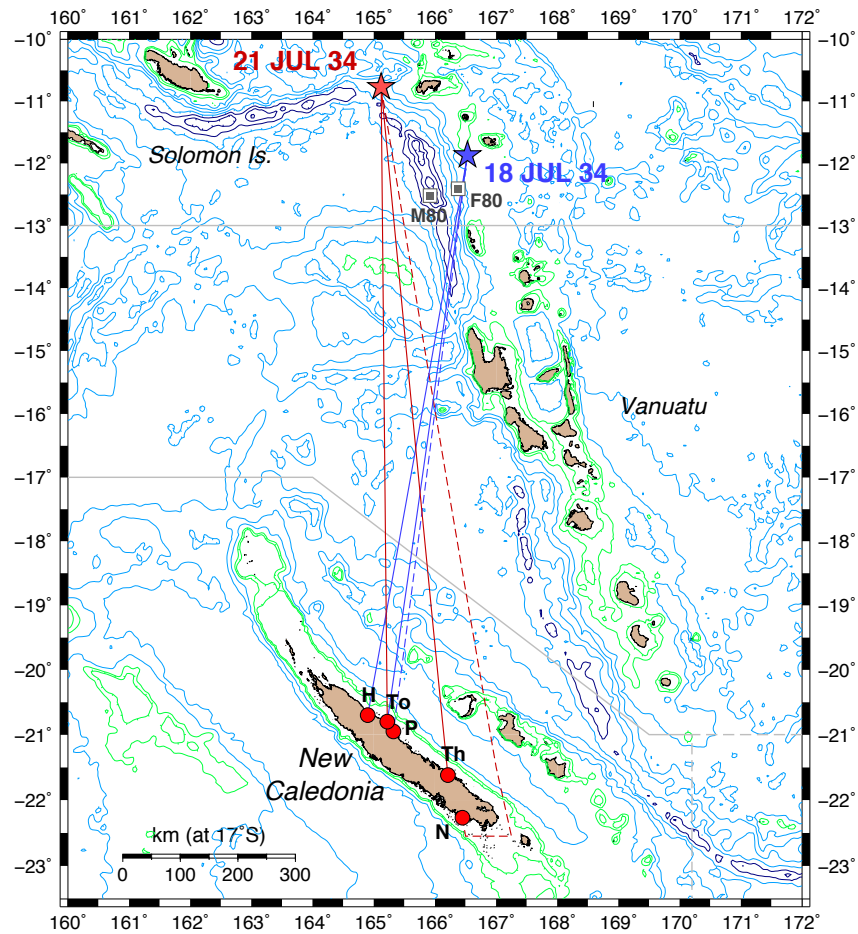


Figure 4.6. Epicenters of the 1934 Santa Cruz mainshock (blue star) and tsunami earthquake (red star) with locations of reported tsunami observations in New Caledonia, and probable paths. H: Hienghène; To: Touho; P: Poindimié; Th: Thio; N: Nouméa. See text for details. The dashed paths refer to the significantly delayed reports at Poindimié and Nouméa. The centered squares are the epicenters of the 1980 foreshock (F80; 8 July) and mainshock (M80; 17 July). Isobaths 500 and 1000 m in green, then at 1000 m intervals; dark blue for depths 6000 m and greater. International boundaries in gray.

the local geometry of the Wadati–Benioff zone rules out intermediate or deep foci.

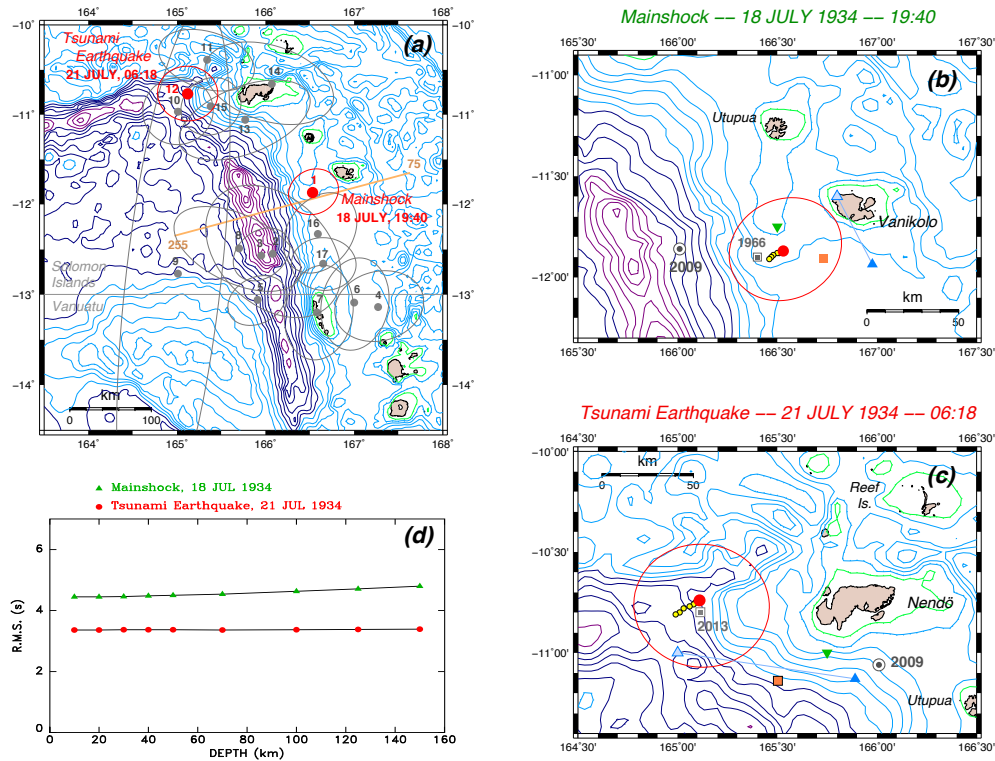


Figure 4.7. Relocation of the 1934 Santa Cruz sequence. (a): Relocated epicenters shown as solid dots (with numbers keyed to Table 4.1), with associated Monte Carlo ellipses computed for $\sigma_G = 5$ s. The mainshock and tsunami earthquakes are shown in red. Isobaths are at 200 m intervals above 1000 m (green), and deeper at 500 m intervals. The brown line shows the strike of the cross section on Fig. 4.15 (b): Close-up of (a) showing the relocation of the mainshock. The blue triangles are the original ISS solution (shaded) and the updated ISC-GEM one (solid). The green inverted triangle is Gutenberg & Richter's (1954) location. The light brown square is the Centennial epicenter (Engdahl & Villaseñor, 2002). The small yellow symbols show the minor moveout of our relocations when the constrained depth is varied from 10 km to 150 km. The bull's eye symbol locates the 2009 reference event, and the centered square the deeper 1966 earthquake. (c): same as (b) for the tsunami earthquake of 21 July 1934. The centered gray square is the epicenter of the slow earthquake of 06 February 2013. (d): Root-Mean-Square residuals for constrained depth relocations as a function of hypocentral depth for the 1934 mainshock (green triangles) and tsunami earthquake aftershock (red dots). Note their nearly constant values (especially in the latter case), expressing the lack of resolution of depth by the available travel-time dataset.

Table 4.1. Relocation of the 1934 Santa Cruz sequence.

Number	Date		Relocation				Magnitude		Remarks	
	D	M (J) Y	Origin Time GMT	Latitude (N°)	Longitude (E°)	Number of arrivals Listed Kept		R.M.S (s)		PAS
1	18	JUL (199) 1934	19:40:18.9	-11.87	166.53	95	87	4.45	8.1	Mainshok
2	18	JUL (199) 1934	21:29:36.2	-12.55	166.08	10	10	5.29		
3	19	JUL (200) 1934	00:06:43.3	-12.57	165.95	48	40	4.77	$6\frac{3}{4}$	
4	19	JUL (200) 1934	05:45:17.5	-13.14	167.27	22	17	5.52	$6\frac{1}{2}$	
5	19	JUL (200) 1934	07:36:56.0	-13.06	165.91	61	50	3.64	6.9	
6	19	JUL (200) 1934	22:57:40.2	-13.09	167.00	10	10	4.65		
7	20	JUL (201) 1934	03:52:25.9	-13.20	166.58	10	10	4.30		
8	20	JUL (201) 1934	16:48:19.6	-12.49	165.70	16	12	3.27		
9	20	JUL (201) 1934	18:05:58.2	-12.77	165.01	6	6	0.59		
10	20	JUL (201) 1934	18:10:23.2	-10.97	165.01	16	14	4.50		
11	20	JUL (201) 1934	18:48:46.8	-10.39	165.34	21	17	4.69		
12	21	JUL (202) 1934	06:18:20.4	-10.77	165.12	85	66	3.56	7.3	Tsunami Earthquake
13	21	JUL (202) 1934	07:22:38.4	-11.06	165.77	21	16	3.54		
14	21	JUL (202) 1934	20:11:27.2	-10.66	166.07	12	10	4.72		
15	22	JUL (203) 1934	02:57:52.8	-10.91	165.38	27	24	4.43	$6\frac{1}{4}$	
16	27	JUL (208) 1934	12:25:38.2	-12.33	166.59	14	13	4.88		
17	07	AUG (219) 1934	03:40:06.4	-12.66	166.65	60	55	2.93	6.9	

The 1934 mainshock locates about 50 km North of the 1980 foreshock-mainshock sequence (F80, M80 on Fig. 4.6), which featured a classical interplate thrust geometry (e.g., Tajima et al. 1990), and also of the large earthquake of 31 December 1966 ($m_b = 5.5$; $M_{PAS} = 7.5$; Fig. 4.7). However, as described in Section 4.4, the latter took place at significant depth (78 km), most probably inside the downgoing slab; its tsunami reached only 2 m on Vanikolo (Solov’ev & Go, 1984a).

While our relocations are in general agreement with other published solutions, we note that, in the case of the tsunami earthquake aftershock, both the Centennial Catalog solution (Engdahl & Villaseñor, 2002) and the ISC-GEM relocation are significantly offset to the ESE (respectively 60 and 100 km). Incidentally, the quality of all relocations of the 21 July aftershock is systematically poorer than for the mainshock: a grade of “B” as opposed to “A” for the mainshock, assigned by

Engdahl & Villaseñor (2002), and a large proportion of arrivals excluded from the datasets (20 out of 85 or 24% in our relocation; 55 out of 202 or 27% for the ISC solution, versus 8% and 3%, respectively for the mainshock). This suggests emergent arrivals, as would be expected from a slow earthquake deficient in high frequencies.

The relocated aftershocks feature a bimodal distribution, largely correlated with time: during the first two days, they cluster around the mainshock, suggesting a fault extending Southeast 150 km along the Vanuatu trench. Starting with Event 10 (and perhaps the poorly located Event 9), they move North and cluster around the tsunami earthquake of 21 July (Event 12), suggesting a fault length of 100 km for the latter. The later events, 16 and 17, return to the area of the mainshock.

We note further that our relocated epicenter for the tsunami earthquake of 21 July 1934 coincides (within 7 km) with that of the large earthquake of 06 February 2013 ($M_0 = 9.4 \times 10^{26}$ dyn cm; gray centered square symbol on Fig. 4.7). That event generated a powerful tsunami running up 12 m and causing 10 deaths on Nendö Island (Fritz et al., 2013), and we have verified that it qualifies as a tsunami earthquake with a parameter $\Theta = -5.94$; it also features a somewhat high ratio of P-wave duration to the cube root of radiated energy E^E , as characterized by their normalized logarithmic ratio Φ (Okal, 2013): with $\Phi = 0.38$, the 2013 Santa Cruz event fits marginally above the threshold of 0.35 proposed for slow events including tsunami earthquakes, and is directly comparable to the 2010 Mentawai

ATE ($\Phi = 0.39$). The 2013 earthquake has also been recognized as deficient in high frequencies by Lay et al. (2013).

4.3.3. Focal mechanism and moment

Unfortunately, we were unable to build a fully constrained focal mechanism for either the mainshock or the aftershock, due to the scarcity and poor azimuthal distribution of stations, and in the case of the tsunami earthquake, to the strongly emergent nature of first arrivals. In the case of the mainshock, we have verified that a mechanism slightly adapted from that of the nearby 1980 mainshock ($\phi = 338^\circ$; $\delta = 23^\circ$; $\lambda = 93^\circ$) is compatible with the few available first motions, and results in an acceptable scatter of moments for a dataset of 13 mantle waves at worldwide stations (Fig. 4.8), suggesting a low-frequency moment $M_0 = 2.5 \times 10^{28}$ dyn cm. In the case of the tsunami earthquake, we use a mechanism derived from that of the 2013 event, but with a steeper dip ($\phi = 340^\circ$; $\delta = 40^\circ$; $\lambda = 70^\circ$), which yields an average moment of 2.7×10^{27} dyn cm; however, the mantle wave spectra feature a strong growth with period, with an average moment of 7.3×10^{27} dyn cm at 170 s, and a slope of -0.1 logarithmic unit per mHz, suggesting a static moment as large as 10^{28} dyn cm (Fig. 4.8). Note that these moment values are generally compatible with the faults lengths (150 and 100 km, respectively) suggested by the aftershock distribution (Fig. 4.7a).

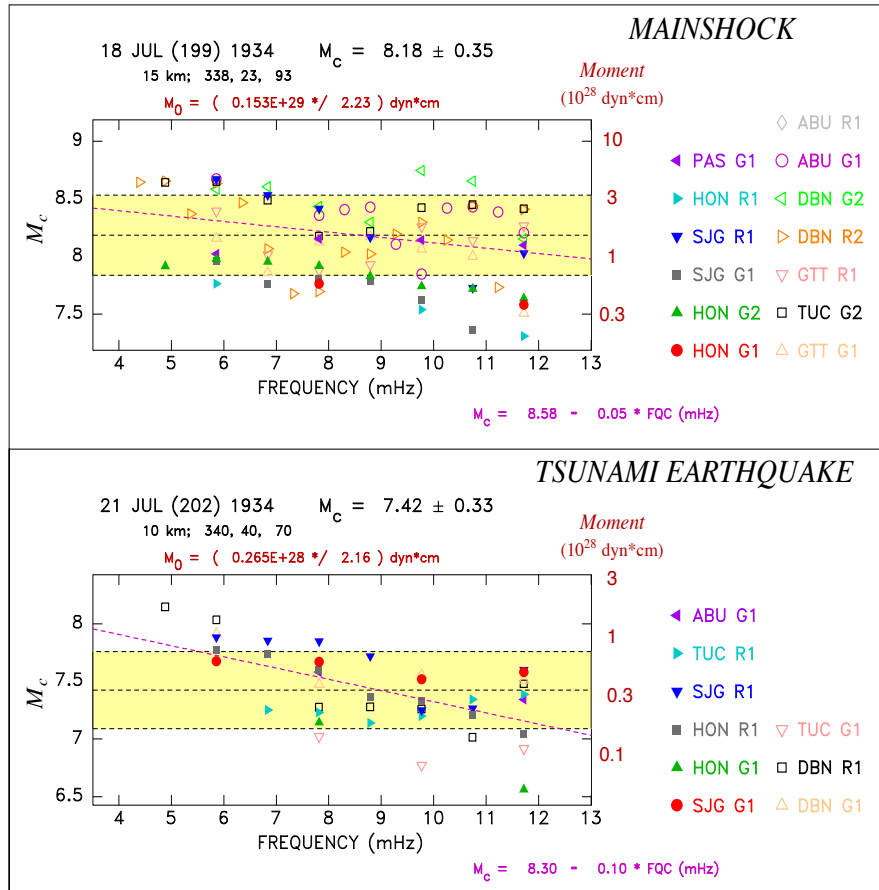


Figure 4.8. Same as Fig. 4.4 for the 1934 Santa Cruz mainshock (Top) and tsunami earthquake aftershock (Bottom). Note the strong increase of moment with period for the latter.

4.3.4. Record available for the computation of estimated energy

The only record available is the Pasadena short-period vertical (Benioff, 1932), whose P wave is shown on Fig. 4.1.

4.4. Extension of the Θ algorithm beyond 80°

4.4.1. Methodology

In this section, we define a procedure to obtain a special distance correction in order to compute a value of E^E at distances greater than 80° . For this purpose, we consider a modern reference event for which an ample dataset of worldwide digital stations in the range $35^\circ < \Delta < 80^\circ$ allows the routine computation of E^E and hence of a reference value Θ_{ref} , using the standard algorithm of Newman & Okal (1998). We then use digital stations (indexed i) recording the same event at distances greater than 80° to study the residual $r_i = \Theta_i - \Theta_{ref}$ as a function of distance, where Θ_i is computed by simply extrapolating the algorithm derived for shorter distances by Newman & Okal (1998). A regressed value of the opposite of the residual can then be used as an empirical correction, allowing an estimate of Θ for the historical event from a single record beyond 80° .

We recall that Newman & Okal's (1998) algorithm corrects the energy flux recorded at a teleseismic station through the combination of geometrical spreading (their Eq. 4), and of a squared-average estimate of the radiation coefficient of the generalized P wave (composed of P , pP and sP), regressed as a function of distance as (Newman & Okal 1998, Eq. 9):

$$(F^{Est.})(\Delta) = 1.171 - 7.271 \times 10^{-3}\Delta + 6.009 \times 10^{-5}\Delta^2 \quad (4.3)$$

where Δ is in degrees. There are *a priori* two contributions to the residual r_i . One is the inadequacy of the correction (4.3) beyond the domain of distances for which it was derived; in particular, lateral heterogeneity at the base of the mantle (Vidale & Hedlin, 1998) will result in scattering which will affect both geometrical spreading and the description of attenuation in terms of a parameter t^* taken as independent of distance. The second contribution to r_i is the effect of focal mechanism, which is ignored in the computation of the estimated energy E^E . As discussed in detail by Newman & Okal (1998), in routine computations of the parameter Θ , the use of a large number of stations with a diversity of distances and azimuths provides an adequate sampling and averaging of the focal sphere, allowing the use of the coefficient $(F^{Est.})^2$ given by (4.3) to obtain the estimated value of E^E . However, in the case of a single station, the true value of the generalized radiation coefficient may depart significantly from (4.3), especially if the station lies in the vicinity of a fault plane on the focal sphere.

In the case of the 1947 Hikurangi events, we have verified the absence, in the GlobalCMT catalog, of any interplate thrust event at latitudes between 40°S and 37°S, with a sufficient moment ($M_0 > 10^{25}$ dyn cm) to be used as a reference event; in this context, we use the Kermadec earthquake of 04 May 2003 (30.53°S; 178.23°W; $M_0 = 1.2 \times 10^{26}$ dyn cm; $M_w = 6.7$). This event features a focal geometry comparable to that of the 1947 events, but being farther North along the trench, it offers a large number of records on the North American continent at distances

between 85° and 100° . We compute a standard parameter $\Theta_{ref} = -4.50$ using 18 stations worldwide, at distances ranging from 35 to 80 degrees. We then select 37 North American stations at epicentral distances of 86° to 97° , within a $\pm 10^\circ$ window of azimuths at the epicenter (Fig. 4.9a), and compute values of Θ_i using (4.3) extrapolated beyond 80° as a distance correction. Results are plotted as residuals r_i on Fig. 4.10. At distances Δ between 85° and 88.5° , the residual is largely independent of distance, with an average value of -0.37 , which we attribute primarily to the effect of focal geometry, expected to result in deficient amplitudes, since the take-off azimuth to North America is close to the fault plane. Starting at about 90° , the residuals become increasingly negative with distance; they can be regressed between 90° and 97° as

$$r = 12.835 - 0.147\Delta = -0.395 - 0.147(\Delta - 90) \quad (4.4a)$$

where r is dimensionless (logarithmic units) and Δ is in degrees, as shown by the solid line on Fig. 4.10.

In the case of the 1934 Santa Cruz tsunami earthquake, we use for reference the event of 07 October 2009 at 11.86°S ; 166.01°E ($M_0 = 6.7 \times 10^{27}$ dyn cm; $M_w = 7.8$), which locates in the vicinity of the 1934 mainshock (see Fig. 4.7b). We similarly compute a value $\Theta_{ref} = -5.47$ from 21 records at distances $35^\circ < \Delta < 80^\circ$, and study the residuals r_i at 92 North American stations ranging in distance from 83.5°

to 98° (Fig. 4.11). The residuals, shown on Fig. 4.12, can be regressed between 90° and 100° as

$$r = 10.178 - 0.119\Delta = -0.510 - 0.119(\Delta - 90) \quad (4.4b)$$

The fact that Eqs (4.4a) and (4.4b) differ reflects differences in focal mechanisms between the two reference events, as well as, probably, in laterally heterogeneous structure of D'' along the two paths. The latter justifies *a posteriori* the conservative upper bound in distances ($\Delta < 80^\circ$) implemented in the routine worldwide algorithm processing modern events for Θ . However, the opposites of the regressed residuals,

$$Corr_{NZ} = 0.395 + 0.147(\Delta - 90) \quad (4.5a)$$

and

$$Corr_{SC} = 0.510 + 0.119(\Delta - 90) \quad (4.5b)$$

will remain adequate corrections when implemented to recover Θ from a measurement beyond 90° , respectively in New Zealand and Santa Cruz, as long as the paths sampled in the lower mantle are similar and the focal mechanism and receiver geometries are also comparable. In both instances (Hikurangi 1947 and Santa Cruz 1934), we have selected the reference events specifically to enforce those conditions. In this respect, Eqs. 4.5a and 4.5b bear no pretense to be universally applicable.

4.4.2. Validation of the approach

Before applying the above algorithm to our historical records, we validate it on recent events in the vicinity of the Hikurangi tsunami earthquakes. In the absence of interplate thrust events, we consider the two nearby normal faulting earthquakes of 16 November 2014 ($M_0 = 1.3 \times 10^{26}$ dyn cm; $M_w = 6.7$) and 01 September 2016 ($M_0 = 4.2 \times 10^{26}$ dyn cm; $M_w = 7.0$). The validation epicenters are shown on Fig. 4.2 as bull's eye symbols, and the geometry of the rays to PAS and TUC on Fig. 4.9(b). While their mechanisms differ from that of the reference earthquake, they share the property that stations in the Southwestern US are close to a focal plane, which legitimizes the use of (4.5a). Using worldwide stations in the $35^\circ - 80^\circ$ distance range, we obtain standard Θ_{ref} parameters of -4.54 (2014) and -4.30 (2016). We then use records at PAS ($\Delta = 91.9^\circ$ and 92.0° , respectively) and TUC ($\Delta = 95.1^\circ$ and 95.2° , respectively) and after using the correction C_{NZ} (4.5a), obtain Θ values of -4.45 (PAS; 2014), -4.49 (TUC; 2014), -4.12 (PAS; 2016) and -4.21 (TUC; 2016); in all four cases, the residuals with respect to Θ_{ref} are less than 0.2 logarithmic units in absolute value.

This experiment thus validates the algorithm extending the computation of Θ to distances greater than 80° through the use of the corrections (4.5).

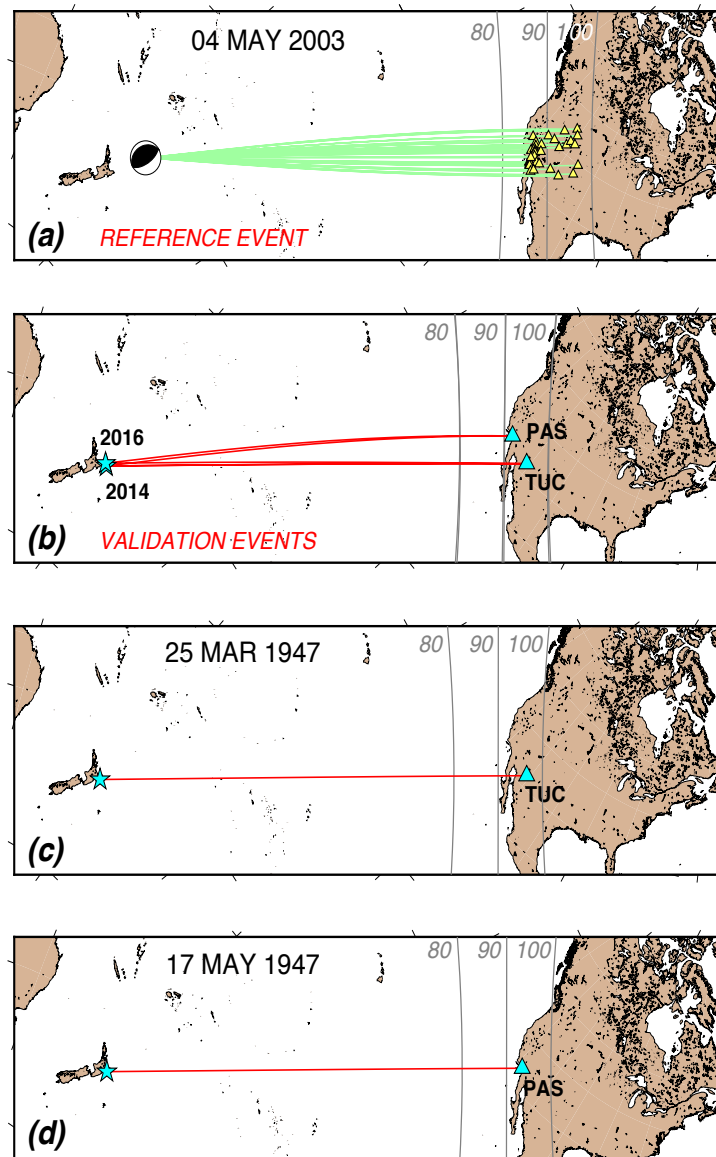


Figure 4.9. Extension of the Θ algorithm beyond 80° in the geometry of the New Zealand earthquakes. The maps are oblique Mercator projections using the great circle from epicenter to receiver (or centroid to receiver) as the Equator. (a): Reference event of 04 May 2003. The individual stations used to compute the residuals r_i are shown as triangles with the great circle paths as green lines. The gray lines are epicentral isodistals for 80° , 90° , and 100° , respectively. (b): Geometry of the validation experiment using the normal faulting events of 2014 and 2016. Note that differences in epicentral location, propagation paths, and isodistals are barely noticeable on the scale of this map. (c) and (d): Geometry of the historical paths of 1947.

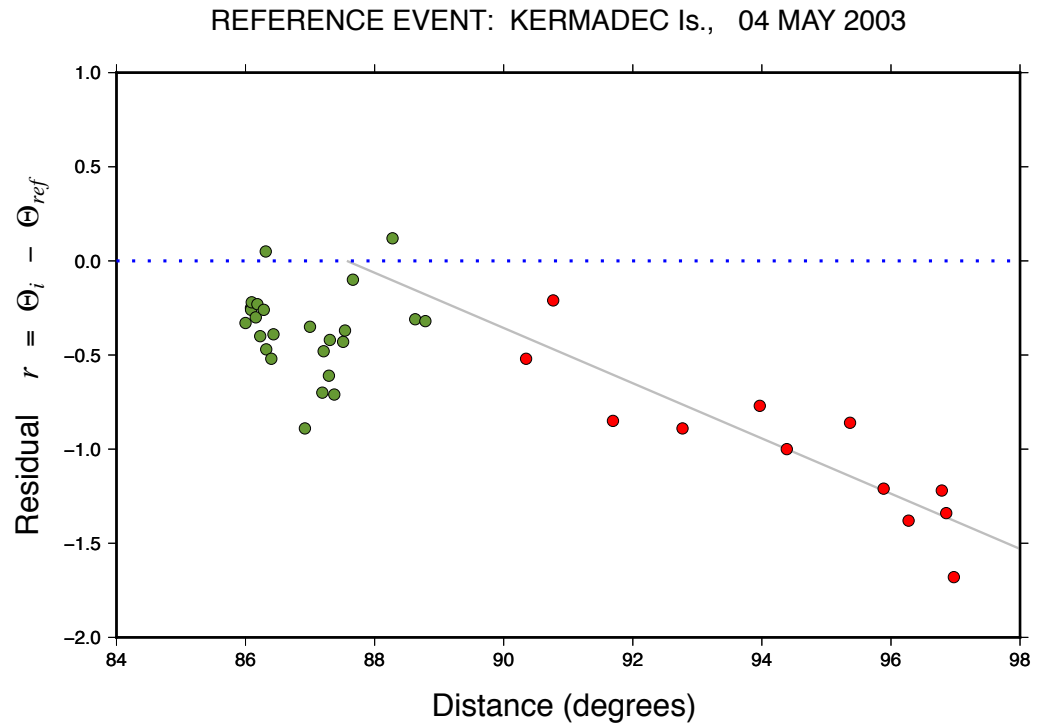


Figure 4.10. Residuals r_i plotted as a function of distance to North American stations beyond 85° for the reference Kermadec event of 04 May 2003. The solid gray line is the linear regression (4.5a) of the red data points, beyond 89° .

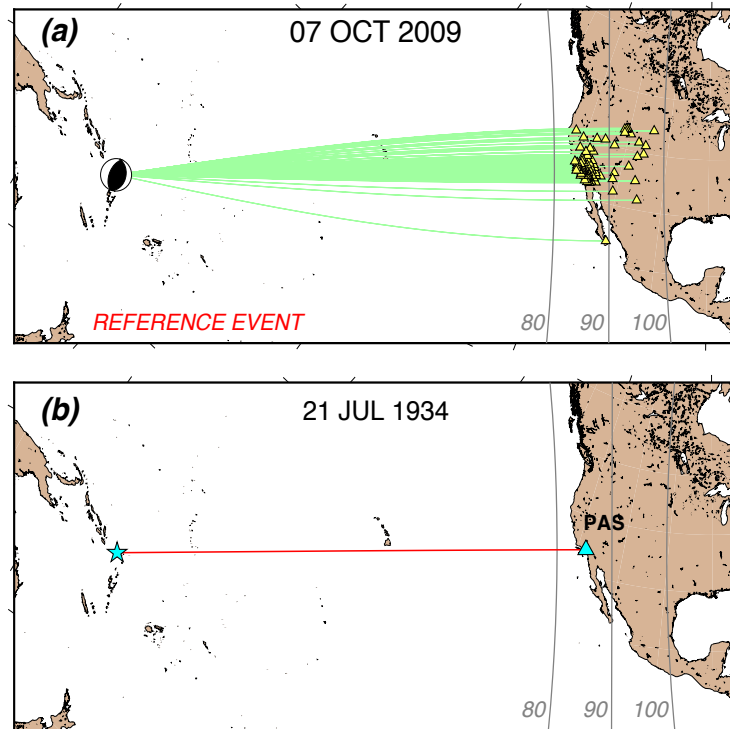


Figure 4.11. Same as Figure 9 for the Santa Cruz tsunami earthquake of 21 July 1934. (a): Reference event of 07 October 2009. (b): Application to the historical earthquake.

4.4.3. Application to historical records

All three records shown on Fig. 4.1 were optically enlarged and digitized at a time sampling of 0.1 s. Instrument responses were obtained from available laboratory ledgers at Caltech for the PAS records (H. Kanamori, personal communication, 2015; see additional discussion in Okal et al. 2016) ; Appendix A details the derivation of the response at TUC in 1947. Computed values of Θ are listed in Table 4.2.

In the case of Event I (Hikurangi, 25 March 1947) at TUC, we obtained a value of the estimated energy using (4.3), of $E^E = 2.27 \times 10^{20}$ erg, which with the moment $M_0 = 4 \times 10^{27}$ dyn cm suggested at very long periods from Section 4.2 and $Corr_{NZ} = 1.31$ from (4.5a), yields $\Theta = -5.94$. Similarly, in the case of Event II (Hikurangi, 17 May 1947) at PAS, we obtain $E^E = 1.50 \times 10^{20}$ erg, and with $M_0 = 3 \times 10^{27}$ dyn cm, $\Theta = -6.51$, using $Corr_{NZ} = 0.89$.

In the case of the Santa Cruz tsunami earthquake of 21 July 1934, we similarly obtain $E^E = 1.41 \times 10^{21}$ erg. However, the distance to PAS is only 85.2° , in a range where (4.5b) may not apply (green points on Fig. 4.12). Rather, we use as a correction the opposite of the average residual for that group of points, $Corr_g = -\bar{r}_g = 0.75$. We have verified that the 2009 residual at PAS (one of the “green” stations on Fig. 4.12), $r_{PAS} = -0.78$, is not significantly different from $-\bar{r}_g$. With an estimated static moment of 10^{28} dyn cm, this yields a final value of $\Theta = -6.10$ for the event of 21 July 1934, confirming its slow character as a tsunami earthquake. Note that even the more conservative value of the seismic moment $M_0 = 7.2 \times 10^{27}$ dyn cm, which is the average of measured values from mantle waves at 170 s (Fig. 4.8), still results in a significantly deficient $\Theta = -5.96$.

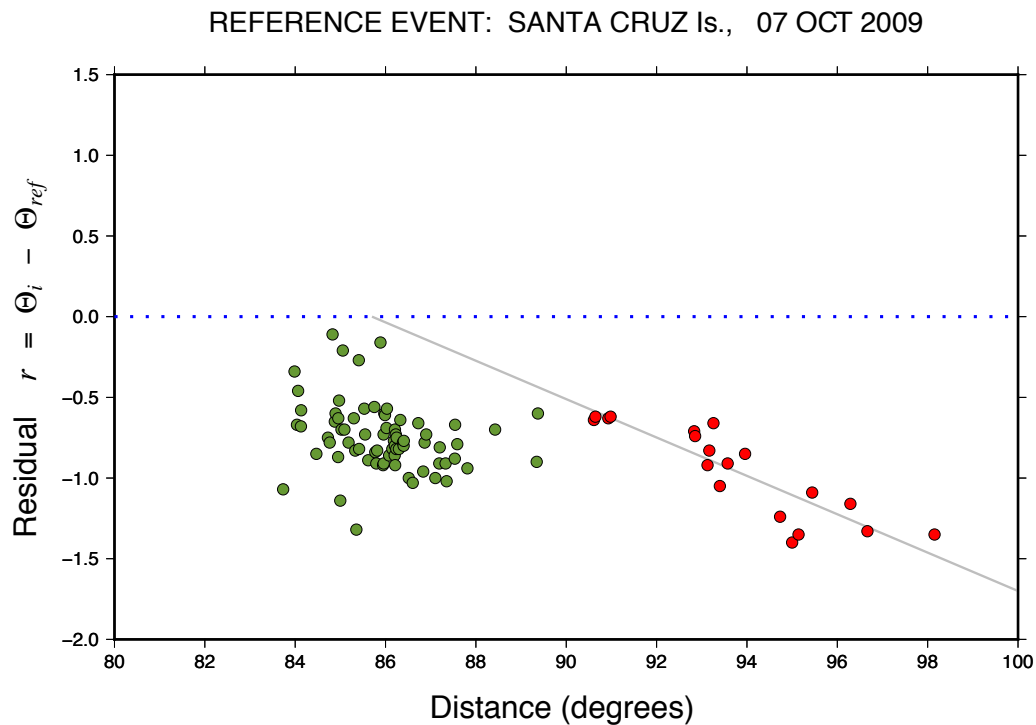


Figure 4.12. Same as Fig. 4.10 for the reference event of 07 October 2009 in Santa Cruz. The solid line is the regression (4.5b).

Results from the three tsunami earthquakes quantified in this study are regrouped on Fig. 4.13, which provides an update to similar plots by Newman & Okal (1998), Okal (2013), and more recently Okal et al. (2016).

In this context, we note that even though some early instruments featured very high magnification, Benioff (1932) experimented with values of up to 100,000 on his short-period seismometer), all of them used analog recording, which featured a very

limited dynamic range, defined by the ratio of the width of the paper record usable before clipping to that of the ink or light trace, in practice 3, at best 4, orders of magnitude. This is in contrast to the 7 (resp. 9) orders of magnitude achieved by a modern instrument using a 24 (resp. 32)–bit digitizer (Wielandt, 2002). In addition, early short–period instruments had a considerably narrower frequency response than present–day broadband digital ones, which raises the legitimate question of whether they can have an adequate response over the frequency range defining the integral of the energy flux in the frequency domain, typically from 0.1 to 2 Hz. This could conceptually lead to spectral components below noise level at frequencies contributing significantly to radiated energy. However, because of their high maximum magnifications, the short–period instruments used here keep an absolute response comparable to that of the torsion instruments used in the analysis of the 1932 Mexican series (Okal & Borrero, 2011), over most of the frequency band relevant to the Parseval integral, and much higher around 1 Hz, where the energy of “tsunami earthquakes” is typically deficient. Since that study was able to clearly identify a tsunami earthquake of comparable moment (4×10^{27} dyn cm), we expect that our results would not be biased by inadequate frequency response. At any rate, this effect would lead to the processing of background noise into the Fourier integral for energy flux, and thus to an artificial increase in the value of Θ ; therefore, it cannot affect our conclusion that the three earthquakes studied are deficient in energy and indeed slow.

4.5. Discussion and Conclusion

We have derived an algorithm allowing the use of stations at epicentral distances greater than 80° to compute the slowness parameter Θ introduced by Newman & Okal (1998), a procedure which may be necessary in the study of historical earthquakes having occurred at large distances from the few stations then equipped with short-period instruments.

4.5.1. Hikurangi Trench

Our application of this method to the 1947 Hikurangi earthquakes allows the quantification of their character as tsunami earthquakes, which was established by the descriptive reports of both felt intensities and tsunami inundation, and the body-wave investigations of Doser & Webb (2003) and Bell et al. (2014). By studying the spectrum of mantle waves from both events, we obtain low-frequency moments significantly (but expectedly) larger than derived from body-wave modeling. As shown on Fig. 4.13, Θ for Event I falls within the range (-6.0 ± 0.1) of the classical PTEs in Java (J94 and J06) and Peru (CP), while Event II ($\Theta=-6.51$) is more comparable to the Nicaragua and El Salvador PTEs (N92 and ES). In this respect, the exceptionally slow ruptures proposed by Bell et al. (2014) for Event I need not translate necessarily into extreme values of the parameter Θ . If the source consists of the jagged rupturing of discrete asperities (Polet & Kanamori, 2000), radiated energy and hence Θ will be controlled primarily by the rise time of each asperity,

and remain relatively insensitive to the time delay between asperities, the latter merely affecting the apparent average rupture velocity.

As mentioned above, these results cannot be compared directly to modern estimates of Θ for nearby events, since the Hikurangi Trench region does not feature even one single entry for a thrust mechanism above 10^{25} dyn cm in the GlobalCMT catalog. In addition, the 1947 earthquakes are the only ones documented in the historical dataset covering the years 1917–1961 analyzed by Doser & Webb (2003); between 1962 and 1975, the only thrust faulting event with a reported magnitude $M \geq 6$ is the 1966 Gisborne earthquake for which Webb et al. (1985) have computed a moment of only 4×10^{24} dyn cm.

Several fundamental questions regarding the nature of large subduction earthquakes at the Hikurangi Trough thus remain wide open.

Table 4.2. Parameters Θ computed in this study: Hikurangi Trench

Date	Origin Time	Epicenter		Depth	Moment	Θ	Remarks
D M (J) Y	(GMT)	(N°)	(E°)	(km)	(10^{27} dyn cm)		
04 MAY (124) 2003	13:15:18.7	-30.53	178.23	62	0.12	-4.50	Reference Event (Kermadec Is)
16 NOV (320) 2014	22:33:20.5	-37.65	179.66	22	0.13	-4.54	Validation Event (Normal Faulting)
01 SEP (245) 2016	16:38:14.5	-37.17	179.15	24	0.42	-4.30	Validation Event (Normal Faulting)
25 MAR (084) 1947	20:32:18.8	-38.85	178.90	8	4	-5.94	Tsunami Earthquake
17 MAY (137) 1947	07:06:34.7	-38.42	178.87	10	3	-6.51	Tsunami Earthquake

- (1) First, is the slowness featured in the two 1947 events a regional trend to be expected for all large interplate events in the area? As documented by Okal & Newman (2001) and later confirmed during the 2006 PTE in the case of the Java Trench, the only known large interplate earthquakes in that subduction zone are slow PTEs, with only a few much smaller shocks featuring standard Θ values. By contrast, the same authors identified a wide range of Θ values, albeit for generally smaller events, along the Central American Trench, confirmed by recent seismicity featuring both a PTE (El Salvador, 2012) and a large event with only a trend towards slowness (Costa Rica, 2012; $\Theta = -5.59$). In Northern Peru, Okal & Newman (2001) described slow PTEs on 21 February 1996 (Chimbote) and 20 November 1960, but values only trending towards slowness for the large events of 17 October 1966 and 03 October 1974. In the absence of any other quantifiable interplate thrust event, there can be no answer to this question in the case of the Hikurangi Trench.
- (2) In addition, could the Hikurangi Trench sustain a so-called “mega-thrust” earthquake (with a moment reaching 10^{29} dyn cm)? In the wake of the 2004 Sumatra earthquake (and more recently of the 2011 Tohoku event), the once promising model of Ruff & Kanamori (1980), correlating the simple plate tectonics parameters of plate age and convergence velocity to maximum earthquake size at subduction zones, had to be abandoned (McCaffrey 2007; Stein & Okal 2007). While Schellart & Rawlinson (2013) have indeed listed

the Hikurangi Trough as the potential site of a mega-thrust event, their model, based on an extensive set of plate and morphological properties, remains at this point tentative.

- (3) In the affirmative, would such a mega-thrust event be slow? While the three largest events ever recorded (Chile, 1960; Sumatra, 2004; and Alaska, 1964) all featured source slowness (Kanamori & Cipar 1974; Nettles et al. 2005; Stein & Okal 2007) this property was not shared by the 2010 Maule and 2011 Tohoku events (Fig. 4.13), and the case of the Hikurangi trench remains totally speculative in this respect.

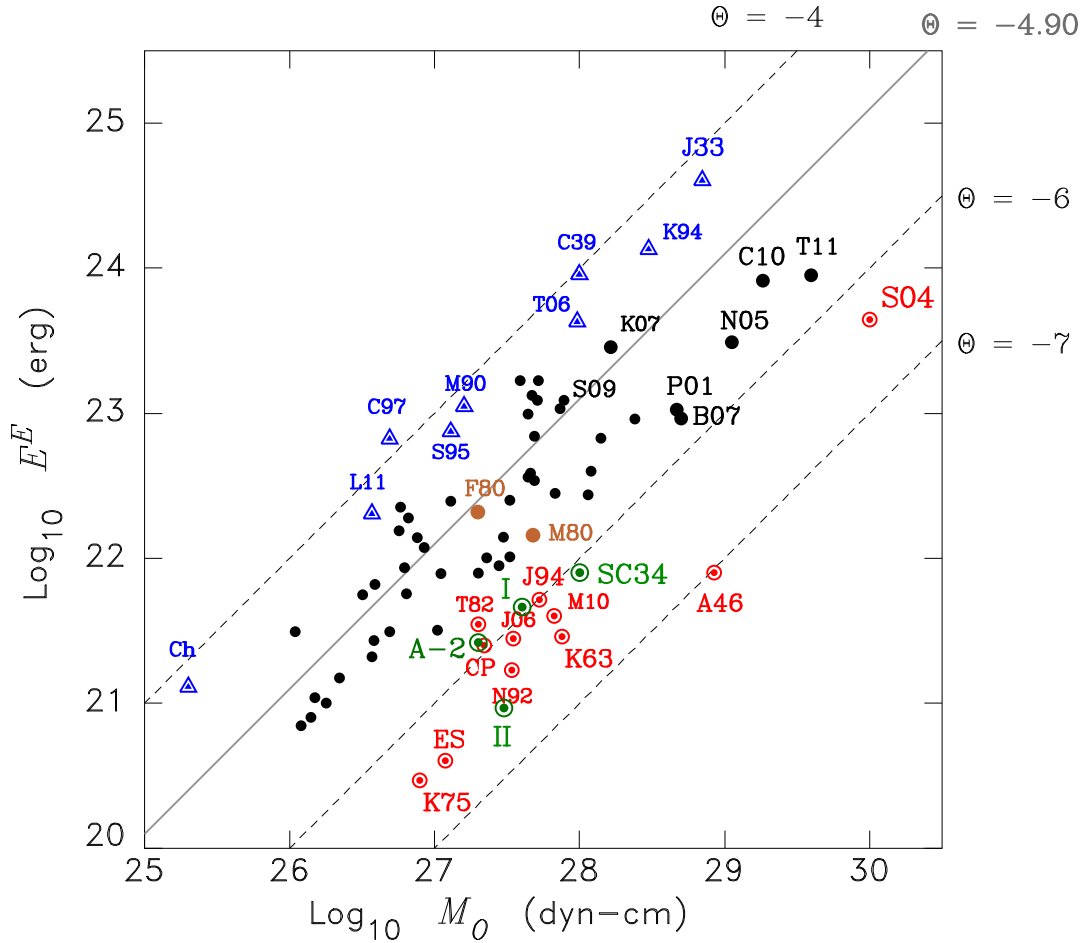


Figure 4.13. Plot of energy E^E versus M_0 , updated from the original work of Newman & Okal (1998) and more recently Okal (2013), to include the results of the present study: Hikurangi Events I and II, Santa Cruz ATE (SC34), 1965 ATE (A-2), and 1980 Santa Cruz foreshock (F80) and mainshock (M80). Previously studied tsunami earthquakes ($\Theta < -5.8$) are shown as red bull's eye symbols (A46, Aleutian 1946; K63, Kuril 1963 (20 Oct.); K75, Kuril 1975; T82, Tonga 1982; N92, Nicaragua 1992; J94, Java 1994; CP, Chimbote, Peru 1996; S04, Sumatra, 2004; J06, Java 2006; M10, Mentawai 2010; ES, El Salvador, 2012). The blue triangles ($\Theta > -4.3$) identify “snappy” earthquakes (J33, Sanriku, 1933; C39, Chillán 1939; M90, Marianas 1990; K94, Kuril 1994; S95, Samoa 1995; C97, Chile 1997; T06, Tonga 2006; Ch, Christchurch 2011; L11, Loyalty Is. 2011) and the black dots a selection of regular events (P01, Peru 2001; N05, Nias 2005; B07, Bengkulu 2007; K07, Kuril 2007; S09, Samoa 2009; C10 Chile 2010; and T11, Tohoku 2011).

4.5.2. Santa Cruz and Vanuatu Trench: Regional variation of Θ

By contrast, the abundant seismicity of the Santa Cruz–Vanuatu subduction system in the vicinity and to the South of the 1934 ATE earthquake ($\Theta = -6.10$) allows comparison with a number of other events. As mentioned in Section 4.2, we have obtained a very comparable $\Theta = -5.94$ for the 2013 PTE in its immediate vicinity. We have computed systematically slowness parameters for all GlobalCMT solutions in the region since 1990 (to allow for a sufficient development of the global digital network) featuring an interplate thrust mechanism and $M_0 \geq 10^{26}$ dyn cm, as well as for a number of key events before 1990. Results, summarized in Table 4.3 and mapped on Fig. 4.14, suggest variations in values of Θ which correlate reasonably well with the local tectonic features of the Santa Cruz–Vanuatu Island chain (Pelletier et al., 1998). The right frame on Fig. 4.14 reproduces the value of Θ as a function of latitude for interplate thrust events, but excludes intra-slab (1966), outer rise (1992) and back-arc (1999) shocks.

In very general terms, one can distinguish five morphologically different regions:

- (1) In the Northern one (“SC” on Fig. 4.14), the plate interface is poorly coupled, with a well-developed trench reaching a depth of 8500 m. Most large interplate thrust earthquakes have $-5.6 \leq \Theta \leq -5.2$ (yellow, with a trend towards slowness), typical of other subduction zones, with only deeper events such as the 1980 foreshock (F80) featuring a standard value around -4.90 (gray). In its Northern part, this segment sustains tsunami

earthquakes (red), either as a PTE (2013), or the ATE of a (presumably) regular earthquake (1934).

- (2) At the latitude of the Torres Islands (“TI”), the collision of the buoyant West Torres Plateau results in shallowing of the trench to no more than 6000 m and uplifting of the Torres Islands (Taylor et al., 1985; Louat & Pelletier, 1989). This region is characterized by standard values of Θ , with no known sources featuring slowness or trending towards it; this reflects a stronger level of coupling at the collision zone.
- (3) The next segment (“SM”) involves the collision of the d’Entrecasteaux system (d’EFZR on Fig. 4.14), a complex feature including both a fossil fracture zone and a passive ridge expressing the distortion of bathymetry at the fracture contact (Taylor et al., 1980) ; it has resulted in the complete disappearance of the trench and in the massive uplift of the two largest islands in Vanuatu, Santo and Malekula. This region was the site of the 1965 earthquake swarm, of which the second aftershock (A-2 in Table 3) was recognized by Ebel (1980) as being particularly anomalous; it generated a significant tsunami with 2-m run-up on Santo (Solov’ev & Go, 1984a). Despite the large size of the mainshock and of A-2, we were able to compute parameters Θ for the five events studied in detail by Ebel (1980), notably by using the correction $Corr_{SC}$ (4.5b) at high-gain North American stations beyond 90° , where the short-period P waves remain on scale; they are plotted as diamonds on Fig. 4.14. As summarized in Table 4.3, the Θ

values for the 1965 swarm range from standard (A-1) to trending (towards slowness), with A-2 featuring a definitely deficient value (-5.88). We also confirm from mantle waves a relatively high value of the low-frequency moment of A-2 (2×10^{27} dyn cm). Finally, we were able to identify T waves from all five major events in the swarm on short period WWSSN records at Kipapa, Hawaii (but unfortunately not at other island stations in the Pacific). Their small amplitude precludes the quantification of their energy fluxes (Okal, 2008b), but still allows qualitative comparison. T waves from A-2 are recorded as traces at a level comparable to those of A-1 (despite a moment 8 times larger), and significantly weaker than from FS-1 and FS-2, whose moments are 3 and 6 times smaller. They are considerably less intense than the clearly emerging T phase from the mainshock, whose moment is only 1.5 times larger than that of A-2. Such a deficiency in T -wave generation is regularly observed in tsunami earthquakes (Okal et al., 2003) as a result of a paucity of high frequencies in their source spectrum.

All these properties clearly characterize aftershock A-2 (13 August 1965; 12:40) as an ATE. Note that Centennial catalog epicentral parameters for the 1965 events (Engdahl & Villaseñor, 2002), listed in Table 3 and mapped as the five diamonds on Fig. 4.14, show that A-2 took place Southwest of

the other events in the swarm, and presumably updip from them, in a geometry typical of other ATEs (Fukao, 1979; Okal & Borrero, 2011)

The only “snappy” event in this sector, in 1992 ($\Theta = -4.54$), is an outer rise shock which, despite a thrust mechanism, does not represent interplate motion. We exclude it from the right frame of Fig. 4.14.

- (4) South of the d’EFZR collision, at the latitude of Efate (“E”), the coupling loosens, the morphological expression of the trench reappears, and Θ values return to a more traditional distribution featuring a gradient across the trench, from snappy or standard downdip to trending towards slowness updip. The lone slow event ($\Theta = -5.90$) in 1981 might have qualified as a tsunami earthquake, but for its mediocre size, too small to generate a significant wave in the first place.
- (5) Finally in Southern Vanutu (“SV”) and despite the presence of a reasonably well defined trench reaching 7000 m, Θ features a standard gradient across the subduction system, but offset towards “snappier” values. This suggests increased coupling, which may reflect the incipient collision of the Loyalty Islands group.

Our results correlate remarkably well with Wyss et al.’s (1983), who mapped on their Figure 10 stress drops inferred from $m_b:M_s$ discrepancies, based on an algorithm by Archambeau (1978). We note in particular the transition from low stress drops in SC to higher ones in TI (labeled ERIR on their Figure 10), back

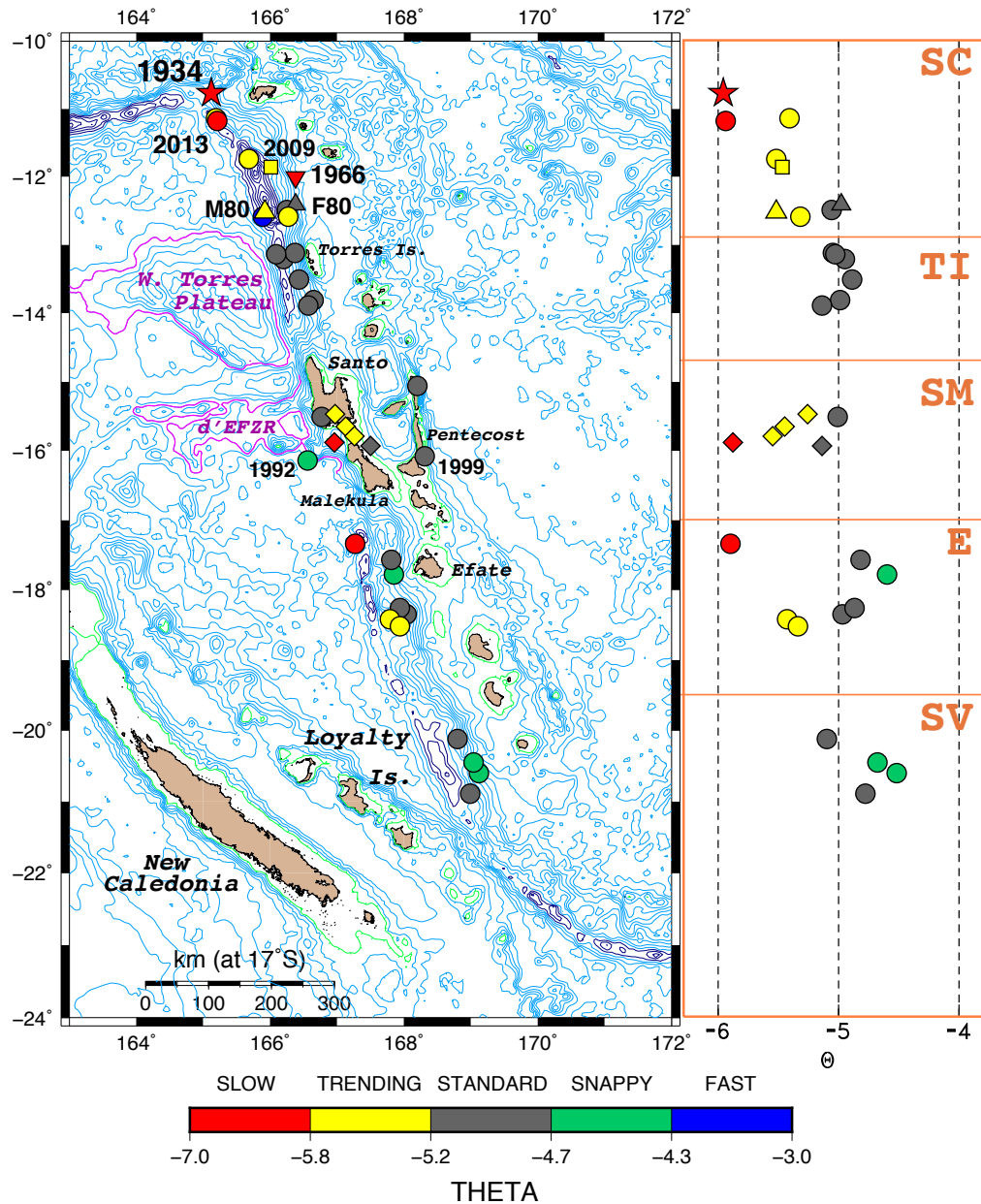


Figure 4.14. Distribution of parameters Θ for shallow thrust faulting events in Northern Vanuatu and Santa Cruz Islands, color-coded according to the palet bar. Left: Map view, with the star as the 1934 tsunami earthquake, the square the reference 2009 event, the triangles the 1980 doublet, the diamonds the 1965 swarm, and the inverted triangle the deeper intraslab 1966 event. The West Torres Plateau and the d'Entrecasteaux Fracture Zone and Ridge system are outlined in magenta at the 3500-m isobath. Right: value of Θ plotted as a function of latitude, with the five regional segments outlined in brown. Non-interplate-thrust events have been excluded. See text for details.

Table 4.3. Parameters Θ computed in this study: Santa Cruz and Vanuatu.

Date	Origin Time	Epicenter		Depth	Moment	Θ	Remarks
D M (J) Y	(GMT)	(N°)	(E°)	(km)	(10^{27} dyn cm)		
07 OCT (280) 2009	22:18:51.2	-11.86	166.01	42	6.7	-5.47	Reference Event
21 JUL (202) 1934	06:18:20.4	-10.77	165.12	10	10	-6.10	Tsunami Earthquake
06 FEB (037) 2013	01:12:25.8	-10.80	165.11	20	9.4	-5.94	Tsunami Earthquake
<i>1965 Series (Ebel, 1980)</i>							
11 AUG (223) 1965	03:40:55.5	-15.47	166.91	23	0.74	-5.26	FS-1
11 AUG (223) 1965	19:52:29.2	-15.64	167.00	20	0.32	-5.45	FS-2
11 AUG (223) 1965	22:31:49.1	-15.75	167.12	28	3.0	-5.55	MS
12 AUG (224) 1965	08:01:44.0	-15.86	167.36	28	0.24	-5.14	A-1
13 AUG (225) 1965	12:40:08.2	-15.88	166.83	30	2.0	-5.88	A-2; Tsunami Earthquake
<i>Background Events</i>							
08 JUL (190) 1980	23:19:19.8	-12.92	166.21	44	2.0	-4.92	
17 JUL (190) 1980	9:42:23.2	-12.44	165.94	34	4.8	-5.52	
24 APR (114) 1981	21:50:06.0	-13.51	166.43	44	0.23	-4.89	
15 JUL (196) 1981	07:59:08.5	-17.34	167.27	30	0.58	-5.90	
21 DEC (355) 1985	01:13:21.0	-13.89	166.57	46	0.57	-5.14	
03 JAN (003) 1987	22:04:07.5	-15.06	168.20	17	0.12	-4.90	
28 SEP (271) 1987	11:47:08.6	-18.42	167.79	23	0.19	-5.43	
05 MAR (064) 1990	16:38:15.0	-18.35	168.04	37	0.33	-4.97	
13 FEB (044) 1992	01:29:15.5	-16.14	166.36	15	0.18	-4.54	
12 FEB (043) 1994	17:58:25.0	-20.45	169.04	43	0.33	-4.68	
21 APR (111) 1997	12:02:26.4	-13.21	166.20	51	4.4	-4.91	
26 NOV (330) 1999	13:21:15.5	-16.42	168.21	20	1.67	-4.88	
29 DEC (363) 1999	13:29:19.6	-11.14	165.19	15	0.23	-5.41	
04 OCT (278) 2000	16:58:44.3	-15.51	166.77	15	0.30	-5.01	
02 JAN (002) 2002	17:22:48.8	-17.78	167.85	40	0.77	-4.60	
17 JUN (168) 2002	21:26:22.9	-12.49	166.25	44	0.14	-5.06	
25 MAR (084) 2007	00:40:01.6	-20.60	169.12	41	0.62	-4.52	
25 MAR (084) 2007	01:08:19.0	-20.89	168.99	31	0.27	-4.78	
02 SEP (245) 2007	01:05:18.1	-11.74	165.68	18	0.9	-5.52	
09 APR (100) 2008	12:46:12.7	-20.12	168.80	35	1.1	-5.10	
07 OCT (280) 2009	22:03:14.5	-12.59	166.27	44	3.3	-5.32	
07 OCT (280) 2009	22:50:15.8	-12.59	165.89	18	0.2	-4.01	
07 OCT (280) 2009	23:13:48.2	-13.12	166.37	43	1.6	-5.05	
08 OCT (281) 2009	08:28:48.0	-13.14	166.09	14	0.16	-5.03	
27 MAY (147) 2010	17:14:46.6	-13.81	166.05	43	0.69	-4.99	
10 AUG (222) 2010	05:23:45.0	-17.57	167.81	32	1.0	-4.82	
20 AUG (232) 2011	16:55:02.8	-18.52	167.94	34	0.63	-5.34	
20 AUG (232) 2011	18:19:23.5	-18.26	167.94	36	0.46	-4.87	
31 DEC (365) 1966	18:23:09.5	-12.01	166.38	78	4	-5.83	Intraslab, deeper, event

to relatively low values around Efate, and to higher ones in SV. Regarding the SM segment, we note that Wyss et al.'s (1983) individual stress drop values (labeled "1")

to “4” on their Figure 10) remain significantly lower than in TI (which features several values of “6”), with the exception of both a presumably intraplate event in the general area of our 1992 “snappy” solution, and a number of back-arc earthquakes in the vicinity of the 1999 Pentecost event, all of which are not representative of the subduction interface. By contrast, several high stress drop shocks (with a label of “6”) are present in the “SV” segment, where we have identified higher values of Θ .

The case of the earthquake of 31 December 1966 (inverted triangle on Fig. 4.14) is more intriguing. This event, which occurred as the mainshock of a complex swarm lasting several days, was given magnitudes $m_b = 5.5$ and $M_{PAS} = 7.5$, suggesting significant source slowness; however, its tsunami was only marginally reported with a maximum run-up of 2 m on Vanikolo (and no known casualties). Johnson & Molnar (1972) published a thrusting focal mechanism ($\phi = 251^\circ; \delta = 50^\circ; \lambda = 110^\circ$), but with a P axis in the azimuth N327°E, that is parallel to the trench. Marthelot (1983) later rotated the mechanism to a geometry marginally consistent with first motion data, but in agreement with interplate thrust motion ($\phi = 337^\circ; \delta = 47^\circ; \lambda = 95^\circ$); on that basis, several authors have interpreted the 1966 event as a genuine interplate thrust earthquake, contributing to the plate motion budget (e.g. Tajima et al. 1990; Lay et al. 2013). A significant issue with this model is the depth of the source, which was originally given as 56 km by the USGS, and 73 km by the ISC. The modern Centennial Catalog relocation puts it at 83 km (Engdahl & Villaseñor, 2002), but the ISC-GEM one uses a constrained depth of 55 km (Storchak et al.,

2013); our own relocation places it at 78 km, with Monte Carlo hypocentral depths (obtained with $\sigma_G = 1$ s in the 1960s) ranging from 67 to 95 km; as shown on (Fig. 4.15a), this locates the source inside the subducting slab, rather than at the plate interface; note that this hypocenter is consistent with the mediocre reported tsunami amplitude, and moots the argument against Johnson & Molnar's (1972) mechanism. The analysis of the strong mantle waves at Pasadena yields a moment of 4×10^{27} dyn cm in Johnson & Molnar's (1972) geometry. In general, P waves at most short-period WWSSN stations are off-scale, but we were able to process the record at Wellington (WEL), written at a particularly low gain of only 6250, and records in North America at distances greater than 80° (Albuquerque, Golden (WWSSN) and Yellowknife (Canadian Network)), and on the Benioff broadband 1–90 record at PAS, spectacularly devoid of high frequencies (Fig. 4.15b). With appropriate corrections for the short distance at WEL (Ebeling & Okal, 2012) and the large ones in North America ($Corr_g$ or $Corr_{SC}$; see above), we obtain $\Theta = -5.83 \pm 0.11$, which supports the large difference in m_b and M_{PAS} values and casts the 1966 event as a rather unique example of intra-slab earthquake, at the limit between classically defined shallow and intermediate events, featuring a significantly deficient Θ (see Chapter 5).

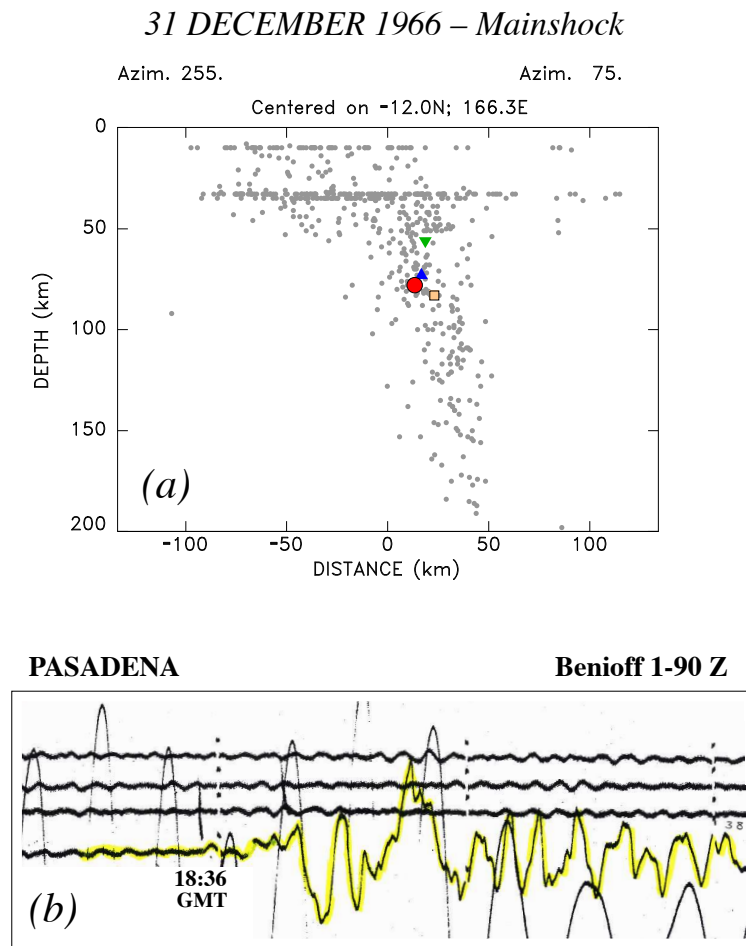


Figure 4.15. (a): Cross-section of the seismicity of the Vanuatu Wadati-Benioff Zone in the azimuth N75°E (brown line on Fig. 4.7). The small gray symbols are unrelocated NEIC hypocenters, the red symbol is our relocation of the large event of 31 December 1966 (18:23 GMT), the blue triangle the ISC location, the green inverted triangle the NEIC one, and the brown square Engdahl & Villaseñor's (2002). (b): Close-up of the *P* wavetrain recorded on the broadband vertical “Benioff 1-90” instrument at Pasadena. The total length of the record is 175 s. Note the virtual absence of high-frequency energy, as compared for example with a similar record for the 1939 Chillán Chile earthquake (Okal & Kirby 2002, Fig.4).

4.6. Conclusion

We have derived a procedure for the extension to distances $\Delta > 80^\circ$ of the slowness parameter Θ defined by Newman & Okal (1998). This allows the quantification of energy-to-moment ratios when appropriate stations are unavailable in the standard distance range, a situation characteristic of the pre-digital era of seismic recording, when short-period stations were either scarce (as in the case of the 1947 and 1934 events), or analog instrumentation resulted in off-scale recording of P waves at conventional distances during large earthquakes (a situation typical of the WWSSN during the years 1963–80).

Because of the influence of lateral heterogeneity in D'' at the high frequencies involved in the computation of estimated energy, we cannot derive a universal correction to the Θ algorithm, but rather must proceed with regionally adapted corrections. Nevertheless, we were able to successfully process three major historical earthquakes. In the Hikurangi province of New Zealand, we confirm the slow character of the two 1947 tsunami earthquakes. Their quantification through the parameter Θ casts Events I and II as comparable to tsunami earthquakes in Java or Northern Peru, and Central America, respectively, with the major difference that no significant background interplate thrust seismicity is known in the region.

In the Santa Cruz Island region, we quantify the event of 21 July 1934 as a tsunami earthquake occurring as an aftershock of a major event, in the immediate vicinity of the recent 2013 primary tsunami earthquake, casting the Santa Cruz corner as a region structurally prone to slow strain release during major events, in either

context. Our comprehensive study of source slowness for more recent events along the Santa Cruz–Vanuatu subduction system identifies a wide diversity in parameters Θ , which correlates with variations in tectonic regime in the context of the collision of fossil features borne by the subducting Australian plate. Of particular interest is the identification of Aftershock A–2 in the 1965 Santo Island series as a tsunami earthquake. This illustrates an additional benefit of the extension of the Θ algorithm beyond 80° , which allows the processing of P -wave data when records at standard distances are systematically off-scale on analog records constituting the only available database during the WWSSN era. It would be anticipated that many more such records could thus be processed in the future for the quantification of crucially important earthquake sources during that time window (1962–1978). This constitutes one more argument (if need be) for the permanent preservation of the relevant archives, and their eventual transfer to digital support Okal (2015).

CHAPTER 5

Extension of the Energy-to-Moment Parameter Θ to Intermediate and Deep Earthquakes

5.1. Introduction: The Slowness Parameter Θ

This chapter, published as Saloor & Okal (2018), extends to intermediate and deep earthquakes the calculation of the parameter Θ introduced by Newman & Okal (1998) to characterize the source slowness of shallow earthquakes, allowing in particular the identification of anomalously slow events. In the context of operational tsunami warning (Weinstein & Okal, 2005), Newman & Okal (1998) were motivated by the need to detect, with a robust and fast algorithm, any possible slowness in the earthquake source with the consequent potential for enhanced tsunami excitation. Using the general framework of Boatwright & Choy's (1986) methodology, this was achieved by comparing quantitative estimates of the earthquake source at low frequencies (seismic moment M_0) and high frequencies (radiated energy E^E), through the parameter

$$\Theta = \log_{10} \frac{E^E}{M_0} \quad (5.1)$$

This formalism differs from Boatwright & Choy’s (1986) in that the estimated energy E^E is computed using an average value of depth and focal mechanism, reflecting the fact that these parameters may not be known exactly under real-time operational conditions. In this respect, the evaluation of Θ shares the general philosophy of a *magnitude* estimate.

In the present study, we extend Newman & Okal’s (1998) methodology to intermediate and deep earthquakes (hereafter “*I*”, $80 \leq h < 300$ km; and “*D*”, $h \geq 300$ km, respectively). We are motivated by the documentation, for shallow earthquakes, of a significant diversity in parameters Θ . While seismic scaling laws (Geller, 1976) would predict an invariant value of $\Theta = -4.90$, Fig. 5.1 documents a subset of shallow events with significant populations featuring deficient values ($\Theta < -5.8$), which correspond to slow earthquakes whose spectra are red-shifted towards low frequencies. They include all so-called “*tsunami earthquakes*” whose tsunamis are significantly larger than predicted by their seismic magnitudes, especially conventional ones (Kanamori, 1972), generally as a result of low rupture velocities (Tanioka et al., 1997; Polet & Kanamori, 2000). On the other hand, Fig. 5.1 also shows a number of events with enhanced values, indicating a spectrum blue-shifted towards high frequencies, usually under the influence of a short source duration. We refer to such earthquakes as “snappy” events, which can feature higher ground accelerations and therefore exceptional levels of destruction, as exemplified by intraplate shocks such as the 2011 event in Christchurch ($\Theta = -4.19$) and the large 1939 Chillán, Chile earthquake (Okal & Kirby, 2002; $\Theta = -4.04$).

Such variations in energy-to-moment ratio for shallow earthquakes, which reflect diversity in tectonic environments, have been described, notably by Choy & Boatwright (1995) and Choy et al. (2006). They can extend over 3 logarithmic units and cast Θ as a “slowness parameter”, a name first introduced by Weinstein & Okal (2005). By extending the computation of Θ to intermediate and deep earthquakes, we seek to explore any potentially similar diversity; we conclude that these deeper sources have much more homogeneous properties in this respect.

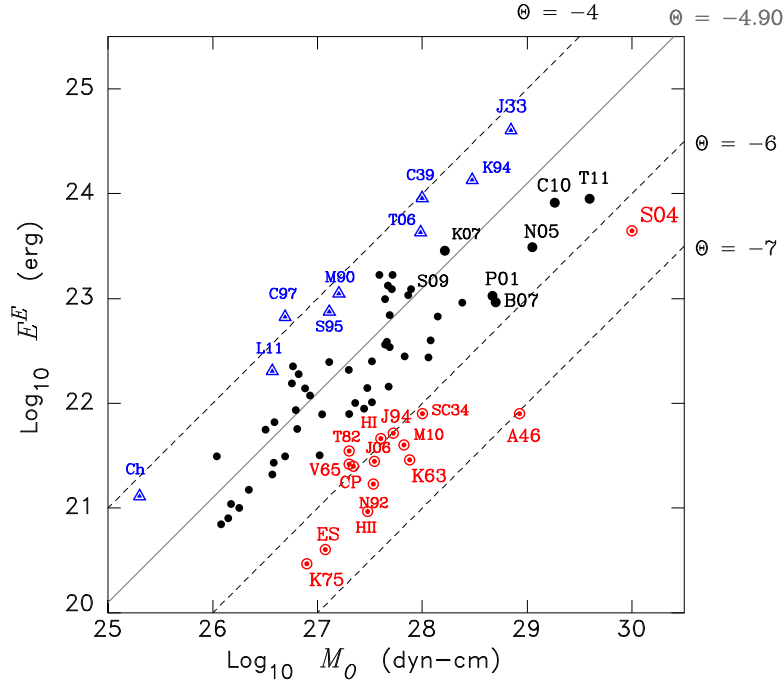


Figure 5.1. Plot of the estimated energy, E^E vs. seismic moment M_0 for shallow events, updated from the original work of Newman & Okal (1998). Previously studied tsunami earthquakes ($\Theta < -5.8$) are shown as red bulls eye symbols (SC34, Santa Cruz, 1934; A46, Aleutian 1946; HI and HII, Hikurangi, 1947; K63, Kuril 1963; V65, Vanuatu 1965; K75, Kuril 1975; T82, Tonga 1982; N92, Nicaragua 1992; J94, Java 1994; CP, Chimbote, Peru 1996; S04, Sumatra, 2004; J06, Java 2006; M10, Mentawai 2010; ES, El Salvador, 2012). The blue triangles ($\Theta > -4.3$) identify “snappy” earthquakes (J33, Sanriku, 1933; C39, Chillán 1939; M90, Marianas 1990; K94, Kuril 1994; S95, Samoa 1995; C97, Chile 1997; T06, Tonga 2006; Ch, Christchurch 2011; L11, Loyalty Is. 2011), and the black dots a selection of regular events (P01, Peru 2001; N05, Nias 2005; B07, Bengkulu 2007; K07, Kuril 2007; S09, Samoa 2009; C10 Chile 2010; and T11, Tohoku 2011).

5.2. Methodology

While the general approach to the computation of energy flux and hence of E^E and Θ is unchanged for deeper sources, significant changes will be required in the details of the algorithm, which carried implicit assumptions on the seismic rays and structural parameters involved. In order to identify those changes, we examine in

detail the various steps in Newman & Okal's (1998) algorithm for the computation of E^E for shallow events, itself derived from Boatwright & Choy (1986).

- a.** First, an energy flux ε is calculated at a teleseismic station as twice the integral over time of the density of kinetic energy, multiplied by the local P -wave velocity α (Wu, 1966):

$$\varepsilon = \rho \alpha \int_0^{\infty} \dot{u}^2(t) dt \quad (5.2)$$

where u is the vertical ground motion (assumed deconvolved from instrument response), and ρ the local crustal density. In practice, this time-domain integral is limited to the duration of the P wavetrain, t_{max} . In the case of shallow events, the so-called generalized P wave includes the source-reflected pP and sP which cannot be separated from direct P . As discussed more in detail below, t_{max} will have to be modified in the case of I or D sources.

- b.** Next, using Parseval's theorem, 5.2 is transformed to the frequency domain

$$\varepsilon^* = \frac{\rho\alpha}{\pi} \int_0^{\infty} |\omega \cdot u(\omega)|^2 \exp [\omega t^*(\omega)] d\omega \quad (5.3)$$

In practice, the integral is computed between the finite bounds $\omega_{min} = 2\pi/10$ and $\omega_{max} = 2\pi/0.5$ rad/s. We include in (5.3) a correction for anelastic attenuation along the ray path, expressed through the parameter

$$t^* = \int_{path} \frac{Q^{-1}}{v(r)} ds \quad (5.4)$$

where Q^{-1} is intrinsic attenuation, and $v(r)$ the local seismic velocity along the path. For shallow sources, it has long been assumed (Carpenter, 1965) that t^* can be taken as independent of distance, and approximately equal to 1 s for P waves (and 4 s for S waves). This reflects the fact that the principal contribution to the integral (5.4) comes from the asthenosphere, where attenuation is significantly higher than in the upper and lower layers of the mantle (Anderson & Hart, 1978). For shallow events, there are two such transits, source-side and receiver-side, largely independent of distance, leading to constant t^* . However, $t^*=1$ s has later been found to overestimate attenuation (Anderson & Given, 1982; Choy & Cormier, 1986), which motivated Choy & Boatwright (1995) and Newman & Okal (1998) to use the frequency-dependent expression (t^* in s and f in Hz):

$$\begin{aligned} t^* &= 0.9 - 0.1 \log_{10} f \quad (f \leq 0.1 \text{ Hz}) \\ t^* &= 0.5 - 0.5 \log_{10} f \quad (0.1 \leq f \leq 1 \text{ Hz}) \\ t^* &= 0.5 - 0.1 \log_{10} f \quad (f \geq 1 \text{ Hz}), \end{aligned} \quad (5.5)$$

based on the work of Choy & Cormier (1986) and Choy & Dewey (1988).

By contrast, for intermediate and deep sources, direct P may undergo only one such transit while the situation with reflected phases is much more

complex, since their upswing parts may or may not benefit from a low attenuation path by riding up the slab. Detailed values of t^* used in this study will be discussed in Section 5.3.

- c. Next, the energy flux ε^* is scaled back to a focal sphere of unit radius, using the concept of geometrical spreading

$$\varepsilon_{FS}^* = (R^P)^2 \varepsilon^* \quad (5.6)$$

where $R^P = \frac{a}{g(\Delta)}$, a is the Earth's radius and the geometrical spreading coefficient $g(\Delta)$ is obtained from the travel time $T(\Delta, h)$ of P waves as:

$$g(\Delta) = \sqrt{\left| \frac{\rho_h \alpha_h \tan i_h v_h}{\rho_0 \alpha_0 \cos i_0 r_h} \frac{d^2 T}{d\Delta^2} \right|} \quad (5.7)$$

adapted, e.g., from Okal (1992).

In Newman & Okal's (1998) algorithm, this is calculated directly from a tabulated version of the Jeffreys-Bullen tables. It can be adapted seamlessly to the case of intermediate and deep sources.

- d. Finally, a focal mechanism correction is effected, in order to restore the full energy radiated by the double-couple into P waves, rather than measured from the generalized P wave (gP) in a single direction.

The energy radiated by a double-couple, integrated over the whole focal sphere, amounts to an average radiation coefficient of P waves $\langle (F^P)^2 \rangle =$

$\frac{4}{15}$. As discussed by Boatwright & Choy (1986), the energy in gP can be described through a generalized radiation coefficient expressing the sum of the energy carried by the three rays, P , pP and sP :

$$(F^{gP})^2 = (F^P)^2 + (\dot{P}\dot{P} \cdot F^{pP})^2 + \frac{2\alpha}{3\beta} q (\dot{S}\dot{P}^{BC} \cdot F^{sP})^2 \quad (5.8)$$

where all terms are detailed in Newman & Okal (1998). The final energy radiated into P waves is then obtained as:

$$E^P = 4\pi \frac{\langle (F^P)^2 \rangle}{(F^{gP})^2} \varepsilon_{FS}^* \quad (5.9)$$

In the context of the calculation of estimated energy E^E , which ignores the exact depth and focal mechanism, Newman & Okal (1998) replaced $(F^{gP})^2$ with its average over focal geometries, regressed with distance Δ (in degrees) as:

$$(F^{Est.})^2(\Delta) = 1.171 - 7.271 \times 10^{-3}\Delta + 6.0009 \times 10^{-3}\Delta^2 \quad (5.10)$$

Replacing (5.8) with (5.10) and adding the contribution of S -wave radiation at the source, the estimated energy E^E is then defined as:

$$E^E = \frac{1+q}{4\pi} \frac{\langle (F^P)^2 \rangle}{(F^{Est.})^2} \cdot \varepsilon_{FS}^* \quad (5.11)$$

where $q = 15.6 = 3^{5/2}$ expresses the partitioning of energy at the source between P and S waves in a Poisson medium (Boatwright & Fletcher, 1984). Then Θ is obtained from (5.1) by using a published value of M_0 (or an estimated one in real time). A final Θ is retained by averaging values obtained at many stations, this procedure serving to correct for the use of the estimated radiation coefficient (5.10) rather than the exact one (5.8) at each station.

In summary, in order to compute E^E and Θ for non-shallow earthquakes, steps **a.** (t_{max}), **b.** (t^*) and **d.** (F^{gP}) will have to be adapted to the particular depth range involved. These adjustments to the algorithm of Newman & Okal (1998) are now discussed in full detail.

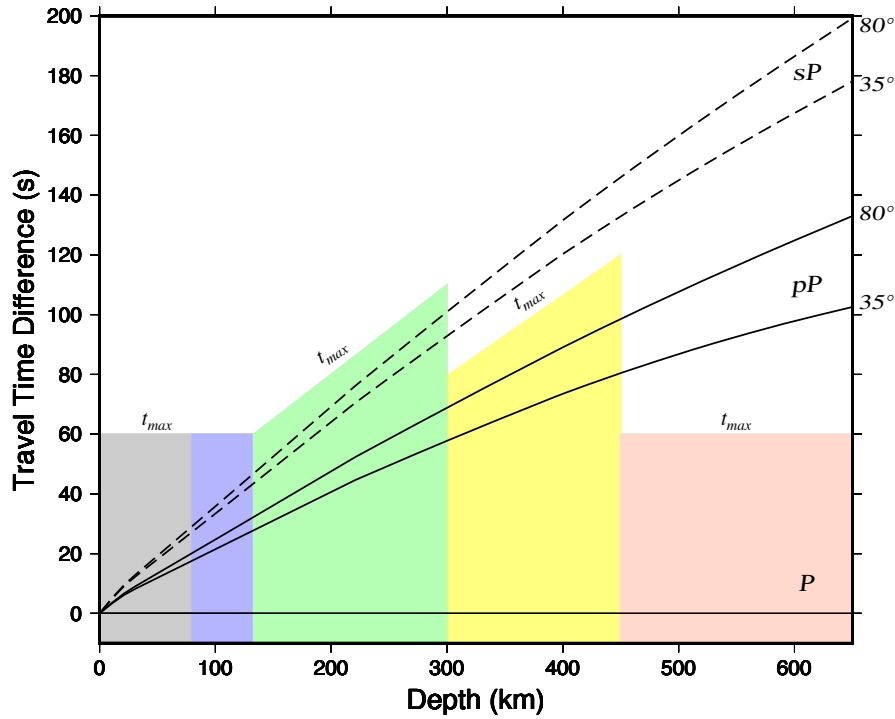


Figure 5.2. Travel-time delays of reflected pP (solid) and sP (dashed) with respect to direct P as a function of source depth, for $35^\circ < \Delta < 80^\circ$. The shaded blocks illustrate the lengths of the time series used to compute Θ in the various depth ranges. See text for details.

5.2.1. Selection of t_{max}

Figure 5.2 plots the travel time differential of the reflected phases pP and sP with respect to direct P as a function of source depth. The grey block at left symbolizes the window used by Newman & Okal (1998) for shallow events (0-80 km), starting 10 s before P and extending for $t_{max} = 70$ s (larger events are given a longer window). In this context, we split intermediate and deep earthquakes into four categories, according to depth:

* **Depth Bin I–1: $80 < h < 135$ km (light blue band in Fig. 5.2)**

In this depth range, the reflected phases pP and sP stay within the 70-s time window used for shallow earthquakes, which thus remains adequate for the computation of the energy flux.

* **Depth Bin I–2: $135 < h < 300$ km (green band in Fig. 5.2)**

The reflected phases now extend beyond 60 s following first arrival, but are not adequately separated from direct P , mandating the use of a depth-dependent t_{max} :

$$t_{max} = 70 + 0.3 \times (h - 135) \quad (5.12)$$

(t_{max} in s and h in km).

* **Depth Bin D–1: $300 < h < 450$ km (yellow band in Fig. 5.2)**

In this depth range, the shear-reflected phase sP becomes adequately separated from pP and the computation can proceed using only direct P and pP , with:

$$t_{max} = 90 + \frac{(h - 300)}{5} \quad (5.13)$$

(t_{max} in s and h in km).

* **Depth Bin D–2: $450 < h < 700$ km (pink band in Fig. 5.2)**

Both reflected phases are now well separated from direct P with pP arriving more than 80 s after the first arrival. The computation can proceed on direct P only, reverting to $t_{max} = 70$ s.

In this context, we wish to stress, as initially pointed out in Newman & Okal (1998), that the Θ algorithm proceeds in the general scope of a *magnitude* computation, which in particular ignores such details as focal mechanism and exact depth (through the simple use of four depth classes). More sophisticated algorithms have been implemented, such as Choy & Boatwright's (1995), these authors using a time window (t_{max}) customized to each seismogram, depending on the fall-off of Direct P with time (Choy & Dewey, 1988). This difference in methodology may lead to disparities in energy values, for example under the scenario of a complex, jagged rupture, with a series of delayed small events.

5.2.2. Selection of t^*

While a constant value of $t^* = 1$ s constitutes a simple but robust approximation to the effect of attenuation on teleseismic P waves from shallow sources, it is clear that it cannot be applied at all depths. We note that for deep sources around 600 km and the phase Direct P , Choy & Cormier (1986) have proposed a model (their Figure 8) which can be approximated by applying to (5.5) a multiplicative factor of 0.55, as originally proposed by Burdick & Helmberger (1974). This comes close to halving the shallow estimate of t^* , a sensible proposition since rays from such sources undergo only one transit through the upper mantle, rather than two for shallow sources. In other depth bins, the situation is much more complex since t^* will be path-dependent, as direct P and *a fortiori* the reflected phases pP and sP to individual stations may travel through a high- Q slab segment, or through strongly

attenuating structures in the mantle wedge and back arc (e.g., Roth et al., 1999) for which appropriate three-dimensional models may not be available in all tectonic regions.

In this context, we take the empirical approach of using, in various depth ranges, a t^* model which simply applies a multiplicative factor varying with depth to a slightly modified version of Eq. 5.5:

$$\begin{aligned}
 t^* &= \gamma(h) \left[0.9 - 0.1 \log_{10} f \right] \quad (f \leq 0.1 \text{ Hz}) \\
 t^* &= \gamma(h) \left[0.4 - 0.6 \log_{10} f \right] \quad (0.1 \leq f \leq 1 \text{ Hz}) \\
 t^* &= \gamma(h) \left[0.4 - 0.1 \log_{10} f \right] \quad (f \geq 1 \text{ Hz}),
 \end{aligned} \tag{5.14}$$

with $\gamma = 0.55$ in Depth Bin D-2, $\gamma = 0.6$ in D-1, $\gamma = 0.75$ between 200 and 300 km, and $\gamma = 0.80$ between 80 and 200 km. This admittedly *ad hoc* model of t^* provides compatibility with Choy & Cormier's (1986) model for deep (D-2) events; in addition, we have verified that it leads to an average $t^* = 0.27$ s used in the integral (5.3) for D-2 events, in agreement with the value of $t^* \approx 0.3$ s proposed in a number of recent investigations (e.g., Ye et al., 2013; Poli & Prieto, 2016). Finally, we note that the use of a large number of stations diversely sampling the hypocentral area should empirically guard against the influence of a regionally inadequate attenuation correction along an individual path.

5.2.3. Selection of $\langle (F^{gP})^2 \rangle$

As in the case of shallow earthquakes (Newman & Okal, 1998), the value of the estimated generalized radiation coefficient, $\langle (F^{gP})^2 \rangle$, is obtained by regressing with distance the expression (5.8), computed for a large number of combinations of actual sources, drawn from the GlobalCMT catalog (Dziewonski et al., 1981; Ekström et al., 2012), and stations of the Global Seismographic Network. For intermediate depth earthquakes (I-1 and I-2), we replace (5.10) with

$$(F^{Est.})^2(\Delta) = 0.8450 + 3.701 \times 10^{-3}\Delta - 4.335 \times 10^{-5}\Delta^2 \quad (5.15)$$

(Δ in degrees).

In the D-1 depth range (300-450 km), where we do not include the shear reflected sP , (5.8) is replaced with

$$(F^{gP})^2 = (F^P)^2 + (\dot{P}\dot{P}.F^{pP})^2 \quad (5.16)$$

which regresses as:

$$(F^{Est.})^2(\Delta) = 0.2353 + 4.109 \times 10^{-3}\Delta - 8.453 \times 10^{-6}\Delta^2 \quad (5.17)$$

(Δ in degrees).

Finally, for the D-2 depth range (450-700 km) where we process only direct P , we

use $(F^{Est.})^2 = \frac{4}{15}$ as the estimate of the average radiation coefficient.

The radiated energy computed using the above algorithm, and its ratio to seismic moment, can be interpreted under the simple model of a trapezoidal source time function and homogeneous slip on a simple fault plane (Vassiliou & Kanamori, 1982). Under this model, Newman & Okal (1998) showed (their Equation 14) that the ratio E^E/M_0 was controlled by the strain released (itself the ratio of seismic slip to fault width) and the velocity of rupture V_R along the fault, with a minor dependence on the ratio of rise time to rupture time (or source duration). In turn, E^E/M_0 will be proportional to stress drop $\Delta\sigma$ and to apparent stress under Orowan's (1960) conditions. This simple interpretation is generally upheld in the case of shallow earthquakes for which events with deficient Θ , such as tsunami earthquakes, have been documented to feature slow rupture velocities (e.g., Polet & Kanamori, 2000; López & Okal, 2006), and those with enhanced Θ , anomalously large displacements, and hence strains (e.g., Beavan et al., 2011). By contrast, in the case of a jagged rupture featuring a series of asperities rupturing in a delayed pattern, the energy-to-moment ratio may keep a regular value, while the rupture velocity averaged over the whole source process would appear deficient.

5.3. Data Selection

Our data selection followed the criteria of Newman & Okal (1998): In each of the four depth bins, we considered all earthquakes with moments $M_0 > 10^{25}$ dyn*cm ($M_w > 5.9$; to ensure adequate signal-to-noise ratio), occurring during the years 1990 – 2016 (to secure a sufficient dataset of digital stations), with seismic moments

obtained from the GlobalCMT catalog (Dziewonski et al., 1981; Ekström et al., 2012). We used records from broadband channels of the Global Seismographic Network, sampled at 20 Hz, with epicentral distances $35^\circ < \Delta < 80^\circ$, thus avoiding complexities due to triplication in the mantle, and interaction with D'' , respectively. While it is in principle possible to adapt the computation of Θ to shorter distances (Ebeling & Okal, 2012), or greater ones (see Chapter 4), this was not deemed necessary here, on account of a sufficiently large number of stations. In this respect, we imposed a minimum of 10 stations per event; the retained dataset then featured an average of 27 stations per event. The insignificant effect, on all our results, of using a different minimum number of stations is discussed in detail in Section 5.4. In addition, we restricted ourselves to permanent stations of the Global Seismographic Network (mainly the networks IU, II and G, occasionally GE, of the Federation of Seismic Networks), excluding systematically such datasets as the United States Transportable Array. In this fashion, we seek to achieve a balanced distribution of stations on the focal sphere, and to guard against the systematic bias that could be introduced, for example when a massive number of stations would be located close to a node of radiation pattern, as was described in the parallel case of mantle magnitudes by Weinstein & Okal (2005).

Our final dataset includes 160 I–1 events (80-135 km), 216 I–2 events (135 -300 km), 51 D–1 events (300 - 450 km) and 171 D–2 events (450 - 700 km), for a grand total of 598 non-shallow earthquakes. These numbers reflect the general distribution of seismicity with depth (e.g., Frohlich, 2006, Chapter 4). The full dataset is listed

in Table A-1, including an additional 93 events with fewer than 10 stations, which were discarded from the final dataset. For reference, we also include in our analysis a dataset of 146 shallow earthquakes from the digital era, similarly listed in Table A-2.

5.4. Results and Discussion

Results for the various depth classes are presented in Fig. 5.3 to 5.6, with Table 5.1 listing all relevant statistical parameters, including for the reference dataset of 146 shallow earthquakes. Fig. 5.7 regroups the values of Θ as a function of depth for the whole dataset. While a large amount of literature exists on the subject, initially suggesting that intermediate and deep earthquakes feature higher stress drops and apparent stresses than shallow ones (e.g., Wyss & Molnar, 1972; Fukao & Kikuchi, 1987; Choy et al., 2006), there is no modern quantitative consensus on such variations (e.g., Frohlich, 2006), with a number of recent studies suggesting comparable apparent stresses at all depths (e.g., Vallée, 2013; Poli & Prieto, 2016). In this context, our homogeneous dataset of 744 Θ values brings additional insight into the behavior of energy-to-moment ratios with depth.

5.4.1. General Results

The main result from this study is that the full dataset of intermediate and deep events features Θ values generally higher than their shallow counterparts, with the difference in their averages, -4.69 and -5.10, amounting to 0.41 logarithmic units or

in rough numbers a factor of 2.5 in the strain release $\frac{E^E}{M_0}$ and, taking into account the increase in elastic constants with depth, a factor of five in apparent stress τ_a . Note that the average Θ for the whole I-D dataset, -4.69 , is in excellent agreement with Vassiliou & Kanamori (1982) values ($\langle \Theta \rangle = -4.65 \pm 0.51$; their Table 2), even though their measurements used a different algorithm, as they estimated the total duration of the source, rather than integrate the recorded seismograms.

In addition, the Θ dataset for I-D sources is relatively homogeneous, with a standard deviation of 0.29 units, significantly smaller than the difference quoted above between shallow and I-D datasets, and than the standard deviation for shallow earthquakes (0.55). This does not preclude the existence of heterogeneity deep inside the slabs, but on a smaller scale than for shallow earthquakes: with the exception of one outlier at the upper limit of the Solomon Islands subduction system (see below), the Θ dataset for I-D sources covers a range of 1.95 logarithmic units, as compared to 3.10 for shallow events.

I-1. 80–135 km 160 EVENTS

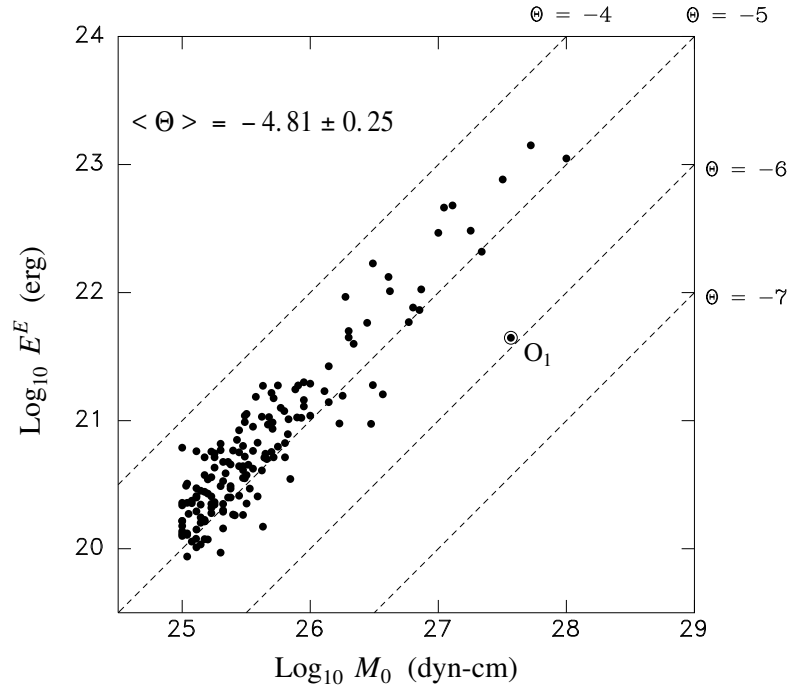


Figure 5.3. Plot of estimated energy E^E vs. seismic moment M_0 , at depths between 80 and 135 km. Lines of constant Θ are shown as dashed lines. O_1 represents the slow outlier in the Solomon Islands subduction system.

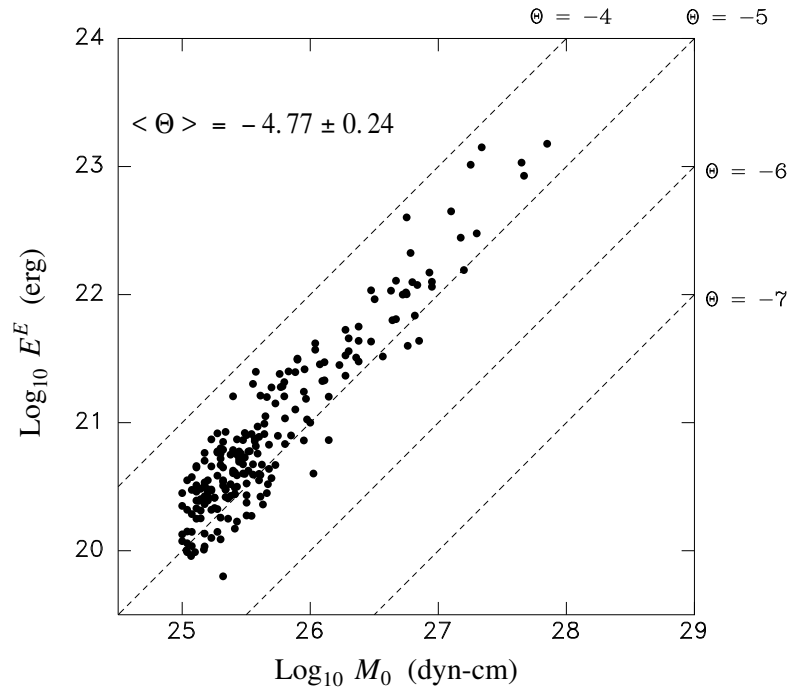
I-2. 135–300 km 215 EVENTS

Figure 5.4. Same as Fig 5.3 for the I-2 dataset (135 to 300 km)

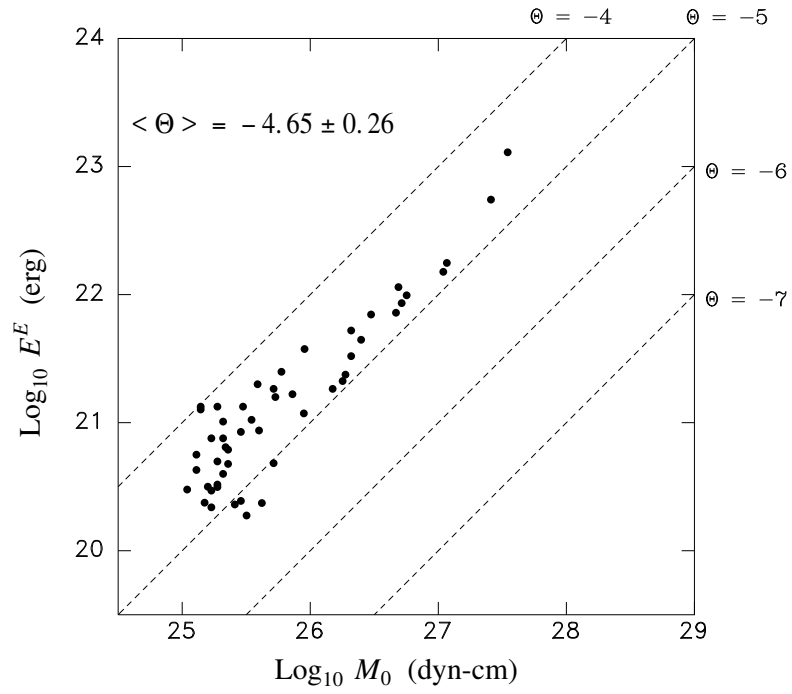
D-1. 300–450 km 51 EVENTS

Figure 5.5. Same as Fig. 5.3 for the D-1 dataset (300 to 450 km)

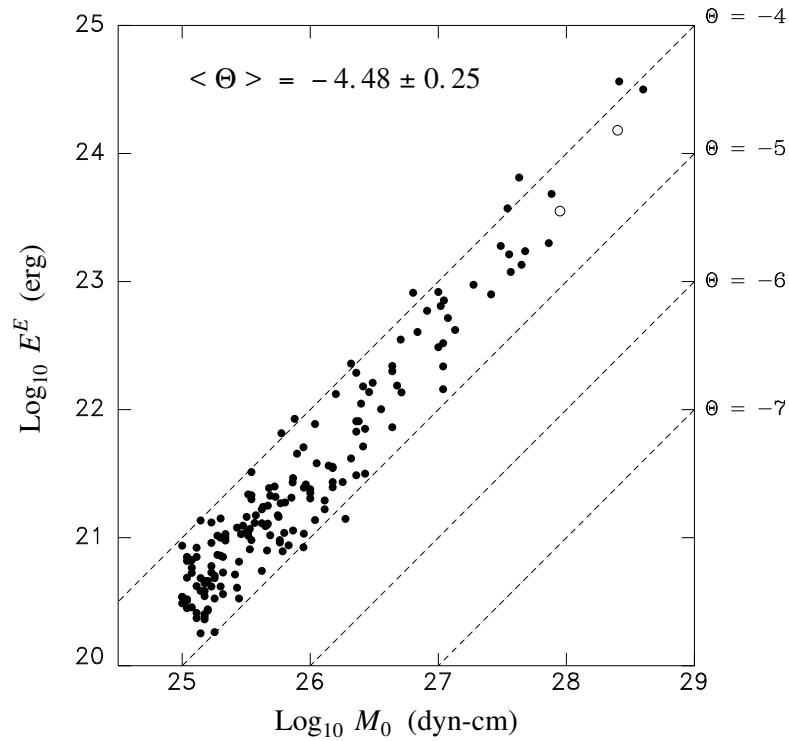
D-2. 450–700 km 171 EVENTS

Figure 5.6. Same as Fig. 5.3 for the D-2 dataset (450 to 700 km). In addition, the open circles identify the two large 2018 events in Fiji, which postdate the completion and publication of this chapter, without affecting its conclusions (see Section 5.4.3).

When I-D is split into its four depth bins (Fig. 5.7), a slight increase of Θ with depth can be detected, but all four one- σ bands share a common interval, ranging from -4.56 to -4.74. By contrast, the reference shallow dataset has an average Θ of -5.10, falling outside all four I-D bands, and a much larger standard deviation, $\sigma_s = 0.55$, more than twice that of all individual I-D bins.

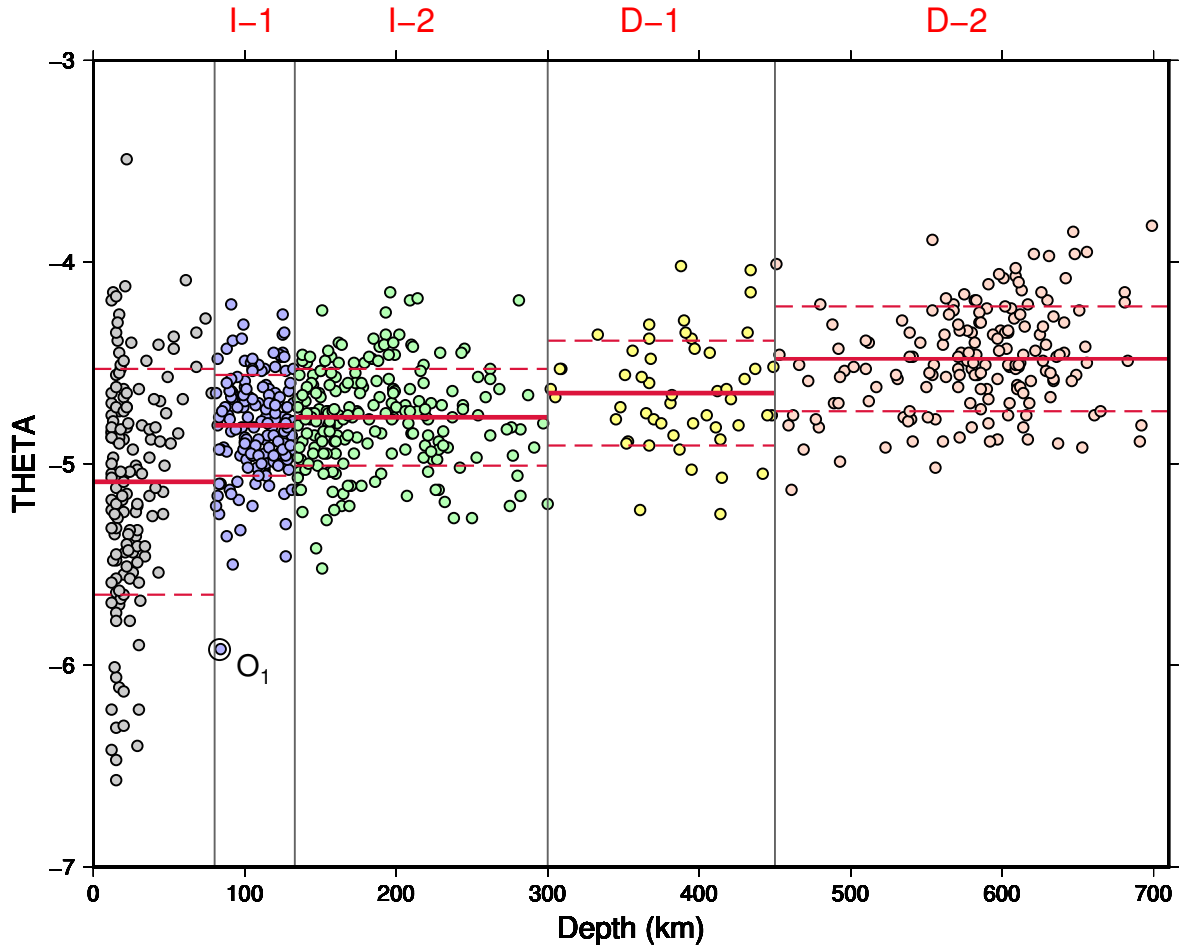


Figure 5.7. Cumulative plot of Θ for all depths categories (0 to 700 km). Average values of Θ and their one- σ bands are shown in red (solid and dashed segments, respectively). Note that shallow events are much more scattered than intermediate and deep ones. The outlier O_1 is identified by a bull's eye symbol.

When further splitting the reference shallow dataset into interplate and intraplate events, we confirm the generally higher Θ values of the latter, as already described by Okal & Kirby (2002) and Choy & Kirby (2004); we find that the mean

and standard deviation of the intraplate values of Θ (-4.68 ± 0.33) are fully comparable to those of the I-D dataset, or for that matter of any of its depth bins, especially the two intermediate ones. This implies that the generally higher values of Θ for I-D events are rooted in their intraplate nature, rather than in the greater source depth. By contrast, the generally lower values observed for interplate shallow sources express a difference between conditions at the interplate contact and within a single plate, with the larger scatter in Θ featured by shallow interplate events being tied to the lateral heterogeneity in those conditions; we stress however that the geographical distribution of shallow interplate outliers, featuring extreme values of Θ , and notably that of the so-called “tsunami earthquakes”, has yet to be modeled in the context of simple tectonic parameters such as lithospheric age or plate kinematics.

In Table 5.1, we further examine the effect, on our results, of imposing a minimum number N_{min} of stations (we recall that the standard dataset uses $N_{min} = 10$). The second group in the table imposes no such minimum, while the third one raises N_{min} to 20. In all cases, the average values of Θ vary by at most a few hundredths of one logarithmic unit. Most remarkably, even the group of 93 earthquakes for which fewer than ten stations were available (last group in Table 5.1) features, in all bins, average values of Θ falling inside the relevant one- σ band of the standard dataset (that class of earthquakes consists primarily of events from the early 1990s,

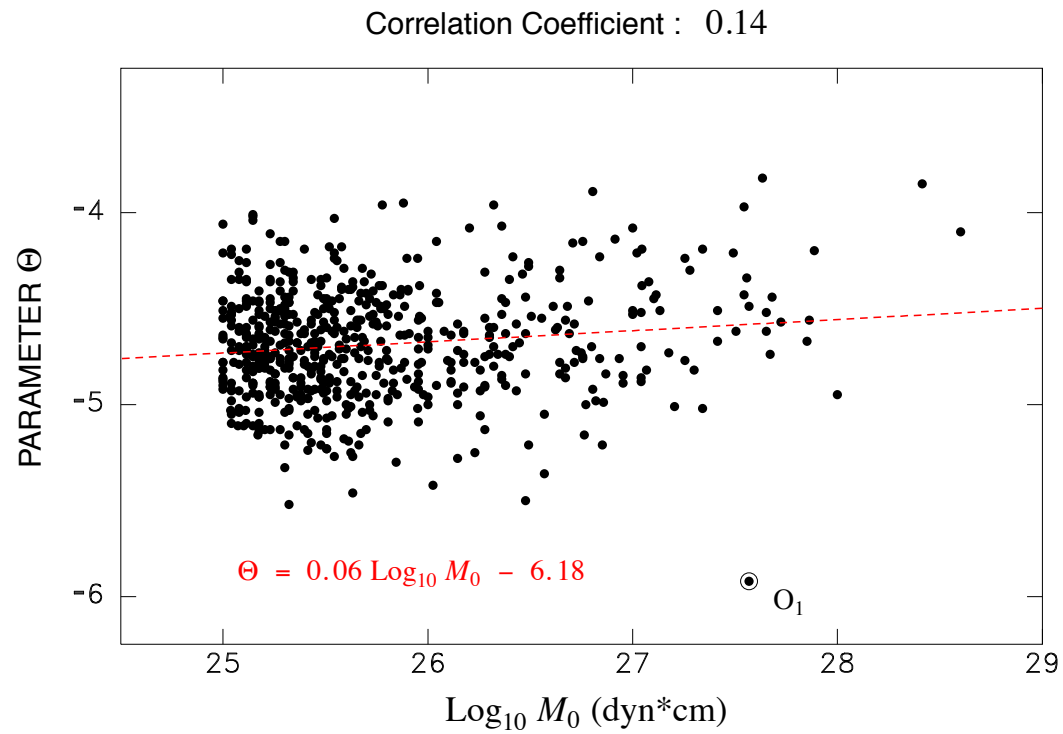


Figure 5.8. Whole dataset of 598 intermediate and deep earthquakes. The dashed line is the best regression. Note the insignificant slope and poor correlation coefficient. The outlier O_1 is identified by a bull's eye symbol.

when the Global Seismic Network was still under development). This experiment underscores the robustness of the concept of the parameter Θ .

On Fig. 5.8, we investigate any possible trend between Θ and earthquake size, by attempting a regression against $\log_{10} M_0$. Any such trend could be the sign of a

putative systematic error, potentially traceable to approximations in our methodology (*e.g.*, the selection of t_{max}). We find no such evidence, with both an insignificant slope (0.06) and a poor correlation between the two quantities (14%).

5.4.2. Possible influence of focal mechanism

We further investigate the I-D dataset by researching any possible dependence of Θ on focal mechanism. We are motivated by the fact that Choy & Boatwright (1995) have suggested that shallow strike-slip earthquakes feature higher energy-to-moment ratios than those with other mechanisms, although Newman & Okal (1998) pointed out a possible bias due to over-correction for strike-slip radiation patterns which could be affected by uncertainties in focal geometry or lateral heterogeneity at the source, and by the expected break-down in scaling laws for strike-slip sources reaching faster saturation of their fault width W , on account of their steeper fault dips. Choy et al.'s (2006) later study, which addressed those reservations, generally supported their initial results, and further indicated a variation in apparent stress (closely related to Θ) with tectonic characteristics of shallow earthquakes such as lithospheric strength and fault maturity. Pérez-Campos & Beroza (2001) also suggested a weak dependence of radiated energy on focal mechanism. In this context, it seems justified to explore any possible variation of Θ with focal geometry in the I-D dataset.

For this purpose, we sort the dataset using the concept of ternary diagrams introduced by Frohlich & Apperson (1992). We recall that, based on the remark

that the three dip angles of the principal axes T, B, P of any double-couple satisfy $\sin^2 \delta_T + \sin^2 \delta_B + \sin^2 \delta_P = 1$, these authors proposed that any such mechanism can be regarded as a barycentric combination of Strike-Slip (SS), Normal (NO) and Thrust (TH) mechanisms, which they plot inside an equilateral triangle with “pure” mechanisms at the apices.¹

Here, we define events as SS, NO, or TH if they have dips δ_B , δ_P or δ_T respectively, satisfying $\sin^2 \delta \geq 2/3$ (or $\delta \geq 54.74^\circ$), this angle being chosen as the complement of the common dip angle of the three axes of a mechanism plotting at the center of the ternary diagram (Frohlich & Apperson, 1992). We call other events Hybrid (HY). This is a more symmetric definition than Frohlich & Apperson’s (1992), who allowed a shallower dip (50°) for TH, as opposed to SS and NO (60°). Under our conventions, a randomly oriented double couple has an equal 18% chance of being classified as SS, NO or TH, and a 45% chance as HY, compared with 14%, 14%, 23%, and 49%, respectively under Frohlich’s.

Fig. 5.9 plots the resulting ternary diagrams for the four depth bins, and Table 5.2 lists the new statistics for the resulting 16 sub-datasets. The population disparity between various classes illustrates partly the greater probability of an HY orientation, and partly the consistency of stresses released by deep earthquakes, as

¹We correct a typographic error in Frohlich & Apperson (1992, p. 285), later reproduced in Frohlich (1992, p. 195). The denominator common to the two lines of their equation 14 should read

$$\begin{aligned} & \sin(35.26^\circ) \sin \delta_B + \cos(35.26^\circ) \cos \delta_B \cos \psi, \\ & \text{instead of} \\ & \sin(35.26^\circ) \sin \delta_B + \cos(35.26^\circ) \sin \delta_B \cos \psi. \end{aligned}$$

initially pointed out in Isacks & Molnar's (1971) landmark study: for example, the deepest earthquakes in bin D-2 are expected to be down-dip compressional as the slab abuts against the more viscous deep mantle, which results in an NO mechanism for steeply sinking slabs, and a dip-slip on a vertical fault (HY) for a shallower dip.

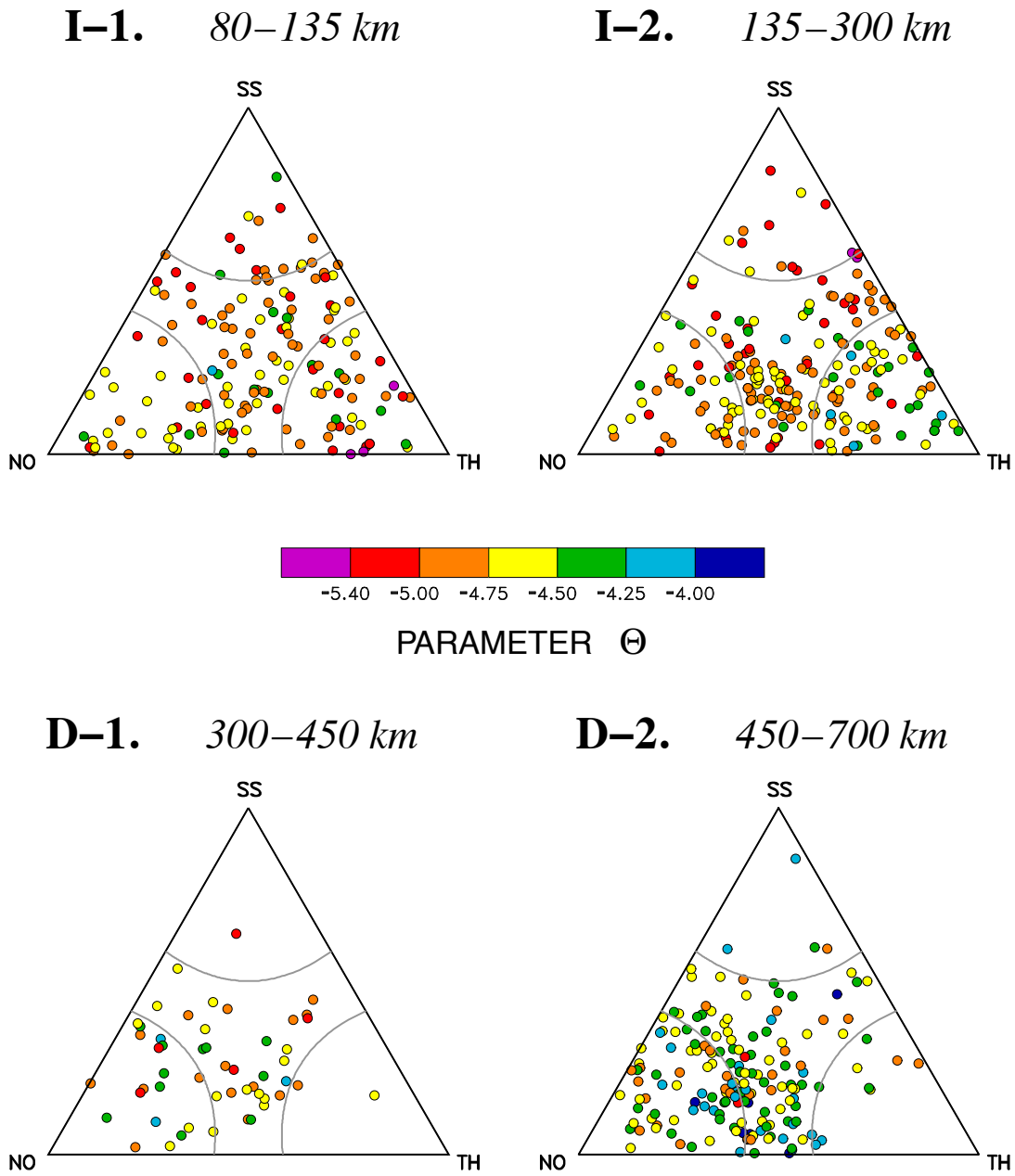


Figure 5.9. Ternary diagrams for the four depth bins. Note the absence of any systematic correlation between Θ and focal mechanism.

Table 5.2. Influence of focal mechanism on populations of Θ

Mechanism Type	Number of Events	Average Θ	Standard Deviation σ
<i>Intermediate I-1: 80-135 km</i>			
SS	16	-4.88	0.30
NO	30	-4.63	0.28
TH	40	-4.72	0.30
HY	74	-4.65	0.27
<i>Intermediate I-2: 135-300 km</i>			
SS	13	-5.04	0.24
NO	41	-4.78	0.22
TH	64	-4.65	0.23
HY	98	-4.81	0.22
<i>Deep D-1: 300-450 km</i>			
SS	1	-5.25	
NO	19	-4.61	0.30
TH	2	-4.71	0.18
HY	29	-4.56	0.22
<i>Deep D-2: 450-700 km</i>			
SS	4	-4.39	0.25
NO	67	-4.49	0.26
TH	10	-4.48	0.27
HY	90	-4.48	0.25
<i>All Depths: 80-700 km</i>			
SS	34	-4.88	0.30
NO	157	-4.63	0.28
TH	116	-4.72	0.30
HY	291	-4.69	0.27

Note that we identify only one strike-slip D -1 event, and therefore this category has no standard deviation. With the possible exception of that one event, which bears no statistical significance, we find no robust variation with focal mechanism in average Θ or standard deviation in any of the four depth bins.

A limitation of the above study is that stresses in descending slabs are controlled by the 3-D kinematics of the subduction, and the nature (TH, NO, SS or HY) of a particular mechanism would be better described in an appropriately rotated frame where the vertical axis is taken as the normal to the Wadati-Benioff plane. On Fig. 5.10, we perform such a rotation for the 147 events located in the Tonga-Kermadec subduction system, which offers sufficiently abundant seismicity to allow significant conclusions. We define the slab as striking N20°E, and dipping 45° North of 27°S and 60° farther South (Sykes, 1966). Fig. 5.10 shows that the majority of I-D earthquakes in Tonga-Kermadec take place in Depth Bin D-2, at the bottom of the slab, where it abuts against the lower mantle, and feature a down-dip compressional axis, an observation going back to Isacks & Molnar (1971). Such events are either classified as TH in the slab geometry, when their null axis is subhorizontal, parallel to the strike of the slab, SS when their T axis takes that orientation, or HY in between. At any rate, the average value of Θ varies insignificantly between the four geometries. At lesser depths, the datasets are much sparser, and as such do not lend themselves to meaningful interpretation, with the possible exception of Depth Bin I-2, where we tentatively recognize a group of down-dip tensional events

(“normal”), and a group of down-dip compressional ones (“thrust”) which could correspond to bending stresses in different layers of the slab; again, we find no significant difference in populations of Θ between the two geometries. We conclude that, even when referred to coordinates defined in the geometry of the subducting slab, focal mechanism has no perceptible effect on the populations of Θ .

We interpret this result once again as an expression of probable structural homogeneity of the intra-slab seismogenic zones. In Choy et al.’s (2006) model, variations in Θ for shallow earthquakes are ascribed to differences in the properties of the relevant faults, such as their inter- or intra-plate character or their degree of maturity. Because in turn these conditions often dictate the focal geometry (e.g., interplate subduction gives rise to thrust mechanisms), a correlation can be found between Θ and focal mechanism. For I-D events, our study suggests that the mechanical properties of the faults supporting rupture are homogenized, probably as a result of the pressure and thermal evolution of the slab material during its long descent into the mantle. In particular, they will not reflect the orientation of the faults (which may or may not correspond to reactivation of subducted shallow faults) that will eventually control the focal geometry.

TONGA – KERMADEC

In Wadati-Benioff Zone Frame

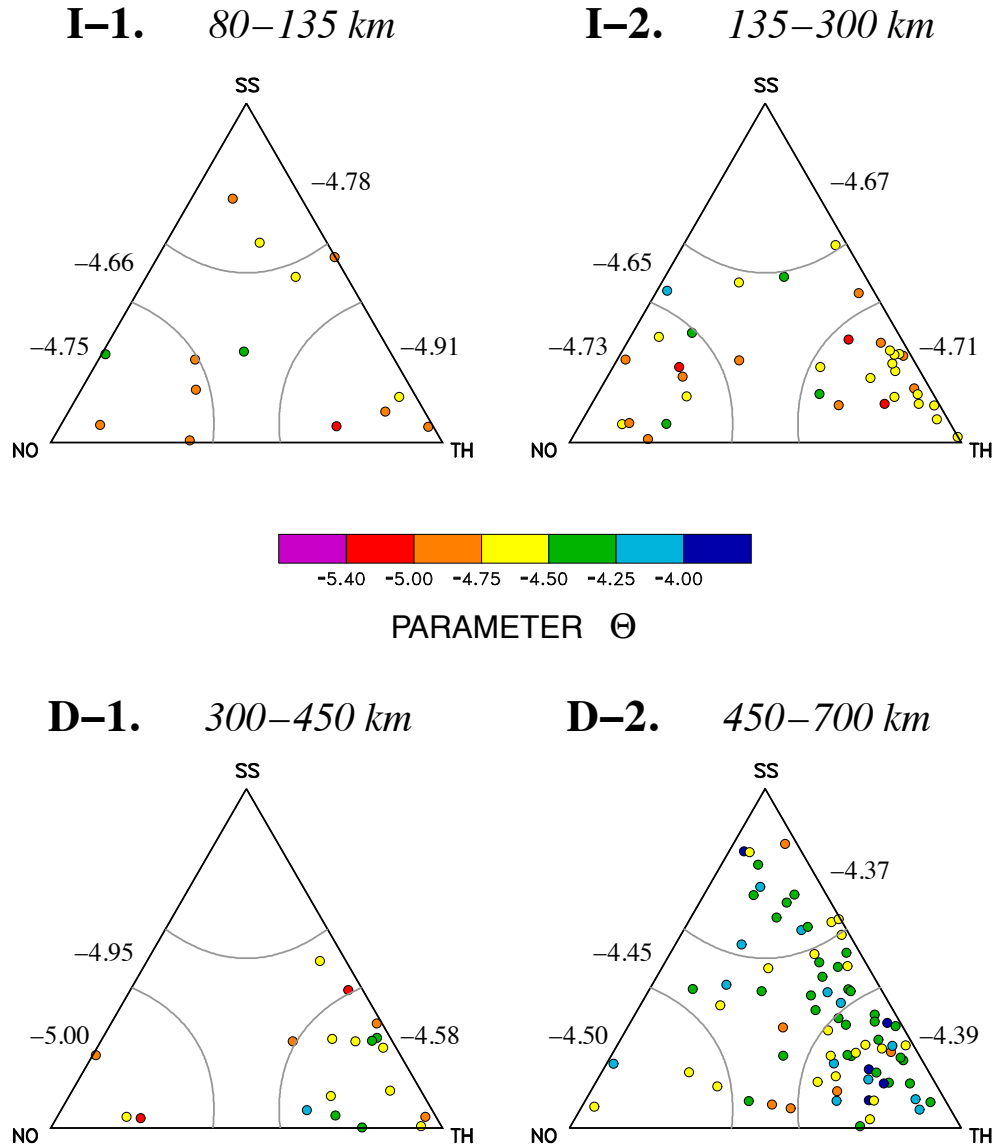


Figure 5.10. Same as Fig. 5.9 for the Tonga-Kermadec subset, after rotation into the frame of the subducting Wadati-Benioff plane. The average values for the 15 combinations of depth bins and focal geometries are shown adjacent to the relevant domains.

5.4.3. Regional trends, outliers and special groups

We examine below in more detail a number of subgroups or regions of particular interest. All relevant numbers are compiled in Table 5.3.

While the I-D dataset is generally more homogeneous than its shallow counterpart, it does feature a clear outlier in Depth Bin I-1, identified by a bull's eye symbol and labeled “ O_1 ” on Fig. 5.3. This large event ($M_0 = 3.7 \times 10^{27}$ dyn*cm) took place on 09 September 2005 in the Solomon Islands subducting slab at a depth of 84 km, and featured an extremely slow value of $\Theta = -5.92$, comparable to those of tsunami earthquakes. In this respect, it is reminiscent of the large earthquake of 31 December 1966 in Santa Cruz ($h = 78$ km; $M_0 = 4 \times 10^{27}$ dyn*cm), for which we have proposed in Chapter 4 a comparable value of $\Theta (-5.83)$ suggesting that anomalous conditions leading to source slowness in shallow earthquakes may occasionally persist immediately below the classical boundary between shallow and intermediate earthquakes.

Next, we examine on Figure 5.11 the geographic distribution of our results, color-coded according to Θ . In order to minimize clutter, we split the data into the four depth bins, and we represent those events with intermediate values of Θ (between -5.00 and -4.25) with smaller symbols, electing to focus on those trending towards deficient $\Theta (< -5.00$; red or magenta), or enhanced $\Theta (> -4.25$; light or dark blue). Figure 5.11 does not reveal any systematic large scale geographic pattern in the diversity of Θ values in any of the four depth bins.

Table 5.3. Values of Θ for specific events or subsets.

Events	Date D M (JJJ) Y	Epicenter		Depth (km)	$\langle \Theta \rangle$	σ
		(°N)	(°E)			
<i>Regional Subsets</i>						
Hindu Kush	19 events	≈ 36.5	≈ 70.5	182-254	-4.57	0.22
Burma	4 events	19-25	≈ 95	86-150	-4.64	0.24
Tonga (D-2)	78 events	-31 to -17	178-183	453-699	-4.41	0.23
Tonga (all depths)	147 events	-31 to -17	178-183	83-699	-4.56	0.28
<i>Individual Events</i>						
O ₁ Solomon Is.	09 SEP (252) 2005	-5.20	153.95	84	-5.92	
Vrancea*	31 MAY (151) 1990	45.67	26.00	87	-4.90	
Bucaramanga	10 MAR (069) 2015	6.83	-73.11	156	-4.61	
Pucallpa	24 AUG (236) 2011	-7.64	-74.53	147	-4.48	
Fiji Basin F-I †	13 APR (103) 1995	-13.34	170.71	646	-4.59	
Fiji Basin F-II †	05 MAR (064) 2014	-14.64	169.80	661	-4.76	
<i>Largest Deep Shocks ($M_0 > 5 \times 10^{27} \text{ dyn} \cdot \text{cm}$)</i>						
Bolivia	09 JUN (160) 1994	-13.82	-67.25	647	-3.85	
Flores Sea	17 JUN (169) 1996	-7.38	123.02	584	-4.56	
Sea of Okhotsk	24 MAY (144) 2013	54.61	153.77	611	-4.01	
Bonin Islands	30 MAY (150) 2015	27.94	140.56	681	-4.20	
South of Fiji	19 AUG (231) 2018	-17.86	-177.85	555	-4.22	
South of Fiji	06 SEP (249) 2018	-18.24	179.86	687	-4.40	

*Fewer than 10 stations, not part of standard dataset.

† Events postdating completion of our study and not included in the statistics in 5.1

The deep (D-2) dataset in Tonga-Kermadec is of particular interest, given the extreme thermal parameter Φ (product of age at subduction by rate of vertical descent (Kostoglodov, 1989; Kirby et al., 1991)) of this subduction system where old, Cretaceous lithosphere plunges at an unparalleled converging rate of up to 24 cm/year (Bevis et al., 1995), thus preserving an exceptionally cold field of temperatures in the deepest part of the slab. Okal & Kirby (1995) showed that this led to a distinct pattern of frequency-size relations; the question then arises naturally whether a distinct trend in Θ may also be present. For the 78 Tonga-Kermadec events deeper than 450 km, and including all focal geometries, we find $\langle \Theta \rangle =$

-4.41 ± 0.23 , again not significantly different from the global average value (-4.48 ± 0.26) for the D-2 bin. Similar results are found in the other depth bins (I-1: 14 events, -4.78 ± 0.20 ; I-2: 36 events, -4.71 ± 0.20 ; D-1: 19 events, -4.70 ± 0.29). We conclude that the exceptional thermal conditions in the Tonga slab have no effect on Θ , regardless of depth.

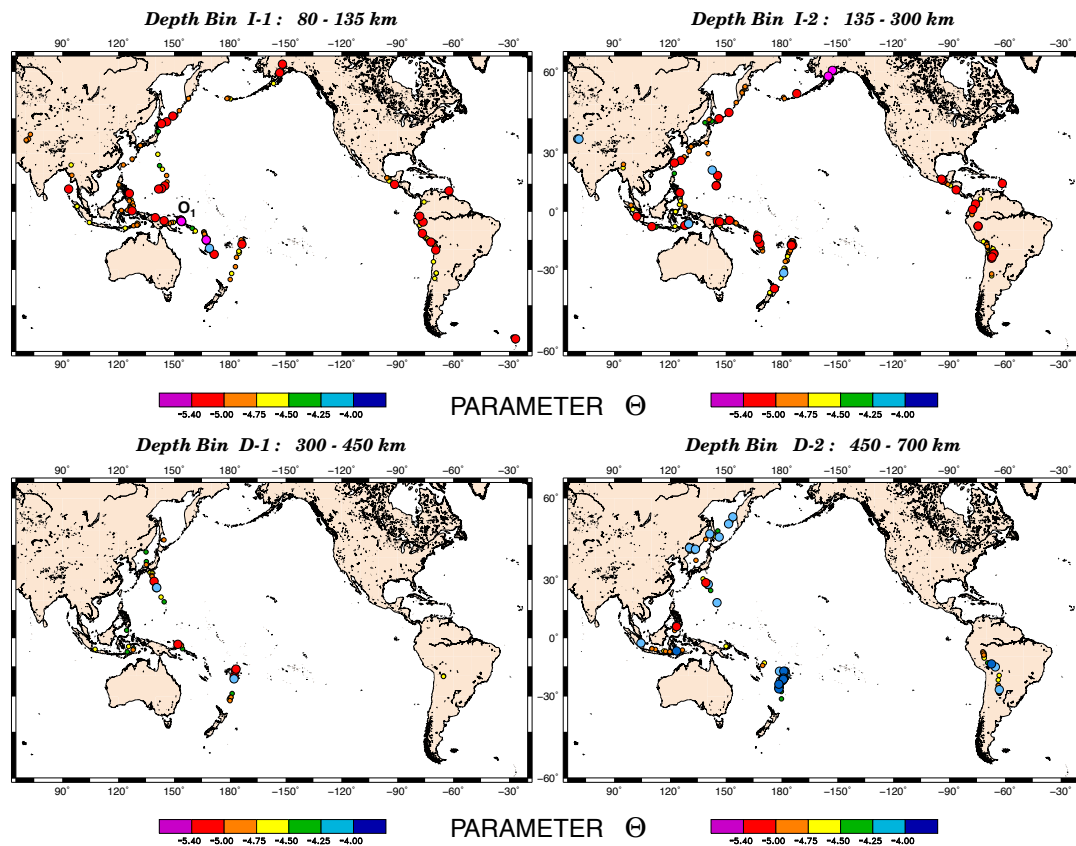


Figure 5.11. Maps of the dataset of 598 intermediate and deep earthquakes, separated in the 4 depth bins and color-coded according to Θ . To avoid clutter, events with average values ($-5.00 < \Theta < -4.25$) are shown with smaller symbols. See text for discussion.

In Figure 5.12, we zoom on the results for the Vanuatu-Santa Cruz subduction zone, for which we have documented in Chapter 4 a strong diversity in Θ at shallow

depths, possibly correlating with the level of coupling in the subduction. We similarly note four slow events (magenta and red symbols; $\Theta = -5.13, -5.21, -5.30, -5.46$) off the central part of Santo, where in Chapter 4 we identified anomalously slow earthquakes, including a documented tsunami earthquake, among the 1965 aftershock series. However, this possible similarity takes place next to a zone of strong diversity in Θ immediately to the North, and may just be fortuitous.

Figure 5.12 also includes two earthquakes, shown as triangles, belonging to the deep Fiji Basin (FB) group, interpreted by Okal & Kirby (1998) as located in a remnant piece of the fossil Vityaz slab, now lying recumbent at the bottom of the transition zone. Because this piece of slab is mechanically detached from any convection cell, its state of stress could conceivably be singular; however the values of Θ for those two lone events (-4.53 and -4.68) fit within the one- σ band for the D-2 bin.

We next consider the case of the Hindu Kush. This region features an intriguing nest of abundant, occasionally strong, intermediate depth seismicity, with most large events ($M \geq 6$) clustering in a volume not exceeding 150 km in all three dimensions, although detailed studies of lower-level seismicity have proposed (Nowroozi, 1971) and later documented (Khalturin et al., 1977) a system of continuous Wadati-Benioff zones now believed to involve a lateral change of subduction polarity (Sippl et al., 2013). Our dataset comprises 24 events in the Hindu-Kush, 19 of which fall in a compact Southern cluster at depths of 182 to 254 km. They are shown in map view and cross-section on Figure 5.13 with the same symbols as on Figure 5.11. For this

group, we find $\langle \Theta \rangle = -4.57 \pm 0.22$, on average slightly higher than for the entire I-2 family, but within its one- σ band (-4.77 ± 0.22).

Zhan & Kanamori (2016) have studied three recent large earthquakes from the Hindu Kush cluster and shown that even though they shared a common hypocenter and focal mechanism, they differed significantly in terms of source duration, rise time and precursory signals. They identified the event of 03 March 2002 as featuring a very short duration (less than 10 s for a moment of 1.3×10^{27} dyn*cm), while the larger earthquake of 26 October 2015 ($M_0 = 2.2 \times 10^{27}$ dyn*cm) did show more source complexity; their third and smaller event (09 August 1993 (12:42), $M_0 = 3.6 \times 10^{26}$ dyn*cm) had a very complex time history with a source lasting 20 s. We obtained Θ values of -4.45 in 2002, -4.19 in 2015 and -4.57 in 1993. Note that the first two events fall outside the one- σ band of the whole I-2 depth bin, and that the third earthquake is not part of the standard dataset, as only 9 stations were available; we have added it as a square on Figure 5.13. We find no resolvable trend between source complexity, as evidenced by Zhan & Kanamori (2016), and Θ ; however the dataset is clearly too small to draw any definitive conclusion.

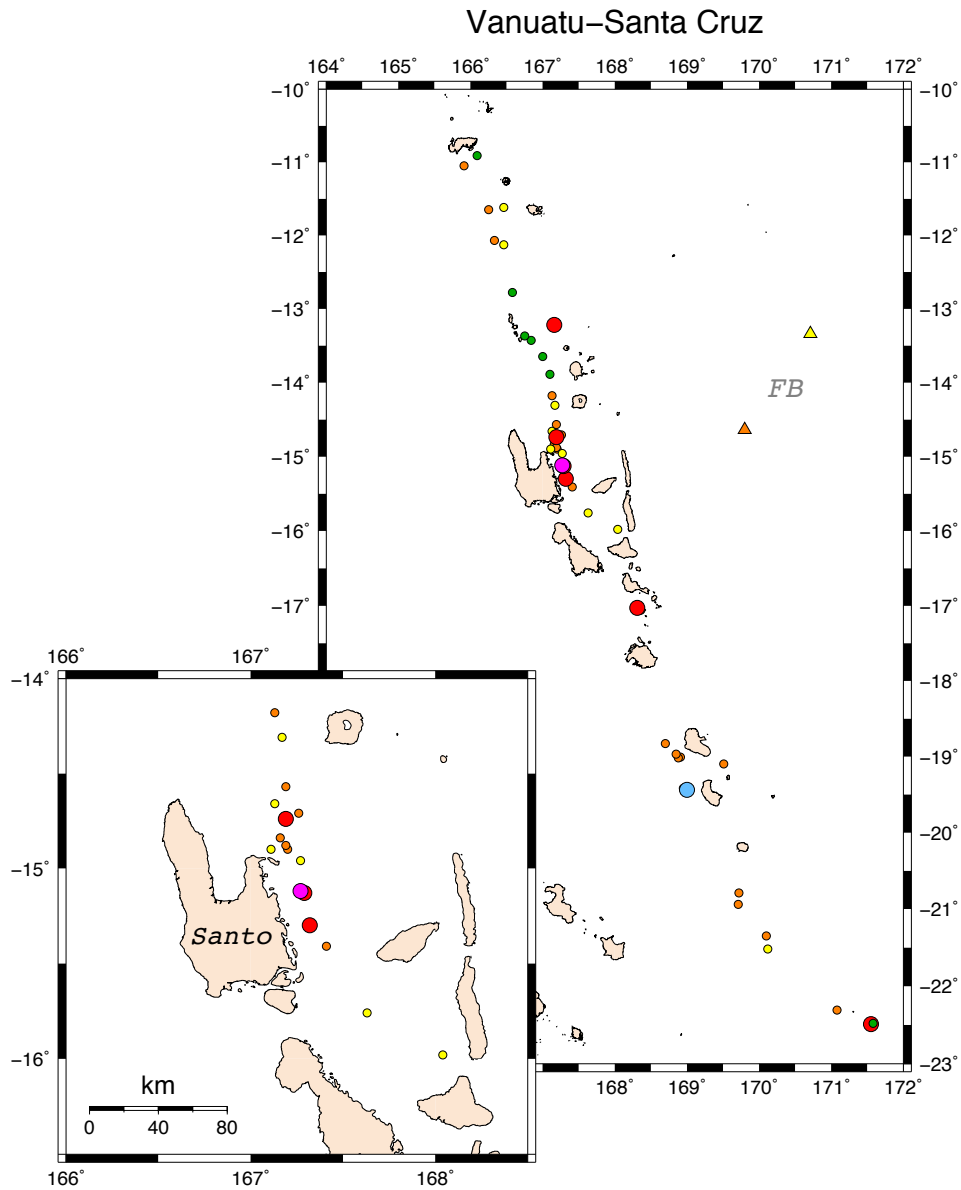


Figure 5.12. Close-up of the results in the Vanuatu-Santa Cruz region. Symbols as on Fig. 5.11. The inset at lower left zooms on the island of Santo, Northern Vanuatu. Note the four earthquakes trending towards slowness (red and magenta symbols, $\Theta < -5.00$) at the exact same latitude as slow shallow events documented in Chapter 4. The two triangles denote D-2 earthquakes belonging to the deep Fiji Basin (FB) cluster.

We similarly examine the subset of intermediate-depth (I-1 and I-2) events in Myanmar (*ex-Burma*), mainly clustered around 24°N , 95°E , and arguably an

Eastern, but shallower and less active, counterpart to the Hindu Kush system. Based on a meager number of events (4), we find a mean value ($\langle \Theta \rangle = -4.64$) comparable to that of the Hindu Kush cluster.

Other areas of potential interest would include Vrancea, Romania (I-1), as well as the Bucaramanga, Colombia and Pucallapa, Peru nests in South America (I-2, Wagner & Okal 2019). Unfortunately, our dataset includes only one event for each of those provinces, all of them featuring regular values of Θ for their respective depth bins.

Finally, we examined four deep (D-2) mega-events, defined as having a moment exceeding 5×10^{27} dyn*cm. We find generally high values of Θ for the 1994 Bolivian, 2013 Okhotsk and 2015 Bonin earthquakes (-3.85, -4.10 and -4.20, respectively), and an average one (-4.56) for the 1996 Flores Sea event.

For the 2013 Sea of Okhotsk earthquake, this translates to an estimated energy $E^E = 3 \times 10^{17}$ J, or twice the value proposed by Ye et al. (2013), but within their claimed factor of uncertainty. We do not find a striking difference in Θ between the 2013 mainshock and its aftershock at 14:56 GMT, for which we note that Ye et al. (2013) use only half the moment value listed in the GlobalCMT catalog. Both events would qualify as “snappy”, in agreement with short durations and fast rupture velocities. The values listed in the National Earthquake Information Center’s Preliminary Determinations of Earthquake Bulletins (9.4×10^{16} and 8.8×10^{14} J, respectively) are significantly smaller than Ye et al.’s (2013).

Regarding the 1994 Bolivian earthquake, our proposed Θ obtained on a dataset of 10 stations, yields an estimated energy of 3×10^{17} J, about a factor of 6 more than quoted by Ye et al. (2013), from Winslow & Ruff (1999). We note however that Winslow & Ruff considered attenuation as “unimportant”; even a low average t^* of 0.3 s would compensate for that factor in the frequency range 0.5 -1 Hz. The significant difference between our estimated energy and the value proposed by the NEIC PDE (3.2×10^{16} J) may reflect a difference in t_{max} for this event featuring a long duration (about 50 s) and a strong source complexity (Lundgren & Giardini, 1995; Chen, 1995).

In the case of the intriguing 2015 Bonin Islands earthquake, which took place roughly 100 km deeper than any previously known seismicity in that subduction system (see Fig. 3.6) , we obtain $E^E = 4.8 \times 10^{16}$ J, within a factor of 3/2 of Ye et al.’s (2016) estimate (3.3×10^{16} J). Finally, for the 1996 Flores event, our estimated energy ($E^E = 2.0 \times 10^{16}$ J) is in excellent agreement with the NEIC PDE estimate ($E^E = 1.8 \times 10^{16}$ J), but again significant larger than Winslow and Ruff’s (1999).

In addition and after the study in this chapter was completed and published as Saloor & Okal (2018), two great deep earthquakes took place at the bottom of the Fiji slab, on 19 August 2018 (Event F-I, h= 555 km, $M_0 = 2.5 \times 10^{28}$ dyn*cm) and 06 September 2018 (Event F-II, h= 687 km, $M_0 = 9 \times 10^{27}$ dyn*cm). These remarkable events, also mentioned in the conclusion of Chapter 3, have the third and sixth largest seismic moments ever measured for deep earthquakes. The Θ values

obtained (-4.22 for F-I and -4.40 for F-II) fall within the one- σ band for Bin D-2, and thus do not change any of our conclusions. The events are included in Table 5.1 and shown as open circles on Fig. 5.6 .

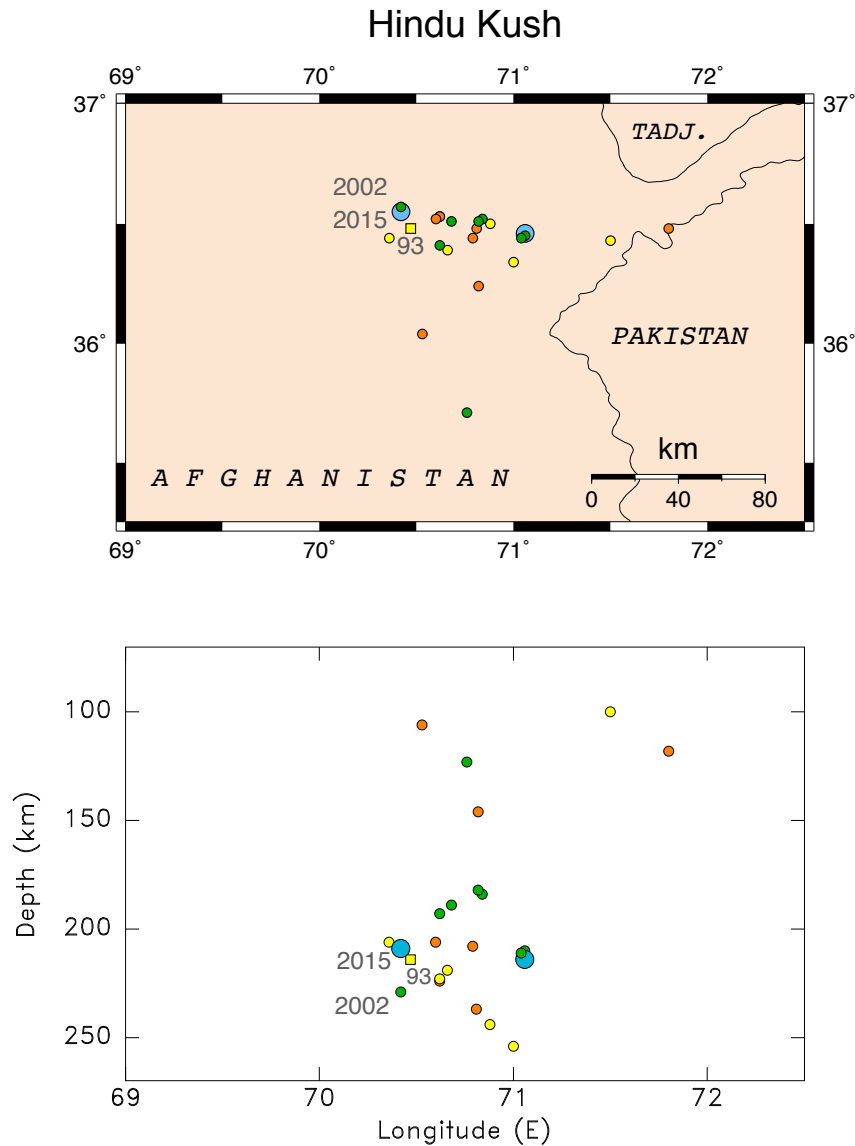


Figure 5.13. *Top*: Map of our results for the Hindu Kush cluster using the same symbols as on Figures 11 and 12. Events studied by Zhan & Kanamori (2016) are identified, with the 1993 one shown as a square. *Bottom*: East-west cross-section of the dataset; no vertical exaggeration.

5.5. Conclusion

We have derived algorithms to extend the computation of the slowness parameter Θ to intermediate and deep earthquakes, and successfully applied them to a global dataset of close to 600 earthquakes. While we document a slight increase of Θ with depth, the most significant aspect of our results is the consistency of the Θ values, which feature a global standard deviation of only 0.31 logarithmic units, as compared to 0.55 units for a reference dataset of 146 shallow earthquakes. This relative constancy of Θ values, shared by shallow intraplate events, suggests a lack of large scale heterogeneity in the state of stress inside the seismogenic zones of slabs, in contrast to the case of shallow interplate earthquakes, for which a diversity of tectonic environments can lead to a greater variability of stresses, and hence of Θ values. Similarly, we found no correlation between Θ and the focal geometry of intermediate and deep earthquakes, which suggests that while the latter generally reflects the orientation of ambient stresses controlled by the local dynamics of subduction, the amplitude of apparent stresses remains unaffected by their geometry.

While differences may persist regarding the detailed thermal regime of subducting slabs, controlled by convergence rate and lithospheric age at subduction, the emerging picture is that of a largely homogeneous field of stresses inside the downgoing slabs, once they have departed the more diverse boundary layer at the surface of the Earth.

References

- Anderson, D. L. & Given, J. W., 1982. Absorption band Q model for the Earth, *Journal of Geophysical Research: Solid Earth*, **87**(B5), 3893–3904.
- Anderson, D. L. & Hart, R., 1978. Attenuation models of the Earth, *Physics of the Earth and Planetary Interiors*, **16**(4), 289–306.
- Anderson, D. L., Ben-Menahem, A., & Archambeau, C. B., 1965. Attenuation of seismic energy in the upper mantle, *Journal of Geophysical Research*, **70**(6), 1441–1448.
- Anderson, J. & Wood, H. O., 1925. Description and theory of the torsion seismometer, *Bulletin of the Seismological Society of America*, **15**(1), 1–72.
- Anonymous, 1935. Envahissement du littoral par la mer à la Nouvelle-Calédonie au cours de l'année 1934-1935, *Annales de la Commission pour l'Etude des Raz-de-Marée*, **5**, 37–38.
- Anonymous, 2013. Summary of working group recommendations, *Intl. Assoc. Seismol. Phys. Earth Inter.*, http://iaspei.org/commissions/commission-on-seismological-observation-and-interpretation/Summary_WG_recommendations_20130327.pdf.
- Archambeau, C., 1978. Estimation of non-hydrostatic stress in the Earth by seismic methods: Lithospheric stress levels along Pacific and Nazca plate subduction

- zones, *US Geol. Surv., Open-File Rept*, **78-943**, 47–138.
- Beavan, J., Fielding, E., Motagh, M., Samsonov, S., & Donnelly, N., 2011. Fault location and slip distribution of the 22 February 2011 $M_w = 6.2$ Christchurch, New Zealand, earthquake from geodetic data, *Seismological Research Letters*, **82**(6), 789–799.
- Bell, R., Holden, C., Power, W., Wang, X., & Downes, G., 2014. Hikurangi Margin tsunami earthquake generated by slow seismic rupture over a subducted seamount, *Earth and Planetary Science Letters*, **397**, 1–9.
- Ben-Menahem, A. & Rosenman, M., 1972. Amplitude patterns of tsunami waves from submarine earthquakes, *Journal of Geophysical Research*, **77**(17), 3097–3128.
- Benioff, H., 1932. A new vertical seismograph, *Bulletin of the Seismological Society of America*, **22**(2), 155–169.
- Bevis, M., Taylor, F. W., Schutz, B., Recy, J., Isacks, B., Helu, S., Singh, R., Kendrick, E., Stowell, J., Taylor, B., et al., 1995. Geodetic observations of very rapid convergence and back-arc extension at the Tonga arc, *Nature*, **374**(6519), 249–251.
- Bilek, S. L. & Lay, T., 2002. Tsunami earthquakes possibly widespread manifestations of frictional conditional stability, *Geophysical Research Letters*, **29**(14), 1673, 4 pp.
- Bina, C. R., 1997. Patterns of deep seismicity reflect buoyancy stresses due to phase transitions, *Geophysical Research Letters*, **24**(24), 3301–3304.

- Bina, C. R., 1998. A note on latent heat release from disequilibrium phase transformations and deep seismogenesis, *Earth, planets and space*, **50**(11-12), 1029–1034.
- Bina, C. R., Stein, S., Marton, F. C., & Van Ark, E. M., 2001. Implications of slab mineralogy for subduction dynamics, *Physics of the Earth and Planetary Interiors*, **127**(1-4), 51–66.
- Boatwright, J. & Choy, G. L., 1986. Teleseismic estimates of the energy radiated by shallow earthquakes, *Journal of Geophysical Research: Solid Earth*, **91**(B2), 2095–2112.
- Boatwright, J. & Fletcher, J. B., 1984. The partition of radiated energy between *P* and *S* waves, *Bulletin of the Seismological Society of America*, **74**(2), 361–376.
- Borrero, J. C., Weiss, R., Okal, E. A., Hidayat, R., Arcas, D., & Titov, V. V., 2009. The tsunami of 2007 September 12, Bengkulu province, Sumatra, Indonesia: Post-tsunami field survey and numerical modelling, *Geophysical Journal International*, **178**(1), 180–194.
- Bridgman, P. W., 1945. Polymorphic transitions and geological phenomena, *American Journal of Science Ser. A*, **243**(1), 90–96.
- Burdick, L. & Helmberger, D., 1974. Time functions appropriate for deep earthquakes, *Bulletin of the Seismological Society of America*, **64**(5), 1419–1427.
- Burdick, L. & Helmberger, D. V., 1978. The upper mantle *P* velocity structure of the Western United States, *Journal of Geophysical Research: Solid Earth*, **83**(B4), 1699–1712.

- Burnley, P. C., Green, H. W., & Prior, D. J., 1991. Faulting associated with the olivine to spinel transformation in Mg_2GeO_4 and its implications for deep-focus earthquakes, *Journal of Geophysical Research: Solid Earth*, **96**(B1), 425–443.
- Carpenter, E., 1965. Attenuation of teleseismic body waves, *Nature*, **207**, 745–746.
- Charlier, C. & van Gils, J.-M., 1953. *Catalogue des station séismologiques mondiales*, Observatoire Royal de Belgique, Uccle.
- Chen, W.-P., 1995. *En échelon* ruptures during the great Bolivian earthquake of 1994, *Geophysical Research Letters*, **22**(16), 2261–2264.
- Chen, Y., Wen, L., & Ji, C., 2014. A cascading failure during the 24 May 2013 great Okhotsk deep earthquake, *Journal of Geophysical Research: Solid Earth*, **119**(4), 3035–3049.
- Chinnery, M., 1960. Some physical aspects of earthquake mechanism, *Journal of Geophysical Research*, **65**(11), 3852–3854.
- Choy, G. L. & Boatwright, J. L., 1995. Global patterns of radiated seismic energy and apparent stress, *Journal of Geophysical Research: Solid Earth*, **100**(B9), 18205–18228.
- Choy, G. L. & Cormier, V. F., 1986. Direct measurement of the mantle attenuation operator from broadband *P* and *S* waveforms, *Journal of Geophysical Research: Solid Earth*, **91**(B7), 7326–7342.
- Choy, G. L. & Dewey, J. W., 1988. Rupture process of an extended earthquake sequence: Teleseismic analysis of the Chilean earthquake of March 3, 1985, *Journal of Geophysical Research: Solid Earth*, **93**(B2), 1103–1118.

- Choy, G. L. & Kirby, S. H., 2004. Apparent stress, fault maturity and seismic hazard for normal-fault earthquakes at subduction zones, *Geophysical Journal International*, **159**(3), 991–1012.
- Choy, G. L., McGarr, A., Kirby, S. H., & Boatwright, J., 2006. An overview of the global variability in radiated energy and apparent stress, *American Geophysical Union Geophysical Monograph Series*, **170**, 43–57.
- Chung, W.-Y. & Kanamori, H., 1976. Source process and tectonic implications of the Spanish deep-focus earthquake of March 29, 1954, *Physics of the Earth and Planetary Interiors*, **13**(2), 85–96.
- Čížková, H. & Bina, C. R., 2015. Geodynamics of trench advance: Insights from a Philippine-Sea-style geometry, *Earth and Planetary Science Letters*, **430**, 408–415.
- Dahlen, F., 1982. The effect of data windows on the estimation of free oscillation parameters, *Geophysical Journal International*, **69**(2), 537–549.
- Dahlen, F. & Sailor, R., 1979. Rotational and elliptical splitting of the free oscillations of the Earth, *Geophysical Journal International*, **58**(3), 609–623.
- Doser, D. I. & Webb, T. H., 2003. Source parameters of large historical (1917–1961) earthquakes, North Island, New Zealand, *Geophysical Journal International*, **152**(3), 795–832.
- Downes, G., Webb, T., McSaveny, M., Darby, D., Doser, D., Chagué-Goff, C., & Barnett, A., 2001. The 26 March and 17 May 1947 Gisborne earthquakes and tsunami: implications for tsunami hazard for the east coast, North Island, New

- Zealand, *in: Tsunami Risk Assessment Beyond 2000: Theory, Practice and Plans*, Proc. Intl. Tsunami Workshop, pp. 14-16, Moscow, Russia.
- Dziewonski, A., Chou, T.-A., & Woodhouse, J., 1981. Determination of earthquake source parameters from waveform data for studies of global and regional seismicity, *Journal of Geophysical Research: Solid Earth*, **86**(B4), 2825–2852.
- Dziewonski, A. M. & Anderson, D. L., 1981. Preliminary reference Earth model, *Physics of the Earth and Planetary Interiors*, **25**(4), 297–356.
- Ebel, J. E., 1980. Source processes of the 1965 New Hebrides Islands earthquakes inferred from teleseismic waveforms, *Geophysical Journal International*, **63**(2), 381–403.
- Ebeling, C. W. & Okal, E. A., 2012. An extension of the E/M_0 tsunami earthquake discriminant Θ to regional distances, *Geophysical Journal International*, **190**(3), 1640–1656.
- Eiby, G., 1947. Two New Zealand tsunamis, *J. Roy. Soc. N.Z.*, **12**, 337–351.
- Ekström, G., Nettles, M., & Dziewoński, A., 2012. The GlobalCMT project 2004–2010: Centroid-moment tensors for 13,017 earthquakes, *Physics of the Earth and Planetary Interiors*, **200**, 1–9.
- Engdahl, E. & Villaseñor, A., 2002. Global seismicity: 1900–1999, **in:** *International Earthquake and Engineering Seismology, Part A*, Eds. Lee, W.H.K., Kanamori, H., Jennings, P.C. & Kisslinger, C., pp. 665-690, Elsevier.
- Engebretson, D. & Kirby, S., 1992. Deep Nazca slab seismicity: Why is it so anomalous?, *Eos, Trans. Am. Geophys. Un.*, **73**(43), 379, [abstract].

- Evernden, J. F., 1967. Magnitude determination at regional and near-regional distances in the United States, *Bulletin of the Seismological Society of America*, **57**(4), 591–639.
- Fritz, H., Papantoniou, A., Biukoto, L., & Albert, G., 2013. The Solomon Islands tsunami of 6 February 2013 field survey in the Santa Cruz Islands, *Eos, Trans. Am. geophys. Un.*, **95**, NH41A-1996, [abstract].
- Frohlich, C., 1992. Triangle diagrams: Ternary graphs to display similarity and diversity of earthquake focal mechanisms, *Physics of the Earth and Planetary Interiors*, **75**(1-3), 193–198.
- Frohlich, C., 2006. *Deep earthquakes*, Cambridge University Press.
- Frohlich, C. & Apperson, K. D., 1992. Earthquake focal mechanisms, moment tensors, and the consistency of seismic activity near plate boundaries, *Tectonics*, **11**(2), 279–296.
- Fukao, Y., 1979. Tsunami earthquakes and subduction processes near deep-sea trenches, *Journal of Geophysical Research: Solid Earth*, **84**(B5), 2303–2314.
- Fukao, Y. & Kikuchi, M., 1987. Source retrieval for mantle earthquakes by iterative deconvolution of long-period *P* waves, *Tectonophysics*, **144**(1-3), 249–269.
- Fukao, Y., Obayashi, M., Inoue, H., & Nenbai, M., 1992. Subducting slabs stagnant in the mantle transition zone, *Journal of Geophysical Research: Solid Earth*, **97**(B4), 4809–4822.
- Garnero, E. J. & Helmberger, D. V., 1996. Seismic detection of a thin laterally varying boundary layer at the base of the mantle beneath the central Pacific,

- Geophysical Research Letters*, **23**(9), 977–980.
- Geller, R. J., 1976. Scaling relations for earthquake source parameters and magnitudes, *Bulletin of the Seismological Society of America*, **66**(5), 1501–1523.
- Gilbert, F., 1971. Excitation of the normal modes of the Earth by earthquake sources, *Geophysical Journal International*, **22**(2), 223–226.
- Gilbert, F. & Dziewonski, A. M., 1975. An application of normal mode theory to the retrieval of structural parameters and source mechanisms from seismic spectra, *Philosophical Transactions of the Royal Society of London. Series A*, **278**(1280), 187–269.
- Glover, D., Meyers, H., Lee, W., & Shimazaki, K., 1988. Historical seismogram filming project: Current status, **in:** *Historical Seismograms and Earthquakes of the World*, Eds: W.H.K Lee, H. Meyers, and K. Shimazaki, pp. 373-379, Academic Press, San Diego.
- Goodstein, J., Kanamori, H., & Lee, W., 1980. Seismology microfiche publications from the Caltech archives, *Bulletin of the Seismological Society of America*, **70**(2), 657–658.
- Goto, K., Suzuki, Z., & Hamaguchi, H., 1987. Stress distribution due to olivine-spinel phase transition in descending plate and deep focus earthquakes, *Journal of Geophysical Research: Solid Earth*, **92**(B13), 13811–13820.
- Green, H. & Burnley, P., 1989. A new self-organizing mechanism for deep-focus earthquakes, *Nature*, **341**(6244), 733.

- Green, H., Scholz, C., Tingle, T., Young, T., & Koczyński, T., 1992. Acoustic emissions produced by anticrack faulting during the olivine→spinel transformation, *Geophysical Research Letters*, **19**(8), 789–792.
- Green, H. W., 2007. Shearing instabilities accompanying high-pressure phase transformations and the mechanics of deep earthquakes, *Proceedings of the National Academy of Sciences*, **104**(22), 9133–9138.
- Green, H. W., Young, T. E., Walker, D., & Scholz, C. H., 1990. Anticrack-associated faulting at very high pressure in natural olivine, *Nature*, **348**(6303), 720–722.
- Gutenberg, B., 1945a. Amplitudes of P , PP , and S and magnitude of shallow earthquakes, *Bulletin of the Seismological Society of America*, **35**(2), 57–69.
- Gutenberg, B., 1945b. Magnitude determination for deep-focus earthquakes, *Bulletin of the Seismological Society of America*, **35**(3), 117–130.
- Gutenberg, B. & Richter, C., 1936. On seismic waves (third paper), *Gerlands Beitr. Geophys*, **47**, 73–131.
- Gutenberg, B. & Richter, C. F., 1942. Earthquake magnitude, intensity, energy, and acceleration, *Bulletin of the Seismological Society of America*, **32**(3), 163–191.
- Gutenberg, B. & Richter, C. F., 1954. *Seismicity of the Earth*, Princeton University Press, 310 p.
- Gutenberg, B. & Richter, C. F., 1956. Magnitude and energy of earthquakes, *Annali di Geofisica*, **9**, 1–15.
- Hara, T. & Kawakatsu, 2016. Full moment tensor inversion for the large deep earthquakes, *Proceeding of the Japan Geoscience Union Meeting*, SCG20–05, [abstract].

- Hara, T., Kuge, K., & Kawakatsu, H., 1995. Determination of the isotropic component of the 1994 Bolivia deep earthquake, *Geophysical Research Letters*, **22**(16), 2265–2268.
- Haskell, N. A., 1962. Crustal reflection of plane P and SV waves, *Journal of Geophysical Research*, **67**(12), 4751–4768.
- Hayes, G. P., Wald, D. J., & Johnson, R. L., 2012. Slab1.0: A three-dimensional model of global subduction zone geometries, *Journal of Geophysical Research: Solid Earth*, **117**(B1), B01302, 15 pp.
- Herrin, E., 1968. Introduction to “1968 seismological tables for P phases”, *Bulletin of the Seismological Society of America*, **58**(4), 1193–1195.
- Herrmann, R. B., 2013. Computer programs in seismology: An evolving tool for instruction and research, *Seismological Research Letters*, **84**(6), 1081–1088.
- Hill, E. M., Borrero, J. C., Huang, Z., Qiu, Q., Banerjee, P., Natawidjaja, D. H., Elosegui, P., Fritz, H. M., Suwargadi, B. W., Pranantyo, I. R., et al., 2012. The 2010 M_w 7.8 Mentawai earthquake: Very shallow source of a rare tsunami earthquake determined from tsunami field survey and near-field GPS data, *Journal of Geophysical Research: Solid Earth*, **117**(B06402).
- Huang, W.-C., Okal, E. A., Ekström, G., & Salganik, M. P., 1997. Centroid moment tensor solutions for deep earthquakes predating the digital era: the World-Wide Standardized Seismograph Network dataset (1962–1976), *Physics of the Earth and Planetary Interiors*, **99**(1-2), 121–129.

- Huang, W.-C., Okal, E. A., Ekström, G., & Salganik, M. P., 1998. Centroid moment tensor solutions for deep earthquakes predating the digital era: the historical dataset (1907–1961), *Physics of the Earth and Planetary Interiors*, **106**(3-4), 181–190.
- Hudson, J., 1969. A quantitative evaluation of seismic signals at teleseismic distances radiation from point sources, *Geophysical Journal of the Royal Astronomical Society*, **18**(3), 233–249.
- Ide, S. & Beroza, G. C., 2001. Does apparent stress vary with earthquake size?, *Geophysical Research Letters*, **28**(17), 3349–3352.
- Isacks, B. & Molnar, P., 1971. Distribution of stresses in the descending lithosphere from a global survey of focal-mechanism solutions of mantle earthquakes, *Reviews of Geophysics*, **9**(1), 103–174.
- Isacks, B., Oliver, J., & Sykes, L. R., 1968. Seismology and the new global tectonics, *Journal of Geophysical Research*, **73**(18), 5855–5899.
- Jeanloz, R. & Thompson, A. B., 1983. Phase transitions and mantle discontinuities, *Reviews of Geophysics*, **21**(1), 51–74.
- Jeffreys, H., 1924. *The Earth. Its origin, history and physical constitution.*, Cambridge Univ. Press, 278 pp.
- Jiang, G., Zhao, D., & Zhang, G., 2015. Detection of metastable olivine wedge in the Western Pacific slab and its geodynamic implications, *Physics of the Earth and Planetary Interiors*, **238**, 1–7.

- Johnson, L. R., 1967. Array measurements of P velocities in the upper mantle, *Journal of Geophysical Research*, **72**(24), 6309–6325.
- Johnson, T. & Molnar, P., 1972. Focal mechanisms and plate tectonics of the Southwest Pacific, *Journal of Geophysical Research*, **77**(26), 5000–5032.
- Julian, B. R. & Anderson, D. L., 1968. Travel times, apparent velocities and amplitudes of body waves, *Bulletin of the Seismological Society of America*, **58**(1), 339–366.
- Kagan, Y., 1991. 3-D rotation of double-couple earthquake sources, *Geophysical Journal International*, **106**(3), 709–716.
- Kanamori, H., 1972. Mechanism of tsunami earthquakes, *Physics of the Earth and Planetary Interiors*, **6**(5), 346–359.
- Kanamori, H., 1977. The energy release in great earthquakes, *Journal of Geophysical Research*, **82**(20), 2981–2987.
- Kanamori, H. & Cipar, J. J., 1974. Focal process of the great Chilean earthquake May 22, 1960, *Physics of the Earth and Planetary Interiors*, **9**(2), 128–136.
- Kanamori, H., Anderson, D. L., & Heaton, T. H., 1998. Frictional melting during the rupture of the 1994 bolivian earthquake, *Science*, **279**(5352), 839–842.
- Kaneshima, S., Okamoto, T., & Takenaka, H., 2007. Evidence for a metastable olivine wedge inside the subducted Mariana slab, *Earth and Planetary Science Letters*, **258**(1-2), 219–227.
- Kárník, V., Kondorskaya, N., Riznitchenko, J. V., Savarensky, E., Soloviev, S., Shebalin, N., Vaněk, J., & Zátopek, A., 1962. Standardization of the earthquake

- magnitude scale, *Studia Geophysica et Geodaetica*, **6**(1), 41–48.
- Kawakatsu, H., 1991. Enigma of earthquakes at ridge-transform-fault plate boundaries distribution of non-double couple parameter of Harvard CMT Solutions, *Geophysical Research Letters*, **18**(6), 1103–1106.
- Kawakatsu, H., 1991a. Insignificant isotropic component in the moment tensor of deep earthquakes, *Nature*, **351**(6321), 50–53.
- Kawakatsu, H., 1996. Observability of the isotropic component of a moment tensor, *Geophysical Journal International*, **126**(2), 525–544.
- Kawakatsu, H. & Yoshioka, S., 2011. Metastable olivine wedge and deep dry cold slab beneath southwest Japan, *Earth and Planetary Science Letters*, **303**(1-2), 1–10.
- Kawasaki, I. & Tanimoto, T., 1981. Radiation patterns of body waves due to the seismic dislocation occurring in an anisotropic source medium, *Bulletin of the Seismological Society of America*, **71**(1), 37–50.
- Kennett, B. L. N., Engdahl, E. R., & Buland, R., 1995. Constraints on seismic velocities in the Earth from travel times, *Geophysical Journal International*, **122**(1), 108–124.
- Khalturin, V., Rautian, T., & Molnar, P., 1977. The spectral content of Pamir-Hindu Kush intermediate depth earthquakes: Evidence for a high- Q zone in the upper mantle, *Journal of Geophysical Research*, **82**, 2931–2943.
- Kikuchi, M. & Kanamori, H., 1994. The mechanism of the deep Bolivia earthquake of June 9, 1994, *Geophysical Research Letters*, **21**(22), 2341–2344.

- Kikuchi, M. & Kanamori, H., 1995. Source characteristics of the 1992 Nicaragua tsunami earthquake inferred from teleseismic body waves, *Pure Applied Geophysics*, **144**, 441–453.
- Kirby, S., Durham, W., & Stern, L., 1992. The ice I–II transformation: Mechanisms and kinetics under hydrostatic and nonhydrostatic conditions, In: Maeno, N., Hondoh, T. (Eds.), *Physics and Chemistry of Ice*. Hokkaido Univ. Press, Sapporo, pp. 456–463.
- Kirby, S., Stein, S., Okal, E. A., & Rubie, D., 1996. Deep earthquakes and metastable mantle phase transformations in subducting oceanic lithosphere, *Rev. Geophys. Space Phys*, **34**, 261–306.
- Kirby, S. H., 1987. Localized polymorphic phase transformations in high-pressure faults and applications to the physical mechanism of deep earthquakes, *Journal of Geophysical Research: Solid Earth*, **92**(B13), 13789–13800.
- Kirby, S. H., Durham, W. B., & Stern, L. A., 1991. Mantle phase changes and deep-earthquake faulting in subducting lithosphere, *Science*, **252**(5003), 216.
- Kirby, S. H., Okal, E. A., & Engdahl, E. R., 1995. The 9 june 94 bolivian deep earthquake: An exceptional event in an extraordinary subduction zone, *Geophysical research letters*, **22**(16), 2233–2236.
- Knopoff, L. & Gilbert, F., 1959. Radiation from a strike-slip fault, *Bulletin of the Seismological Society of America*, **49**(2), 163–178.

- Kostoglodov, V., 1989. Maximum depth of earthquakes and phase transformation within the lithospheric slab descending in the mantle, *Physics and Interior Structure of the Earth*, Nauka, Moscow, pp. 52–57 [in Russian].
- Lay, T., Ye, L., Kanamori, H., Yamazaki, Y., Cheung, K. F., & Ammon, C. J., 2013. The February 6, 2013 M_w 8.0 Santa Cruz Islands earthquake and tsunami, *Tectonophysics*, **608**, 1109–1121.
- Leith, A. & Sharpe, J., 1936. Deep-focus earthquakes and their geological significance, *Journal of Geology*, **44**(8), 877–917.
- López, A. M. & Okal, E. A., 2006. A seismological reassessment of the source of the 1946 Aleutian ‘tsunami’ earthquake, *Geophysical Journal International*, **165**(3), 835–849.
- Louat, R. & Pelletier, B., 1989. Seismotectonics and present-day relative plate motions in the New Hebrides-North Fiji basin region, *Tectonophysics*, **167**(1), 41–55.
- Lundgren, P. & Giardini, D., 1995. The June 9 Bolivia and March 9 Fiji deep earthquakes of 1994: I. Source processes, *Geophysical Research Letters*, **22**(16), 2241–2244.
- Mainka, C., 1915. Über Zeitdifferenzen auffallender Einsätze in einem Seismogramm gegen den ersten, *Gerlands Beiträge. zur Geophysik*, **14**, 39–84.
- Marthelot, J., 1983. Patterns of seismicity in the Vanuatu (New Hebrides) arc: Regional variation and synthetics evolution., *PhD Thesis, Cornell University*, pp. 127 Ithaca, NY.

- McCaffrey, R., 2007. The next great earthquake, *Science*, **315**(5819), 1675–1676.
- McCaffrey, R. & Abers, G., 1988. SYN3: A program for inversion of teleseismic body waveforms on microcomputers, Tech. rep., Southeastern Center for Electrical Engineering Education Inc, St Cloud, FL.
- McComb, H. E., , & West, C., 1931. List of seismological stations of the world, *Bulletin of the National Research Council*, pp. 1–119.
- Meng, L., Ampuero, J.-P., & Bürgmann, R., 2014. The 2013 Okhotsk deep-focus earthquake: Rupture beyond the metastable olivine wedge and thermally controlled rise time near the edge of a slab, *Geophysical Research Letters*, **41**(11), 3779–3785.
- Millot-Langet, R., 2004. *Modélisation des modes propres et des sismogrammes longue-période d'une Terre anélastique en rotation: vers une tomographie anélastique du manteau*, Ph.D. thesis, Paris, Institut de Physique du Globe.
- Milne, J., 1886. *Earthquakes and other Earth movements*, *The International Scientific Series*, vol. LV, D. Appleton and Company.
- Montagner, J.-P. & Kennett, B., 1996. How to reconcile body-wave and normal-mode reference Earth models, *Geophysical Journal International*, **125**(1), 229–248.
- Myers, S. C., Wallace, T. C., Beck, S. L., Silver, P. G., Zandt, G., Vandecar, J., & Minaya, E., 1995. Implications of spatial and temporal development of the aftershock sequence for the M_w 8.3 June 9, 1994 deep Bolivian earthquake, *Geophysical Research Letters*, **22**(16), 2269–2272.

- Nakano, H., 1923. Notes on the nature of forces which give rise to earthquake motions, *Seismological Bulletin, Central Meteorological Observatory, Japan*, **1**, 91–120.
- Nettles, M., Ekström, G., Dziewonski, A., & Maternovskaya, N., 2005. Source characteristics of the great Sumatra earthquake and its aftershocks, *Eos, Trans. Am. geophys. Un.*, **86**(18), JA11 [abstract].
- Newman, A. V. & Okal, E. A., 1998. Teleseismic estimates of radiated seismic energy: The E/M_0 discriminant for tsunami earthquakes, *Journal of Geophysical Research*, **103**, 26885–26898.
- Nowroozi, A. A., 1971. Seismo-tectonics of the Persian plateau, Eastern Turkey, Caucasus, and Hindu-Kush regions, *Bulletin of the Seismological Society of America*, **61**(2), 317–341.
- Officer, T. & Secco, R. A., 2020. Detection of high p, t transformational faulting in fe2sio4 via in-situ acoustic emission: Relevance to deep-focus earthquakes, *Physics of the Earth and Planetary Interiors*, p. 106429.
- Okal, E. A., 1978. A physical classification of the Earth's spheroidal modes, *Journal of Physics of the Earth*, **26**(1), 75–103.
- Okal, E. A., 1988. Seismic parameters controlling far-field tsunami amplitudes: A review, *Natural Hazards*, **1**(1), 67–96.
- Okal, E. A., 1992. A student's guide to teleseismic body-wave amplitudes, *Seismological Research Letters*, **63**(2), 169–180.

- Okal, E. A., 1996. Radial modes from the great 1994 Bolivian earthquake: No evidence for an isotropic component to the source, *Geophysical research letters*, **23**(5), 431–434.
- Okal, E. A., 2001. “Detached” deep earthquakes: are they really?, *Physics of the Earth and Planetary Interiors*, **127**(1-4), 109–143.
- Okal, E. A., 2008a. The excitation of tsunami by earthquakes, **in:** *The Sea: Ideas and Observations on Progress in the study of the Seas*, **15**, Eds. Bernard, E.N. & Robinson, A.R., pp. 137-177, Harvard Univ. Press.
- Okal, E. A., 2008b. The generation of T waves by earthquakes, *Advances in Geophysics*, **49**, 1–65.
- Okal, E. A., 2012. The South of Java earthquake of 1921 September 11: A negative search for a large interplate thrust event at the Java Trench, *Geophysical Journal International*, **190**(3), 1657–1672.
- Okal, E. A., 2013. From 3-Hz P waves to ${}_0S_2$: No evidence of a slow component to the source of the 2011 Tohoku earthquake, *Pure and Applied Geophysics*, **170**(6-8), 963–973.
- Okal, E. A., 2014. Far-field tsunami detection and warning, 1854–2014: One hundred and sixty years in the intricate relation between earthquake source and tsunami, *Seismological Research Letter*, **85**, 522, [abstract].
- Okal, E. A., 2015. Historical seismograms: Preserving an endangered species, *Geo-ResJ*, **6**, 53–64.

- Okal, E. A., 2019. Energy and magnitude: A historical perspective, *Pure and Applied Geophysics*, **176**(9), 3815–3849.
- Okal, E. A. & Bina, C. R., 1994. The deep earthquakes of 1921–1922 in Northern Peru, *Physics of the Earth and Planetary Interiors*, **87**(1-2), 33–54.
- Okal, E. A. & Borrero, J. C., 2011. The ‘tsunami earthquake’ of 1932 June 22 in Manzanillo, Mexico: Seismological study and tsunami simulations, *Geophysical Journal International*, **187**(3), 1443–1459.
- Okal, E. A. & Geller, R., 1979. On the observability of isotropic seismic sources: The July 31, 1970 Colombian earthquake, *Physics of the Earth and Planetary Interiors*, **18**, 176–196.
- Okal, E. A. & Jo, B.-G., 1990. Q measurements for phase X overtones, *Pure and Applied Geophysics*, **132**(1-2), 331–362.
- Okal, E. A. & Kirby, S. H., 1995. Frequency-moment distribution of deep earthquakes; Implications for the seismogenic zone at the bottom of slabs, *Physics of the Earth and Planetary Interiors*, **92**(3-4), 169–187.
- Okal, E. A. & Kirby, S. H., 1998. Deep earthquakes beneath the Fiji Basin, SW Pacific: Earth’s most intense deep seismicity in stagnant slabs, *Physics of the Earth and Planetary Interiors*, **109**(1), 25–63.
- Okal, E. A. & Kirby, S. H., 2002. Energy-to-moment ratios for damaging intraslab earthquakes; Preliminary results on a few case studies, *USGS Open File Report*, **02-328**, 127–131.

- Okal, E. A. & Kirby, S. H., 2016. The large Bonin deep event of 30 May 2015: Seismogenesis in a detached and fragmented slab, *Geophysical Research Abstracts*, **18**, EGU2016-10715 [abstract].
- Okal, E. A. & Newman, A. V., 2001. Tsunami earthquakes: The quest for a regional signal, *Physics of the Earth and Planetary Interiors*, **124**(1-2), 45–70.
- Okal, E. A. & Saloor, N., 2017. Historical tsunami earthquakes in the Southwest Pacific: An extension to $\Delta > 80^\circ$ of the energy-to-moment parameter Θ , *Geophysical Journal International*, **210**(2), 852–873.
- Okal, E. A. & Stein, S., 2009. Observations of ultra-long period normal modes from the 2004 Sumatra–Andaman earthquake, *Physics of the Earth and Planetary Interiors*, **175**(1-2), 53–62.
- Okal, E. A. & Talandier, J., 1989. M_m : A variable-period mantle magnitude, *Journal of Geophysical Research: Solid Earth*, **94**(B4), 4169–4193.
- Okal, E. A., Alasset, P.-J., Hyvernaud, O., & Schindel e, F., 2003. The deficient T waves of tsunami earthquakes, *Geophysical Journal International*, **152**(2), 416–432.
- Okal, E. A., Fritz, H. M., Raveloson, R., Joelson, G., Pan ořkova, P., & Rambo-lamanana, G., 2006. Madagascar field survey after the December 2004 Indian Ocean tsunami, *Earthquake Spectra*, **22**(S3), 263–283.
- Okal, E. A., Hongsresawat, S., & Stein, S., 2012. Split-mode evidence for no ultra-slow component to the source of the 2010 Maule, Chile, earthquake, *Bulletin of the Seismological Society of America*, **102**(1), 391–397.

- Okal, E. A., Kirby, S. H., & Kalligeris, N., 2016. The Showa Sanriku earthquake of 1933 March 2: A global seismological reassessment, *Geophysical Journal International*, **206**(3), 1492–1514.
- Okal, E. A., Saloor, N., Kirby, S. H., & Nettles, M., 2018. An implosive component to the source of the deep sea of okhotsk earthquake of 24 may 2013: Evidence from radial modes and cmt inversion, *Physics of the Earth and Planetary Interiors*, **281**, 68–78.
- Orowan, E., 1960. Mechanism of seismic faulting, *Geological Society of America Memoirs*, **79**, 323–346.
- Parham, R., Greenhalgh, S., & McCue, K., 1988. The South Australian seismic network, *BMR Journal of Australian Geology and Geophysics*, **10**, 345–355.
- Pelayo, A. M. & Wiens, D. A., 1992. Tsunami earthquakes: Slow thrust-faulting events in the accretionary wedge, *Journal of Geophysical Research: Solid Earth*, **97**(B11), 15321–15337.
- Pelletier, B., Calmant, S., & Pillet, R., 1998. Current tectonics of the Tonga–New Hebrides region, *Earth and Planetary Science Letters*, **164**(1-2), 263–276.
- Pérez-Campos, X. & Beroza, G. C., 2001. An apparent mechanism dependence of radiated seismic energy, *Journal of Geophysical Research: Solid Earth*, **106**(B6), 11127–11136.
- Peterson, J. & Hutt, C. R., 2014. World-wide standardized seismograph network: A data users guide, *US Geological Survey, Open-File Report*, 2014-1218, 74 pp.

- Pilgrim, L., 1913. Die Berechnung der Laufzeiten eines Erdstosses mit Berücksichtigung der Herdtiefen, gestützt auf neuere Beobachtungen., *Gerlands Beiträge. zur Geophysik*, **12**, 363–483.
- Polet, J. & Kanamori, H., 2000. Shallow subduction zone earthquakes and their tsunamigenic potential, *Geophysical Journal International*, **142**(3), 684–702.
- Poli, P. & Prieto, G. A., 2016. Global rupture parameters for deep and intermediate-depth earthquakes, *Journal of Geophysical Research: Solid Earth*, **121**(12), 8871–8887.
- Renshaw, C. E. & Schulson, E. M., 2017. Strength-limiting mechanisms in high-confinement brittle-like failure: Adiabatic transformational faulting, *Journal of Geophysical Research: Solid Earth*, **122**(2), 1088–1106.
- Richter, C. F., 1935. An instrumental earthquake magnitude scale, *Bulletin of the Seismological Society of America*, **25**(1), 1–32.
- Richter, C. F., 1958. *Elementary Seismology*, W.H. Freeman and Company, 768 p.
- Romanowicz, B. & Mitchell, B. J., 2007. Deep Earth structure: Q of the Earth from crust to core, *Treatise on Geophysics*, **1**(21), 731–774.
- Roth, E. G., Wiens, D. A., Dorman, L. M., Hildebrand, J., & Webb, S. C., 1999. Seismic attenuation tomography of the Tonga-Fiji region using phase pair methods, *Journal of Geophysical Research: Solid Earth*, **104**(B3), 4795–4809.
- Ruff, L. & Kanamori, H., 1980. Seismicity and the subduction process, *Physics of the Earth and Planetary interiors*, **23**(3), 240–252.

- Russakoff, D., Ekström, G., & Tromp, J., 1997. A new analysis of the great 1970 Colombia earthquake and its isotropic component, *Journal of Geophysical Research: Solid Earth*, **102**(B9), 20423–20434.
- Salaree, A., 2019. Theoretical and computational contributions to the modeling of global tsunamis, *PhD Dissertation*, Northwestern University, 359 p.
- Saloor, N. & Okal, E. A., 2018. Extension of the energy-to-moment parameter Θ to intermediate and deep earthquakes, *Physics of the Earth and Planetary Interiors*, **274**, 37–48.
- Schellart, W. P. & Rawlinson, N., 2013. Global correlations between maximum magnitudes of subduction zone interface thrust earthquakes and physical parameters of subduction zones, *Physics of the Earth and Planetary Interiors*, **225**, 41–67.
- Schubnel, A., Brunet, F., Hilairet, N., Gasc, J., Wang, Y., & Green, H. W., 2013. Deep-focus earthquake analogs recorded at high pressure and temperature in the laboratory, *Science*, **341**(6152), 1377–1380.
- Silver, P. G., Beck, S. L., Wallace, T. C., Meade, C., Myers, S. C., James, D. E., & Kuehnel, R., 1995. Rupture characteristics of the deep Bolivian earthquake of 9 June 1994 and the mechanism of deep-focus earthquakes, *Science*, **268**(5207), 69–73.
- Sippl, C., Schurr, B., Yuan, X., Mechie, J., Schneider, F., Gadoev, M., Orunbaev, S., Oimahmadov, I., Haberland, C., Abdybachaev, U., et al., 2013. Geometry of the Pamir-Hindu Kush intermediate-depth earthquake zone from local seismic data, *Journal of Geophysical Research: Solid Earth*, **118**(4), 1438–1457.

- Solov'ev, S. & Go, C., 1984a. Catalogue of tsunamis on the Eastern shore of the Pacific Ocean, *Can. Transl. Fish. Aquat. Sci.*, **5078**, 293 pp.
- Solov'ev, S. & Go, C., 1984b. Catalogue of tsunamis on the Western shore of the Pacific Ocean, *Can. Transl. Fish. Aquat. Sci.*, **5077**, 439 pp.
- Stechsulte, V. C., 1932. The Japanese earthquake of March 29, 1928, and the problem of depth of focus, *Bulletin of the Seismological Society of America*, **22**(2), 81–137.
- Stein, S. & Geller, R. J., 1977. Amplitudes of the Earth's split normal modes, *Journal of Physics of the Earth*, **25**(2), 117–142.
- Stein, S. & Okal, E. A., 2005. Speed and size of the Sumatra earthquake, *Nature*, **434**(7033), 581–582.
- Stein, S. & Okal, E. A., 2007. Ultralong period seismic study of the December 2004 Indian Ocean earthquake and implications for regional tectonics and the subduction process, *Bulletin of the Seismological Society of America*, **97**(1A), S279–S295.
- Stein, S., Spencer, B. D., & Brooks, E. M., 2015. Metrics for assessing earthquake-hazard map performance, *Bulletin of the Seismological Society of America*, **105**(4), 2160–2173.
- Steketee, J., 1958. Some geophysical applications of the elasticity theory of dislocations, *Canadian Journal of Physics*, **36**(9), 1168–1198.
- Storchak, D. A., Di Giacomo, D., Bondár, I., Engdahl, E. R., Harris, J., Lee, W. H., Villaseñor, A., & Bormann, P., 2013. Public release of the ISC–GEM global

- instrumental earthquake catalogue (1900–2009), *Seismological Research Letters*, **84**(5), 810–815.
- Sykes, L. R., 1966. The seismicity and deep structure of island arcs, *Journal of Geophysical Research*, **71**(12), 2981–3006.
- Tajima, F., Ruff, L. J., Kanamori, H., Zhang, J., & Mogi, K., 1990. Earthquake source processes and subduction regime in the Santa Cruz Islands region, *Physics of the Earth and Planetary Interiors*, **61**(3-4), 269–290.
- Tanioka, Y., Ruff, L., & Satake, K., 1997. What controls the lateral variation of large earthquake occurrence along the Japan Trench?, *Island Arc*, **6**(3), 261–266.
- Taylor, F. W., Isacks, B., Jouannic, C., Bloom, A., & Dubois, J., 1980. Coseismic and Quaternary vertical tectonic movements, Santo and Malekula Islands, New Hebrides island arc, *Journal of Geophysical Research: Solid Earth*, **85**(B10), 5367–5381.
- Taylor, F. W., Jouannic, C., & Bloom, A., 1985. Quaternary uplift of the Torres Islands, Northern New Hebrides frontal arc: Comparison with Santo and Malekula Islands, Central New Hebrides frontal arc, *Journal of Geology*, **93**(4), 419–438.
- Teng, T.-L., 1968. Attenuation of body waves and the Q structure of the mantle, *Journal of Geophysical Research*, **73**(6), 2195–2208.
- Tibi, R., Bock, G., & Wiens, D. A., 2003. Source characteristics of large deep earthquakes: Constraint on the faulting mechanism at great depths, *Journal of Geophysical Research: Solid Earth*, **108**(B2), B001948, 25 pp.

- Tsuboi, S., Miyoshi, T., Nakamura, T., Obayashi, M., & Tono, Y., 2013. Source mechanism of May 24, 2013 Sea of Okhotsk deep earthquake ($M_w = 8.3$) estimated by broadband waveform modeling, *Eos Transaction of American Geophysical Union*, **94**, (53), S41C-07 [abstract].
- Turner, H., 1922. On the arrival of earthquake waves at the antipodes, and on the measurement of the focal depth of an earthquake., *Geophysical Supplements to the Monthly Notices of the Royal Astronomical Society*, **1**, 1–13.
- Vaišnys, J. R. & Pilbeam, C. C., 1976. Deep-earthquake initiation by phase transformations, *Journal of Geophysical Research*, **81**(5), 985–988.
- Vallée, M., 2013. Source time function properties indicate a strain drop independent of earthquake depth and magnitude, *Nature Communications*, **4**, 2606, 6 p.
- Van der Hilst, R., 1995. Complex morphology of subducted lithosphere in the mantle beneath the Tonga trench, *Nature*, **374**, 154–157.
- Vassiliou, M. & Kanamori, H., 1982. The energy release in earthquakes, *Bulletin of the Seismological Society of America*, **72**(2), 371–387.
- Vavryčuk, V., 2004. Inversion for anisotropy from non-double-couple components of moment tensors, *Journal of Geophysical Research: Solid Earth*, **109**(B7), B07306 13p.
- Vavryčuk, V., 2005. Focal mechanisms in anisotropic media, *Geophysical Journal International*, **161**(2), 334–346.
- Veith, K. & Clawson, G., 1972. Magnitude from short-period *P*-wave data, *Bulletin of the Seismological Society of America*, **62**(2), 435–452.

- Vidale, J. E. & Hedlin, M. A., 1998. Evidence for partial melt at the core-mantle boundary north of Tonga from the strong scattering of seismic waves, *Nature*, **391**(6668), 682–685.
- Vvedenskaya, A., 1956. Opredelenie poleĭ smeshcheniĭ pri zemletryaseniĭakh s pomoshch'yu teorii dislokatsii, *Akademia Nauk SSSR, Seria Geofizicheskaya*, **6**, 277–284, [in Russian].
- Wadati, K., 1927. Existence and study of deep-focus earthquakes, *J. Meteorol. Soc. Jpn., Ser. 2*, **5**, 119–145.
- Wadati, K., 1928. Shallow and deep earthquakes, *Geophys. Mag.*, **1**, 162–202.
- Wadati, K., 1929. Shallow and deep earthquakes (2nd paper), *Geophys. Mag.*, **2**, 1–36.
- Wagner, L. S. & Okal, E. A., 2019. The Pucallpa Nest and its constraints on the geometry of the Peruvian Flat Slab, *Tectonophysics*, **762**, 97–108.
- Wang, Y., Zhu, L., Shi, F., Schubnel, A., Hilairet, N., Yu, T., Rivers, M., Gasc, J., Addad, A., Deldicque, D., et al., 2017. A laboratory nanoseismological study on deep-focus earthquake micromechanics, *Science advances*, **3**(7), e1601896, 12 p.
- Webb, T. H., Wesnousky, S. G., & Helmberger, D. V., 1985. A body-wave analysis of the 1966 Gisborne, New Zealand, earthquake, *Tectonophysics*, **113**(3-4), 271–282.
- Wei, S., Helmberger, D., Zhan, Z., & Graves, R., 2013. Rupture complexity of the M_w 8.3 Sea of Okhotsk earthquake: Rapid triggering of complementary earthquakes?, *Geophysical Research Letters*, **40**(19), 5034–5039.

- Weinstein, S. A. & Okal, E. A., 2005. The mantle magnitude M_m and the slowness parameter Θ : Five years of real-time use in the context of tsunami warning, *Bulletin of the Seismological Society of America*, **95**(3), 779–799.
- Wiechert, E., 1903. *Theorie der automatischen Seismographen*, Weidmannsche Buchhandlung.
- Wielandt, E., 2002. Seismometry, *International Handbook of Earthquake and Engineering Seismology, Part A*, eds Lee, W.H.K., Kanamori, H., Jennings, P.C. & Kisslinger, C., pp. 283-304, Academic Press.
- Wiens, D. A. & McGuire, J. J., 1995. The 1994 Bolivia and Tonga events: Fundamentally different types of deep earthquakes?, *Geophysical Research Letters*, **22**(16), 2245–2248.
- Wiens, D. A., McGuire, J. J., Shore, P. J., Bevis, M. G., Draunidalo, K., Prasad, G., & Helu, S. P., 1994. A deep earthquake aftershock sequence and implications for the rupture mechanism of deep earthquakes, *Nature*, **372**(6506), 540–543.
- Winslow, N. W. & Ruff, L. J., 1999. A hybrid method for calculating the radiated wave energy of deep earthquakes, *Physics of the Earth and Planetary Interiors*, **115**(3), 181–190.
- Woodhouse, J., 1980. The coupling and attenuation of nearly resonant multiplets in the Earth's free oscillation spectrum, *Geophysical Journal International*, **61**(2), 261–283.
- Wu, F. T., 1966. Lower limit of the total energy of earthquakes and partitioning of energy among seismic waves. Reflected waves and crustal structures, *PhD*

Dissertation, California Institute of Technology.

- Wysession, M. E., Okal, E. A., & Miller, K. L., 1991. Intraplate seismicity of the Pacific Basin, 1913–1988, *Pure and Applied Geophysics*, **135**(2), 261–359.
- Wyss, M. & Molnar, P., 1972. Source parameters of intermediate and deep focus earthquakes in the Tonga arc, *Physics of the Earth and Planetary Interiors*, **6**(4), 279–292.
- Wyss, M., Habermann, R., & Heiniger, C., 1983. Seismic quiescence, stress drops, and asperities in the New Hebrides arc, *Bulletin of the Seismological Society of America*, **73**(1), 219–236.
- Ye, L., Lay, T., Kanamori, H., & Koper, K. D., 2013. Energy release of the 2013 M_w 8.3 Sea of Okhotsk earthquake and deep slab stress heterogeneity, *Science*, **341**(6152), 1380–1384.
- Ye, L., Lay, T., Zhan, Z., Kanamori, H., & Hao, J.-L., 2016. The isolated ~ 680 km deep 30 May 2015 $M_w = 7.9$ Ogasawara (Bonin) Islands earthquake, *Earth and Planetary Science Letters*, **433**, 169–179.
- Zhan, Z. & Kanamori, H., 2016. Recurring large deep earthquakes in Hindu Kush driven by a sinking slab, *Geophysical Research Letters*, **43**(14), 7433–7441.
- Zhan, Z., Kanamori, H., Tsai, V. C., Helmberger, D. V., & Wei, S., 2014. Rupture complexity of the 1994 Bolivia and 2013 Sea of Okhotsk deep earthquakes, *Earth and Planetary Science Letters*, **385**, 89–96.
- Zhang, H., van der Lee, S., Bina, C. R., & Ge, Z., 2016. Multi-segment frequency-dependent rupture process: Rupture mechanism of the May 24, 2013 $M_w = 8.3$

Sea of Okhotsk deep-focus earthquake, *Seismological Research Letters*, **87**, 543–544, [abstract].

Zhao, D., Fujisawa, M., & Toyokuni, G., 2017. Tomography of the subducting Pacific slab and the 2015 Bonin deepest earthquake (M_w 7.9), *Scientific reports*, **7**, 44487 8 p.

Zöppritz, K., Geiger, L., & Gutenberg, B., 1912. Über Erdbebenwellen. V, *Nachr. k. Gess. d. Wiss. z. Göttingen, math.-phys. Kl.*, pp. 121–206.

APPENDIX A

**Determination of 1947 short-period instrument
magnification at Tucson (TUC)**

The record at Tucson used in Chapter 4 for the Hikurangi earthquake of 25 March 1947 was written on a Benioff short-period seismometer (Benioff, 1932). Its mechanical properties (pendulum period $T_p = 1$ s; galvanometer period $T_g = 0.24$ s) are described on the film rolls of the Historical Seismogram Filming Project (HSFP; Glover et al. 1988), and reported in Charlier & van Gils's (1953) generally authoritative catalog. However, the most critical parameter, namely the maximum magnification, V_{max} , is not documented on the rolls; a value of 3×10^4 is listed by Charlier & van Gils's (1953) for the broadband combination ($T_p = 1$ s; $T_g = 77$ s) reproducing (with a slightly shorter galvanometer period) the famous Pasadena "1 - 90" instrument (Fig. A1a), but this is excessive since typical magnifications used for this type of instrument were in the range of 3000, a factor of 10 smaller. We surmise that the listed value of 3×10^4 results from a typographic error (by one line) and really pertains to the short-period instrument. Similarly, the coupling constants " μ^2 " of 0.8 and 1.0 listed by Charlier & van Gils's (1953) for the broadband and short-period systems are probably erroneous since coupling constants for electromagnetic instruments were usually very small (0.05 for the Benioff short-period at Pasadena),

and those values (0.8 and 1.0) are actually listed as damping constants H on the microfilmed metadata (Fig. A1b). We thus propose, tentatively, that the constants of the short-period system at Tucson were $T_p = 1$ s; $T_g = 0.24$ s; $\mu^2 = 0.05$; $H_p = 0.8$; $H_g = 1$; $V_{max} = 30000$.

In order to verify the value of V_{max} , we compare estimates of body-wave magnitudes m_b which we measured at TUC and PAS for two events occurring in 1946 and 1947 at shorter distances and well recorded at both stations on what amounts to the same instruments, except for a possible difference of magnification. In 1947, and following some experimentation by V.H. Benioff in the 1930s, the magnification at Pasadena had been standardized at $V_{max}^{PAS} = 30000$, as documented by operational ledgers at the California Institute of Technology (H. Kanamori, personal communication, 2015), and reported in Charlier & van Gils (1953).

We use the earthquakes of 10 November 1946 and 01 November 1947 in Peru, for which we compute magnitudes at Pasadena of $m_b = 7.14$ and 7.19 , respectively. Matching these numbers at Tucson would require parameters $V_{max} = 28,650$ and $48,650$, respectively, with a geometrical average of $37,300$. Under the circumstances, it seems legitimate to take as V_{max} for the short-period system at Tucson the value of $30,000$ listed by Charlier & van Gils (1953) for the broadband instrument.

(a) TUCSON Entry in Charlier and van Gils [1953]

Fiche n°		Casier:		Station : TUCSON												
Lat.: 32°14', 8 N.		Long.: 110°50', 1 W.		Altitude: 770 m. Pays : U.S.A.												
Temps utilisé : Temps Moyen de Greenwich (signaux horaires scientifiques)																
Sous-sol : Caliche et moraine		Profondeur: 1 m.		Température: Piliers: béton												
Enregistrements troublés par microséismes: oui, légèrement.																
Constantes :																
Type de l'instrument	Composante	Enregistrement	Amortissement	Construction	Marque de temps	Défilement: t min.	Sens du mouvement masse	T _g	V _m	T _p	K	μ^2	A _r	l _r	M	v
Benioff	V	gal	ém	1936	d	30	+	77,0	3,10	1,0		0,80				gr.
					d	60	+	0,236				1,0				

(b) TUCSON Metadata, HSFP, March 1947

STATION CONSTANTS					
Month, year		Mar. 1947		Observer J.H. Nelson	
Lat. 32 ° 15 ' N		Long. 110 ° 50 ' W		Elev. 770m	
INSTRUMENT	COMPONENT	T _g	V _m	DAMPING	U _p *
W-A	N-S	8.0	466	.81	S
W-A	EW	8.0	457	.83	E
Benioff	Vert	1.0		.80	Up
SP Galv		.236		1.0	
LP Galv		77		1.0	

* Rapid upward movements of the traces correspond to the ground movements indicated in this column. The traces progress from ~~left~~ to ~~right~~. The day's run begins at the ~~top~~ of the gram.
 May 1946 (W-A)
 June 1937 (Benioff)

REMARKS:
 Benioff period measured frequently during month.
 Adjusted when necessary.

Figure A1. (a) Excerpt from the entry for station Tucson in Charlier & van Gils's (1953) catalog. Note the magnification listed for the broadband 1-77 system (red arrow), and the coupling μ^2 , both of them probably mistyped. (b) Metadata for station Tucson from the film rolls of the HSFP. Note the more probable interpretation of the parameters 0.8 and 1 in (a) as damping constants (blue arrow). See text for details.

APPENDIX B

Tables

Table B.1. Full dataset used in Chapter 5

Date	Origin	Epicenter		Depth		Moment	Number	Θ	
Year	Jul	Time (GMT)	(°N)	(°E)	(km)	Bin	(dyn × cm)	of stations	
<i>Final Dataset</i>									
1990	132	04:50	48.94	141.38	613	D-2	0.820E+27	10	-4.05
1991	023	01:12	52.13	179.02	102	I-1	0.510E+26	12	-4.67
1992	073	16:01	52.39	-178.96	210	I-2	0.480E+26	11	-4.75
1992	242	19:19	33.40	138.09	309	D-1	0.290E+26	11	-4.45
1992	246	05:50	-6.11	112.21	637	D-2	0.110E+27	10	-4.78
1992	292	13:08	-6.30	130.09	136	I-2	0.200E+26	10	-4.94
1993	019	14:39	38.70	133.96	462	D-2	0.630E+26	12	-4.67
1993	108	09:16	-11.67	-76.58	113	I-1	0.280E+26	10	-4.95
1993	150	17:08	1.56	127.25	113	I-1	0.170E+26	11	-4.83
1993	154	09:38	-14.71	167.26	144	I-2	0.150E+26	10	-4.65
1993	159	23:17	-31.62	-69.13	125	I-1	0.320E+26	11	-4.35
1993	166	13:06	-5.19	145.48	228	I-2	0.190E+26	10	-5.03
1993	219	00:00	26.68	125.84	165	I-2	0.470E+26	13	-5.06
1993	261	05:02	36.48	71.80	118	I-1	0.170E+26	13	-4.72
1993	272	11:16	0.62	121.70	89	I-1	0.390E+26	11	-4.68
1993	284	15:54	32.12	138.02	365	D-1	0.250E+27	18	-4.66
1994	010	15:53	-13.28	-69.27	604	D-2	0.250E+27	10	-4.23
1994	019	16:26	-17.37	-178.28	561	D-2	0.140E+26	11	-4.86
1994	055	15:25	-17.33	-173.69	128	I-1	0.180E+26	16	-4.85
1994	068	23:28	-17.69	-178.11	568	D-2	0.310E+28	10	-4.17
1994	160	00:33	-13.82	-67.25	647	D-2	0.260E+29	10	-3.77

1994	181	09:23	36.34	71.00	254	I-2	0.310E+26	15	-4.45
1994	194	11:45	-7.63	127.90	179	I-2	0.610E+26	14	-4.38
1994	202	18:36	42.30	133.04	489	D-2	0.110E+28	24	-3.84
1994	220	21:08	24.76	94.97	146	I-2	0.180E+26	23	-4.79
1994	231	10:02	-26.72	-63.42	563	D-2	0.560E+26	11	-4.50
1994	234	17:26	-11.62	166.46	150	I-2	0.200E+26	12	-4.47
1994	242	19:42	-6.97	124.31	604	D-2	0.210E+26	11	-4.67
1994	243	09:07	43.60	146.03	82	I-1	0.210E+26	26	-5.03
1994	271	16:39	-5.75	110.28	653	D-2	0.900E+26	19	-4.82
1994	289	05:10	45.78	149.32	121	I-1	0.140E+27	24	-4.91
1994	300	22:20	-25.75	179.39	541	D-2	0.113E+27	11	-3.56
1994	308	01:13	-9.40	-71.07	619	D-2	0.150E+26	12	-4.53
1994	319	20:18	-5.61	110.29	571	D-2	0.640E+26	19	-4.42
1994	346	07:41	-17.44	-69.66	161	I-2	0.260E+26	12	-4.73
1994	364	15:12	18.66	145.59	228	I-2	0.310E+26	22	-4.80
1995	017	16:54	-20.71	-179.13	649	D-2	0.350E+26	12	-4.50
1995	084	22:44	-11.05	165.91	82	I-1	0.200E+26	15	-4.72
1995	090	14:01	38.16	135.11	367	D-1	0.210E+26	27	-4.20
1995	097	22:06	-15.37	-173.15	88	I-1	0.130E+28	17	-4.40
1995	098	17:45	21.93	142.68	281	I-2	0.250E+26	24	-4.02
1995	103	02:34	-13.34	170.71	646	D-2	0.210E+26	14	-4.53
1995	110	08:45	6.33	126.89	103	I-1	0.590E+26	18	-4.55
1995	113	06:38	6.39	124.17	535	D-2	0.160E+26	17	-4.70
1995	122	06:06	-3.77	-77.07	113	I-1	0.130E+27	11	-4.76
1995	175	06:58	-3.83	153.93	387	D-1	0.180E+27	17	-4.84
1995	180	12:24	-19.42	168.95	143	I-2	0.930E+26	12	-4.71
1995	209	14:29	-21.18	-174.90	125	I-1	0.430E+26	16	-4.25
1995	231	21:43	5.22	-75.69	129	I-1	0.770E+26	10	-4.58
1995	235	07:06	18.88	145.30	599	D-2	0.440E+27	21	-4.25
1995	236	01:55	18.93	145.19	594	D-2	0.220E+26	22	-4.28
1995	236	07:54	18.79	145.33	612	D-2	0.170E+26	23	-4.44
1995	236	07:55	18.85	145.35	610	D-2	0.170E+26	23	-4.55
1995	259	01:03	-6.18	155.50	156	I-2	0.150E+26	13	-4.65
1995	261	06:56	-6.76	129.30	177	I-2	0.118E+26	21	-4.20
1995	274	17:06	29.30	139.02	448	D-1	0.170E+26	25	-4.64
1995	282	13:43	-21.35	170.10	115	I-1	0.330E+26	10	-4.79

1995	287	08:00	-25.53	-177.17	172	I-2	0.230E+26	10	-4.82
1995	293	19:21	19.19	145.58	207	I-2	0.148E+26	24	-4.59
1995	294	02:38	16.67	-93.42	164	I-2	0.710E+27	10	-5.09
1995	302	19:40	-21.72	-179.26	634	D-2	0.170E+26	14	-4.16
1995	344	23:47	-21.52	-177.78	434	D-1	0.190E+26	13	-4.06
1995	359	04:43	-6.93	129.65	161	I-2	0.470E+27	15	-4.74
1996	017	10:06	-4.23	139.98	97	I-1	0.150E+26	16	-4.85
1996	032	07:18	44.79	146.33	170	I-2	0.230E+26	31	-4.96
1996	053	14:59	45.29	148.56	130	I-1	0.360E+26	29	-4.53
1996	059	09:44	2.03	126.29	92	I-1	0.480E+26	16	-4.54
1996	077	14:48	-14.57	167.19	171	I-2	0.125E+27	13	-3.98
1996	107	00:30	-23.98	-176.47	116	I-1	0.640E+27	12	-4.81
1996	147	01:43	-22.49	171.55	112	I-1	0.129E+26	12	-4.26
1996	161	01:12	17.36	145.98	160	I-2	0.710E+26	18	-4.83
1996	169	11:22	-7.38	123.02	584	D-2	0.730E+28	19	-4.48
1996	178	03:22	27.82	139.85	479	D-2	0.270E+26	26	-4.73
1996	188	21:36	22.02	142.99	253	I-2	0.260E+26	20	-4.79
1996	197	16:51	18.76	145.82	189	I-2	0.280E+26	20	-4.52
1996	218	22:38	-20.72	-178.16	555	D-2	0.136E+28	16	-3.86
1996	272	14:10	10.19	125.33	238	I-2	0.350E+26	23	-5.12
1996	293	14:53	-20.47	-178.24	606	D-2	0.260E+27	13	-4.19
1996	310	09:41	-30.95	-179.73	367	D-1	0.150E+27	11	-4.82
1996	316	09:22	19.27	95.05	86	I-1	0.110E+26	27	-3.76
1996	319	13:47	-21.29	-176.10	202	I-2	0.190E+26	16	-4.28
1996	322	21:11	-22.22	-179.57	602	D-2	0.120E+26	11	-4.28
1996	336	23:09	-30.46	-179.40	370	D-1	0.190E+26	10	-4.75
1996	357	14:53	43.29	138.78	245	I-2	0.680E+26	30	-4.33
1997	017	11:20	-8.88	123.72	113	I-1	0.200E+26	15	-4.41
1997	023	02:15	-22.04	-65.92	282	I-2	0.580E+27	17	-5.04
1997	080	12:07	-31.18	179.90	453	D-2	0.320E+26	13	-4.39
1997	084	16:44	-8.86	-71.25	618	D-2	0.130E+26	14	-4.65
1997	113	19:44	13.83	145.05	95	I-1	0.640E+26	20	-4.99
1997	123	16:46	-31.70	-179.06	119	I-1	0.280E+27	10	-4.63
1997	133	14:13	36.51	70.68	189	I-2	0.500E+26	21	-4.31
1997	145	23:22	-32.02	-179.95	345	D-1	0.520E+27	12	-4.71
1997	247	04:23	-26.45	178.52	621	D-2	0.210E+27	15	-3.85

1997	269	15:48	-5.29	129.13	268	I-2	0.130E+26	20	-4.49
1997	279	12:30	9.79	125.95	114	I-1	0.520E+26	22	-4.88
1997	287	09:53	-21.94	-176.15	166	I-2	0.450E+28	11	-4.54
1997	301	06:15	-4.44	-76.55	119	I-1	0.720E+27	12	-4.90
1997	307	19:17	-6.72	129.11	221	I-2	0.160E+26	21	-4.67
1997	313	22:56	13.88	-89.30	178	I-2	0.390E+26	10	-4.55
1997	319	07:05	43.82	145.07	157	I-2	0.150E+26	33	-4.33
1997	345	07:56	4.11	-75.84	190	I-2	0.400E+26	14	-4.95
1997	351	05:51	36.53	70.62	224	I-2	0.320E+26	25	-4.86
1997	356	02:05	-5.56	148.05	197	I-2	0.630E+27	18	-4.62
1998	001	06:11	24.12	142.21	92	I-1	0.380E+26	23	-4.29
1998	004	06:11	-22.31	171.08	114	I-1	0.180E+28	14	-4.70
1998	027	19:55	-22.53	179.29	617	D-2	0.350E+26	14	-4.14
1998	027	21:05	-22.39	179.29	629	D-2	0.540E+26	14	-4.32
1998	038	01:18	24.92	141.87	534	D-2	0.480E+26	28	-4.18
1998	051	12:18	36.50	70.88	244	I-2	0.400E+26	25	-4.60
1998	088	19:48	-17.57	-178.85	554	D-2	0.640E+27	17	-3.85
1998	093	22:01	-7.96	-74.48	154	I-2	0.950E+26	12	-4.83
1998	104	03:41	-23.73	-179.81	510	D-2	0.150E+26	17	-4.47
1998	135	05:58	13.99	144.99	168	I-2	0.126E+26	25	-4.32
1998	136	02:22	-22.27	-179.35	609	D-2	0.230E+27	17	-3.98
1998	190	14:45	-30.51	-178.71	155	I-2	0.240E+27	11	-4.65
1998	190	19:39	60.39	-152.74	151	I-2	0.210E+26	42	-5.36
1998	197	11:56	-10.91	166.09	100	I-1	0.410E+27	19	-4.46
1998	232	06:40	28.99	139.47	426	D-1	0.470E+27	28	-4.67
1998	271	13:34	-8.36	112.40	153	I-2	0.770E+26	20	-4.37
1998	276	11:15	28.40	127.66	219	I-2	0.170E+26	25	-4.82
1998	281	04:51	-16.02	-71.59	141	I-2	0.200E+26	15	-4.39
1998	319	02:44	-21.55	-175.87	171	I-2	0.280E+26	22	-4.64
1998	348	19:35	-14.96	167.27	127	I-1	0.108E+26	17	-3.71
1998	361	00:38	-21.69	-175.86	160	I-2	0.200E+27	15	-4.56
1999	019	03:35	-4.72	153.66	88	I-1	0.370E+27	21	-5.29
1999	028	18:24	-4.50	153.55	96	I-1	0.390E+26	20	-5.13
1999	037	21:47	-12.78	166.58	98	I-1	0.111E+28	13	-3.46
1999	093	06:17	-16.38	-72.54	89	I-1	0.200E+27	14	-4.53
1999	095	11:08	-5.65	149.71	149	I-2	0.150E+28	21	-4.70

1999	098	13:10	43.66	130.47	575	D-2	0.510E+27	34	-4.07
1999	099	12:16	-26.37	178.28	636	D-2	0.210E+26	14	-4.41
1999	103	10:38	-21.54	-175.89	173	I-2	0.190E+27	12	-4.45
1999	130	20:33	-5.38	150.97	145	I-2	0.470E+27	13	-4.52
1999	132	17:59	43.12	143.70	96	I-1	0.240E+26	32	-4.60
1999	138	04:19	-5.89	148.60	124	I-1	0.140E+26	21	-4.85
1999	184	05:30	26.29	140.55	434	D-1	0.140E+26	32	-3.91
1999	226	00:16	-5.86	104.46	99	I-1	0.510E+26	17	-4.56
1999	240	12:40	-1.36	-77.75	198	I-2	0.250E+26	18	-4.67
1999	258	03:01	-20.73	-67.37	218	I-2	0.450E+26	18	-4.48
1999	312	16:45	36.48	70.81	237	I-2	0.640E+26	31	-4.64
1999	315	18:05	1.15	100.03	218	I-2	0.190E+26	29	-4.30
1999	334	04:01	-19.01	-69.37	138	I-2	0.770E+26	16	-4.67
1999	341	21:29	-15.75	-173.62	149	I-2	0.440E+26	12	-4.52
2000	008	16:47	-16.84	-173.81	162	I-2	0.690E+27	24	-4.69
2000	057	08:11	13.79	144.98	126	I-1	0.210E+26	25	-4.85
2000	063	22:09	-7.37	128.55	162	I-2	0.410E+26	27	-4.28
2000	088	11:00	22.32	143.76	100	I-1	0.320E+28	31	-4.54
2000	094	15:20	4.10	125.75	140	I-2	0.190E+26	25	-4.56
2000	114	09:27	-28.41	-63.04	608	D-2	0.310E+27	20	-4.17
2000	114	17:01	-28.43	-62.96	610	D-2	0.150E+26	19	-4.53
2000	125	20:36	-17.72	-178.31	540	D-2	0.580E+26	22	-4.70
2000	129	10:28	-4.38	150.14	496	D-2	0.160E+26	23	-4.45
2000	133	18:43	-23.72	-66.85	227	I-2	0.660E+27	21	-4.88
2000	133	23:10	36.04	70.53	106	I-1	0.300E+26	28	-4.81
2000	161	23:31	30.47	137.79	492	D-2	0.260E+26	31	-4.60
2000	166	02:15	-25.45	178.38	615	D-2	0.530E+26	21	-4.25
2000	166	17:00	4.75	127.61	111	I-1	0.360E+26	25	-4.65
2000	168	07:55	-33.95	-69.92	109	I-1	0.470E+26	19	-4.63
2000	199	22:53	36.24	70.82	146	I-2	0.340E+26	26	-4.62
2000	219	07:27	28.89	139.68	411	D-1	0.117E+28	30	-3.90
2000	220	14:33	-6.95	123.53	648	D-2	0.600E+26	22	-3.87
2000	228	04:30	-31.42	-179.95	367	D-1	0.910E+26	17	-4.31
2000	255	17:17	-15.74	-173.33	125	I-1	0.310E+26	21	-4.66
2000	278	14:37	11.16	-62.29	110	I-1	0.210E+26	25	-4.94
2000	295	05:25	-17.40	-174.79	300	D-1	0.270E+26	22	-5.13

2000	301	04:21	26.31	140.69	388	D-1	0.140E+26	34	-3.87
2000	303	08:37	-5.21	153.95	92	I-1	0.300E+27	23	-5.42
2000	312	07:50	-5.39	154.18	90	I-1	0.250E+26	24	-5.05
2000	353	01:19	-21.11	-178.98	656	D-2	0.760E+26	16	-3.84
2000	357	10:13	44.76	147.14	141	I-2	0.200E+26	34	-4.50
2001	009	16:49	-14.90	167.11	114	I-1	0.420E+27	20	-4.54
2001	047	05:59	-7.11	117.62	538	D-2	0.150E+26	26	-4.68
2001	056	02:21	36.41	70.62	193	I-2	0.170E+26	27	-4.21
2001	057	05:58	46.79	144.54	396	D-1	0.150E+26	40	-4.72
2001	118	04:49	-18.07	-176.68	367	D-1	0.210E+27	23	-4.51
2001	145	05:06	-8.07	110.24	135	I-2	0.320E+26	25	-4.94
2001	146	10:57	-20.25	-177.65	414	D-1	0.420E+26	21	-5.14
2001	154	02:41	-29.37	-178.23	199	I-2	0.610E+27	20	-4.37
2001	180	18:35	-19.68	-66.39	287	I-2	0.150E+26	21	-4.55
2001	184	13:10	21.66	142.99	308	D-1	0.540E+26	26	-4.35
2001	185	07:06	-21.81	-176.31	187	I-2	0.630E+26	23	-4.49
2001	209	07:32	58.82	-154.97	147	I-2	0.106E+27	43	-4.18
2001	255	08:48	-20.84	-178.90	634	D-2	0.570E+26	17	-4.52
2001	261	02:19	-7.49	127.97	140	I-2	0.109E+26	25	-4.06
2001	275	00:48	-16.20	-173.36	109	I-1	0.170E+26	21	-4.80
2001	309	23:07	-17.12	-178.96	580	D-2	0.270E+26	21	-4.28
2001	327	20:43	36.43	71.50	100	I-1	0.140E+26	27	-4.58
2001	336	13:01	39.49	141.09	124	I-1	0.560E+26	34	-4.34
2001	343	18:15	-0.02	122.96	154	I-2	0.135E+26	23	-4.22
2001	361	10:54	-14.66	167.13	162	I-2	0.190E+26	20	-4.39
2002	001	11:29	6.35	125.87	131	I-1	0.300E+26	28	-4.77
2002	002	14:50	-17.63	178.84	681	D-2	0.200E+26	18	-4.07
2002	003	07:05	35.71	70.76	123	I-1	0.150E+26	26	-4.37
2002	022	04:53	35.53	26.59	90	I-1	0.210E+26	29	-4.51
2002	062	12:08	36.57	70.42	229	I-2	0.127E+28	32	-3.72
2002	068	12:27	-56.00	-27.30	128	I-1	0.113E+26	16	-3.93
2002	087	04:56	-21.69	-68.57	138	I-2	0.590E+26	22	-4.40
2002	128	05:26	-17.85	-174.06	138	I-2	0.260E+26	22	-5.15
2002	178	07:16	-13.43	166.84	195	I-2	0.130E+26	20	-4.37
2002	179	17:19	43.74	130.45	582	D-2	0.111E+28	39	-3.61
2002	181	21:29	-22.13	179.43	632	D-2	0.490E+26	19	-4.59

2002	214	23:11	29.35	139.25	442	D-1	0.260E+26	32	-4.95
2002	221	13:31	-16.25	-175.85	381	D-1	0.160E+26	27	-4.62
2002	231	11:01	-21.74	-179.08	631	D-2	0.350E+28	22	-3.90
2002	231	11:08	-24.16	178.49	699	D-2	0.430E+28	23	-3.76
2002	258	08:39	44.77	130.04	589	D-2	0.420E+26	34	-4.39
2002	267	03:57	-31.48	-69.12	120	I-1	0.280E+26	25	-4.44
2002	277	19:05	-20.86	-178.74	651	D-2	0.350E+26	20	-4.14
2002	285	20:09	-8.30	-71.66	539	D-2	0.240E+27	25	-4.38
2002	289	10:12	51.84	157.58	105	I-1	0.230E+26	41	-4.86
2002	290	04:23	-19.80	-178.23	622	D-2	0.200E+26	24	-4.38
2002	295	11:39	-20.50	-178.30	561	D-2	0.190E+26	23	-4.36
2002	316	01:46	-56.49	-26.89	116	I-1	0.250E+26	13	-4.52
2002	321	04:53	47.81	146.45	480	D-2	0.105E+28	40	-3.51
2002	344	04:27	-24.02	179.28	539	D-2	0.110E+26	22	-4.30
2003	004	05:15	-20.72	-177.32	395	D-1	0.600E+26	23	-4.42
2003	069	02:09	1.74	127.23	100	I-1	0.420E+26	30	-4.47
2003	073	12:54	-17.50	-174.77	282	I-2	0.390E+26	27	-4.71
2003	117	16:03	-20.94	169.71	84	I-1	0.320E+26	23	-4.84
2003	125	15:50	0.44	127.38	122	I-1	0.420E+26	27	-4.90
2003	146	23:13	6.90	123.85	580	D-2	0.230E+27	31	-4.45
2003	163	08:59	-5.97	154.95	185	I-2	0.280E+26	28	-4.56
2003	167	22:08	55.48	160.25	181	I-2	0.240E+27	45	-4.81
2003	171	06:19	-7.37	-71.89	556	D-2	0.440E+27	25	-4.67
2003	182	05:52	4.69	122.67	605	D-2	0.110E+26	26	-4.40
2003	202	13:53	-5.61	149.01	193	I-2	0.360E+26	28	-4.16
2003	208	02:04	-21.09	-176.12	216	I-2	0.910E+26	27	-4.45
2003	208	06:25	46.99	139.23	477	D-2	0.150E+27	43	-4.67
2003	208	11:41	-20.05	-65.19	351	D-1	0.110E+26	25	-4.43
2003	223	21:22	12.16	93.35	84	I-1	0.130E+26	37	-4.98
2003	242	00:05	-14.84	167.16	137	I-2	0.110E+26	24	-4.88
2003	243	23:08	43.38	132.37	493	D-2	0.180E+26	34	-4.91
2003	290	10:19	-5.55	154.07	138	I-2	0.460E+26	28	-4.32
2003	316	08:26	33.31	137.09	382	D-1	0.400E+26	32	-4.57
2004	011	09:29	-20.21	-179.20	683	D-2	0.130E+26	22	-4.45
2004	025	11:43	-16.75	-173.79	143	I-2	0.110E+27	26	-4.41
2004	051	05:58	-11.65	166.25	90	I-1	0.100E+26	27	-4.71

2004	072	22:13	-15.48	-174.74	291	I-2	0.100E+26	12	-4.86
2004	077	03:21	-21.24	-65.60	297	I-2	0.160E+26	22	-4.70
2004	096	21:24	36.52	70.84	184	I-2	0.630E+26	33	-4.37
2004	100	15:23	-13.22	167.16	226	I-2	0.500E+26	23	-5.05
2004	162	15:19	55.79	160.32	190	I-2	0.230E+27	27	-4.75
2004	177	02:35	-6.63	130.59	83	I-1	0.160E+26	28	-4.62
2004	182	23:37	0.79	124.95	101	I-1	0.240E+26	27	-4.86
2004	190	10:30	47.12	151.69	135	I-2	0.320E+26	23	-5.01
2004	197	04:27	-17.68	-178.52	577	D-2	0.480E+27	22	-4.43
2004	207	14:35	-2.68	104.38	601	D-2	0.100E+28	28	-4.01
2004	223	01:47	36.52	70.60	206	I-2	0.120E+26	13	-4.76
2004	259	19:10	14.39	120.30	106	I-1	0.100E+26	38	-4.68
2004	282	14:36	13.91	120.50	111	I-1	0.520E+26	41	-4.46
2004	289	04:08	24.48	122.74	102	I-1	0.860E+26	40	-4.81
2004	312	02:02	47.93	144.52	493	D-2	0.180E+26	42	-4.48
2004	317	06:36	-26.85	-63.18	583	D-2	0.140E+26	26	-4.47
2004	322	21:09	-19.87	-178.40	629	D-2	0.720E+26	20	-4.46
2004	341	16:26	-18.84	-178.27	466	D-2	0.150E+26	21	-4.47
2005	033	02:30	13.86	144.81	159	I-2	0.320E+26	29	-5.13
2005	036	03:34	15.88	146.19	132	I-1	0.900E+26	31	-4.64
2005	036	12:23	5.47	123.67	531	D-2	0.520E+27	31	-4.50
2005	039	14:48	-14.18	167.13	197	I-2	0.130E+27	21	-4.67
2005	061	10:42	-6.54	129.99	196	I-2	0.570E+27	26	-4.03
2005	076	13:37	15.20	-91.63	182	I-2	0.210E+26	22	-4.70
2005	078	17:34	-21.88	-179.27	609	D-2	0.350E+26	18	-3.99
2005	080	12:23	-24.88	-63.54	572	D-2	0.230E+27	26	-4.80
2005	080	12:43	-24.71	-63.56	572	D-2	0.470E+26	52	-4.50
2005	089	17:41	-22.31	-179.64	585	D-2	0.200E+26	20	-4.24
2005	101	14:54	-7.36	-77.96	132	I-1	0.110E+26	24	-4.44
2005	138	09:10	-56.43	-26.50	107	I-1	0.110E+26	16	-5.00
2005	140	12:40	-24.43	179.04	573	D-2	0.100E+26	22	-4.40
2005	153	10:56	-24.35	-67.21	193	I-2	0.140E+26	24	-4.65
2005	163	19:26	-56.40	-26.70	98	I-1	0.130E+26	14	-4.72
2005	164	22:44	-20.02	-69.23	95	I-1	0.530E+28	22	-4.51
2005	252	07:26	-5.20	153.95	84	I-1	0.370E+28	26	-5.83
2005	264	02:25	43.90	146.41	107	I-1	0.130E+26	40	-4.61

2005	269	01:55	-5.60	-76.20	108	I-1	0.220E+28	20	-4.95
2005	288	15:51	25.29	123.43	195	I-2	0.540E+26	41	-4.47
2005	321	19:26	-22.46	-68.13	155	I-2	0.190E+27	24	-4.65
2005	325	15:36	30.97	130.31	155	I-2	0.210E+26	37	-4.70
2005	342	09:01	-5.52	147.11	219	I-2	0.170E+26	28	-4.65
2005	346	21:47	36.45	71.06	210	I-2	0.800E+26	32	-4.32
2005	357	21:47	-1.59	-77.76	197	I-2	0.190E+26	23	-4.84
2006	002	22:13	-19.80	-177.72	590	D-2	0.690E+27	21	-4.16
2006	015	11:58	-7.92	122.70	262	I-2	0.210E+26	13	-4.43
2006	027	16:58	-5.61	128.20	397	D-1	0.350E+28	31	-4.29
2006	033	12:48	-17.77	-178.13	612	D-2	0.150E+27	24	-4.55
2006	055	14:15	-17.94	-179.42	641	D-2	0.170E+26	23	-4.36
2006	057	03:08	-23.59	-179.82	554	D-2	0.460E+26	22	-4.49
2006	064	08:07	-20.09	-175.22	214	I-2	0.160E+26	24	-4.62
2006	066	06:28	-14.90	167.20	144	I-2	0.210E+26	23	-4.66
2006	120	08:17	-15.13	167.29	130	I-1	0.170E+26	22	-4.82
2006	136	10:39	-31.41	-178.91	151	I-2	0.180E+28	18	-4.14
2006	142	13:08	54.19	158.87	198	I-2	0.240E+26	45	-4.52
2006	153	07:31	-20.77	-178.54	585	D-2	0.120E+26	21	-4.18
2006	160	05:58	-17.36	-178.62	586	D-2	0.180E+26	23	-4.67
2006	162	20:01	33.15	131.34	145	I-2	0.420E+26	39	-4.84
2006	173	10:53	45.37	149.52	105	I-1	0.110E+26	40	-4.54
2006	178	02:59	-19.77	-178.04	597	D-2	0.300E+26	22	-4.33
2006	219	22:18	-15.76	167.63	158	I-2	0.200E+27	22	-4.62
2006	237	00:44	-24.44	-67.18	186	I-2	0.900E+26	22	-4.97
2006	252	04:13	-7.23	120.27	583	D-2	0.340E+26	25	-4.35
2006	260	09:34	-31.90	-67.15	146	I-2	0.220E+26	23	-4.75
2006	265	02:32	-26.85	-63.05	602	D-2	0.110E+26	25	-4.19
2006	273	16:26	-15.72	-73.34	120	I-1	0.100E+26	24	-4.71
2006	276	18:03	-19.01	168.91	166	I-2	0.360E+26	21	-4.75
2006	291	10:45	-15.12	167.27	127	I-1	0.430E+26	23	-5.36
2006	310	20:56	-5.47	146.71	160	I-2	0.110E+26	28	-4.92
2006	317	01:26	-26.10	-63.47	573	D-2	0.230E+27	27	-4.38
2006	318	14:21	-6.34	127.99	353	D-1	0.170E+26	27	-4.79
2006	335	03:58	3.46	99.05	208	I-2	0.380E+26	29	-4.63
2006	346	15:48	3.83	125.10	215	I-2	0.370E+26	28	-4.56

2006	361	20:15	-5.73	154.49	368	D-1	0.130E+26	25	-4.34
2007	017	04:28	-3.28	139.89	102	I-1	0.120E+26	27	-4.94
2007	067	05:03	29.89	140.52	135	I-2	0.160E+26	38	-4.65
2007	068	03:22	43.22	133.65	451	D-2	0.140E+26	40	-3.92
2007	093	03:35	36.53	70.62	223	I-2	0.290E+26	33	-4.58
2007	099	02:24	-20.00	-177.97	614	D-2	0.100E+26	24	-4.40
2007	111	07:12	-3.46	151.46	405	D-1	0.190E+26	30	-4.66
2007	119	12:41	51.89	-179.81	122	I-1	0.280E+26	48	-4.62
2007	126	21:11	-19.44	-179.04	691	D-2	0.610E+26	22	-4.81
2007	126	22:01	-19.31	-179.05	692	D-2	0.150E+26	23	-4.76
2007	149	01:03	-4.71	151.96	137	I-2	0.170E+26	29	-5.06
2007	150	20:22	52.01	157.78	123	I-1	0.560E+26	45	-4.87
2007	187	01:09	16.48	-93.89	114	I-1	0.150E+26	22	-4.64
2007	193	05:23	-8.00	-74.42	156	I-2	0.150E+26	23	-4.89
2007	197	14:17	36.84	135.03	375	D-1	0.210E+27	38	-4.70
2007	202	13:27	-8.08	-71.30	638	D-2	0.140E+26	21	-4.35
2007	202	15:34	-22.31	-66.00	280	I-2	0.540E+26	23	-4.96
2007	213	17:08	-15.41	167.41	126	I-1	0.740E+27	22	-4.78
2007	220	17:04	-6.03	107.58	305	D-1	0.260E+28	30	-4.60
2007	238	12:37	-17.34	-173.84	130	I-1	0.150E+26	25	-4.86
2007	246	16:14	45.77	150.33	100	I-1	0.240E+26	39	-4.78
2007	268	05:16	-30.69	-179.85	421	D-1	0.230E+26	20	-4.70
2007	271	13:38	21.94	143.07	276	I-2	0.200E+28	38	-4.70
2007	278	07:17	-25.27	179.50	541	D-2	0.680E+26	22	-4.83
2007	289	21:05	-25.70	179.72	512	D-2	0.100E+27	22	-4.68
2007	304	03:30	18.83	145.59	211	I-2	0.900E+27	35	-4.76
2007	320	03:13	-2.50	-78.00	114	I-1	0.180E+27	26	-4.98
2007	322	05:40	-22.67	-66.48	262	I-2	0.130E+26	22	-4.73
2007	323	00:52	-21.05	-178.63	563	D-2	0.330E+26	23	-4.12
2007	333	19:00	15.06	-61.41	148	I-2	0.160E+28	31	-4.91
2007	343	07:28	-25.75	-177.22	150	I-2	0.710E+28	21	-4.60
2007	349	08:03	-7.75	127.59	176	I-2	0.130E+26	32	-4.54
2008	006	05:14	36.98	22.87	92	I-1	0.230E+26	28	-4.55
2008	015	17:52	-22.05	-179.34	603	D-2	0.730E+26	23	-4.34
2008	032	12:10	-21.53	-179.27	630	D-2	0.130E+26	23	-4.10
2008	043	12:50	16.35	-94.51	87	I-1	0.630E+26	22	-4.65

2008	047	14:45	-21.58	-68.77	135	I-2	0.160E+26	24	-4.61
2008	082	21:24	51.98	-178.50	135	I-2	0.260E+26	49	-4.89
2008	084	20:39	-20.31	-69.42	129	I-1	0.210E+26	21	-4.91
2008	105	09:45	-56.04	-27.75	115	I-1	0.140E+26	16	-4.68
2008	109	20:39	-17.26	-178.98	578	D-2	0.370E+26	25	-4.39
2008	130	21:51	12.36	143.28	83	I-1	0.170E+27	31	-5.16
2008	155	16:20	-10.46	161.42	91	I-1	0.270E+26	27	-4.48
2008	158	13:42	-7.63	127.87	138	I-2	0.110E+26	34	-4.80
2008	185	03:02	-23.41	-179.69	590	D-2	0.280E+26	24	-4.52
2008	187	02:12	54.12	153.37	611	D-2	0.450E+28	50	-4.43
2008	190	09:13	-16.26	-72.00	126	I-1	0.260E+26	23	-5.06
2008	201	22:39	-17.22	-177.05	395	D-1	0.520E+26	25	-4.91
2008	205	15:26	39.73	141.51	99	I-1	0.190E+27	44	-4.22
2008	217	20:45	-5.93	130.47	174	I-2	0.300E+26	32	-4.73
2008	239	21:00	-7.76	-74.49	158	I-2	0.480E+26	22	-4.93
2008	243	06:54	-6.33	147.49	88	I-1	0.500E+26	29	-4.83
2008	245	04:00	-25.51	-177.25	172	I-2	0.120E+26	20	-4.40
2008	247	11:25	-26.85	-63.30	571	D-2	0.330E+26	26	-4.38
2008	252	18:52	-13.37	166.75	125	I-1	0.310E+27	23	-4.19
2008	255	00:00	1.91	127.34	120	I-1	0.900E+26	32	-4.54
2008	286	20:55	-20.30	-65.23	362	D-1	0.230E+26	27	-4.45
2008	296	12:55	-18.40	-174.98	244	I-2	0.440E+26	28	-4.62
2008	309	18:35	-17.03	168.31	232	I-2	0.410E+26	24	-5.08
2008	313	07:49	-15.07	-173.94	132	I-1	0.110E+26	28	-4.82
2008	326	07:05	-8.97	159.73	126	I-1	0.130E+26	27	-4.25
2008	329	09:02	54.27	154.71	502	D-2	0.110E+28	47	-4.43
2008	337	12:31	19.17	145.99	119	I-1	0.100E+26	36	-4.76
2008	341	10:55	-7.44	124.84	407	D-1	0.520E+26	30	-4.36
2008	344	17:28	-15.98	168.04	237	I-2	0.150E+26	25	-4.56
2008	360	03:20	5.74	125.66	198	I-2	0.350E+26	32	-4.53
2009	003	20:23	36.44	70.36	206	I-2	0.900E+26	34	-4.66
2009	022	20:16	-7.51	128.55	160	I-2	0.170E+26	33	-4.46
2009	087	17:59	-2.89	139.66	91	I-1	0.100E+26	31	-4.55
2009	111	05:26	50.64	155.59	152	I-2	0.240E+26	49	-4.85
2009	116	00:06	-30.19	-178.24	152	I-2	0.180E+26	22	-4.71
2009	123	16:21	14.56	-91.50	91	I-1	0.320E+26	26	-5.08

2009	132	01:26	-5.83	149.62	91	I-1	0.170E+26	29	-4.58
2009	221	10:55	33.05	138.19	302	D-1	0.490E+27	43	-4.54
2009	230	21:20	-25.99	-178.08	277	I-2	0.360E+26	19	-4.86
2009	240	01:51	-7.09	123.46	634	D-2	0.270E+27	30	-4.48
2009	245	18:00	-29.24	-178.67	259	I-2	0.210E+26	20	-4.59
2009	246	13:26	31.08	130.19	168	I-2	0.240E+26	42	-4.77
2009	277	10:58	6.77	123.56	626	D-2	0.110E+27	33	-4.08
2009	280	21:41	4.11	122.51	580	D-2	0.180E+27	35	-4.70
2009	283	21:24	47.77	152.79	126	I-1	0.100E+26	48	-4.77
2009	288	12:11	-3.04	139.45	105	I-1	0.130E+26	30	-4.86
2009	295	19:51	36.51	70.82	182	I-2	0.210E+26	34	-4.36
2009	297	14:40	-6.10	130.57	155	I-2	0.300E+27	34	-4.32
2009	302	17:44	36.39	70.66	219	I-2	0.280E+26	35	-4.63
2009	313	10:44	-17.11	178.53	604	D-2	0.100E+28	23	-4.41
2009	318	19:44	-23.04	-66.83	221	I-2	0.220E+26	27	-4.77
2009	326	22:47	-31.47	179.66	437	D-1	0.220E+26	20	-4.53
2009	344	02:30	53.44	152.77	656	D-2	0.330E+26	52	-4.41
2009	358	00:23	42.12	134.93	390	D-1	0.390E+26	46	-4.22
2010	046	21:51	-7.39	128.76	136	I-2	0.270E+26	34	-4.48
2010	049	01:13	42.48	130.66	579	D-2	0.260E+27	46	-4.60
2010	063	14:02	-13.65	167.00	185	I-2	0.580E+26	21	-4.31
2010	067	09:47	19.26	144.67	432	D-1	0.170E+26	36	-4.27
2010	079	14:00	-3.32	152.33	414	D-1	0.900E+26	31	-4.80
2010	101	22:08	37.10	-3.69	617	D-2	0.420E+26	47	-4.79
2010	123	10:27	29.58	141.28	99	I-1	0.160E+26	44	-4.55
2010	139	04:15	-5.13	-77.55	132	I-1	0.130E+26	25	-4.61
2010	143	22:46	-14.03	-74.52	109	I-1	0.180E+26	23	-4.43
2010	144	16:18	-8.08	-71.64	591	D-2	0.580E+26	26	-4.72
2010	151	19:51	11.16	93.70	128	I-1	0.640E+26	42	-4.90
2010	181	04:31	-23.19	179.26	582	D-2	0.450E+26	23	-4.47
2010	193	00:11	-22.40	-68.61	135	I-2	0.270E+26	26	-4.59
2010	202	09:16	3.08	128.09	122	I-1	0.180E+26	32	-4.79
2010	204	22:08	6.54	123.59	597	D-2	0.110E+28	34	-4.78
2010	204	22:51	6.62	123.90	577	D-2	0.360E+28	36	-4.27
2010	204	23:15	6.83	123.48	641	D-2	0.190E+28	36	-4.21
2010	205	05:35	6.23	123.56	556	D-2	0.890E+26	37	-4.94

2010	210	07:31	6.69	123.41	614	D-2	0.100E+27	33	-4.54
2010	216	07:15	-5.59	146.90	218	I-2	0.640E+26	29	-4.88
2010	227	15:09	-5.85	148.41	174	I-2	0.330E+26	28	-4.65
2010	228	19:35	-20.74	-178.67	604	D-2	0.220E+26	23	-4.29
2010	247	08:52	-17.33	-173.54	83	I-1	0.150E+26	29	-5.00
2010	260	19:21	36.44	70.79	208	I-2	0.300E+26	31	-4.66
2010	281	05:43	2.83	128.10	136	I-2	0.220E+26	34	-4.80
2010	334	03:24	28.69	139.26	461	D-2	0.190E+27	45	-5.03
2010	347	01:14	-6.61	155.71	145	I-2	0.250E+26	27	-4.52
2010	349	11:29	-7.46	128.80	147	I-2	0.120E+26	38	-4.68
2010	362	08:34	-23.49	-179.73	571	D-2	0.340E+26	22	-4.54
2011	001	09:56	-27.02	-63.21	586	D-2	0.440E+27	25	-4.22
2011	005	06:46	-22.48	171.58	126	I-1	0.170E+26	20	-4.37
2011	012	21:32	26.94	139.94	512	D-2	0.740E+26	46	-4.31
2011	024	02:45	38.50	72.78	119	I-1	0.150E+26	36	-4.82
2011	031	06:03	-21.91	-175.13	90	I-1	0.130E+26	27	-4.53
2011	035	13:53	24.46	94.68	104	I-1	0.310E+26	42	-4.35
2011	041	14:39	4.14	122.91	521	D-2	0.770E+26	38	-4.52
2011	041	14:41	4.22	123.28	518	D-2	0.770E+26	38	-4.39
2011	043	17:57	-20.93	-175.19	112	I-1	0.180E+26	28	-4.54
2011	052	10:57	-25.95	178.47	568	D-2	0.790E+26	22	-4.13
2011	056	13:07	17.98	-95.20	128	I-1	0.120E+26	28	-4.64
2011	065	12:31	-18.28	-69.73	126	I-1	0.310E+26	25	-4.78
2011	065	14:32	-56.41	-26.68	101	I-1	0.810E+26	18	-4.53
2011	069	17:08	-6.95	116.71	517	D-2	0.100E+27	37	-4.54
2011	093	14:07	-17.65	-178.45	562	D-2	0.490E+26	27	-4.30
2011	097	13:11	17.28	-94.12	154	I-2	0.140E+27	26	-5.19
2011	108	13:03	-34.40	-179.83	100	I-1	0.790E+26	20	-4.76
2011	159	03:06	-17.37	-69.84	150	I-2	0.100E+26	29	-4.77
2011	164	14:31	2.74	126.35	82	I-1	0.500E+26	15	-4.35
2011	210	07:42	-23.78	179.92	539	D-2	0.150E+27	25	-4.66
2011	231	03:54	-16.52	-176.73	415	D-1	0.290E+26	27	-4.98
2011	236	17:46	-7.68	-74.66	144	I-2	0.430E+27	28	-4.48
2011	242	06:57	-6.47	126.68	469	D-2	0.270E+27	37	-4.86
2011	245	13:47	-28.56	-63.08	597	D-2	0.140E+27	27	-4.46
2011	246	04:48	-56.57	-26.44	99	I-1	0.440E+26	20	-4.85

2011	246	22:55	-20.79	169.72	152	I-2	0.440E+27	22	-4.75
2011	248	17:55	2.88	97.86	95	I-1	0.140E+27	36	-4.58
2011	258	19:31	-21.61	-179.21	625	D-2	0.120E+28	20	-4.25
2011	294	08:02	43.83	142.52	192	I-2	0.220E+26	50	-4.29
2011	300	00:15	-17.98	-179.40	609	D-2	0.110E+26	26	-4.48
2011	311	22:35	11.60	-85.98	173	I-2	0.130E+26	28	-4.53
2011	312	02:59	27.13	125.77	231	I-2	0.300E+27	45	-4.77
2011	326	18:48	-15.40	-65.18	554	D-2	0.890E+26	32	-4.13
2011	345	09:54	-55.97	-27.78	123	I-1	0.300E+26	21	-4.58
2011	347	07:52	0.01	123.14	164	I-2	0.150E+26	38	-4.31
2011	348	05:04	-7.49	146.83	135	I-2	0.530E+27	30	-4.61
2012	001	05:27	31.61	138.17	352	D-1	0.190E+27	46	-4.79
2012	024	00:52	-25.00	178.72	582	D-2	0.420E+26	26	-4.35
2012	036	00:15	-19.02	168.88	156	I-2	0.180E+26	24	-4.77
2012	041	01:47	-17.98	-178.42	598	D-2	0.100E+26	25	-4.00
2012	065	07:46	-28.19	-63.27	565	D-2	0.190E+26	28	-4.16
2012	081	22:15	-6.26	145.96	127	I-1	0.100E+27	28	-4.86
2012	097	16:15	-4.68	153.55	97	I-1	0.200E+26	30	-5.25
2012	108	07:13	-5.66	147.16	209	I-2	0.240E+27	33	-4.57
2012	114	17:36	-28.51	-177.05	101	I-1	0.100E+26	21	-4.76
2012	119	10:08	-18.79	-174.26	141	I-2	0.120E+27	30	-4.54
2012	135	10:00	-18.00	-69.94	119	I-1	0.310E+26	29	-4.34
2012	147	21:48	26.87	140.17	472	D-2	0.110E+26	47	-4.51
2012	149	05:07	-28.25	-63.07	592	D-2	0.130E+27	27	-4.81
2012	154	07:52	-22.08	-63.59	550	D-2	0.120E+26	30	-4.53
2012	159	16:03	-15.98	-72.70	120	I-1	0.220E+26	30	-4.67
2012	175	04:34	2.98	97.77	105	I-1	0.200E+26	38	-4.35
2012	185	10:36	-40.05	173.63	230	I-2	0.370E+26	23	-4.59
2012	188	02:28	-14.74	167.19	169	I-2	0.460E+26	20	-5.13
2012	215	09:38	-8.58	-74.36	151	I-2	0.140E+26	27	-4.77
2012	227	02:59	49.97	145.70	598	D-2	0.480E+28	49	-4.34
2012	232	22:41	-4.92	144.60	81	I-1	0.300E+26	31	-5.07
2012	239	15:05	2.16	126.81	91	I-1	0.900E+26	37	-4.72
2012	274	16:31	1.89	-76.22	159	I-2	0.900E+27	29	-4.77
2012	291	04:42	4.26	124.49	333	D-1	0.130E+26	39	-4.22
2012	342	18:19	-38.31	176.08	165	I-2	0.400E+26	23	-4.90

2012	345	16:53	-6.65	129.83	159	I-2	0.560E+27	35	-4.65
2012	356	22:28	-14.31	167.17	199	I-2	0.130E+27	23	-4.57
2013	033	14:17	42.85	143.24	105	I-1	0.310E+27	47	-5.04
2013	040	14:16	1.16	-77.40	152	I-2	0.370E+27	29	-4.92
2013	047	04:37	5.77	125.95	107	I-1	0.240E+26	37	-4.77
2013	053	12:01	-27.89	-63.00	586	D-2	0.180E+26	27	-4.45
2013	084	23:02	14.62	-90.71	186	I-2	0.270E+26	23	-4.76
2013	095	13:00	42.77	131.02	572	D-2	0.320E+26	44	-4.22
2013	103	22:49	-19.10	169.51	273	I-2	0.140E+26	23	-4.74
2013	109	03:05	46.00	150.92	105	I-1	0.100E+28	48	-4.41
2013	110	04:51	-6.26	130.21	116	I-1	0.100E+26	33	-4.50
2013	111	03:22	30.02	138.88	430	D-1	0.190E+26	42	-4.42
2013	116	06:53	-28.67	-178.82	356	D-1	0.210E+26	23	-4.37
2013	131	20:46	-17.89	-174.74	242	I-2	0.410E+26	30	-4.94
2013	134	00:32	18.67	145.35	605	D-2	0.210E+27	36	-4.62
2013	143	21:07	-20.67	-175.29	160	I-2	0.330E+26	26	-4.80
2013	144	05:44	54.61	153.77	611	D-2	0.400E+29	52	-4.01
2013	144	14:56	52.36	151.48	642	D-2	0.160E+27	53	-3.97
2013	166	11:20	-33.82	179.63	200	I-2	0.130E+26	19	-4.62
2013	188	18:35	-4.10	153.98	383	D-1	0.110E+28	27	-4.78
2013	205	03:32	-23.23	-176.81	169	I-2	0.110E+26	26	-4.57
2013	207	07:07	-15.30	167.32	131	I-1	0.160E+26	22	-5.01
2013	224	00:53	-7.24	129.83	105	I-1	0.180E+26	33	-4.42
2013	224	04:16	-30.46	-179.58	348	D-1	0.210E+26	20	-4.56
2013	240	02:54	-27.73	179.84	492	D-2	0.290E+26	20	-4.33
2013	244	11:52	-7.61	128.24	128	I-1	0.680E+26	37	-4.70
2013	247	00:18	30.02	138.79	412	D-1	0.730E+26	39	-4.55
2013	249	11:33	20.24	122.31	188	I-2	0.110E+26	42	-4.33
2013	264	01:39	-7.32	119.92	551	D-2	0.150E+26	34	-4.67
2013	274	03:38	53.20	152.81	586	D-2	0.150E+27	50	-4.58
2013	279	16:38	12.14	141.72	116	I-1	0.140E+26	34	-4.99
2013	284	21:25	-30.57	-178.43	156	I-2	0.250E+26	20	-4.71
2013	296	08:23	-23.08	-176.74	168	I-2	0.120E+26	25	-4.50
2014	001	16:03	-13.89	167.10	198	I-2	0.800E+26	23	-4.30
2014	032	03:58	-56.97	-26.72	132	I-1	0.210E+26	18	-4.65
2014	038	08:40	-15.13	167.29	127	I-1	0.700E+26	24	-5.21

2014	057	21:13	53.60	-171.87	275	I-2	0.200E+26	54	-5.09
2014	061	20:11	27.34	127.46	125	I-1	0.670E+26	43	-4.85
2014	064	09:56	-14.64	169.80	661	D-2	0.460E+26	24	-4.68
2014	072	17:06	33.62	131.82	83	I-1	0.360E+26	43	-4.84
2014	085	03:29	-26.14	179.32	510	D-2	0.430E+26	22	-4.32
2014	086	03:49	-12.13	166.46	116	I-1	0.120E+26	26	-4.63
2014	101	20:29	11.70	-86.22	142	I-2	0.100E+27	26	-4.94
2014	121	06:36	-21.52	170.12	120	I-1	0.100E+27	22	-4.63
2014	124	09:15	-24.67	179.12	530	D-2	0.900E+26	25	-4.46
2014	124	09:25	-25.80	178.25	655	D-2	0.470E+26	24	-4.35
2014	124	20:18	34.89	139.48	165	I-2	0.130E+26	46	-4.63
2014	174	20:53	52.00	178.43	104	I-1	0.100E+29	55	-4.87
2014	181	19:55	28.42	138.75	523	D-2	0.280E+26	44	-4.83
2014	200	12:27	-15.64	-174.18	234	I-2	0.260E+26	29	-4.85
2014	202	14:54	-19.68	-178.32	627	D-2	0.290E+27	25	-4.23
2014	210	10:46	17.97	-95.69	109	I-1	0.460E+26	31	-4.82
2014	236	23:21	-14.61	-73.72	85	I-1	0.220E+27	27	-4.69
2014	260	06:14	13.54	144.51	140	I-2	0.170E+27	35	-4.70
2014	267	11:16	-23.78	-66.72	228	I-2	0.270E+26	27	-4.83
2014	268	17:51	62.00	-151.78	109	I-1	0.340E+26	53	-4.95
2014	305	18:57	-19.76	-177.61	445	D-1	0.570E+27	26	-4.74
2014	336	05:11	6.31	123.17	632	D-2	0.930E+26	40	-4.47
2014	340	22:05	-6.12	130.57	138	I-2	0.140E+26	39	-4.54
2014	344	21:03	25.51	122.40	262	I-2	0.200E+26	47	-4.49
2014	364	21:17	-20.27	-178.59	612	D-2	0.130E+26	23	-4.18
2014	365	00:06	-20.28	-178.61	609	D-2	0.100E+26	24	-4.45
2015	023	03:47	-17.06	168.36	231	I-2	0.190E+27	23	-4.84
2015	028	02:43	-20.97	-178.23	488	D-2	0.220E+26	23	-4.24
2015	033	10:49	-32.77	-67.14	177	I-2	0.320E+26	27	-4.49
2015	042	18:57	-23.14	-66.80	223	I-2	0.140E+27	29	-4.84
2015	058	13:45	-7.35	122.50	552	D-2	0.360E+27	37	-4.46
2015	069	20:55	6.83	-73.11	156	I-2	0.300E+26	30	-4.50
2015	075	03:00	-4.09	152.00	198	I-2	0.100E+26	33	-4.56
2015	081	05:46	-17.84	-178.48	616	D-2	0.160E+26	27	-4.71
2015	082	04:51	-18.47	-69.44	141	I-2	0.560E+26	28	-4.77
2015	112	22:57	-12.07	166.33	94	I-1	0.300E+26	27	-4.75

2015	118	16:39	-20.79	-178.71	591	D-2	0.170E+26	23	-4.05
2015	135	20:26	-2.61	102.14	158	I-2	0.150E+26	40	-5.00
2015	140	00:30	-19.35	-175.14	206	I-2	0.140E+26	30	-4.64
2015	149	07:00	56.71	-156.52	81	I-1	0.200E+27	56	-4.54
2015	150	11:23	27.94	140.56	681	D-2	0.770E+28	45	-4.18
2015	161	13:52	-22.48	-68.47	147	I-2	0.160E+26	27	-4.55
2015	167	06:17	-20.42	-178.93	665	D-2	0.130E+26	23	-4.64
2015	171	23:39	-23.53	-176.82	157	I-2	0.100E+26	24	-4.43
2015	172	21:28	-20.34	-178.36	571	D-2	0.120E+26	25	-4.22
2015	174	12:18	27.68	139.85	459	D-2	0.740E+26	44	-4.71
2015	210	02:35	60.02	-153.15	130	I-1	0.450E+26	58	-4.81
2015	236	09:41	-30.33	-178.86	243	I-2	0.130E+26	21	-4.36
2015	271	15:28	-23.84	-66.89	221	I-2	0.120E+26	26	-4.93
2015	293	21:52	-14.88	167.19	141	I-2	0.570E+27	25	-4.68
2015	299	09:09	36.55	70.42	209	I-2	0.220E+28	36	-4.13
2015	325	09:06	-7.22	130.11	100	I-1	0.140E+26	37	-4.76
2015	328	13:21	18.82	145.26	583	D-2	0.110E+26	38	-4.14
2015	328	22:45	-10.73	-71.12	611	D-2	0.260E+28	26	-4.42
2015	328	22:50	-10.11	-71.28	627	D-2	0.370E+28	26	-4.40
2015	330	05:45	-9.14	-71.35	614	D-2	0.130E+27	26	-4.77
2015	359	19:14	36.46	71.06	214	I-2	0.380E+26	39	-4.05
2016	011	17:08	44.46	141.01	254	I-2	0.310E+26	49	-4.65
2016	014	03:25	-19.77	-63.11	591	D-2	0.200E+26	26	-4.58
2016	024	10:30	59.75	-153.27	111	I-1	0.590E+27	54	-4.91
2016	030	03:25	53.86	158.73	168	I-2	0.860E+27	56	-4.64
2016	032	19:00	-30.81	-179.82	391	D-1	0.300E+26	23	-4.28
2016	101	10:28	36.44	71.04	211	I-2	0.110E+27	38	-4.33
2016	104	13:55	23.02	94.78	150	I-2	0.320E+27	46	-4.42
2016	109	13:06	-19.44	169.00	91	I-1	0.100E+26	24	-4.11
2016	148	04:08	-20.77	-178.61	581	D-2	0.590E+26	24	-4.43
2016	149	05:38	-22.13	-178.17	418	D-1	0.300E+27	28	-4.59
2016	152	05:23	25.42	122.35	250	I-2	0.430E+26	47	-5.13
2016	157	16:25	-4.51	125.56	449	D-1	0.350E+26	48	-4.38
2016	166	13:49	-18.83	168.70	127	I-1	0.280E+26	24	-4.72
2016	173	17:12	-3.37	152.03	361	D-1	0.320E+26	44	-5.13
2016	202	15:13	-18.97	168.85	175	I-2	0.170E+26	24	-4.61

2016	207	17:26	-26.15	-70.63	88	I-1	0.150E+26	26	-4.51
2016	211	21:18	18.50	145.70	209	I-2	0.470E+28	38	-4.63

Table B.2. Reference dataset of 146 shallow earthquakes used in Chapter 5

Date		Origin	Epicenter		Depth	Moment	Θ
_____		Time	_____		(km)	(dyn \times cm)	
Year	Jul	(GMT)	($^{\circ}$ N)	($^{\circ}$ E)			
1980	211	14:58	29.42	80.95	22	0.830E+26	-3.49
1981	114	21:50	-13.51	166.43	44	0.230E+27	-4.89
1981	196	07:59	-17.34	167.27	30	0.580E+27	-5.90
1985	355	01:13	-13.89	166.57	46	0.570E+27	-5.14
1987	003	22:04	-15.06	168.20	17	0.120E+27	-4.90
1987	271	11:47	-18.42	167.79	23	0.190E+27	-5.43
1988	233	23:09	26.52	86.64	35	0.230E+27	-4.49
1990	064	16:38	-18.35	168.04	37	0.330E+27	-4.97
1990	095	21:12	15.57	148.08	15	0.160E+28	-4.17
1991	112	21:56	10.10	-82.77	15	0.330E+28	-5.57
1991	292	21:23	30.22	78.24	15	0.180E+27	-4.62
1992	200	08:36	39.47	143.54	15	0.270E+27	-5.20
1992	246	00:16	11.20	-87.81	15	0.340E+28	-6.47
1992	347	05:29	-8.34	122.49	20	0.510E+28	-4.88
1993	193	13:17	42.71	139.28	17	0.470E+28	-4.55
1993	220	08:34	13.06	145.31	59	0.520E+28	-4.68
1994	153	18:17	-11.03	113.04	15	0.530E+28	-6.57
1994	277	13:22	43.60	147.63	68	0.300E+29	-4.52
1995	136	20:12	-23.05	170.00	25	0.390E+28	-4.40
1995	211	05:11	-24.17	-70.74	29	0.121E+29	-5.41
1995	228	10:27	-5.51	153.64	46	0.460E+28	-5.25
1995	282	15:35	19.34	-104.80	15	0.115E+29	-5.78
1995	337	18:01	44.82	150.17	26	0.820E+28	-5.44
1996	001	08:05	0.74	119.93	15	0.780E+28	-5.48
1996	047	15:22	37.32	142.31	40	0.133E+27	-4.68
1996	048	05:59	-0.67	136.62	15	0.240E+29	-5.74
1996	052	12:51	-9.95	-80.23	15	0.220E+28	-6.06
1996	162	04:03	51.10	-177.41	29	0.810E+28	-5.49
1996	317	16:59	-15.04	-75.37	37	0.460E+28	-5.16

1997	339	11:26	54.31	161.91	34	0.530E+28	-5.46
1998	084	03:12	-62.99	148.64	29	0.170E+29	-5.33
1999	087	19:05	30.38	79.21	15	0.780E+26	-4.35
1999	229	00:01	41.01	29.97	17	0.288E+28	-5.70
1999	263	17:47	24.15	120.80	21	0.340E+28	-5.05
1999	273	16:31	16.20	-96.96	47	0.170E+28	-5.01
1999	330	13:21	-16.08	168.31	15	0.167E+28	-4.88
2000	156	16:28	-4.73	101.94	44	0.750E+28	-4.69
2000	170	14:44	-13.47	97.17	15	0.790E+28	-5.26
2000	321	04:54	-4.56	152.79	24	0.124E+29	-5.57
2000	321	07:42	-5.03	153.17	31	0.650E+28	-5.68
2000	322	21:01	-5.26	152.34	17	0.560E+28	-6.11
2001	013	17:33	12.97	-89.13	56	0.460E+28	-4.85
2001	026	03:16	23.63	70.24	20	0.340E+28	-4.67
2001	174	20:33	-17.28	-72.71	30	0.470E+29	-6.22
2001	318	09:26	35.80	92.91	15	0.590E+28	-6.31
2002	064	21:16	5.92	124.25	29	0.194E+28	-5.21
2002	108	05:02	16.79	-101.22	15	0.150E+27	-5.45
2002	307	22:12	63.23	-144.89	15	0.750E+28	-5.46
2003	141	18:44	36.93	3.58	15	0.201E+27	-4.56
2003	146	09:24	38.94	141.57	61	0.390E+27	-4.09
2003	196	20:27	-1.42	69.47	15	0.251E+28	-5.64
2003	233	12:12	-45.01	166.87	32	0.748E+27	-4.81
2003	268	19:50	42.21	143.84	28	0.300E+29	-5.36
2003	304	01:06	37.89	142.68	15	0.350E+27	-5.32
2003	321	06:43	51.14	177.86	22	0.530E+28	-5.51
2004	283	21:26	11.25	-87.02	39	0.301E+27	-5.26
2004	358	14:59	-49.91	161.25	28	0.160E+29	-5.01
2004	361	00:58	3.09	94.26	29	0.100E+31	-6.40
2005	087	16:09	1.67	97.07	26	0.100E+30	-5.54
2005	166	02:50	41.15	-126.42	20	0.830E+27	-5.55
2005	205	15:42	7.92	91.88	12	0.888E+27	-4.84
2005	228	02:46	38.24	142.05	37	0.760E+27	-4.83
2005	239	18:38	6.77	-82.36	20	0.150E+26	-5.09
2005	281	03:50	34.38	73.47	12	0.294E+28	-4.87
2005	318	21:38	38.22	144.97	18	0.370E+27	-4.53

2005	364	18:26	7.44	-82.33	18	0.160E+26	-4.83
2006	002	06:10	-61.12	-21.39	20	0.137E+28	-5.24
2006	006	03:39	6.60	-82.35	15	0.130E+26	-4.72
2006	053	22:19	-21.20	33.33	12	0.416E+27	-4.70
2006	110	23:25	60.89	167.05	12	0.306E+28	-5.23
2006	123	15:26	-20.39	-173.47	68	0.964E+28	-4.35
2006	198	08:19	-10.28	107.78	20	0.396E+28	-6.13
2006	232	03:41	-61.27	-34.52	17	0.363E+27	-4.74
2006	271	06:22	-16.63	-171.66	16	0.250E+27	-4.39
2006	288	17:07	19.83	-155.94	48	0.131E+27	-4.75
2006	319	11:14	46.71	154.33	14	0.337E+29	-6.01
2006	360	12:26	21.81	120.52	20	0.330E+27	-4.63
2007	013	04:23	46.17	154.80	12	0.165E+29	-4.76
2007	021	11:27	1.10	126.21	22	0.201E+28	-4.82
2007	091	20:39	-7.79	156.34	14	0.160E+29	-5.35
2007	111	17:53	-45.48	-72.95	12	0.280E+26	-4.85
2007	227	23:40	-13.73	-77.04	34	0.111E+29	-5.41
2007	245	01:05	-11.74	165.68	18	0.112E+28	-5.67
2007	255	11:10	-3.78	100.99	24	0.505E+29	-5.78
2007	255	23:49	-2.46	100.13	43	0.150E+29	-5.54
2007	256	03:35	-2.31	99.39	17	0.436E+27	-4.87
2007	273	05:23	-49.26	164.10	13	0.153E+28	-4.79
2007	318	15:40	-22.64	-70.62	38	0.465E+28	-4.88
2007	353	09:30	51.02	-179.27	28	0.630E+27	-5.24
2007	354	07:55	-38.92	178.40	30	0.900E+26	-4.63
2008	128	16:45	36.18	141.61	26	0.240E+27	-4.93
2008	133	06:28	31.44	104.10	13	0.943E+28	-4.97
2008	293	05:10	-21.82	-173.56	43	0.279E+27	-4.41
2008	321	17:02	1.50	122.05	29	0.120E+28	-5.03
2009	003	19:43	-0.38	132.83	15	0.343E+28	-5.12
2009	078	18:17	-23.08	-174.23	49	0.400E+28	-4.57
2009	096	01:32	42.29	13.35	12	0.340E+26	-5.05
2009	148	08:24	16.50	-87.17	12	0.130E+28	-5.00
2009	182	09:30	34.00	25.50	12	0.539E+26	-5.07
2009	196	09:22	-45.85	166.26	24	0.601E+28	-5.33
2009	222	19:55	14.16	92.94	22	0.208E+28	-4.72

2009	245	07:55	-8.12	107.33	53	0.560E+27	-4.43
2009	272	17:48	-15.13	-171.97	12	0.120E+29	-4.82
2009	273	10:16	-0.79	99.67	78	0.267E+28	-4.65
2009	295	00:51	6.64	-82.69	23	0.100E+26	-4.80
2010	003	22:36	-8.88	157.21	12	0.530E+27	-5.18
2010	012	21:53	18.61	-72.62	12	0.440E+27	-4.65
2010	057	20:31	25.86	128.61	18	0.300E+27	-4.51
2010	058	06:34	-35.98	-73.15	23	0.184E+30	-5.35
2010	058	08:01	-38.09	-75.41	20	0.140E+28	-4.49
2010	070	14:39	-34.54	-72.11	13	0.210E+27	-4.15
2010	094	22:40	32.31	-115.39	13	0.728E+27	-5.48
2010	103	23:49	33.05	96.79	16	0.253E+27	-5.27
2010	146	08:53	25.80	130.01	12	0.530E+26	-4.87
2010	298	14:42	-3.71	99.32	12	0.666E+28	-6.22
2010	355	17:19	27.10	143.76	16	0.180E+28	-4.30
2010	359	13:16	-19.67	168.04	17	0.110E+28	-4.45
2011	002	20:20	-38.71	-73.84	19	0.564E+27	-5.18
2011	013	16:16	-20.68	168.34	17	0.370E+27	-4.26
2011	052	23:51	-43.60	172.52	12	0.200E+26	-4.19
2011	068	02:45	38.56	142.78	14	0.120E+28	-5.25
2011	070	05:46	37.52	143.05	20	0.400E+30	-5.65
2011	070	06:25	38.27	144.63	21	0.310E+28	-4.12
2011	097	14:32	38.32	141.85	53	0.590E+27	-4.37
2011	173	21:50	39.99	142.51	41	0.150E+27	-4.82
2011	175	03:09	52.09	-171.77	74	0.740E+27	-4.28
2011	187	19:03	-29.22	-175.83	22	0.300E+28	-4.72
2011	191	00:57	37.98	143.33	22	0.400E+27	-4.65
2012	010	18:37	2.59	92.98	24	0.710E+27	-5.04
2012	240	04:37	12.02	-89.17	12	0.118E+28	-6.42
2012	249	14:42	10.00	-85.64	30	0.340E+28	-5.59
2012	302	03:04	52.61	-132.06	12	0.740E+28	-5.59
2012	312	16:35	14.11	-92.43	21	0.147E+28	-5.44
2012	324	09:44	-5.90	151.79	20	0.136E+26	-4.74
2013	037	01:12	-11.18	165.21	20	0.116E+29	-6.30
2013	106	10:44	27.89	62.21	51	0.511E+28	-4.90
2013	106	22:55	-3.13	142.61	18	0.620E+26	-5.04

2013	267	11:29	26.70	65.04	12	0.481E+28	-5.32
2014	091	23:46	-19.70	-70.81	22	0.231E+29	-5.40
2014	093	05:26	-20.72	-70.90	32	0.707E+26	-5.05
2014	287	03:51	12.33	-88.45	41	0.110E+28	-5.12
2015	259	22:54	-31.13	-72.09	17	0.320E+29	-5.63
2015	338	22:24	-47.74	85.23	29	0.587E+27	-5.20
2016	107	23:58	-0.12	-80.25	22	0.553E+28	-5.15
2016	318	11:02	-42.03	173.85	19	0.704E+28	-5.16
2016	344	19:10	-10.95	161.06	12	0.279E+27	-5.69
